Radiative capture reactions and spectroscopy of multipolar anions in the framework of GamowShell Model.

K. Fossez

Université de Caen Basse-Normandie
U.F.R. de Sciences
ÉCOLE DOCTORALE SIMEM

Thèse de doctorat

présentée et soutenue le : 21 Novembre 2014
par

M. Kévin Fossez

pour obtenir le

DOCTORAT de l'UNIVERSITÉ de CAEN BASSE-NORMANDIE

Spécialité : Constituants élémentaires et physique théorique

Réactions de capture radiative et spectroscopie d'anions multipolaires dans le cadre du Gamow Shell Model

MEMBRES du JURY :

M. W. Ray Garrett (***Rapporteur***)
Professeur, University of Tennessee, Knoxville, TN, USA

M. Morten Hjorth-Jensen (***Rapporteur***)
Professeur, University of Oslo, Norway and Michigan State University, East Lansing, MI, USA

Me. Francesca Gulminelli
Professeure, Université de Caen Basse-Normandie, LPC Caen, France

M. Van Giai Nguyen
Directeur de recherche émérite CNRS, IPNO, Orsay, France

M. Marek Płoszajczak (***Directeur de thèse***)
Directeur de recherche CEA, GANIL, Caen, France

GANIL T 2014-03

Remerciements

Les remerciements n'ont jamais été mon fort, mais j'espère néanmoins que toutes celles et tous ceux qui m'ont apporté quelque chose de positif pourront reconnaître la gratitude que j'éprouve pour eux.

Mes premiers mots formels mais sincères vont aux directeurs du GANIL, Sydney Gales et Florent Staley, qui m'ont permis de faire ma thèse dans ce laboratoire, ainsi qu'aux personnes de l'administration pour leur aide, notamment Virginie Lefebvre et Sabrina Lecerf qui se sont toujours montrées accueillantes. Je tiens également à remercier Michel Lion pour les innombrables articles qu'il m'a trouvé et sa sympathie.

L'achèvement de cette thèse n'aurait pas été possible sans la participation des membres du jury : Francesca Gulminelli et Van Giai Nguyen, ainsi que mes rapporteurs : Ray Garrett et Morten Hjorth-Jensen. Je les remercie notamment pour leur évaluation de mon travail qui est un passage essentiel pour la réalisation de mes objectifs scientifiques, mais également pour les encouragements et leur soutien dans le futur.

Maintenant le plus difficile reste à faire : comment évaluer tout ce que mes collaborateurs m'ont apporté afin de les remercier en conséquence ? Pour commencer je souhaite remercier Marek Płoszajczak, mon directeur de thèse, pour deux choses très différentes. La première concerne l'aspect professionnel. Il m'a non seulement poussé dans la bonne direction afin d'avoir le niveau adéquat pour faire de la recherche, mais surtout cela a été fait avec un *timing* parfait. J'ai également conscience de l'avantage décisif que Marek m'a apporté en me montrant qu'elles étaient les écoles et conférences pertinentes pour moi, car cela m'a permis de m'intégrer dans la communauté travaillant dans le domaine, d'acquérir des connaissances me permettant d'avancer, etc. Il m'a ainsi donné les moyens de ne pas perdre mon temps et une place dans un réseau international. La seconde chose pour laquelle je tiens à remercier Marek, qui est pour moi plus importante que le travail, c'est le comportement. J'avais déjà noté l'humour récurrent et les anecdotes sélectionnées, ainsi que les petites explications culturelles ou historiques, mais il y avait aussi de temps en temps des remarques comme "la famille passe avant le reste". Il n'a pas manqué de prendre des nouvelles de Niels, mon fils, ainsi que de Cécile et est même revenu de Pologne en partant à 3h du matin pour être là à mon mariage. À mon sens, faire preuve d'humanité est bien plus révélateur de l'intelligence que de savoir résoudre des équations.

Nicolas Michel, plus discret, mais tout aussi important mérite lui aussi des remerciements dignes de ce nom. Je sais que Nicolas aime bien être tranquille, mais je souhaite que ceux qui liront cette thèse se rendent compte de l'aide qu'il m'a apporté et par conséquent de ce qu'il pourrait apporter à tous. D'abord, sans l'énorme quantité de travail que Nicolas a fourni en écrivant le code du Gamow Shell Model je n'aurais pas fait grand-chose. Deuxièmement, à chaque fois que j'avais un problème avec le code il finissait toujours par trouver la solution même si cela lui coûtait plusieurs jours de travail. J'ai ainsi eu la chance de travailler avec quelqu'un de compétent et fiable, ce qui est un atout considérable pour réussir. Il a aussi fait preuve d'une ouverture qui m'a mainte fois surpris, en discutant philosophie, économie, politique, jeux vidéo, musique, art, etc. C'est d'ailleurs un expert en ce qui concerne les impôts et les assurances... J'ai eu de plus le plaisir qu'il vienne lui aussi à mon mariage et j'étais très content de voir qu'il me demandait régulièrement comment allait mon fils.

Enfin, le dernier collaborateur important que je souhaite remercier, Witek Nazarewicz, m'a donné un bon aperçu de ce qui m'attendait aux USA. J'ai apprécié les nombreuses critiques constructives et suggestions qui ont relevé le niveau de mon travail et là encore j'ai senti que j'avais en face de moi quelqu'un de franc

et direct, ce qui ne plait pas à beaucoup de monde, mais qui est pourtant un véritable cadeau. Cela est de bon augure et très motivant pour l'avenir. Je tiens aussi à le remercier de l'opportunité qu'il m'a offert de venir aux USA avec ma famille.

En parlant de motivation, je souhaite remercier Olivier Juillet pour la qualité des cours qu'il a donnés lorsque j'étais à l'Université et qui m'ont convaincu de choisir la Physique plutôt que les Mathématiques. J'ai aussi beaucoup aimé le stage qu'il m'a offert à la fin de ma première année de Master, car j'ai eu une idée plus précise du personnage, mais surtout parce que je me suis bien amusé (au sens où les théoriciens l'entendent).

Pour ce qui est des collègues au GANIL, tous ont contribué à la vie du laboratoire et donc à ma thèse, positivement ou non, mais certains en particulier m'ont apporté un peu plus. Je voudrais remercier : François De Olivera pour les discussions sur la vie, l'Univers et tout le reste, mais aussi parce que cela fait toujours plaisir de voir quelqu'un de passionné ; Navin Alahari pour les groupes de discussions que nous avons fait fonctionner quelques temps et pour avoir rappelé qu'un peu de philosophie est très important pour faire de la recherche, là aussi c'est quelqu'un de très motivant ; Beyhan Bastin pour s'être arreté au feu rouge quand je lui ai demandé, meme si une femme ivre a ensuite percuté l'arriere de sa voiture la rendant inutilisable, mais aussi parce que c'est quelqu'un de volontaire ce que j'apprécie ; et Jean-Charles Thomas pour les visites du GANIL qu'il a bien voulu faire pour mes amis alors qu'il n'avait rien à y gagner. Il me reste à remercier les doctorants et postdocs Yannen, Aurore, Guillain et Olivier pour la bonne ambiance quand je suis arrivé, les restos et les discussions, mais aussi Jimmy, George, Paula et Danilo pour les sorties entre postdocs (cherchez l'erreur) et enfin Emil, Roman, Guillaume, Haïfa, Florent, Marija, Jose, Hongliang, Pierre, Matthieu, Quentin, Guoxiang et tous ceux que j'aurais pu oublier. Un peu dans le désordre, je souhaite aussi remercier mes amis de l'Est Maxim et Vladimir pour les blagues russes et les discussions, ainsi que tous ceux avec qui j'ai gardé un lien depuis longtemps comme Dimitri et Élise, Clément, Fleur et Samuel (Momo), Julien et Florent...

Mon début de thèse a commencé par une prise de conscience plutôt désagréable sur la nature humaine, mais de façon assez innatendue ma fin de thèse a été marquée par trois découvertes importantes qui ont nuancé ma prise de conscience initiale. La première fut celle de mon collègue de bureau québécois Mark Boisjoli, qui était là juste devant moi et comme un idiot je n'avais même pas remarqué qu'il était non seulement sympa, mais surtout très humain, bien plus que la plupart des gens. J'ai ainsi eu le plaisir de faire du sport, des sorties et des soirées en sa compagnie et de constater que je venais de trouver le genre d'ami que l'on garde toute sa vie et pour cela je le remercie. À peu près au même moment, j'ai eu le plaisir de connaître Camille, Florie et Amélie que je remercie pour tous les bons moments avec Cécile, Mark et Alexis. La deuxième découverte fut celle des amis de Cyceron, qui étaient à quelques mètres de mon bureau et tout ce qu'il manquait pour les connaître c'était un peu de culot et d'intérêt pour les neurosciences. J'ai ici aussi trouvé des personnes qui ont enrichi mon quotidien par leur sympathie, leur humour et leur accueil. Je tiens à remercier en premier lieu Marie qui m'a aidé à organiser les sorties et les visites de nos laboratoires respectifs. Sans elle je n'aurais jamais pu satisfaire ma curiosité pour les neurosciences et elle s'est avérée être une personne authentique. Je pense avoir trouvé là aussi une amie digne de ce nom. Je souhaite également dire merci à Éloïse et Flavie, pour qui c'est aussi la fin de la thèse, car j'ai apprécié leur présence, ainsi qu'à Mathilde qui me semble indissociable de ce petit groupe et que je souhaite aussi revoir à l'avenir. Enfin, je remercie Camille, Arnaud, Romain, Nolwenn, Eric et les autres pour leur bonne humeur, les sorties et les visites de leur laboratoire. La troisième et dernière découverte c'est Alexis, je m'attendais à un blaireau, mais non. Tous les jours, je découvre que nous avons plus de points communs que n'importe qui dans mon entourage, ce qui laisse entendre que j'ai de nouveau trouvé un bon ami. Il a organisé ma fin de soutenance et je ferai de mon mieux pour lui rendre la pareille. Au delà de nos ressemblances ou de notre bonne entente, nous avons heureusement bien assez de différences pour avoir des débats très amusants sur à peu près tout et n'importe quoi, ce qui quelque chose de rare et appréciable.

Finalement, dans les remerciements la partie immergée de l'iceberg c'est la famille, ce qui est dit est

loin de rendre compte de la réalité. Mon père m'a toujours dit que je devais aller le plus loin possible pour faire un métier qui me plait : c'est fait. Ma mère m'a toujours dit de ne pas me prendre la tête : dans un sens, c'est fait aussi, j'ai suivi mon goût pour les sciences sans me forcer à quoi que ce soit. J'ai surtout eu la garantie qu'en cas de problème je ne serais pas seul et j'en ai eu la preuve, ce qui m'a donné beaucoup de confiance. Je n'ai réalisé que très tard l'importance que mon frère avait pour moi, mais bizarrement lui l'a toujours compris, son soutien moral m'a ainsi doublement aidé. Dans la famille, je rajoute deux amis car pour eux la différence n'est pas évidente : Audric et Romain, car même si je ne les vois pas souvent ils ont toujours été là.

Je souhaite aussi remercier mes beaux-parents, car sans rien leur demander ils m'ont aidé à bien des niveaux et m'ont fait gagner beaucoup de temps pour ma thèse.

Pendant ma thèse, j'ai aussi eu la chance de fonder ma propre famille et c'est probablement ce que j'ai fait de mieux en trois ans. Un grand merci à Cécile pour tout ce qu'elle a fait pour moi et en particulier de m'avoir permis de travailler autant que possible en s'occupant de Niels, mais aussi pour avoir préparé un pot de thèse excellent. J'ai très peu de certitudes dans la vie, mais ta présence en fait partie. Merci aussi à Niels d'avoir pimenté cette fin de thèse, toujours accompagné de Spin qui n'a pas fini de courir.

J'étais loin d'imaginer tout cela en commençant ma thèse !

Contents

Introduction

> This chapter of physics, known as "nuclear physics", to which Rutherford contributed so much, is, from the experimental point of view, the most interesting. But a theory, simple in its fundamental ideas and connecting the rich variety of facts in the domain of nuclear physics, is still lacking.
>
> A. Einstein and L. Infeld, The evolution of physics, 1936

Nowadays, the experimental and theoretical studies of open quantum systems (OQS) became a challenge in various fields of physics: nuclear physics, atomic and molecular physics, quantum optics, etc. These systems are strongly coupled to the environment of scattering states and decay channels, and have generic properties which are common to all weakly bound and unbound mesoscopic systems [1, 2].

OQSs are characterized by their bound states, resonances and decay channels (scattering states). While bound and scattering states are ordinary objects in the standard quantum mechanics, the resonances occupy a particular place since they describe time-asymmetric processes. Resonances are intrinsic properties of quantum systems, associated with their natural frequencies. They are defined by a real energy E and a decay width Γ or a half-life $T_{1/2} = \hbar \ln(2)/\Gamma$. The resonances are omnipresent in quantum systems: from hadrons and atomic nuclei to quantum dots, and provide the backbone of their experimental studies. Spectacular examples of OQSs in nuclear physics are the halo nuclei with halo nucleons in the classically forbidden region [3], the Borromean nuclei [4] which are weakly bound three-body systems characterized by pairwise constituents with no bound states, and the near-threshold correlated structures or clusters like dineutron/diproton or α-cluster states. In atomic and molecular physics, the variety of interactions (Coulomb, atom-atom, dipole-dipole, dipole-electron, etc.) and the experimental possibilities of either tuning [5] the scattering length of the two-body interaction or controlling the external environment of the studied system using laser fields, make these domains of physics particularly propitious for studies of salient features of the OQSs. Recent experimental discoveries and theoretical developments concern, for example: Rydberg atoms [6], Efimov states [7–9], superradiance phenomena [10, 11], exceptional points [12–14], or near-threshold clustering phenomena [15, 16]. All these different developments are encompassed in the non-Hermitian quantum mechanics [17] which aims at describing the closed quantum systems (CQS) and OQS in a unified formalism.

Historically, the study of low energy spectra of atomic nuclei has been done in the bound state approximation, where the nucleus is considered as the CQS. This approximation is used in the nuclear Shell Model (SM) [18–20]. In this model, nucleons occupy selected (sub)shells of a harmonic oscillator (HO) potential. Tremendous success of SM in the description of low energy nuclear spectroscopy did not help to stimulate efforts to generalize the SM. Moreover, the necessary mathematical framework was not avaible at that time to make a sensible proposition of such an OQS generalization. At the same time, the reaction theory was unable to include the underlying complex structure of the target and the projectile nuclei microscopically. The reconciliation of the reaction theory with the SM description of nuclear structure was identified very

early as a key challenge to the nuclear theory. In the attempt to face this challenge, Feshbach introduced the projection operator formalism [21–24] which led to the development of the Continuum Shell Model (CSM) [24–26].

In nuclear physics, there is a strong interplay between the many-body dynamics, the nuclear interaction and the continuum effects for weakly bound and unbound states. Therefore it is of utmost importance to understand both structure and reaction aspects of the nuclear many-body problem in a unified framework. Such a framework is provided by the CSM, which is the OQS extension of the SM in Hilbert space. CSM is formulated in the CC framework which is well suited for decay processes and reactions. On the other hand, the description of spectroscopy in the CSM requires its reformulation to include the discrete part of the continuum spectrum (s.p. resonances) in the configuration mixing. A recent realization of this approach using realistic SM interactions, the Shell Model Embedded in the Continuum (SMEC) [27, 28], allows to include reaction (decay) channels with up to two nucleons in the scattering continuum. One should mention that the continuum couplings generate the many-body correlations in the SM wave functions, which cannot be distinguished from effects of the many-body interaction in truncated subspaces of Hilbert space.

An alternative approach, the so-called Gamow Shell Model (GSM) [29–31], is the complex-energy formulation of the CSM based on the Berggren ensemble of single particle (s.p.) states which includes bound states, decaying resonances and complex-energy scattering states [32, 33]. The many-body Schrödinger equation in GSM is solved in the basis of Slater determinants generated by s.p. states of the Berggren ensemble. In this formulation, one cannot describe reactions since, even if all decay channels are included, the physical decay channels cannot be identified with the GSM eigenstates. Therefore, 50 years later, we face again the same challenge to reconciliate the modern configuration interaction approach, the GSM, with the reaction theory.

The accumulation of experimental data on weakly bound and unbound nuclei motivates the development of various microscopic approaches which take into account some aspects of the continuum to solve the nuclear many-body problem. Using an inert core, the GSM approach can be applied for a description of the spectroscopy of exotic nuclei with, *a priori*, no restriction on the number of nucleons in the s.p. continuum. Up to now, only phenomenological two-body interactions have been used. One should remind that, as in the real-energy CSM/SMEC, the couplings to continuum states generate many-body interactions. Importance of these many-body interactions, and the external configuration mixing of unperturbed SM states *via* the coupling to the decay (reaction) channels, is still an open question. Different approaches, such as the No-Core Shell Model (NCSM) [34–36], the Coupled Cluster Theory (CCT) [37–39], and the No-Core Gamow Shell Model (NCGSM) [40], are able to describe the spectroscopy of nuclei in an *ab initio* framework, using interactions derived from first principles using the chiral perturbation theory. The NCSM can be extended to the description of nuclear reactions using the Resonating Group Method (RGM) [41, 42]. In this extension, denoted NCSM/RGM [43], the target and the projectile are still described in the bound state approximation and the continuum of a system projectile plus target is approximated *via* the outgoing boundary conditions of channel states. The CCT is an *ab initio* approach to describe the structure of medium-heavy nuclei with up to two nucleons outside of the nearest closed (sub)shell nucleus and, as in the GSM, can be formulated in the Berggren ensemble. CCT is using modern chiral interactions and results can be improved systematically by including additional many-body correlations [44]. Finally, the NCGSM is an exact *ab initio* approach based on the GSM, which can describe the structure of bound and resonance states in light nuclei ($A < 7$) using chiral and two- and three-body interactions [40].

The formulation of the GSM in the coupled-channel (CC) framework (GSM-CC) for elastic and inelastic reactions with one-body projectile has been achieved recently [45]. The present work focuses on extending the GSM-CC approach for the description of proton/neutron radiative capture processes. This approach is of particular interest in the study of radiative capture reactions at astrophysical energies, since it is difficult if not impossible to measure directly the cross sections at such low energies. Several issues are important in this context: (i) the many-body structure of target and projectile nuclei, (ii) the antisymmetry of their wavefunctions, and (iii) the treatment of both the individual continua of target and projectile, and the

continuum of a composite target plus projectile system. The GSM-CC approach adresses all these issues with the GSM description of the target and the projectile, and a full treatment of the antisymmetry in a combined target plus projectile system. The present version of GSM-CC code for proton/neutron radiative capture reactions includes only the resonant channels. This may not be sufficient, in particular for weakly bound target nuclei. The importance of these missing nonresonant channels in the description of the target plus projectile system can be checked by comparing energies of discrete states (resonances) in GSM-CC with those obtained in GSM. In the present work, the GSM-CC approach is tested and applied to the description of $^{17}\mathrm{F}(p,\gamma)^{18}\mathrm{Ne}$, $^{7}\mathrm{Be}(p,\gamma)^{8}\mathrm{B}$ and $^{7}\mathrm{Li}(n,\gamma)^{8}\mathrm{Li}$ radiative capture reactions.

Theoretical tools which have been developed to describe nuclear OQSs can be used also in other fields of physics. The GSM is using basis states that are not normalizable in the usual sense and their treatment requires new mathematical concepts of the Rigged Hilbert Space (RHS) [46–48]. RHS is a construction designed to link the distribution and square-integrable aspects of functional analysis. It provides a natural setting of quantum mechanics, in which resonance spectrum, Dirac bras and kets formulation and Heisenberg uncertainty relations have place. In GSM, s.p. resonances are explicitly introduced using the Berggren basis. This s.p. basis is well suited for the description of certain molecular system like the dipolar anions. Indeed, the dipolar anions are composed of a neutral dipolar molecule and a valence electron. The long-range dipolar potential is proportional to $-1/r^2$, where r is the distance between the neutral molecule and the valence electron, and its asymptotic solutions are not known analytically. It has been shown [49,50] that realistic bound spectra for dipolar anions can be obtained if the rotational motion of the dipole is taken into account. The correct description of such systems requires a precise treatment of the asymptotics, as well as the complete treatment of couplings between the external electron and the rotating dipolar molecule. Up to now, only bound spectra of dipolar anions have been calculated in the CC framework by a direct integration of the Schrödinger equation [49,51,52]. In the present work, the first investigation of resonances in dipolar anions is achieved using the Berggren ensemble method (BEM) [53,54].

Weakly bound and unbound nuclei, as well as dipolar anions are both OQSs. The common theoretical formalism is presented in the first part of Sec.1. In particular, the Gamow states, the RHS formalism and the Berggren basis used in the description of dipolar anions are presented in Sec.1.1.3. Then, the GSM which is used to describe nuclear many-body open quantum systems (MBOQS) is introduced in Sec.1.1.4. The second part of Sec.1 is dedicated to the formulation of the GSM in the CC representation. The definition of channels and the derivation of CC equations are done in Secs.1.2.1 and 1.2.2. Finally, the numerical methods used in GSM-CC calculations are presented in Sec.1.2.3.

In Sec.2, the GSM-CC formalism for the description of proton/neutron radiative capture reactions is introduced. This section contains a presentation of the radiative capture process in Sec.2.2, the radiative proton/neutron cross section in Sec.2.3, and the method of calculation in Secs.2.4 and 2.5. Finally, GSM-CC results for $^{17}\mathrm{F}(p,\gamma)^{18}\mathrm{Ne}$, $^{7}\mathrm{Be}(p,\gamma)^{8}\mathrm{B}$ and $^{7}\mathrm{Li}(n,\gamma)^{8}\mathrm{Li}$ reactions are presented in Sec.2.6.

The study of dipolar anions is discussed in Sec.3. Dipolar anions and their effective Hamiltonian are introduced in Secs.3.1 and 3.2. The CC formulation of the one-body Schrödinger equation is done in Sec.3.3, and the formula for the density of the valence electron in the body-fixed frame is discussed in Sec.3.4. Then, the results for bound states of LiI^-, LiCl^-, LiF^- and LiH^- are presented in Sec.3.5 which serve as a test to compare the commonly used direct integration method (DIM) with the BEM. Finally, results for bound states and resonances of HCN^- anion are presented in Sec.3.6.

Chapter 1

Towards a unified description of nuclear structure and reactions

In 1932, Bartlett [55, 56] proposed an analogy between the shell structure of atoms and nuclei. One year later, Elsasser [57–59] pointed out the experimental evidence for the existence of "magic numbers" of nucleons and suggested an independent particle approach. It is only in 1948-49 that Maria Goeppert-Mayer [18, 19] and independantly O. Haxel, J. H. D. Jensen and H. E. Suess [20] formulated the nuclear shell model, by introducing the spin-orbit interaction in order to explain the magic numbers of nucleons. The explanation of the shell structure comes from the short range of the interaction between nucleons and from the Pauli principle, which combined allow to consider the nucleons as quasi-independent. This approximation underlies the nuclear shell model, which is still a basic tool in the studies of spectra of nuclei (see Refs. [60, 61] for recent reviews).

The SM was formulated for CQS, *i.e.* without couplings to the decay channels and the scattering continuum. As such, the SM has been applied successfully to the description of low-lying states in stable nuclei, but fails to describe nuclear resonances. In particular, the SM is unable to describe unstable nuclei with respeect to the emission of particles (proton, neutron, α, etc.) or the spontaneous fission. Indeed, there exist extreme cases in the vicinity of nuclear drip-lines where the influence of the continuum can no longer be neglected. This is the case of the halo nuclei, discovered in eighties by I. Tanihata [3], whose structure resembles a well bound core surrounded by a halo of one or more nucleons in the classically forbidden region. Moreover, the low energy reactions involving weakly bound nuclei exhibit new features which cannot be properly described using the standard reaction theory.

Thus, the formulation of the SM for OQS appears as a natural solution to the problem of the description of weakly bound and unbound nuclei. The mathematical formulation goes back to Feshbach [21–23], Fano [62] and Mahaux and Weidenmüller [24] who introduced the projection operator formalism. This has given foundation of the CSM [25, 26, 63–65] in Hilbert space. The first realistic version of the CSM, the Shell Model Embedded in the Continuum, was developed in 1998 by Bennaceur *et al.* [15, 27, 66–76]. In CSM, the total wave function is obtained in the CC formalism and consists of an internal part given by the SM wave function and an external part given by the continuum wave function (see Ref. [28] for a detailed discussion).

Recently, the SM for OQS has also been formulated in the complex-energy plane [29–31, 77–84] using the complete s.p. Berggren basis [32, 33, 85, 86], which contains bound states, resonances and complex-energy scattering states. In the resulting GSM, the norm of resonances is calculated using the exterior complex-scaling method [87]. The GSM can be conveniently formulated in an extended Hilbert space: the RHS [46–48, 88–93]. The RHS, also called Gel'fand triple, nested Hilbert space, or equipped Hilbert space, is also suitable for extending quantum mechanics into the time-asymmetric processes, offering a unified treatment of bound, resonance and scattering states.

The aim of this chapter is to present physical concepts and mathematical tools to formulate a unified

description of the structure and the reactions within the framework of the GSM.

In Sec.1.1, the GSM formalism used in the description of spectroscopy of bound and unbound nuclei is presented. A first part is dedicated to the standard SM and the CSM/SMEC approaches. Then, the complex-energy continuum, the Gamow states, the RHS, the Berggren basis and the normalization of resonances are introduced. These concepts are also employed in the description of dipolar anions in Sec.3. Finally, the GSM formalism is detailed.

In Sec.1.2, the formulation of GSM in the CC formalism is presented. The definition of reaction channels and the derivation of CC equations are done in a general case, since these equations are also used for the description of dipolar anions. Then, salient features of the CC formulation of the GSM are detailed. In particular, the expansion of channel states in the Berggren basis, the calculation of Hamiltonian matrix elements, the orthogonalization of channel states, the method of equivalent potential and its symmetrization, and the Direct Integration Method are presented in details.

Finally, Sec.1.3 gives a brief overview of the methods to include the scattering continuum.

1.1 From discrete states to the continuum

1.1.1 The nuclear shell model

The nuclear SM[1] [18–20,60,61] is a tool of choice in the study of nuclear structure. It allows to explain the existence of the magic numbers of nucleons observed experimentally, but also to describe numerous nuclear moments and electromagnetic transitions. The SM is a non-relativistic approach which solves the N-body stationary Schrödinger equation in a chosen subspace of Hilbert space. In the first approximation, due to the short range of the nuclear interaction and to the Pauli principle, nucleons can be considered as independent particles that evolve in a mean-field potential generated by all other particles. In the independent particle picture, the Hamiltonian of a nucleus with A nucleons writes:

$$\hat{H} = \sum_{i=1}^{A} \hat{h}_i \tag{1.1}$$

with $\hat{h}_i$ the Hamiltonian associated with the nucleon i, which contains the kinetic energy term:

$$\hat{h}_i = \frac{\hat{\vec{p}}_i^2}{2m} + U(\hat{r}_i) \tag{1.2}$$

and the mean-field potential:

$$U(\hat{r}) = \frac{1}{2} m w^2 \hat{\vec{r}}^2 + V_{so} \hat{\vec{l}}.\hat{\vec{s}} \tag{1.3}$$

The harmonic oscillator potential in (1.3) is a parabolic approximation of a true mean-field potential. The last term in this equation is the spin-orbit potential [19]. In this approximation, to solve the N-body stationary Schrödinger equation one solves N one-body problems. Indeed, the energy E_i associated with a Slater determinant is the sum of single-particle energies.

This independent particle approach can reproduce the magic numbers of nucleons but is not sufficient to explain the detailed spectroscopy of nuclei. For that, it is necessary to introduce an interaction between nucleons:

$$\hat{H} = \sum_{i=1}^{A} \hat{t}_i + \sum_{i<j}^{A} \hat{V}_{ij} + \sum_{i<j<k}^{A} \hat{V}_{ijk} + \cdots \tag{1.4}$$

First SM calculations with a residual two-body interaction have been done by Lane [94] and Kurath [95] in fiftieth of the last century. Recently, more and more studies show the importance of the three-body

[1] The SM or Interacting Shell Model is also called the Configuration Interaction model in quantum chemistry.

interaction, even in well bound nuclei [96–103]. However still today most of SM calculations are performed using a two-body interaction to describe the spectroscopy of nuclei. Also in this study, only the two-body interaction is considered.

Standard SM calculations are performed in a space consisting of a closed-shell core, considered as inert, and N_{val} valence nucleons distributed in the shells above the core. The Hamiltonian is divided into three parts:

$$\hat{H} = \hat{H}_c + \sum_{i=1}^{N_{\text{val}}} \hat{t}_i + \sum_{i<j}^{N_{\text{val}}} \hat{V}_{ij} \tag{1.5}$$

where $\hat{H}_c$ is the Hamiltonian of the core. Adding and substracting the one-body mean field, one obtains:

$$\hat{H} = \hat{H}_c + \sum_{i=1}^{N_{\text{val}}} \hat{t}_i + \sum_{i<j}^{N_{\text{val}}} \hat{V}_{ij} = \underbrace{\hat{H}_c + \sum_{i=1}^{N_{\text{val}}} U(\hat{r}_i)}_{\hat{H}_{\text{base}}} + \sum_{i=1}^{N_{\text{val}}} \hat{t}_i + \underbrace{\left(\sum_{i<j}^{N_{\text{val}}} \hat{V}_{ij} - \sum_{i=1}^{N_{\text{val}}} U(\hat{r}_i) \right)}_{\hat{H}_{\text{res}}} \tag{1.6}$$

where $\hat{H}_{\text{base}}$ is the potential which generates the s.p. basis, and $\hat{H}_{\text{res}}$ is the residual term. The Schrödinger equation of SM is then a matrix problem in the basis formed by all Slater determinants generated by $\hat{H}_{\text{base}}$.

1.1.2 The real-energy continuum

The insufficiency of SM to describe the spectroscopy of weakly bound and unbound nuclei, led to the elaboration of models which take into account continuum states explicitly. This is the case in particular of the CSM [25, 26, 28, 63–65, 104–106] and the SMEC [27, 28, 66–74] whose common mathematical foundation will be briefly presented hereafter.

1.1.2.1 The Newton basis

CSM/SMEC approaches in Hilbert space use the one-body Newton basis [107], formed by the real energy discrete and continuum eigenstates of a one-body potential:

$$\sum_{n\epsilon(b)} |u(k_n)\rangle \langle u(k_n)| + \int_0^\infty dk \, |u(k)\rangle \langle u(k)| = \hat{\mathbb{1}} \tag{1.7}$$

The discrete sum runs over bound (b) states and the integral is over the real-energy continuum. The bound states are normalized in a usual sense, while the continuum states are normalized to the Dirac distribution:

$$\langle u(k)|u(k')\rangle = \delta(k - k') \tag{1.8}$$

1.1.2.2 The Continuum Shell Model (CSM)

The Feshbach projection formalism [21–23] allows to separate the Hilbert space into the subspace Q of N-body bound states, and the subspace P of $(N-n)$-body bound states coupled to $n = 1, 2, \cdots, p$ nucleons in the continuum: $P = P_1 \oplus P_2 \oplus \cdots \oplus P_p$. The projection operators into the Q and P subspaces are denoted $\hat{Q}$ and $\hat{P}$, respectively, and satisfy: $\hat{P} + \hat{Q} = \hat{\mathbb{1}}$. This theoreretical development gave rise to the CSM [25, 104, 106] and the SMEC [28]. The $\hat{P}$ projector for $p \leq N$ active particles splits into $\hat{P}_n$ operators $(n = 1, 2, \cdots, p)$, each one projecting into a subspace containing the $(N-n)$-body bound states coupled to $n \leq p$ particles in the continuum. In SMEC [72, 108, 109], the maximal number of particles in the continuum states is $p = 2$.

In the limit of one particle in the continuum, the CSM/SMEC Hamiltonian writes:

$$\hat{H} = \hat{Q}\hat{H}\hat{Q} + \hat{P}\hat{H}\hat{P} + \hat{P}\hat{H}\hat{Q} + \hat{Q}\hat{H}\hat{P} = \hat{H}_{QQ} + \hat{H}_{PP} + \hat{H}_{PQ} + \hat{H}_{QP} \tag{1.9}$$

and the total wave function is:

$$|\Psi\rangle = (\hat{P} + \hat{Q})\,|\Psi\rangle = |\Psi_P\rangle + |\Psi_Q\rangle \tag{1.10}$$

Then, to obtain the CSM/SMEC equations, one projects the Schrödinger equation into the subspaces P and Q:

$$\begin{aligned} (\hat{H}_{QQ} - E)\,|\Psi_Q\rangle &= -\hat{H}_{QP}\,|\Psi_P\rangle \\ (\hat{H}_{PP} - E)\,|\Psi_P\rangle &= -\hat{H}_{PQ}\,|\Psi_Q\rangle \end{aligned} \tag{1.11}$$

For more particles in the scattering continuum and, hence, more subspaces $P_1, \cdots, P_p$, the number of different couplings between all subspaces increases very fast making the formalism rather cumbersome. This is mainly due to the use of Jacobi coordinates, to have intrinsic states and avoid the spurious center-of-mass (CM) components in the wave functions. Jacobi coordinates do not correspond to particle positions, and therefore the antisymmetrization is difficult.

The SMEC approach [28], which provides a unified approach for nuclear structure and reactions in Hilbert space, allows to describe numerous reactions, such as neutron and proton elastic scattering reactions [27], or radiative capture reactions [66–68, 73]. The importance of the structure of the target has been pointed out in Coulomb dissociation reactions [69], and in the first-forbidden β-decay [70]. The extension to two particles in the continuum allowed the study of the spontaneous $2p$ radiactivity [71, 72, 74, 108]. Recently, the SMEC approach has been used to study the nuclear clustering as a universal near-threshold effect [15, 16].

The identification of decay channels allows for a unified description of the structure and of reactions, but it also implies that for each considered channel one has one scattering continuum. The description of many-body resonances requires the inclusion of a large number of channels, severely limiting numerical applications. This problem is common to the CSM/SMEC [25–28], the GSM [29–31], and to the No-Core Shell Model with Continuum (NCSMC) [36, 110, 111] approaches.

1.1.3 The complex-energy continuum

Gamow Shell Model has been proposed in 2002 by Michel, Nazarewicz and Płoszajczak [29, 31, 77, 79, 112, 113]. A similar approach has been developed independently by the Stockholm-Debrecen group [30, 78, 82, 114]. As compared to CSM/SMEC, in GSM there is a configuration mixing in the full space and not only in the Q subspace. On the other hand, there is no separation between different decay channels so only the total decay width can be calculated. The lack of separation of the decay channels in GSM is an obstacle for the description of reactions, and thus it is the reason why its CC formulation has been proposed recently [45].

The generalization of SM in the complex-energy plane requires new mathematical tools and concepts, which have been developed over many years by physicists and mathematicians. It is this convolution of ideas, new mathematical concepts and numerical tools which finally lead to the formulation of the GSM.

1.1.3.1 Gamow states

In order to describe α radioactivity, Gamow introduced discrete solutions of the quasi-stationary Schrödinger equation that are regular at the origin and with outgoing boundary conditions [115]. These states are associated with complex-energies:

$$\tilde{E}_n = E_n + i\frac{\Gamma_n}{2} \tag{1.12}$$

and lead to wave functions which are decaying as:

$$e^{\frac{i}{\hbar}\tilde{E}_n t} = e^{\frac{i}{\hbar}E_n t} e^{-\frac{\Gamma_n t}{2\hbar}} \tag{1.13}$$

A comparison with experiment shows that Γ_n is the width of the resonance and corresponds to its life-time *via*:

$$T_{\frac{1}{2},n} = \frac{\hbar \ln 2}{\Gamma_n} \tag{1.14}$$

Later, Siegert[2] rediscovers Gamow states [116] in searching how to obtain analytically the Breit-Wigner formula [117]. These works lead to the first application of Gamow (or Siegert) states in reaction theory [118].

1.1.3.2 Spectrum of Hilbert space operators

Complex-energy eigenstates of the Schrödinger equation allow to describe certain time-dependent phenomena within the quasi-stationary formalism. The relation between the imaginary part of a complex energy and the life-time comes from a comparison between an exponential decrease of the wave function in time (1.13), and an exponential decay of the excited states in quantum systems. The counterpart of this temporal decrease is an exponential divergence of the radial wave function to ensure the flux conservation [119]. From the complex eigenenergy $\tilde{E}_n$ of the system, it is possible to calculate the wave number of the system:

$$k_n = \sqrt{\frac{2\mu\tilde{E}_n}{\hbar^2}} = \kappa_n - i\gamma_n \tag{1.15}$$

with $\kappa_n, \gamma_n > 0$ in the case of a decaying state. Thus, at long distances, the radial part of the wave function is proportional to:

$$e^{ik_n r} = e^{i\kappa_n r} e^{\gamma_n r} \tag{1.16}$$

and increases exponentially. States with $k = -i\gamma$ and $\gamma > 0$ are called anti-bound states or virtual states. They are associated with negative energies like bound states, but they can be seen as unstable states which decay if there is any small perturbation. Finally, the capturing resonances, with $k_n = -\kappa_n - i\gamma_n$ and $\kappa_n, \gamma_n > 0$, are situated in the third quadrant of the k-plane. They have a radial wave function with the following asymptotics:

$$e^{ik_n r} = e^{-i\kappa_n r} e^{-\gamma_n r} \tag{1.17}$$

Capturing resonances are obtained by a time reversal operation $t \to -t$ applied to decaying resonances [120].

In a more general way, the spectrum $\Sigma(\hat{H})$ of a Hamiltonian $\hat{H}$ in Hilbert space is defined as the set $\{\lambda\} \in \mathbb{C}$ such that the inverse of $\lambda\hat{\mathbb{1}} - \hat{H}$ is not defined. It can be shown that to find this spectrum is equivalent to:

- In a Hilbert space of finite dimension, to solve:

$$\det(\lambda\hat{\mathbb{1}} - \hat{H}) = 0 \tag{1.18}$$

  or equivalently:

$$\hat{H}\,|\Psi\rangle = \lambda\,|\Psi\rangle \tag{1.19}$$

  with $|\Psi\rangle \neq 0$. This is the problem encountered in the SM.

[2] In atomic physics it is more common to speak about the Siegert states, and in nuclear physics to speak about the Gamow states.

- In a Hilbert space of infinite dimension, to introduce the resolvent operator:

$$\hat{R}(\lambda) = (\lambda\hat{\mathbb{1}} - \hat{H})^{-1} \tag{1.20}$$

and to find its singularities. This operator is defined on the set $\lambda \in \rho(\hat{H}) = \mathbb{C}\backslash\{\Sigma(\hat{H})\}$, called the resolvent ensemble of the operator $\hat{H}$, on which $\hat{R}(\lambda)$ is bijective.

From a physical point of view, the interest of the resolvent operator lies in different categories in which the spectrum of $\hat{H}$ can be divided:

1. The point spectrum, which is defined as the set $\lambda \in \Sigma(\hat{H})$ such that the operator $(\lambda\hat{\mathbb{1}} - \hat{H})$ is not injective. This set contains all the solutions of Eq.(1.19). The point spectrum corresponds to the bound states.

2. The continuous spectrum, which is defined as the set $\lambda \in \Sigma(\hat{H})$ such that the operator $(\lambda\hat{\mathbb{1}} - \hat{H})$ is injective but not surjective, and its image is dense in the Hilbert space. The continuous spectrum corresponds to the continuum of scattering states.

3. The residual spectrum which is defined as the set $\lambda \in \Sigma(\hat{H})$ such that the operator $(\lambda\hat{\mathbb{1}} - \hat{H})$ is injective but not surjective, and its image is not dense in the Hilbert space. The residual spectrum corresponds to the resonances.

The link between the residual spectrum of the resolvent operator associated with the Hamiltonian of a system and the Gamow states has been found by Peierls [121]. In this article, the residual spectrum elements are called the poles of the propagator, which are just the singularities of the Green's function (the resolvent operator in the coordinate space).

1.1.3.3 Rigged Hilbert Space

The research of singularities of the resolvent operator showed that a quasi-stationary description of a decaying system leads to a more general spectrum than the one known for closed quantum systems. Nevertheless, the additional spectrum (continuous and residual) does not lie in Hilbert space. Indeed, the exponential growth of the radial part of the wave function for resonances excluded the usual normalization:

$$\int_0^\infty d\vec{r}\,|\chi(\vec{r})|^2 \to \infty \tag{1.21}$$

This inconsistency in the Hilbert space formulation of quantum mechanics was noticed by Dirac in the book [122] where 'bras' and 'kets' notation and the δ-distribution (the Dirac distribution) were introduced for the first time. In 1932, von Neumann formulated quantum mechanics in Hilbert space [123], even though he knew that it was not correct to deal with the continuum states. He made a step further in 1949, by formulating the spectral theory for Hermitian operators [124] and thus succeeded to complete the formalism for closed quantum systems.

It is only in the sixties of the last century that Gel'fand, Vilenkin *et al.* [46] and, independently, Maurin [47] formulated the rigged Hilbert space [3] in order to generalize the Hilbert space to the distributions, called at that time the generalized functions. Moreover, they proved the spectral theorem where discrete and continuum states are treated in the same way (see Ref. [125] for a recent discussion). Independently, Kristensen *et al.* studied solutions of the equation $\hat{p}\hat{q} - \hat{q}\hat{p} = -i\hat{\mathbb{1}}$ and showed that in the case of infinitely dimensional Hilbert space, the solutions lie in a larger space [126–128]. Finally, Schwartz gave a precise definition of the Dirac distribution and founded the distribution theory [129]. It is only during the period

[3] The term *rigged* comes from a bad translation of the russian word "оснащенное"(оснащенное пространства Гильберта) which means equiped or enriched Hilbert space.

Figure 1.1 – Figure from http://arxiv.org/abs/quant-ph/0005024

1964-69 that Böhm [130], Roberts [131, 132], Antoine [133, 134] and Melsheimer [135, 136] realized that RHS provides the rigorous mathematical framework for quantum mechanics. For a recent discussion, see Refs. [137–139].

The RHS [140–144], also called the Gel'fand triplet, is a triad of spaces:

$$\Phi \subset \mathcal{H} \subset \Phi^{\times} \tag{1.22}$$

each one having a topology $(\tau_{\Phi}, \tau_{\mathcal{H}}, \tau_{\Phi^{\times}})$, where $\mathcal{H}$ is a Hilbert space, Φ is a dense subspace of $\mathcal{H}$ and $\Phi^{\times}$ is the space of anti-dual of Φ, *i.e.* the space formed by the anti-linear fonctionals on Φ.

Reminder:

- When a space is completed by a topology, then the elements which are the limits of Cauchy series obtained with the convergence criterium, are adjoint to the space.
- An anti-linear function $f : \mathcal{E} \to \mathbb{C}$ with $\mathcal{E}$ a complex vector space, satisfies the following property:

$$f(x + \lambda y) = f(x) + \lambda^* f(y) \tag{1.23}$$

with $(x, y) \in \mathcal{E}^2$ and $\lambda \in \mathbb{C}$.

The triad is obtained from the linear space with the scalar product Ψ, by supplementing it with three toologies τ_{Φ}, $\tau_{\mathcal{H}}$ and $\tau_{\Phi^{\times}}$. From a mathematical point of view, Φ is the space of test functions, and $\Phi^{\times}$ is the space of distributions. From a physical point of view, the kets of Dirac are in $\Phi^{\times}$. To obtain the bras, it is sufficient to construct a second RHS associated to the first:

$$\Phi \subset \mathcal{H} \subset \Phi' \tag{1.24}$$

where Φ' is the dual space of Φ, which is formed by the linear functional on Φ. To summarize, the resonances and the continuum states are in $\Phi^{\times}$ and Φ', the bound states are in $\mathcal{H}$ and the unbounded operators (*e.g.* the position operator $\hat{x}$) are defined in Φ. It is thus possible to give a meaning to complex mean values and commutation relations.

The RHS gives a rigorous framework for quantum mechanics, by dealing in a unified formalism with the bound states, resonances and scattering states. The norm of a wave function is given by:

$$\int_0^{\infty} dr\, \Psi^2(r) \tag{1.25}$$

which, for bound states, is equivalent to the usual norm in the Hilbert space. It has been shown [145], that the probability amplitude of a transition between an isolated state (Gamow state) and a continuum state is proportional to the Breit-Wigner distribution [117], which leads to a cross section with the Lorentzian profile as observed experimentally. Numerous books [140–144] and articles [137, 146–149] on the RHS are avaible for more details.

1.1.3.4 Normalization of the Gamow states and the Berggren basis

In reaction theory, the problem of the normalization of resonances appeared independently of the developments leading to the RHS. Indeed, contrary to the continuum states, resonances have a probability density which is not constant but increases exponentially in space. A first method of normalization based on the use of a convergence factor $\epsilon > 0$ in the calculation of matrix elements:

$$\langle \psi_f | \hat{O} | \psi_i \rangle = \int_0^\infty dr\, e^{-\epsilon r^2} \psi_f O(r) \psi_i \tag{1.26}$$

has been proposed in 1960 by Zel'dovich for the radial wave functions of neutral particles [150]. In this expression, $|\psi_f\rangle$ and $|\psi_i\rangle$ are one-body Gamow states, and $\hat{O}$ is a bounded operator. The Zel'dovich normalization method was the first step to build the one-body basis including resonances. Indeed, to form such a basis, it is necessary to show that Gamow states are not only normalizable but also orthogonal among each other and with bound states. Humblet and Rosenfeld [118] knew that poles of the scattering matrix are associated with the complex energies corresponding to the resonances, but there was no proof of the orthogonality of these states. It was in 1968 that Tore Berggren [32] used the normalization method of Zel'dovich to show that Gamow states are mutually orthogonal and can be normalized for neutral particles. In this paper, the first one-body basis including explicitly bound states, resonances and scattering states has been formulated. This basis, called the Berggren basis, is described hereafter. The proof of the completeness of Berggren basis for charged particles has been done later by Michel, Nazarewicz and Płoszajczak [79,151].

——— *The Berggren basis* ———

The Berggren s.p. basis [32] is an extension of Newton basis (1.7) in the complex-energy plane. The real-energy continuum is replaced by a complex contour L^+ in k-plane which encompasses the resonances, and then joins the real-k axis and continues to $k \to \infty$. Thus, the residue theorem allows to isolate resonances (poles of the resolvent operator) between the complex contour and the real axis:

$$\sum_{n \in (b,d)} |u(k_n)\rangle \langle u(k_n)| + \int_{L^+} dk\, |u(k)\rangle \langle u(k)| = \hat{\mathbb{1}} \tag{1.27}$$

The contour L^+ lies in the fourth quadrant ($\arg(k_n) > -\pi/4$), as it is shown in Fig.1.2, and surrounds only decaying resonances ($k_n = \kappa_n - i\gamma_n$ and $\kappa_n > \gamma_n > 0$). In practice, resonances are discrete solutions with outgoing boundary conditions of a one-body Woods-Saxon (WS) or Hartree-Fock potential. Due to the Cauchy's integral theorem, for a given set of resonances, the precise form of the contour L^+ is of no importance. The derivation of the Berggren completeness relation (1.27) in the simplest case, *i.e.* for scattering states with the plane wave asymptotics [77], is detailed in Appendix A.2.

Anti-bound states (virtual) states ($k = -i\gamma$ and $\gamma > 0$) cannot be observed directly, but their presence near the threshold increases the cross section of a low-energy scattering process [107, 152–154] since the density of states increases near the poles of the resolvent operator [155].

——— *Uniform complex scaling* ———

The normalization method of Zel'dovich (1.26) is numerically unstable because it requires handling very large numbers in the calculation of integrals. To circumvent this problem Hokkyo proposed the uniform complex-scaling approach [156]. Few years later, Romo proposed an alternative method based on the use of

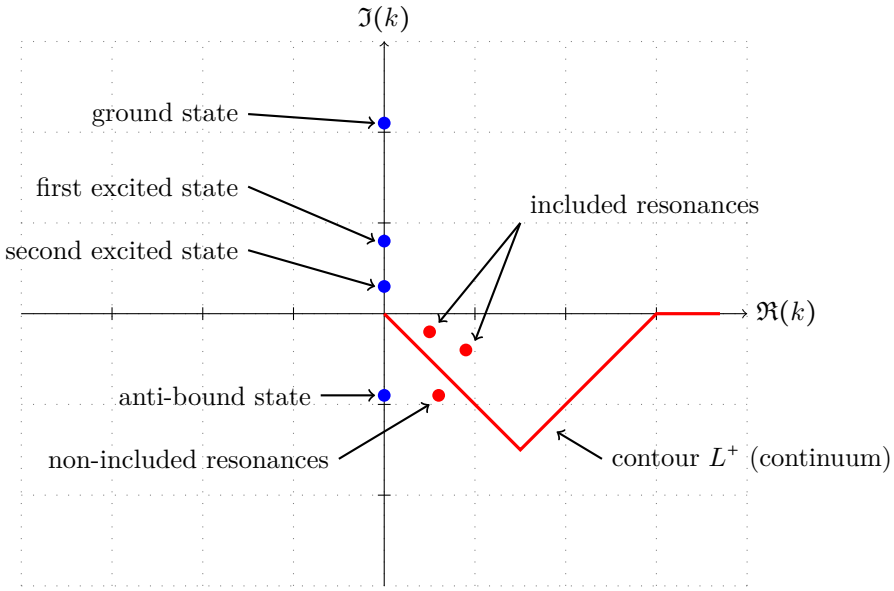

Figure 1.2 – Berggren basis in the complex k-plane.

the Green's function and its analytic continuation in the complex energy plane [157]. The uniform complex-scaling method consists of the rotation $\vec{r} \to e^{i\theta}\vec{r}$ in a complex plane, by applying the operator $\hat{U}(\theta)$ on the one-body wave functions [158, 159]:

$$\hat{U}(\theta)\psi(\vec{r}) = e^{i\frac{3}{2}\theta}\psi(\vec{r}e^{i\theta}) \tag{1.28}$$

The factor $e^{i\frac{3}{2}\theta}$ in the above expression comes from the dimension of the space [160]. This transformation guarantees that wave functions associated to resonances are normalizable [161–163]. Thus, the transformed Hamiltonian becomes:

$$\hat{h}_\theta(\vec{r}) = \hat{U}(\theta)\hat{h}(\vec{r})\hat{U}^{-1}(\theta) \tag{1.29}$$

If $\hat{h}_\theta(\vec{r})$ is dilatation-analytic [164], it has the same bound states as $\hat{h}(\vec{r})$. The general derivation for this particular category of Hamiltonians is given by the Aguilar–Balslev–Combes (ABC) theorem [161,162]. The uniform complex-scaling thus appears as a generalization of quantum mechanics to include resonances [163] which is different from the RHS approach.

——— *Exterior complex-scaling* ———

In nuclear physics, most of potentials are not dilatation-analytic. Consequently, the uniform complex-scaling is not adapted to a the general problem. In 1971, Gyarmati and Vertse [87] proved the equivalence between the Zel'dovich method and the uniform complex-scaling and then introduced the exterior complex-scaling method. They also proved the existence of a norm for charged particles (protons). The exterior complex-scaling [165] transforms only the tail of the radial wave function of the resonance by a rotation operator $\hat{U}_a(\theta)$:

$$\begin{aligned} \hat{U}_a(\theta)\chi(r) &= \chi(r) && \text{if } r \le r_a \\ &= \chi(r_a + |r - r_a|e^{i\theta}) && \text{if } |r| > r_a \end{aligned} \tag{1.30}$$

Thus, this method can be applied to any potential and the result, if converged, does not depend on the parameters a and θ.

——— *Practical use of the Berggren basis* ———

The first application of the Berggren basis in an SM type calculation has been achieved by Michel *et al.* [29], paving the way for a unified description of structure and reactions. Several other attempts were done by extending the complex contour to include anti-bound states [82,112,114]. These studies have shown that the generalized contour including anti-bound states is less efficient for practical applications [112] because it requires significantly denser discretization of the contour.

——— *Interpretation of the complex eigenvalues* ———

In Hilbert space formulation of quantum mechanics, *i.e.* for closed quantum systems, the mean value of an operator $\hat{o}$ associated to an observable in an eigenstate $|\psi(k)\rangle$ is always real:

$$\langle\psi(k)|\hat{o}|\psi(k)\rangle = \langle\hat{o}\rangle_{\psi(k)} \in \mathbb{R} \tag{1.31}$$

This is not the case in RHS formulation of quantum mechanics, where time-dependent phenomena like resonances can be treated. For the resonance, the mean value of an operator $\hat{o}$ is:

$$\langle\hat{o}\rangle_{\psi(k)} = \Re\langle\hat{o}\rangle_{\psi(k)} + i\Im\langle\hat{o}\rangle_{\psi(k)} \tag{1.32}$$

The interpretation of real and imaginary parts of the cross section associated with the formation of a narrow resonance has been discussed by Berggren [166]. He showed that the real part corresponds to the cross section and the imaginary part, which is due to the interferences between the resonance and the continuum, corresponds to the uncertainty of the cross section. Later, he extended this interpretation to all operators which commute with the Hamiltonian [86]. In this interpretation, the real part corresponds to the measured value and the imaginary part to the uncertainty of this value due to the finite life-time of the resonance. In the RHS, for a Gamow state $|\psi(k)\rangle$, the mean value of an operator $\hat{o}$ which commutes with the Hamiltonian is given by $\langle\psi^*(k)|\hat{o}|\psi(k)\rangle$ with $|\psi^*(k)\rangle$ the dual of $|\psi(k)\rangle$ [145,147,167]. What Berggren proposed is to use $\Re\langle\psi(k)|\hat{o}|\psi(k)\rangle$ instead of the mean value, *i.e.* to take the lowest order of the Taylor expansion of $\langle\psi^*(k)|\hat{o}|\psi(k)\rangle$ in γ. This interpretation is also valid for the root mean square radius [168].

1.1.4 Gamow Shell Model (GSM)

Different developments which lead to the formulation of the GSM happened independently from each other. The construction of RHS was a mathematical problem [46,47]: How to reconcile Hilbert space with the theory of distributions ? Finally, it appeared that the RHS not only provides a rigorous framework for quantum mechanics including Dirac's bras and kets, but also offers a natural formulation of time-asymmetric processes such as the decaying resonances.

1.1.4.1 Discretization of the one-body Berggren basis

In GSM, the one-body harmonic oscillator basis of SM is replaced by the Berggren basis which includes bound states, resonances and scattering states. The normalization of resonances is solved by the exterior complex-scaling. The completeness of one-body Berggren basis has to be assured by a sufficiently dense discretization of the contour L^+ in the complex k-plane, because Cauchy's theorem is valid for the continuous contour only. Due to numerical limitations, the contour L^+ has to stop at a certain maximal value of $k = k_{\max}$ on the real k-axis. Thus, the N-point quadrature of the integral on the contour reads:

$$\int_{L^+} dk\, |u(k)\rangle\langle u(k)| \approx \sum_{j=1}^{N} w_j\, |u(k_j)\rangle\langle u(k_j)| \tag{1.33}$$

where $\{k_j\}$ and $\{w_j\}$ are values and weights given by the Gauss-Legendre iterative method. By normalizing kets $|u(k_j)\rangle$ with a factor $\sqrt{w_j}$, one obtains:

$$\sum_{j=1}^{N} w_j \left|u(k_j)\right\rangle \left\langle u(k_j)\right| \rightarrow \sum_{j=1}^{N} \left|u(k_j)\right\rangle \left\langle u(k_j)\right| \tag{1.34}$$

The Berggren basis can thus be written as any other discrete basis:

$$\begin{aligned}\sum_{n\in(b,d)} \left|u(k_n)\right\rangle \left\langle u(k_n)\right| + \int_{L^+} dk \left|u(k)\right\rangle \left\langle u(k)\right| &\approx \sum_{n\in(b,d)} \left|u(k_n)\right\rangle \left\langle u(k_n)\right| + \sum_{j=1}^{N} \left|u(k_j)\right\rangle \left\langle u(k_j)\right| \\ &\approx \sum_{n\in(b,d,c)} \left|u(k_n)\right\rangle \left\langle u(k_n)\right| \end{aligned} \tag{1.35}$$

The N-body basis states $\{|\Psi_n\rangle\}$ can then be constructed from the one-body Berggren basis states $\{|u(k_n)\rangle\}$ like in the case of the HO basis. Because nucleons are fermions, a possible N-body basis state $|\Psi_n\rangle$ is obtained by putting each particle i in one of the possible states $|u(k_j)\rangle$, and then antisymmetrizing. Such a state is a Slater determinant:

$$|\Psi_n\rangle = \frac{1}{\sqrt{N!}} \begin{vmatrix} |1:u(k_1)\rangle & |2:u(k_1)\rangle & \cdots & |N:u(k_1)\rangle \\ |1:u(k_2)\rangle & \ddots & & \vdots \\ \vdots & & & \\ |1:u(k_N)\rangle & & & |N:u(k_N)\rangle \end{vmatrix} \tag{1.36}$$

where the usual product "." is replaced by the tensorial product "$\otimes$" and where $|i:u(k_j)\rangle$ is the state associated with the particle i in the state j. With the usual convention for fermions, this state can also be written as:

$$|\Psi_n\rangle = |u(k_1)\, u(k_2) \cdots u(k_N)\rangle \tag{1.37}$$

Another state $|\Psi_{n'}\rangle$ of the N-body basis can be obtained by permuting any two particles. These N-body states form a complete basis spanned by Slater determinants built using the complete Berggren ensemble of states [31]:

$$\sum_{n} |\Psi_n\rangle \langle\Psi_n| = \hat{\mathbb{1}} \tag{1.38}$$

In the coordinate basis $\{|r_i\rangle\}$, where i is the index of a particle, the N-body state is given by:

$$\Psi_n(\vec{r}_1, \vec{r}_2, \cdots, \vec{r}_N) = \frac{1}{\sqrt{N!}} \begin{vmatrix} u_1(\vec{r}_1) & u_1(\vec{r}_1) & \cdots & u_1(\vec{r}_1) \\ u_2(\vec{r}_1) & \ddots & & \vdots \\ \vdots & & & \\ u_N(\vec{r}_1) & & & u_N(\vec{r}_N) \end{vmatrix} \tag{1.39}$$

where $\Psi_n(\vec{r}_1, \vec{r}_2, \cdots, \vec{r}_N) = \langle \vec{r}_1, \vec{r}_2, \cdots, \vec{r}_N | \Psi_n \rangle$ and $u_j(\vec{r}_i) = \langle \vec{r}_i | u(k_j) \rangle$ is the wave function associated with the particle i in the state j.

1.1.4.2 Hamiltonian of the GSM

In the standard SM, the CM excitations are removed using the Lawson method [169–171]. In the GSM, this method cannot be used because Berggren states are not eigenstates of the HO potential. Thus in order to eliminate the CM excitations, the GSM Hamiltonian is expressed in the intrinsic nucleon-core coordinates of the Cluster-Orbital Shell Model (COSM) [172]:

$$\hat{H} = \sum_{i=1}^{N_{\text{val}}} \left(\frac{\hat{\vec{p}}_i^2}{2\mu_i} + U_c(\hat{r}_i) \right) + \sum_{i<j}^{N_{\text{val}}} \left(V(\hat{\vec{r}}_i - \hat{\vec{r}}_j) + \frac{\hat{\vec{p}}_i . \hat{\vec{p}}_j}{M_c} \right) \tag{1.40}$$

where N_{val} is the number of valence nucleons, M_c is the mass of the core, and:

$$\frac{1}{\mu_i} = \frac{1}{M_c} + \frac{1}{m_i} \tag{1.41}$$

is the reduced mass of the i-th nucleon. The single-particle potential $U_c(\hat{r})$ describes the field of the core and $V(\hat{\vec{r}}_i - \hat{\vec{r}}_j)$ is the two-body interaction. The Hamiltonian $\hat{H}$ can then be recast in a form similar to the SM (1.5):

$$\hat{H} = \hat{U}_{\text{basis}} + \hat{T} + \hat{V}_{\text{res}} \tag{1.42}$$

where $\hat{U}_{\text{basis}}$ is the potential which generates the basis, and $\hat{V}_{\text{res}}$ is the residual interaction. Moreover, the introduction of a one-body potential as in (1.6) is a convenient way to remove approximately the long-range component in $\hat{V}_{\text{res}}$.

1.1.4.3 Construction of the one-body Berggren basis

The one-body basis potential $\hat{U}_{\text{basis}} = U_{\text{basis}}(\hat{r})$ is usually either a WS potential with the spin-orbit and Coulomb terms or a HF potential. Berggren basis states are discrete solutions of the one-body Schrödinger equation with outgoing boundary conditions:

$$\frac{\partial^2 u_l(k,r)}{\partial r^2} = \left(\frac{l(l+1)}{r^2} + \frac{2m}{\hbar^2} V(r) - k^2 \right) u_l(k,r) \qquad \text{with} \qquad E = \frac{\hbar^2 k^2}{2m} \tag{1.43}$$

where l is the orbital angular momentum of the particle and m its mass. The reduced radial solutions $u_l(k,r)$ are regular at the origin:

$$u_l(k,r) \underset{r\sim 0}{\sim} C_0(k) r^{l+1} \tag{1.44}$$

with $C_0(k)$ being independent of r. Consequently, following the Cauchy-Lipschitz (or Picard-Lindelöf) theorem, the boundary condition (1.44) uniquely defines the solution $u_l(k,r)$. Moreover, at large distances where the nuclear part of the potential is negligible, the Berggren basis states $u_l(k,r)$ are solutions of:

$$\frac{\partial^2 u_l(k,r)}{\partial r^2} = \left(\frac{l(l+1)}{r^2} + \frac{2\eta k}{r} - k^2 \right) u_l(k,r) \tag{1.45}$$

where η is:

$$\eta = \frac{mZ}{\hbar^2 k} \tag{1.46}$$

the Sommerfeld parameter. The linearly independent solutions of Eq.(1.45) are regular and irregular Coulomb functions $F_{l,\eta}(kr)$ and $G_{l,\eta}(kr)$ respectively. To speak about incoming and outgoing solutions it is more convenient to use the linearly independent incoming and outgoing Coulomb functions:

$$H^{\pm}_{l,\eta}(kr) = G_{l,\eta}(kr) \pm i F_{l,\eta}(kr) \tag{1.47}$$

Then the Berggren basis states $u_l(k,r)$ write:

$$u_l(k,r) \underset{r\to\infty}{\sim} C_+(k) H^+_{l,\eta}(kr) + C_-(k) H^-_{l,\eta}(kr) \tag{1.48}$$

where $C_-(k) = 0$ and $C_+(k) \neq 0$. For bound and resonance states, $C_-(k) = 0$ and $C_+(k) \neq 0$, and for scattering states $C_-(k) \neq 0$ and $C_+(k) \neq 0$. Consequently, due to the boundary conditions (1.44) and (1.48), the solutions $u_l(k,r)$ are unique and can be written as:

$$u_l(k,r) = C_+(k) u^+_l(k,r) + C_-(k) u^-_l(k,r) \tag{1.49}$$

with $u_l^+(k,r)$ and $u_l^-(k,r)$ the two linearly independent solutions of Eq.(1.43).

Remark:

For neutrons, $\eta = 0$ and then the corresponding incoming and outgoing Coulomb functions are called the spherical Hankel functions. They are normally written as $H_l^{\pm}(kr)$ instead of $H_{l,0}^{\pm}(kr)$.

The $C_0(k)$, $C_+(k)$ and $C_-(k)$ constants in Eq.(1.49) are fixed by the normalization of the Berggren basis states either to the unity (bound states and resonances) or to the Dirac delta function (scattering states), and are defined for each orbital angular momentum value. It has been shown in Refs. [79,151] that the normalization to a Dirac delta function is equivalent to the condition:

$$C_+(k)C_-(k) = \frac{1}{2\pi} \quad \forall k \tag{1.50}$$

In practice, the constants $C_+(k)$ and $C_-(k)$ are determined by the matching condition between the radial wave function $u_l(k,r)$ and its asymptotic form at a given point $R >> 0$:

$$\begin{aligned} &\frac{d}{dr}\left(C_+(k)H_{l,\eta}^+(kR) + C_-(k)H_{l,\eta}^-(kR)\right) = \frac{du_l(k,R)}{dr} \\ &C_+(k)H_{l,\eta}^+(kR) + C_-(k)H_{l,\eta}^-(kR) = u_l(k,R) \end{aligned} \tag{1.51}$$

$C_0(k)$ is then obtained by normalizing the Berggren basis state. For bound states and resonances, $C_-(k) = 0$ and the $C_0(k)$ value is chosen such that:

$$\int_0^\infty u_l^2(k,r) = 1 \tag{1.52}$$

while for scattering states it satisfies Eq.(1.50). Consequently, for bound states and resonances the conditions (1.51) and (1.52) ensure the continuity of radial wave functions but not their differentiability. The differentiability of radial wave functions is achieved using the Jost functions [107] defined in Appendix A.1:

$$\mathcal{J}^{\pm}(k) = W(u_l^+(k,r), u_l(k,r)) = u_l^+(k,r)\frac{du_l(k,r)}{dr} - u_l(k,r)\frac{du_l^+(k,r)}{dr} \tag{1.53}$$

In the above equation, $W(f,g)$ is the Wronskian. Jost functions do not depend on r, because $u_l(k,r)$ and $u_l^+(k,r)$ are linearly independent. Thus, the differentiability condition for $u_l(k,r)$:

$$\mathcal{J}^+(k) = 0 \tag{1.54}$$

can be satisfied by varying k.

1.1.4.4 Diagonalization of the Hamiltonian

The calculation of Hamiltonian matrix elements leads to the complex-symmetric matrix:

$$^tH = H \qquad \text{with } H_{ij} \in \mathbb{C} \tag{1.55}$$

where H is the Hamiltonian matrix and H_{ij} an element of H. This matrix can be diagonalized using the Lanczos' algorithm [173] generalized to complex-symmetric matrices. However, the Lanczos' algorithm always converges to a lowest-energy eigenstate which is not necessarily the many-body resonance. Indeed, it is always possible to find scattering states with smaller energies than the resonance states.

1.1.4.5 The overlap method

The problem of the identification of resonances is solved with the so-called overlap method [29, 77]. First, an approximate s.p. Berggren basis, including only bound states and resonances, is used to generate the N-body basis and to diagonalize the Hamiltonian. In this N-body space (the pole space) the Lanczos' algorithm can be applied. The resulting spectrum is a zero-order approximation of the full spectrum which includes the scattering continuum. The overlap method consists of using each eigenstate found in the pole approximation as a pivot for the Davidson method [174] which is more precise for excited states. The Hamiltonian is diagonalized in the subspaces of the full space generated by successive pivots. The last step consists in selecting those eigenstates of the full space which have a maximal overlap with the eigenstates of in the pole space. In general, the value of the maximal overlap is greater than 70%.

1.1.4.6 Summary of the GSM achievements

The GSM has been applied to the description of bound and unbound states in the spectra of $^{18-22}$O [29, 77], ^{80}Ni [30, 78], $^{5-10}$He [77, 80], $^{5-11}$Li [79, 80]. Several other aspects have also been studied like the radial overlap functions, spectroscopic factors, the asymptotic normalization coefficients [76, 175, 176], the charge radii and the neutron-neutron correlations [177]. The role of antibound states in Berggren basis calculations has been studied in Refs. [82, 112, 114]. The use of Lee-Suzuki regularization method [178] in GSM has been done in Ref. [84] for the schematic interaction, and in Refs. [179, 180] for the realistic interaction. A detailed comparison between the GSM and the Gaussian expansion method has been done for ^{6}He and ^{6}Be [181]. An important step has been achieved with the No-Core Gamow Shell Model calculations [40] in ^{3}H and ^{3,4,5}He, using the realistic EFT interactions. NCGSM requires the use of the Density Matrix Renormalization Group (DMRG) method [182,183] in order to determine the lowest energy eigenvalues of the Hamiltonian matrix.

1.2 Extension of the GSM to reaction theory

The new generation of accelerators which provide the radioactive ion beams, make possible the study of exotic nuclei far from the valley of stability. The structure of these nuclei is probed with the nuclear and electromagnetic interactions *via* the elastic and inelastic scattering reactions, the radiative capture reactions, the transfer and knockout reactions, etc. The theoretical description of these reactions involving exotic weakly-bound nuclei requires not only the full account of continuum, but also the full antisymmetry of projectile and target wave functions.

GSM (see Sec.1.1.4) cannot describe the reaction processes because of the inherent configuration mixing in full space, which prohibits the association of GSM eigenstates with physical decay channels. Consequently, the application of GSM to nuclear reactions requires the reformulation of GSM in the CC representation Sec.1.2.2. This method, called GSM-CC, is an alternative to the CSM/SMEC and can describe the structure and reactions in a unified framework.

1.2.1 Definition of channels

In the description of reactions, the problem of solving the Schrödinger equation for an interacting target-projectile system can be conveniently formulated in the channel representation. A general introduction is given in Refs. [184, 185]. The main idea is to describe the reaction by the radial relative motion of a target and a projectile plus some other degrees of freedom[4]. These other degrees of freedom include the angular momenta of the target and the projectile, the internal excitation degrees of freedom of the target, etc. Here

[4]The separation of radial and angular parts of the relative motion of the target and the projectile is possible only if the Hamiltonian, the total angular momentum squared $\hat{J}^2$, and $\hat{J}_z$ have common eigenstates, or in other words if they commute. It is always the case in the applications considered here, so the radial relative motion is just called the relative motion.

they are called channel degrees of freedom. The formalism allows also to describe inelastic reactions by including internal excitations of the target and the projectile.

For a system with n channel degrees of freedom, its state $|\Psi\rangle$ lies in a Hilbert space $\mathcal{E}$, formed by the tensor product of n subspaces $\{\mathcal{E}_i\}$ associated with each channel degree of freedom and of the subspace $\mathcal{E}_{\text{rel}}$ associated with the relative motion:

$$\mathcal{E} = \left(\bigotimes_{i=1}^{n} \mathcal{E}_i\right) \otimes \mathcal{E}_{\text{rel}} \tag{1.56}$$

The basis of $\mathcal{E}_{\text{rel}}$ is the radial position basis $\{|r\rangle\}$, where $|r\rangle$ is associated with the relative distance between the target and the projectile. In spherical coordinates, the space $\mathcal{E}_{\text{rel}}$ has a complete basis given by:

$$\int_0^\infty dr\, r^2\, |r\rangle\, \langle r| = \hat{\mathbb{1}}_{\mathcal{E}_{\text{rel}}} \tag{1.57}$$

In the basis of the full space $\mathcal{E}$ (1.56), each state is labelled by a set of quantum numbers denoted c and called the channel. Then the full basis writes:

$$\sum\!\!\!\!\!\!\int_c \int_0^\infty dr\, r^2\, (|r\rangle \otimes |c\rangle)\, (\langle r| \otimes \langle c|) = \hat{\mathbb{1}}_{\mathcal{E}} \tag{1.58}$$

where $\{|c\rangle\}$ are channel states. The channel states form a basis of the tensor product of the subspaces $\{\mathcal{E}_i\}_{i=1,\dots,n}$ denoted $\hat{\mathbb{1}}_{\mathcal{E}_{\text{cha}}}$ and called the channel space:

$$\sum\!\!\!\!\!\!\int_c |c\rangle\, \langle c| = \bigotimes_{i=1}^{n} \hat{\mathbb{1}}_{\mathcal{E}_i} = \hat{\mathbb{1}}_{\mathcal{E}_{\text{cha}}} \tag{1.59}$$

If there are no couplings between channels, then it is always possible to rewrite the free Hamiltonian for a system target-projectile as the sum of two operators acting in differents subspaces which correspond to the channel degrees of freedom (angular momenta, excitations of the target, etc.) and to the relative motion of the target and the projectile. Therefore, without the two-body interaction, the free eigenstate $|\Psi_0\rangle$ of a system is:

$$|\Psi_0\rangle = |\Psi_0^{\text{rel}}\rangle \otimes |\Psi_0^{\text{cha}}\rangle \tag{1.60}$$

where $|\Psi_0^{\text{rel}}\rangle$ is associated with the relative motion, and $|\Psi_0^{\text{cha}}\rangle$ is associated with the channel degrees of freedom. This free state can be expanded in the full basis (1.58):

$$|\Psi_0\rangle = \sum\!\!\!\!\!\!\int_c \int_0^\infty dr\, r^2\, \langle r|\Psi_0^{\text{rel}}\rangle\, \langle c|\Psi_0^{\text{cha}}\rangle\, |r\rangle \otimes |c\rangle = \sum\!\!\!\!\!\!\int_c \int_0^\infty dr\, r^2 \Psi_{0,c}(r)\, |r\rangle \otimes |c\rangle \tag{1.61}$$

Remark:

The $\langle r|\Psi_0^{\text{rel}}\rangle\, \langle c|\Psi_0^{\text{cha}}\rangle = \Psi_{0,c}(r)$ coefficients are called the channel wave functions, even if they are not the projection of a channel state $|c\rangle$. They are usually written as:

$$\Psi_{0,c}(r) = \frac{u_{0,c}(r)}{r} \tag{1.62}$$

1.2.2 Coupled-channel equations

The first step to obtain CC equations is to expand eigenstates of the Schrödinger equation in the basis of channel states. The importance of each channel is determined by its contribution to the individual eigenenergies and eigenstates. In the applications considered here, the eigenstates are antisymmetric so it

is possible to restrict the calculations to the space of antisymmetric states $\mathcal{E}_{\rm as}$. The basis of this restricted space is obtained by applying the antisymmetrization operator $\hat{\mathcal{A}}$ on the expansion of $|\Psi\rangle$ in the full space:

$$\begin{aligned} |\Psi\rangle &= \sum\!\!\!\!\!\!\int_c \int_0^\infty dr\, r^2 \left(\left(\langle r| \otimes \langle c| \right) |\Psi\rangle \right) |r\rangle \otimes |c\rangle \\ \Leftrightarrow \quad \hat{\mathcal{A}}|\Psi\rangle &= \sum\!\!\!\!\!\!\int_c \int_0^\infty dr\, r^2 \left(\left(\langle r| \otimes \langle c| \right) \hat{\mathcal{A}}|\Psi\rangle \right) \hat{\mathcal{A}}|r\rangle \otimes |c\rangle \\ \Leftrightarrow \quad |\Psi\rangle &= \sum\!\!\!\!\!\!\int_c \int_0^\infty dr\, r^2 \langle r, c|\Psi\rangle |r, c\rangle \end{aligned} \tag{1.63}$$

where $|\Psi\rangle = \hat{\mathcal{A}}|\Psi\rangle$, and the antisymmetrized basis states are defined as: $|r, c\rangle = \hat{\mathcal{A}}(|r\rangle \otimes |c\rangle)$. Thus, the basis of the space of antisymmetric states $\mathcal{E}_{\rm as}$ is:

$$\sum\!\!\!\!\!\!\int_c \int_0^\infty dr\, r^2 |r, c\rangle \langle r, c| = \hat{\mathbb{1}}_{\mathcal{E}_{\rm as}} \tag{1.64}$$

The coefficients $\langle r, c|\Psi\rangle$ are the antisymmetrized channel wave functions:

$$\langle r, c|\Psi\rangle = \Psi_c(r) = \frac{u_c(r)}{r} \tag{1.65}$$

Using this notation, the expansion of the eigenstate is:

$$|\Psi\rangle = \sum\!\!\!\!\!\!\int_c \int_0^\infty dr\, r^2 \frac{u_c(r)}{r} |r, c\rangle \tag{1.66}$$

The second step in the derivation of CC equations is to use the expansion (1.66) in the stationary Schrödinger equation and then project on a particular basis state $\langle r', c'|$:

$$\sum\!\!\!\!\!\!\int_c \int_0^\infty dr\, r^2 (H_{c',c}(r', r) - E N_{c',c}(r', r)) \frac{u_c(r)}{r} = 0 \tag{1.67}$$

where:

$$H_{c',c}(r', r) = \langle r', c'|\hat{H}|r, c\rangle \tag{1.68}$$

are Hamiltonian matrix elements, and:

$$N_{c',c}(r', r) = \langle r', c'|r, c\rangle \tag{1.69}$$

are the norm matrix elements in the channel representation.

The resolution of CC equations with the appropriate boundary conditions gives channel wave functions $u_c(r)/r$ which describe the relative motion of a target and a projectile in a given reaction process. The set of CC equations can be truncated further to keep only most important channels.

1.2.3 Link with the GSM

GSM in the CC representation provides the connection between the structure of target and projectile nuclei, and the reaction process involving them. This link exists *via* channel states $\{|c\rangle\}$ which contain information about the structure of the target and the projectile. To express channel states in terms of the respective target and projectile GSM states, one may apply the RGM [41, 42]. In RGM, one assumes that nucleons in a reaction process spend most of the time grouped in clusters, namely the target nucleus and the projectile nucleus [186–188]. The mathematical expression of this ansatz for the channel state $|c\rangle$ is:

$$|c\rangle = |c_{\text{proj}}\rangle \otimes |c_{\text{targ}}\rangle \tag{1.70}$$

where the indices c_{proj} and c_{targ} denote the sets of quantum numbers associated with, respectively, the projectile and the target. The channel space $\mathcal{E}_{\text{cha}}$ can be splitted into $\mathcal{E}^{\text{cha , proj}}$ and $\mathcal{E}^{\text{cha , targ}}$, corresponding to the projectile channel subspace and target channel subspace, respectively. Moreover, following (1.59), two bases $\{|c_{\text{proj}}\rangle\}$ and $\{|c_{\text{targ}}\rangle\}$ can be defined:

$$\left(\sum\!\!\!\!\!\!\int_{c_{\text{proj}}} |c_{\text{proj}}\rangle\langle c_{\text{proj}}|\right) \otimes \left(\sum\!\!\!\!\!\!\int_{c_{\text{targ}}} |c_{\text{targ}}\rangle \otimes \langle c_{\text{targ}}|\right) = \hat{\mathbb{1}}_{\mathcal{E}^{\text{cha , proj}}} \otimes \hat{\mathbb{1}}_{\mathcal{E}^{\text{cha , targ}}} = \hat{\mathbb{1}}_{\mathcal{E}^{\text{cha}}} \tag{1.71}$$

Because of the RGM ansatz (1.70), the GSM target and projectile states can be directly used in the expression for the target and projectile channel states $|c_{\text{proj}}\rangle$ and $|c_{\text{proj}}\rangle$. Reference articles about the CC formalism in nuclear physics can be found in Refs. [189, 190]. The first application of the GSM-CC formalism to the elastic and inelastic scattering of protons has been made by Jaganathen, Michel and Płoszajczak [191].

1.2.3.1 Channel states expansion in the Berggren basis

In the present case, the projectile is considered to be a one-body system. In GSM, the target channel state $|c_{\text{targ}}\rangle$ of $A-1$ nucleons is an antisymmetrized state given in terms of Slater determinants:

$$|c_{\text{targ}}\rangle = \sum_i \langle \text{SD}_i^{(A-1)}|c_{\text{targ}}\rangle\, |\text{SD}_i^{(A-1)}\rangle = \sum_i a_{i,c_{\text{targ}}}\, |\text{SD}_i^{(A-1)}\rangle \tag{1.72}$$

The Slater determinants $|\text{SD}_i^{(A-1)}\rangle$ are built from a one-body Berggren basis generated by the target potential. Also the antisymmetrized basis states: $|r, c_{\text{proj}}\rangle = \hat{\mathcal{A}}(|r\rangle \otimes |c_{\text{proj}}\rangle)$, can be expanded in a one-body Berggren basis generated by the target potential:

$$\sum_j |\phi_j\rangle\langle\phi_j| = \hat{\mathbb{1}}_{\mathcal{E}_{\text{as}}^{\text{proj}}} \tag{1.73}$$

where each Berggren state $|\phi_i\rangle$ is an antisymmetrized state formed by radial and angular parts:

$$|\phi_i\rangle = \hat{\mathcal{A}}(|\phi_i^{\text{rad}}\rangle \otimes |l, s; j, m_j\rangle) \tag{1.74}$$

In the above expression, l is the orbital momentum of the nucleon, s its spin and j is the total angular momentum with the projection m_j. For a one-body projectile, the channel state is:

$$|c_{\text{proj}}\rangle = |l, s; j, m_j\rangle \tag{1.75}$$

Thus the state $|r, c_{\text{proj}}\rangle$ writes:

$$|r, c_{\text{proj}}\rangle = \sum_j \frac{u_j(r)}{r}\, |\phi_j\rangle \tag{1.76}$$

where $\langle\phi_j^{\text{rad}}|r\rangle = u_j(r)/r$ and $\hat{\mathcal{A}}(|\phi_j^{\text{rad}}\rangle \otimes |c_{\text{proj}}\rangle) = |\phi_j\rangle$. Finally, with the help of Eq.(1.76), the basis states can be written as:

$$|r, c\rangle = \sum_j \frac{u_j(r)}{r}\, |\phi_j^{\text{rad}}, c\rangle \tag{1.77}$$

where $|\phi_j^{\text{rad}}, c\rangle = \hat{\mathcal{A}}(|\phi_j^{\text{rad}}\rangle \otimes |c\rangle)$.

1.2.3.2 Hamiltonian matrix elements

The matrix elements $H_{c',c}(r',r)$ and $N_{c',c}(r',r)$ in Eqs.(1.68) and (1.69), can be expressed with the help of the expansion (1.77). The advantage of this expansion is the exact treatment of the antisymmetry in a projectile-target system. The antisymmetry is neglected for high-energy states, since the target in GSM is always in a bound or resonance state. Consequently, only a finite number of Slater determinants contribute significantly to the target state and thus, the antisymmetry between these low-energy target states and the high-energy projectile states is not very important and can be neglected in most cases.

The high-energy terms in (1.77) correspond to basis states associated with the high k-values or high-j indices $j > j_{\max}$, where $j_{\max}$ depends on the channel c. Hence, the expansion (1.77) splits into low-energy and high-energy parts:

$$|r,c\rangle = \sum_{j=1}^{N} \frac{u_j(r)}{r} |\phi_j^{\rm rad}, c\rangle = \sum_{j=1}^{j_{\max}-1} \frac{u_j(r)}{r} |\phi_j^{\rm rad}, c\rangle + \sum_{j=j_{\max}}^{N} \frac{u_j(r)}{r} |\phi_j^{\rm rad}, c\rangle \tag{1.78}$$

with N the number of discretized states of the one-body Berggren basis $\{|\phi_j\rangle\}$, and $j_{\max}$ the index from which the antisymmetry effects are neglected:

$$\sum_{j=j_{\max}}^{N} \frac{u_j(r)}{r} |\phi_j^{\rm rad}, c\rangle = \sum_{j=j_{\max}}^{N} \frac{u_j(r)}{r} |\phi_j^{\rm rad}\rangle \otimes |c\rangle \tag{1.79}$$

The calculation of high-energy matrix elements of the kinetic energy operator and the Coulomb potential needs a special attention. The applicability of an expansion (1.77) to express the matrix elements (1.68) and (1.69), is valid only if $k_{\max}$ and N in the Berggren basis expansion are both sufficiently large. Indeed, the completeness of the one-body Berggren basis is ensured for a continuous complex contour, *i.e.* when the number of discretization points N goes to infinity. Therefore, the non-antisymmetrized high-energy terms in the expansion (1.79) have to be evaluated differently. The idea is to take advantage of the analyticity of matrix elements (1.68) and (1.69) if $|r,c\rangle$ are non-antisymmetrized ($|r,c\rangle = |r\rangle \otimes |c\rangle$). Eq.(1.79) becomes then:

$$\sum_{j=j_{\max}}^{N} \frac{u_j(r)}{r} |\phi_j^{\rm rad}\rangle \otimes |c\rangle = |r\rangle \otimes |c\rangle - \sum_{j=1}^{j_{\max}-1} \frac{u_j(r)}{r} |\phi_j\rangle \otimes |c_{\rm targ}\rangle \tag{1.80}$$

The Hamiltonian (1.42) can thus split into terms acting on the projectile states $|\phi_j\rangle$ and the target states $|c_{\rm targ}\rangle$:

$$\hat{H} = \hat{U}_{\rm basis} + \hat{T} + \hat{V}_{\rm res} = \sum_{i=1}^{N_{\rm val}} U_{\rm basis}(\hat{r}_i) + \sum_{i=1}^{N_{\rm val}} \frac{\hat{\vec{p}}_i^{\,2}}{2\mu_i} + \hat{V}_{\rm res} = \hat{H}_{\rm proj} + \hat{H}_{\rm targ} \tag{1.81}$$

with $\hat{H}_{\rm proj}$ which contains the basis potential and kinetic terms acting on the projectile states, and $\hat{H}_{\rm targ}$ which contains the basis potential and kinetic terms acting on the target, plus the residual interaction. Therefore:

$$\hat{H}_{\rm proj} |\phi_j\rangle = E_{j,c_{\rm proj}} |\phi_j\rangle \qquad \text{and} \qquad \hat{H}_{\rm targ} |c_{\rm targ}\rangle = E_{c_{\rm targ}} |c_{\rm targ}\rangle \tag{1.82}$$

The matrix elements (1.68) and (1.69) can then be evaluated using the expansion (1.77):

$$H_{c',c}(r',r) = \sum_{j'=1}^{N} \sum_{j=1}^{N} \frac{u_{j'}(r')}{r'} \frac{u_j(r)}{r} H_{c',c}(j',j) \tag{1.83}$$

and:

$$N_{c',c}(r',r) = \sum_{j'=1}^{N}\sum_{j=1}^{N} \frac{u_{j'}(r')}{r'}\frac{u_j(r)}{r} N_{c',c}(j',j) \tag{1.84}$$

where $H_{c',c}(j',j) = \langle \phi^{\text{rad}}_{j'}, c'|\hat{H}|\phi^{\text{rad}}_{j}, c\rangle$ and $N_{c',c}(j',j) = \langle \phi^{\text{rad}}_{j'}, c'|\phi^{\text{rad}}_{j}, c\rangle$.

In the calculation of sums in Eqs.(1.83) and (1.84), four cases have to be considered. In the first case: $j < j_{\max}$ and $j' < j_{\max}$, the matrix elements are calculated in terms of Slater determinants to take into account the antisymmetry. In the second and third cases: $j < j_{\max}$ and $j' \geq j_{\max}$, and $j \geq j_{\max}$ and $j' < j_{\max}$, which are symmetric with respect to the exchange of j and j', the matrix elements are both equal to zero because the Berggren states $|\phi_j\rangle$ and $|\phi_{j'}\rangle$ with j or $j \geq j_{\max}$ are orthogonal to all the states in the target states. In the last case: $j \geq j_{\max}$ and $j' \geq j_{\max}$, there is no antisymmetry effect, thus only terms with $j = j'$ are non-zero, and consequently the method of Eq.(1.80) can be used. Finally, the last term: $j > j_{\max}$ and $j' > j_{\max}$ writes:

$$\sum_{j'=j_{\max}}^{N}\sum_{j=j_{\max}}^{N} \frac{u_{j'}(r')}{r'}\frac{u_j(r)}{r} H_{c',c}(j',j)\delta_{j,j'} = \sum_{j=1}^{N} \frac{u_j(r')}{r'}\frac{u_j(r)}{r} H_{c',c}(j,j) - \sum_{j=1}^{j_{\max}-1} \frac{u_j(r')}{r'}\frac{u_j(r)}{r} H_{c',c}(j,j) \tag{1.85}$$

In this non-antisymmetrized case, the matrix elements $H_{c',c}(j,j)$ can be evaluated as:

$$H_{c',c}(j,j) = E_{j,c_{\text{proj}}}\delta_{c'_{\text{targ}},c_{\text{targ}}} + E_{c_{\text{targ}}}\delta_{j,j'} \tag{1.86}$$

In Eq.(1.85), the second sum is calculated numerically, whereas the first sum writes:

$$\sum_{j=1}^{N} \frac{u_j(r')}{r'}\frac{u_j(r)}{r} H_{c',c}(j,j) = \sum_{j=1}^{N} \frac{u_j(r')}{r'} E_{j,c_{\text{proj}}} \frac{u_j(r)}{r}\delta_{c'_{\text{targ}},c_{\text{targ}}} + E_{c_{\text{targ}}} \sum_{j=1}^{N} \frac{u_j(r')}{r'}\frac{u_j(r)}{r} \tag{1.87}$$

But because of Eqs.(1.75) and (1.73):

$$\sum_{j=1}^{N} \frac{u_j(r')}{r'} E_{j,c_{\text{proj}}} \frac{u_j(r)}{r}\delta_{c'_{\text{targ}},c_{\text{targ}}} = \left(U_{\text{basis}}(r) - \frac{\hbar^2}{2\mu}\frac{1}{r}\frac{\partial^2(r\cdot)}{\partial r^2} + \frac{\hbar^2 l(l+1)}{2\mu r^2}\right)\frac{\delta(r-r')}{r^2}\delta_{c'_{\text{targ}},c_{\text{targ}}} \tag{1.88}$$

with $\langle r|r'\rangle = \delta(r-r')/r^2$. In the same way:

$$E_{c_{\text{targ}}} \sum_{j=1}^{N} \frac{u_j(r')}{r'}\frac{u_j(r)}{r} = E_{c_{\text{targ}}}\frac{\delta(r-r')}{r^2} \tag{1.89}$$

Finally, the matrix elements (1.68) and (1.69) are:

$$H_{c',c}(r',r) = -\frac{\hbar^2}{2\mu}\left(\frac{1}{r}\frac{\partial^2(r\cdot)}{\partial r^2} - \frac{l(l+1)}{r^2} - k^2_{c_{\text{targ}}}\right)\frac{\delta(r-r')}{r^2}\delta_{c'_{\text{targ}},c_{\text{targ}}} + V_{c',c}(r',r) \tag{1.90}$$

where:

$$k^2_{c_{\text{targ}}} = \frac{2\mu E_{c_{\text{targ}}}}{\hbar^2} \tag{1.91}$$

and:

$$V_{c',c}(r',r) = U_{\text{basis}}(r)\frac{\delta(r-r')}{r^2}\delta_{c'_{\text{targ}},c_{\text{targ}}} + \tilde{V}_{c',c}(r',r) \tag{1.92}$$

with:

$$\tilde{V}_{c',c}(r',r) = \sum_{j'=1}^{j_{\max}-1}\sum_{j=1}^{j_{\max}-1}\frac{u_{j'}(r')}{r'}\frac{u_j(r)}{r}H_{c',c}(j',j) - \sum_{j=1}^{j_{\max}-1}\frac{u_j(r')}{r'}\frac{u_j(r)}{r}(E_{j,c_{\text{proj}}}\delta_{c'_{\text{targ}},c_{\text{targ}}} + E_{c_{\text{targ}}}) \tag{1.93}$$

In the same way:

$$N_{c',c}(r',r) = \frac{\delta(r-r')}{r^2}\delta_{c'_{\text{targ}},c_{\text{targ}}} + \tilde{N}_{c',c}(r',r) \tag{1.94}$$

with:

$$\tilde{N}_{c',c}(r',r) = \sum_{j'=1}^{j_{\max}-1}\sum_{j=1}^{j_{\max}-1}\frac{u_{j'}(r')}{r'}\frac{u_j(r)}{r}N_{c',c}(j',j) - \sum_{j=1}^{j_{\max}-1}\frac{u_j(r')}{r'}\frac{u_j(r)}{r}\delta_{c'_{\text{targ}},c_{\text{targ}}} \tag{1.95}$$

1.2.3.3 Orthogonalization of the channel states

In general, the CC formalism leads to the generalized eigenvalue problem because different channel states are non-orthogonal:

$$\langle r',c'|r,c\rangle \neq 0 \tag{1.96}$$

The non-orthogonality of channel states comes from the antisymmetry between the projectile and target states. For example, in a simplified case of two target states:

$$\begin{aligned}|c_0\rangle &= a_0\,|SD_a\rangle + b_0\,|SD_b\rangle\\ |c_1\rangle &= a_1\,|SD_a\rangle + b_1\,|SD_b\rangle\end{aligned} \tag{1.97}$$

with:

$$\langle c_0|c_1\rangle = 0 \qquad \Leftrightarrow \qquad a_0a_1 + b_0b_1 = 0 \tag{1.98}$$

and with a projectile state $|\phi_j\rangle \in |SD_a\rangle \Rightarrow |\phi_j, SD_a\rangle = 0$, antisymmetrized overlap equals:

$$\langle \phi_j, c_0|\phi_j, c_1\rangle = b_0b_1 \neq 0 \tag{1.99}$$

In order to formulate CC equations as a generalized eigenvalue problem, Eq.(1.67) must be expressed in a new channel basis $\{|r,c\rangle_o\}$, called the orthogonal channel basis, where:

$${}_o\langle r',c'|r,c\rangle_o = \frac{\delta(r'-r)}{r^2}\delta_{c'c} \tag{1.100}$$

The transformation from the non-orthogonal states $|r,c\rangle$ to the orthogonal states $|r,c\rangle_o$ is achieved with an operator denoted $\hat{O}$ such that:

$$|r,c\rangle = \hat{O}^{\frac{1}{2}}\,|r,c\rangle_o \qquad \Leftrightarrow \qquad |r,c\rangle_o = \hat{O}^{-\frac{1}{2}}\,|r,c\rangle \tag{1.101}$$

Thus, the matrix elements in Eq.(1.67) can be expressed in the new basis as:

$$\langle r',c'|r,c\rangle = {}_o\langle r',c'|\hat{O}^{\frac{1}{2}}\hat{O}^{\frac{1}{2}}|r,c\rangle_o = {}_o\langle r',c'|\hat{O}|r,c\rangle_o \tag{1.102}$$

Eq.(1.102) defines matrix elements of the operator $\hat{O}$ in the orthogonal channel basis. For this reason, the operator $\hat{O}$ is usually called the overlap operator.

In the same way, the Hamiltonian matrix elements can be expressed as:

$$\langle r', c'|\hat{H}|r, c\rangle = \langle r', c'|\hat{O}^{-\frac{1}{2}}\hat{O}^{\frac{1}{2}}\hat{H}\hat{O}^{\frac{1}{2}}\hat{O}^{-\frac{1}{2}}|r, c\rangle = {}_o\langle r', c'|\hat{H}_o|r, c\rangle_o \tag{1.103}$$

with $\hat{H}_o = \hat{O}^{\frac{1}{2}}\hat{H}\hat{O}^{\frac{1}{2}}$. Also:

$$\langle r, c|\Psi\rangle = {}_o\langle r, c|\hat{O}^{\frac{1}{2}}|\Psi\rangle = {}_o\langle r, c|\Psi_o\rangle \tag{1.104}$$

with $|\Psi_o\rangle = \hat{O}^{\frac{1}{2}}|\Psi\rangle$.

The CC equations (1.67) can thus be transformed into:

$$\sum\!\!\!\!\!\!\int_c \int_0^\infty dr\, r^2 ({}_o\langle r', c'|\hat{O}|r, c\rangle_o - E_o\langle r', c'|\hat{O}|r, c\rangle_o)_o\langle r, c|\Psi_o\rangle = 0 \tag{1.105}$$

This equation corresponds to the following generalized eigenvalue problem:

$$\hat{H}_o|\Psi_o\rangle = E\hat{O}|\Psi_o\rangle \tag{1.106}$$

The method to transform Eq.(1.106) into a standard eigenvalue problem is the following:

$$\hat{H}_o|\Psi_o\rangle = E\hat{O}|\Psi_o\rangle \quad \Leftrightarrow \quad \hat{O}^{\frac{1}{2}}\hat{H}\hat{O}|\Psi\rangle = \hat{O}^{\frac{1}{2}}E\hat{O}|\Psi\rangle \quad \Leftrightarrow \quad \hat{H}|\Phi\rangle = E|\Phi\rangle \tag{1.107}$$

with $|\Phi\rangle = \hat{O}|\Psi\rangle$. Thus, Eq.(1.107) in the orthogonal channel basis takes the form:

$$\sum\!\!\!\!\!\!\int_c \int_0^\infty dr\, r^2 ({}_o\langle r', c'|\hat{H}|r, c\rangle_o - E_o\langle r', c'|r, c\rangle_o)_o\langle r, c|\Phi\rangle = 0 \tag{1.108}$$

with:

$${}_o\langle r, c|\Phi\rangle = \langle r, c|\hat{O}^{\frac{1}{2}}|\Psi\rangle = \frac{w_c(r)}{r} \tag{1.109}$$

The overlap between orthogonal channel states is given in Eq.(1.100). The Hamiltonian matrix elements in Eq.(1.108) are expressed in the non-orthogonal channel basis:

$${}_o\langle r', c'|\hat{H}|r, c\rangle_o = \langle r', c'|\hat{O}^{-\frac{1}{2}}\hat{H}\hat{O}^{-\frac{1}{2}}|r, c\rangle = \langle r', c'|\hat{H}_m|r, c\rangle \tag{1.110}$$

with $\hat{H}_m = \hat{O}^{-\frac{1}{2}}\hat{H}\hat{O}^{-\frac{1}{2}}$ the modified Hamiltonian. The CC equations which are used for numerical applications are thus:

$$\sum\!\!\!\!\!\!\int_c \int_0^\infty dr\, r^2 \langle r', c'|\hat{H}_m|r, c\rangle \frac{w_c(r)}{r} = E\frac{w_{c'}(r')}{r'} \tag{1.111}$$

In order to solve Eq.(1.111), the $\hat{H}_m$ matrix elements have to be calculated. Instead of calculating them directly, one can separate their low-energy and high-energy parts to treat the antisymmetry. If the channel states are expanded in a basis $\{|\phi_j^{\text{rad}}, c\rangle\}$ formed with the help of a radial Berggren basis basis $\{|\phi_j^{\text{rad}}\rangle\}$, like in Eq.(1.77), the overlap operator $\hat{O}$ has a matrix representation O which looks like:

$$O = \begin{pmatrix} O_{0,0} & \cdots & O_{0,i} & 0 & 0 & 0 \\ \vdots & \ddots & & 0 & 0 & 0 \\ O_{i',0} & & O_{i',i} & 0 & 0 & 0 \\ 0 & 0 & 0 & 1 & 0 & 0 \\ 0 & 0 & 0 & 0 & 1 & 0 \\ 0 & 0 & 0 & 0 & 0 & 1 \end{pmatrix} \tag{1.112}$$

where $i = (c, j)$ and $O_{i',i} = O_{c',c}(j', j) = \langle \phi^{\text{rad}}_{j'}, c' | \hat{O} | \phi^{\text{rad}}_{j}, c \rangle \in \mathbb{C}$. The $O_{i',i}$ elements are equal 1 for the high-energy terms because channel states are orthogonal in this case. The matrix representation of $\hat{O}^{-\frac{1}{2}}$ has the same form. In practice, the calculation of $\hat{O}^{-\frac{1}{2}}$ makes use of the Moore-Penrose pseudo-inverse described in Appendix.A.3.

In order to have a precise treatment of the antisymmetry in the calculation of matrix elements of the modified Hamiltonian, a new operator $\hat{\Delta}$ can be defined:

$$\hat{O}^{-\frac{1}{2}} = \hat{\Delta} + \hat{\mathbb{1}} \tag{1.113}$$

which is associated with the part of $\hat{O}^{-\frac{1}{2}}$ acting on the low-energy channel states. Then, instead of calculating the matrix elements of $\hat{H}_m$ directly, it is possible to calculate them as:

$$H_m = O^{-\frac{1}{2}} H O^{-\frac{1}{2}} = (\Delta + \mathbb{1}) H (\Delta + \mathbb{1}) = H + H\Delta + \Delta H + \Delta H \Delta \tag{1.114}$$

In this formulation, the non-antisymmetrized terms are taken into account exactly with the identity operator. This method is thus more precise from a numerical point of view. In practice, calculations of the matrices $O^{\frac{1}{2}}$, $O^{-\frac{1}{2}}$ and H_m are done in the HO basis.

Finally, inserting the expansion (1.114) of the modified Hamiltonian $\hat{H}_m$ in CC equations, one obtains:

$$\sum\!\!\!\!\!\!\int_c \int_0^\infty dr\, r^2 (\langle r', c' | \hat{H} | r, c \rangle + \langle r', c' | \hat{H}\hat{\Delta} | r, c \rangle + \langle r', c' | \hat{\Delta}\hat{H} | r, c \rangle + \langle r', c' | \hat{\Delta}\hat{H}\hat{\Delta} | r, c \rangle) \frac{w_c(r)}{r} = E \frac{w_{c'}(r')}{r'} \tag{1.115}$$

The Hamiltonian matrix elements $\langle r', c' | \hat{H} | r, c \rangle$ can be replaced by their expression in Eq.(1.90):

$$\begin{aligned} &\sum_c \int_0^\infty dr\, r^2 \left(-\frac{\hbar^2}{2\mu} \left(\frac{1}{r} \frac{\partial^2 (r\cdot)}{\partial r^2} - \frac{l(l+1)}{r^2} - k^2_{c_{\text{targ}}} \right) \frac{\delta(r - r')}{r^2} \delta_{c'_{\text{targ}}, c_{\text{targ}}} + V_{c',c}(r', r) - E\delta_{c',c} \right. \\ &\left. + \langle r', c' | \hat{H}\hat{\Delta} | r, c \rangle + \langle r', c' | \hat{\Delta}\hat{H} | r, c \rangle + \langle r', c' | \hat{\Delta}\hat{H}\hat{\Delta} | r, c \rangle \right) \frac{w_c(r)}{r} = 0 \end{aligned} \tag{1.116}$$

The matrix elements $V_{c',c}(r', r)$ can also be replaced by Eq.(1.92), to finally give the CC equations for the reduced radial wave functions $w_c(r)/r$:

$$\begin{aligned} &\left(-\frac{\hbar^2}{2\mu} \left(\frac{1}{r} \frac{\partial^2 (r\cdot)}{\partial r^2} - \frac{l(l+1)}{r^2} \right) + V^{(\text{loc})}_c(r) \right) \frac{w_c(r)}{r} \frac{\delta(r - r')}{r^2} \delta_{c'_{\text{targ}}, c_{\text{targ}}} + \sum_{c'} \int_0^\infty dr'\, r r'^2 \frac{V^{(\text{non-loc})}_{c,c'}(r, r')}{r r'} \frac{w_{c'}(r')}{r'} \\ &= (E - E_{c_{\text{targ}}}) \frac{\delta(r - r')}{r^2} \frac{w_c(r)}{r} \delta_{c'_{\text{targ}}, c_{\text{targ}}} \end{aligned} \tag{1.117}$$

with the local potential $V^{(\text{loc})}_c(r) = U_{\text{basis}}(r)$ which may depend on the channel c and the non-local potential:

$$\frac{1}{r'r} V^{(\text{non-loc})}_{c',c}(r', r) = \tilde{V}_{c',c}(r', r) + \langle r', c' | \hat{H}\hat{\Delta} | r, c \rangle + \langle r', c' | \hat{\Delta}\hat{H} | r, c \rangle + \langle r', c' | \hat{\Delta}\hat{H}\hat{\Delta} | r, c \rangle \tag{1.118}$$

Once the Eq.(1.117) is solved, one has to use the equation:

$$\frac{u_c(r)}{r} = \frac{w_c(r)}{r} + \sum_{c'} \int_0^\infty dr'\, r'^2 \langle r, c | \hat{O}^{\frac{1}{2}} \hat{\Delta} \hat{O}^{\frac{1}{2}} | r', c' \rangle \frac{w_{c'}(r')}{r'} \tag{1.119}$$

to get back to the original radial channel wave functions $u_c(r)/r$ from $w_c(r)/r$.

1.2.3.4 Method of the equivalent potential

CC equations (1.117) contain a non-local potential which has to be treated using a generalization of the method of the equivalent potential [45, 192]. The basic idea is to find an effective local potential and a source term which would replace the non-local potential. The CC equations are thus put in the form:

$$\frac{\partial^2 w_c(r)}{\partial r^2} = \left(\frac{l(l+1)}{r^2} - \frac{2\mu}{\hbar^2}(E - E_{c_{\text{targ}}})\right) w_c(r) + \frac{2\mu}{\hbar^2}\left(V_c^{(\text{loc})}(r) w_c(r) + \sum_{c'} \int_0^\infty dr'\, V_{c,c'}^{(\text{non-loc})}(r, r') w_{c'}(r')\right) \tag{1.120}$$

Then, the potentials are replaced by:

$$V_c^{(\text{loc})}(r) w_c(r) + \sum_{c'} \int_0^\infty dr'\, V_{c,c'}^{(\text{non-loc})}(r, r') w_{c'}(r') = \sum_{c'} V_{c,c'}^{(\text{eq})}(r) w_{c'}(r) + S_c(r) \tag{1.121}$$

where the equivalent potential is defined by:

$$V_{c,c'}^{(\text{eq})}(r) = V_c^{(\text{loc})}(r)\delta_{c',c} + \frac{1 - F_{c'}(r)}{w_{c'}(r)} \sum_{c'} \int_0^\infty dr'\, V_{c,c'}^{(\text{non-loc})}(r, r') w_{c'}(r') \tag{1.122}$$

and the source term is:

$$S_c(r) = F_{c'}(r) \sum_{c'} \int_0^\infty dr'\, V_{c,c'}^{(\text{non-loc})}(r, r') w_{c'}(r') \tag{1.123}$$

The $F_c(r)$ function is a smoothing function to cancel divergences of the equivalent potential $V_{c,c'}^{(\text{eq})}(r)$ close to zeroes of $w_c(r)$, except for $r = 0$ because there is no divergence of $V_{c,c'}^{(\text{eq})}(r)$ at this point. Moreover, the $F_c(r)$ function is such that $F_c(r) \approx 1$ close to the zero of $w_c(r)$ and negligible elsewhere. The ansatz for $F_c(r)$ is the following:

$$F_c(r) = e^{-\alpha \left|\frac{w_c(r)}{w_c'(r)}\right|^2} \left(1 - e^{-\alpha \left|\frac{w_c^{\text{asymp}}(r)}{w_c(r)} - 1\right|^2}\right) \tag{1.124}$$

with:

$$w_c'(r) = \frac{\partial w_c(r)}{\partial r} \tag{1.125}$$

w_c^{asymp} in Eq.(1.124) is the asymptotic form of $w_c(r)$ when $r \sim 0$. The parameter α is typically chosen between 10 and 100. Thus the CC equations are:

$$\frac{\partial^2 w_c(r)}{\partial r^2} = \left(\frac{l(l+1)}{r^2} - k_c^2\right) w_c(r) + \frac{2\mu}{\hbar^2}\left(\sum_{c'} V_{c,c'}^{(\text{eq})}(r) w_{c'}(r) + S_c(r)\right) \tag{1.126}$$

where:

$$k_c^2 = \frac{2\mu}{\hbar^2}(E - E_{c_{\text{targ}}}) \tag{1.127}$$

These equations are solved iteratively to determine the equivalent potential, the source term, and the mutally orthogonal radial wave functions $w_c(r)$.

1.2.3.5 Symmetrization of the equivalent potential

Due to the asymmetry of the equivalent potential with respect to the exchange of channels c and c':

$$V^{(\mathrm{eq})}_{c,c'}(r) \neq V^{(\mathrm{eq})}_{c',c}(r) \tag{1.128}$$

the iterative resolution of CC equations (1.126) leads to unphysical results. To solve this problem, one has to introduce the symmetrized equivalent potential:

$$V^{(\mathrm{eq\ ,\ sy})}_{c,c'}(r) = \frac{V^{(\mathrm{eq})}_{c,c'}(r) + V^{(\mathrm{eq})}_{c',c}(r)}{2} \qquad (c' \neq c) \tag{1.129}$$

$$= V^{(\mathrm{eq})}_{c,c}(r) + \frac{1 - F_c(r)}{w_c(r)} \sum_{c' \neq c} \frac{V^{(\mathrm{eq})}_{c,c'}(r) - V^{(\mathrm{eq})}_{c',c}(r)}{2} w_{c'}(r) \qquad (c' = c) \tag{1.130}$$

and the corresponding source term:

$$S^{(\mathrm{sy})}_c(r) = S_c(r) + F_c(r) \sum_{c' \neq c} \frac{V^{(\mathrm{eq})}_{c,c'}(r) - V^{(\mathrm{eq})}_{c',c}(r)}{2} w_{c'}(r) \tag{1.131}$$

To keep the form of CC equations (1.126) unchanged, the symmetrization of terms with $c' \neq c$ requires the modification of both the term with $c' = c$ (Eq.(1.130)) and the source term (Eq. (1.131)). Finally, the CC equations write:

$$\frac{\partial^2 w_c(r)}{\partial r^2} = \left(\frac{l(l+1)}{r^2} - k_c^2 \right) w_c(r) + \frac{2\mu}{\hbar^2} \left(\sum_{c'} V^{(\mathrm{eq\ ,\ sy})}_{c,c'}(r) w_{c'}(r) + S^{(\mathrm{sy})}_c(r) \right) \tag{1.132}$$

Starting point for solving Eqs.(1.132) is provided by a set of radial channel wave functions $\{w_c(r)\}$ obtained by the diagonalization of CC equations (1.111) in the pole space.

1.2.3.6 Direct integration method

The CC equations (1.132) for $r \sim 0$ are:

$$\frac{\partial^2 w_c(r)}{\partial r^2} = \left(\frac{l(l+1)}{r^2} - a_c \right) w_c(r) + \sum_{c' \neq c} a_{c,c'} w_{c'}(r) \tag{1.133}$$

In this limit, the source term can be neglected because it is important only close to the zeroes of the radial wave functions $w_c(r)$, with the exception of point $r = 0$. In the above equations:

$$a_c = \frac{2\mu}{\hbar^2} V^{(\mathrm{eq\ ,\ sy})}_{c,c}(0) - k_c^2 \tag{1.134}$$

$$a_{c,c'} = \frac{2\mu}{\hbar^2} V^{(\mathrm{eq\ ,\ sy})}_{c,c'}(0) \tag{1.135}$$

Due to the channel-channel couplings, the boundary conditions at $r \sim 0$ are not always $w_c(r) \sim r^{l+1}$. To solve this problem, the radial wave functions $w_c(r)$ are expanded in the forward basis corresponding to the internal region: $0 \leq r \leq R$, where the nuclear part of the potential is not negligible, and in the backward basis corresponding to the asymptotic region: $R \leq r \leq R_{\max}$, where the nuclear part of the potential is negligible. The expansion of the CC equations in the forward basis is integrated from $r = 0$ to $r = R$, and the expansion in the backward basis is integrated from $r = R_{\max}$ to $r = R$. Contrary to the radial wave functions $w_c(r)$, these new basis states have the correct boundary conditions. Thus the CC equations can be integrated numerically in each region, with the matching condition at $r = R$.

The expansion in the internal region $0 \leq r \leq R$ is:

$$w_c(r) = \sum_b A_b^{(0)} w_{c,b}^{(0)}(r) \tag{1.136}$$

with $A_b^{(0)}$ a constant which is determined by the matching condition. For a given channel b, the forward basis states have the following boundary conditions:

$$\begin{aligned} w_{c,b}^{(0)}(r) &\underset{r\sim 0}{\sim} r^{l_b+1} \qquad (c = b) \\ &\underset{r\sim 0}{\sim} \frac{a_{c,b}}{(l_b+2)(l_b+3) - l_c(l_c+1)} C_b^{(0)} r^{l_b+3} \qquad (c \neq b, l_c \neq l_b+2) \\ &\underset{r\sim 0}{\sim} \frac{a_{c,b}}{2l_b+5} C_b^{(0)} r^{l_b+3} \ln(r) \qquad (c \neq b, l_c = l_b+2) \end{aligned} \tag{1.137}$$

where l_b is the orbital angular momentum associated with the channel b, and $C_b^{(0)}$ is a constant determined by the previous iteration.

In the same way, the expansion in the asymptotic region $R \leq r \leq R_{\max}$ is:

$$w_c(r) = \sum_b A_b^{(+)} w_{c,b}^{(+)}(r) + w_c^{(-)}(r) \tag{1.138}$$

where $w_c^{(-)}(r)$ is an incoming channel wave function which equals zero if $w_c(r)$ is associated with a bound state or a decaying resonance. The boundary conditions are in this case given by:

$$\begin{aligned} w_{c,b}^{(+)}(r) &\underset{r\to\infty}{\sim} C_b^{(+)} H_{l_b}^{+}(\eta_b, k_b r) \qquad (c = b) \\ &\underset{r\to\infty}{=} 0 \qquad (c \neq b) \end{aligned} \tag{1.139}$$

and:

$$\begin{aligned} w_c^{(-)}(r) &\underset{r\to\infty}{\sim} H_{l_c}^{-}(\eta_c, k_c r) \qquad (c = c_0) \\ &\underset{r\to\infty}{=} 0 \qquad (c \neq c_0) \end{aligned} \tag{1.140}$$

with c_0 the entrance channel and η_c the Sommerfeld parameter of the channel c. The matching conditions thus write:

$$\sum_b \left(A_b^{(0)} w_{c,b}^{(0)}(R) - A_b^{(+)} w_{c,b}^{(+)}(R) \right) = w_c^{(-)}(R) \tag{1.141}$$

and:

$$\sum_b \left(A_b^{(0)} \left.\frac{\partial w_{c,b}^{(0)}(r)}{\partial r}\right|_{r=R} - A_b^{(+)} \left.\frac{\partial w_{c,b}^{(+)}(r)}{\partial r}\right|_{r=R} \right) = \left.\frac{\partial w_c^{(-)}(r)}{\partial r}\right|_{r=R} \tag{1.142}$$

or in a matrix form without the incoming wave functions:

$$\begin{pmatrix} w_{0,0}^{(0)}(R) & 0 & 0 & \cdots & 0 & w_{0,0}^{(+)}(R) & 0 & 0 & \cdots & 0 \\ w'^{(0)}_{0,0}(R) & 0 & 0 & \cdots & 0 & w'^{(+)}_{0,0}(R) & 0 & 0 & \cdots & 0 \\ 0 & w_{1,1}^{(0)}(R) & 0 & \cdots & 0 & 0 & w_{1,1}^{(+)}(R) & 0 & \cdots & 0 \\ 0 & w'^{(0)}_{1,1}(R) & 0 & \cdots & 0 & 0 & w'^{(+)}_{1,1}(R) & 0 & \cdots & 0 \\ 0 & 0 & \ddots & \cdots & 0 & 0 & 0 & \ddots & \cdots & 0 \\ 0 & 0 & \ddots & \cdots & 0 & 0 & 0 & \ddots & \cdots & 0 \\ 0 & 0 & 0 & \cdots & w_{c,b}^{(0)}(R) & 0 & 0 & 0 & \cdots & w_{c,b}^{(+)}(R) \\ 0 & 0 & 0 & \cdots & w'^{(0)}_{c,b}(R) & 0 & 0 & 0 & \cdots & w'^{(+)}_{c,b}(R) \end{pmatrix} \begin{pmatrix} A_0^{(0)} \\ A_1^{(0)} \\ \vdots \\ A_b^{(0)} \\ A_0^{(+)} \\ A_1^{(+)} \\ \vdots \\ A_b^{(+)} \end{pmatrix} = 0 \tag{1.143}$$

with:

$$w'^{(0/+)}_{c,b}(R) = \left.\frac{\partial w_{c,b}^{(0/+)}(r)}{\partial r}\right|_{r=R} \tag{1.144}$$

For bound states and resonances, Eq.(1.143) is the generalization of the Jost function to an arbitrary number of channels.

Finally, the Schrödinger equation (1.133) for $w_{c,b}^{(0)}(r)$ in the internal region and for $w_{c,b}^{(+)}(r)$ in the external region, is solved using the Bulirsch-Stoer method [193]. The radial wave functions $w_c(r)$ are then obtained using the matching conditions (1.141) and (1.142) and the corresponding expansions (1.136) and (1.138).

1.3 Overview of the other methods including the continuum

Other microscopic methods are avaible to solve the nuclear N-body problem with an explicit treatment of the continuum. In this section, a brief and non-exhaustive review of these methods is done.

- The CSM/SMEC approaches, presented in Sec.1.1.2.2, give a unified framework for the description of structure and reactions with up to two nucleons in the scattering continuum.
- The continuum Quasiparticle Random Phase Approximation (QRPA) calculations [194–196] are performed in a box and thus with a discretized continuum. A variant of QRPA with the Berggren basis has been tested in Ref. [197].
- The Lorentz Integral Transform (LIT) method [198,199] calculates inelastic response functions $r(E)$ from the inversion of their integral transform $L(\sigma)$ with a Lorentz kernel $K(\sigma, E)$:

  $$L(\sigma) = \int K(\sigma, E) r(E) \tag{1.145}$$

  The integral transfrom $L(\sigma)$ can be obtained using bound-state methods. Due to the numerical inaccuracies of the inverse transformation, this method is limited to narrow resonances.
- The Quantum Monte Carlo (QMC) method described in Ref. [200], which is limited to low-lying narrow resonances.
- The Coupled-Cluster Theory is an *ab initio* approach which is well adapted to the description of medium-heavy mass nuclei [201] with the interactions derived from EFT [202]. This approach can be used to describe systems with up to two nucleons outside of the closed (sub)shell nuclei. The use of Berggren basis in the CCT [103,203–205] allows to describe long chains of isotopes from well bound to

unbound ones. The recent application of the CCT to neutron-rich isotopes of Ca [206], demonstrate the potential of this approach in the regions of nuclear chart which are not accessible by any other *ab initio* approach.

- The No-Core Shell Model with Resonating Group Method (NCSM/RGM) is an extension of the NCSM to the reactions. The NCSM/RGM employs interactions derived from EFT. The continuum of the projectile and the target is approximated *via* the outgoing boundary conditions of the channel states. Recently, NCSM/RGM has been used to describe one-body elastic and inelastic scattering reactions [35, 43, 207], radiative capture reactions [208], deuteron scattering reactions [209, 210] and fusion reaction [211]

- The No-Core Shell Model with Continuum is an *ab initio* approach based on the NCSM and its extension to the reactions, the NCSM/RGM. In the NCSM, the N-body eigenstates of the system can be written symbolically as $\{|\text{NCSM}\rangle_\lambda\}$, where λ is the index of the eigenstate. In the NCSM/RGM, the channel states formed by the $(N-n)$-body target states and the n-body projectile states are denoted $\{|\text{NCSM/RGM}\rangle_\alpha\}$ where α is the index of the channel. Then, it is possible to write bound and unbound eigenstates of the system as:

$$|\Psi\rangle = \sum_\lambda |\text{NCSM}\rangle_\lambda + \sum\!\!\!\!\!\!\int_\alpha |\text{NCSM/RGM}\rangle_\alpha \tag{1.146}$$

  The formulation of NCSMC resembles the CSM/SMEC but neglects the feedback of the continuum couplings on the discrete states of the NCSM. The NCSMC approach has been applied recently for the description of resonances of ^{7}He [110, 111].

- The No-Core Gamow Shell Model is an exact *ab initio* approach based on the GSM with interactions derived from EFT. It has been applied to the description of bound states and resonances in ^{3}H and ^{3,4,5}He [40]. The NCGSM approach to calculate bound states, resonances and scattering states leads to the dimensional explosion which can be somewhat tamed using the DMRG method [182, 183], a powerful truncation scheme to select the most important continuum configurations by retaining only the largest eigenvalues of the density matrix at each iteration.

Chapter 2

Gamow shell model description of proton and neutron radiative capture reactions

2.1 Introduction

Nuclear physics drives many astrophysical processes [212–214]. These include the Big Bang nucleosynthesis and the evolution of stars. The observed abundances of the elements in the Universe cannot be explained without nuclear reaction rates. The lifetimes of stars depend on the stellar mass and the time scale of the internal nuclear processes. A reliable description of the underlying astrophysical scenarios depends on the nuclear properties in the different regions of the Segré chart, involving both nuclei close to the valley of stability as well as exotic nuclei close to the drip lines.

Capture cross sections for most of the nuclei involved in the Big Bang nucleosynthesis and the stellar nucleosynthesis are difficult if not impossible to measure in laboratory, and thus indirect experimental approaches have to be employed. Often, capture cross sections have to be extrapolated at low-energies since no data are available, but the presence of resonances near the threshold can complicate these extrapolations.

In the present study, the proton and neutron radiative capture processes are considered. The radiative capture process is defined as[1] $A_1 + A_2 \rightarrow A + \gamma$, where A_1 and A_2 are the target and the projectile, and A is the compound nucleus formed by the capture of A_2 by A_1 with the emission of a photon γ. This process is governed by the nuclear forces and the electromagnetic interaction, and it is thus a probe for astrophysical phenomena. In particular, the proton and neutron radiative capture reactions are the dominant radiative capture reactions in the nucleosynthesis. They play an important role in the Big Bang and stellar nucleosynthesis, in the cold and hot[2] CNO cycles, in the proton-proton (pp) chains reactions, and in the stationary and explosive hydrogen burning chains. A review on CNO cycles and pp chain reactions is given in [215] and those cited hereafter are detailed in Appendix A.4.

In this work, three reactions are investigated using the GSM-CC formalism:

- The $^{17}\mathrm{F}(p,\gamma)^{18}\mathrm{Ne}$ reaction is in competition with the $^{17}\mathrm{F}(\beta^+)^{18}\mathrm{O}$ beta decay reaction in the cold CNO-II cycle to give the hot CNO-II cycle. The $^{17}\mathrm{F}(p,\gamma)^{18}\mathrm{Ne}$ reaction is also involved in the hot CNO-III cycle, and is expected to play a role in a possible transition from the hot CNO cycles to the *rp*-process in novae [216, 217]. There are no experimental data for $^{17}\mathrm{F}(p,\gamma)^{18}\mathrm{Ne}$ reaction, but it has been studied theoretically in a microscopic cluster model [218] and in SMEC [73].

- The $^{7}\mathrm{Be}(p,\gamma)^{8}\mathrm{B}$ reaction is of particular importance in astrophysics, since it is involved in the pp-II and pp-III chains. Indeed, the relative rates of the $^{7}\mathrm{Be}(e^-,\nu_e)^{7}\mathrm{Li}$ reaction and the $^{7}\mathrm{Be}(p,\gamma)^{8}\mathrm{B}$ reaction determine the pp-I/pp-II branching ratio, and thus the ratio of the neutrino fluxes coming from $^{7}\mathrm{Be}$

[1] This reaction is usually denoted $A_1(A_2,\gamma)A$ in nuclear physics.

[2] The hot CNO cycles are dominant at high pressure and temperature, when the proton capture becomes competitive to the β^+ decay.

and ^{8}B [215]. Also, from all solar neutrinos coming from the Sun, those due to ^{8}B beta decay have the higher energies [219]. Moreover, the ^{7}Be$(p,\gamma)^8$B reaction is involved in the stationary hydrogen burning chain. This reaction has been studied experimentally by the direct proton capture [220–230] and the Coulomb dissociation of ^{8}B [231–235]. Several theoretical descriptions are avaible for this reaction: the SMEC [67], the microscopic cluster model [236] and the NCSM/RGM [208].

- The ^{7}Li$(n,\gamma)^8$Li reaction is involved in the Big Bang nucleosynthesis. This reaction, which is the mirror reaction of ^{7}Be$(p,\gamma)^8$B, has been studied experimentally [237–240] and theoretically with the SMEC [67] and a microscopic cluster model [241].

In Sec.2.2, proton/neutron radiative capture processes and their description in the GSM-CC approach are presented. Then, the cross section formulae (Sec.2.3), the method of calculation (Sec.2.4) and the matrix elements (Sec.2.5) are discussed. Finally, results for ^{17}F$(p,\gamma)^{18}$Ne, ^{7}Be$(p,\gamma)^8$B and ^{7}Li$(n,\gamma)^8$Li reactions are presented as a proof of principle for the applicability of GSM-CC framework to nuclear radiative capture reactions.

2.2 Radiative capture process

In the transition from an initial state of angular momentum J_i and parity π_i, to a final state of angular momentum J_f and parity π_f, with the emission of a photon of angular momentum L, the conservation of the total angular momentum implies: $\hat{\vec{J}}_i = \hat{\vec{J}}_f + \hat{\vec{L}}$. In the initial state: $\hat{\vec{J}}_i = \hat{\vec{j}} + \hat{\vec{J}}_{\rm targ}$, $\hat{\vec{j}}$ is the angular momentum of the one-body projectile (proton or neutron) with the projection $m_j = \pm 1/2$, and $\hat{\vec{J}}_{\rm targ}$ is the total angular momentum of the target with the projection $M_{\rm targ}$. The total angular momentum projection on the (Oz) axis M_i satisfies: $|m_j - M_{\rm targ}| \leq M_i \leq m_j + M_{\rm targ}$. In the final state: $\hat{\vec{J}}_i = \hat{\vec{J}}_f + \hat{\vec{L}}$. Conservation of the total angular momentum and the angular momentum projection in the reaction implies:

$$\hat{\vec{L}} = \hat{\vec{J}}_i - \hat{\vec{J}}_f \qquad \text{and} \qquad |M_i - M_f| \leq M_L \leq M_i + M_f \tag{2.1}$$

where M_f, $\hat{\vec{L}}$, and M_L are the projection of the final angular momentum, the photon angular momentum, and its projection, respectively. The parity conservation implies that electric (E) and magnetic (M) transitions of multipolarity L carry the parity:

$$(\mathrm{E}L) \quad \pi_{\rm E} = (-1)^L \tag{2.2}$$

$$(\mathrm{M}L) \quad \pi_{\rm M} = (-1)^{L+1} \tag{2.3}$$

The GSM-CC calculations are done in COSM coordinates but the radiative capture cross section is expressed in the CM frame of reference. The initial energy is:

$$E_i^{(\rm COSM)} = E_{\rm proj}^{(\rm COSM)} + E_T^{(\rm COSM)} \tag{2.4}$$

where $E_i^{(\rm COSM)}$, $E_{\rm proj}^{(\rm COSM)}$ and $E_T^{(\rm COSM)}$ are the total energy, the projectile energy, and the GSM target binding energy, respectively. All energies are calculated in the COSM reference system. The link between the projectile energies in COSM and CM frames of reference is given by:

$$E_{\rm proj}^{(\rm COSM)} = E_{\rm proj}^{(\rm CM)} \frac{A}{A-1} = \frac{\hbar^2 (k_{\rm proj}^{(\rm CM)})^2}{2m_p} \frac{A}{A-1} \tag{2.5}$$

where $k_{\rm proj}^{(\rm CM)}$ is the linear momentum of the projectile given in input. Energy conservation implies that the final energy is:

$$E_i^{(\mathrm{COSM})} = E_f^{(\mathrm{COSM})} + E_\gamma \tag{2.6}$$

where $E_f^{(\mathrm{COSM})}$ is the compound system binding energy in the COSM frame of reference, and $E_\gamma = k_\gamma \hbar c$ is the photon energy which does not depend on the chosen reference system.

Resonances in the spectrum of the $(A+1)$-nucleon composite system correspond to the peaks in the radiative capture cross section at the CM energy:

$$E_{\mathrm{CM}} = E_i^{(A+1)}[\text{GSM-CC}] - E_0^{(A)}[\text{GSM}] \tag{2.7}$$

Here $E_i^{(A+1)}[\text{GSM-CC}]$ is the GSM-CC energy of the resonance 'i' in the $(A+1)$-system, and $E_0^{(A)}[\text{GSM}]$ is the GSM ground state energy of the target nucleus.

The cross section for a final state of the total angular momentum J_f is:

$$\sigma_{J_f}(E_{\mathrm{CM}}) = \int_0^{2\pi} d\varphi_\gamma \int_0^{\pi} \sin\theta_\gamma d\theta_\gamma \frac{d\sigma_{J_f}(E_{\mathrm{CM}}, \theta_\gamma, \varphi_\gamma)}{d\Omega\gamma} \tag{2.8}$$

The expression for the differential cross section will be given in the next subsection. The total cross section is thus:

$$\sigma(E_{\mathrm{CM}}) = \sum_{J_f} \sigma_{J_f}(E_{\mathrm{CM}}) \tag{2.9}$$

In practical applications, one often shows the astrophysical factor:

$$S(E_{\mathrm{CM}}) = \sigma(E_{\mathrm{CM}}) E_{\mathrm{CM}} e^{2\pi\eta} \tag{2.10}$$

which removes the trivial exponential dependence of the cross section at low energies due to the Coulomb barrier. The parameter η in (2.10) is the Sommerfeld parameter (1.46).

The description of electromagnetic transitions requires effective charges for proton and neutron. For E1 electromagnetic transitions, the standard values are [242]:

$$\begin{aligned} e^p_{\mathrm{eff}} &= e\left(1 - \frac{Z}{A}\right) \\ e^n_{\mathrm{eff}} &= -e\frac{Z}{A} \end{aligned} \tag{2.11}$$

where Z and A are the proton number and the total number of nucleons, respectively. The standard values for E2 transitions are:

$$\begin{aligned} e^p_{\mathrm{eff}} &= e\left(1 - \frac{Z}{A} + \frac{Z}{A^2}\right) \\ e^n_{\mathrm{eff}} &= -e\frac{Z}{A^2} \end{aligned} \tag{2.12}$$

There is no need for effective charges for M1 transitions. One should keep in mind that the effective charges extracted experimentally show often significant deviations from these theoretical estimates [243].

2.2.1 Description of the ^{17}F$(p,\gamma)^{18}$Ne reaction

The ground state of the ^{17}F target ($J^{\pi}_{\text{targ}} = 5/2^+_1$) is bound by 0.6 MeV with respect to ^{16}O. The final system ^{18}Ne has five bound states $J^{\pi} = 0^+_1, 2^+_1, 4^+_1, 0^+_2, 2^+_2$ below the proton emission threshold at the energy $S_p = 3.922$ MeV.

The model space in GSM and GSM-CC calculations of ^{17}F and ^{18}Ne is limited by the inert core of ^{16}O. The core is described by a WS potential (see Tab.2.1) for each considered partial wave $l = 0$ and 1. The radius of the Coulomb potential is $r_c = 3.050$ fm.

Parameter	Value
a	0.65 fm
R_0	3.050 fm
$V_{\text{o}}(l = 0, 1)$	55.5238 MeV
$V_{\text{so}}(l = 0, 1)$	6.149 MeV

Table 2.1 – Parameters of the WS potential for ^{16}O nucleus in the description of ^{17}F and ^{18}Ne.

Valence nucleons can occupy the $0d_{5/2}$ and $1s_{1/2}$ discrete s.p. states (see Fig.2.1) and several non-resonant s.p. continuum states on discretized contours: $L^+_{s_{1/2}}$, $L^+_{p_{1/2}}$, $L^+_{p_{3/2}}$, $L^+_{d_{3/2}}$ and $L^+_{d_{5/2}}$. Each contour consists of three segments joining the points: $k = 0$, $k_{\text{peak}} = 0.5 - i0.5$ fm^{-1}, $k_{\text{middle}} = 1.0$ fm^{-1} and $k_{\text{max}} = 3.0$ fm^{-1}, and each segment is discretized by respectively 7, 7 and 15 points. Each bound or scattering s.p. state becomes a new shell in the many-body calculations. Hence, GSM and GSM-CC calculations for ^{18}Ne are done in 147 shells: 30 $s_{1/2}$ and $d_{5/2}$ shells, and 29 $p_{1/2}$, $p_{3/2}$, $d_{3/2}$ shells.

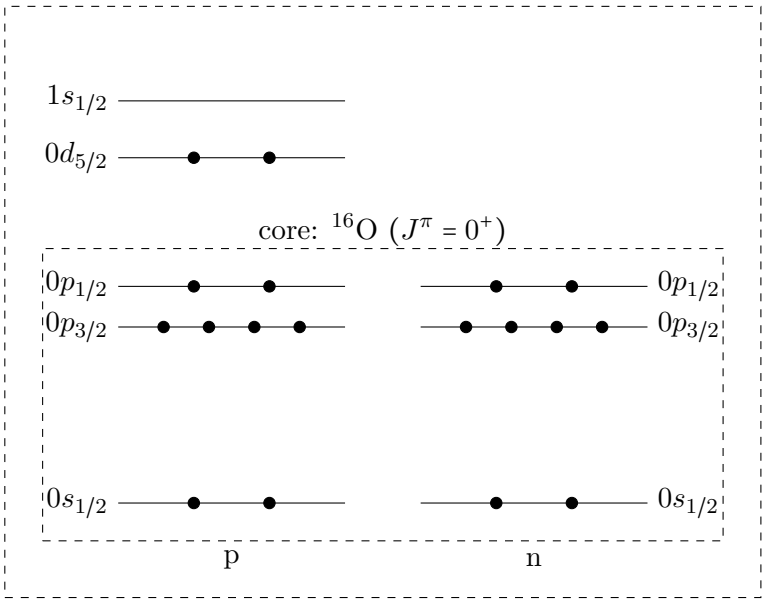

Figure 2.1 – The configuration space of ^{18}Ne.

The two-body interaction in ^{18}Ne is given by the modified surface Gaussian interaction (MSGI) [113]:

$$\hat{V}_{T,J}(\vec{r}_1,\vec{r}_2) = V^{(0)}_{T,J} e^{-\left(\frac{r_1-R_0}{\mu}\right)^2} e^{-\left(\frac{r_2-R_0}{\mu}\right)^2} F(R_0,r_1)F(R_0,r_2) \sum_{l=0}^{l_{\text{max}}} \left[\hat{\mathbf{Y}}_l(\vec{u}_{r_1}) \otimes \hat{\mathbf{Y}}_l(\vec{u}_{r_2})\right]^0_0 \tag{2.13}$$

where:

$$F(R_0,r) = \frac{1}{1 + e^{\frac{r-2R_0+r_f}{\mu_F}}} \tag{2.14}$$

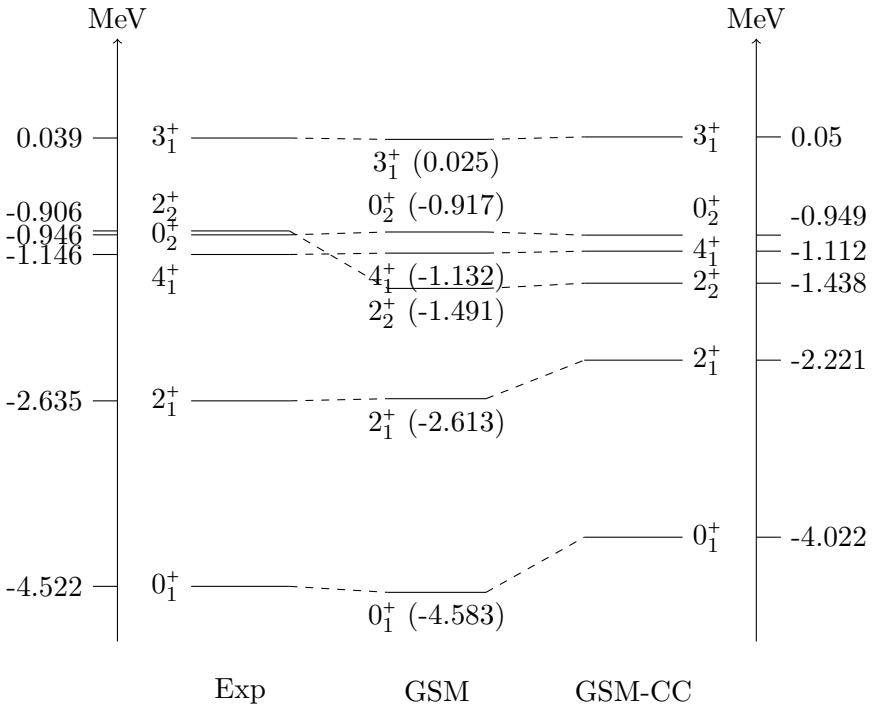

Figure 2.2 – Spectrum of ^{18}Ne with a core of ^{16}O. Energies are given relative to the ^{16}O core.

is the Fermi function with $r_f = 1$ fm and $\mu_F = 0.05$ fm. $F(R_0, r)$ is almost zero for $r > 2R_0$. Parameters of the MSGI interaction are given in Tab.2.2.

Parameter	Value
R_0	3.4 fm
μ	1.0 fm
$V_{T=1,J=0}$	-8.55 MeV
$V_{T=1,J=2}$	-5.75 MeV
$V_{T=1,J=3}$	4 MeV
$V_{T=1,J=4}$	-2.5 MeV

Table 2.2 – Parameters of the MSGI interaction for ^{18}Ne. Remaining $V_{T,J}$ parameters are all equal zero.

In GSM, the ground state of ^{17}F is bound by 0.617 MeV with respect to ^{16}O, which is close to the experimental value. Reaction channels in GSM-CC calculations are generated by a coupling of the ground state $J^\pi_{\text{targ}} = 5/2^+$ of ^{17}F and the proton partial waves: $s_{1/2}$, $p_{1/2}$, $p_{3/2}$, $d_{3/2}$ and $d_{5/2}$. The composite states of ^{18}Ne ($[^{17}\text{F}(J^\pi_{\text{targ}}) \otimes p(l,j)]^{J^\pi_f}$) are: $J^\pi_f = 0^+_1$, 2^+_1, 4^+_1, 0^+_2, 2^+_2 bound states and 3^+_1 resonance.

The spectra of ^{18}Ne calculated using GSM and GSM-CC are compared with the experimental data in Fig.2.2. According to the Eq.(2.7), the 3^+_1 resonance peak in ^{18}Ne is expected to be found at $E_{\text{CM}} = 0.667$ MeV. This resonance should be seen in M1 and E2 transitions. Using the same formula, the calculated proton separation energy in ^{18}Ne is: $S_{\text{p}}^{(\text{th})} = -E^{(0)}_{\text{CM}} = 3.405$ MeV, below the experimental value $S_{\text{p}} = 3.922$ MeV.

The proton and neutron effective charges in this reaction correspond to theoretical estimates given in Eqs.(2.11) and (2.12): $e^p_{\text{eff}}(\text{E1}) = 0.444$, $e^n_{\text{eff}}(\text{E1}) = -0.555$ and: $e^p_{\text{eff}}(\text{E2}) = 0.475$, $e^n_{\text{eff}}(\text{E2}) = -0.031$ for E1 and E2 transitions, respectively.

2.2.2 Description of the ^{7}Be$(p,\gamma)^8$B reaction

The ground state $J^\pi_{\text{targ}} = 3/2^-_1$ of ^{7}Be is bound by 5.6 MeV with respect to the proton emission threshold. The final system ^{8}B has one weakly bound state $J^\pi = 2^+_1$ below the proton emission threshold at the energy $S_{\text{p}} = 0.1375$ MeV.

The model space in GSM and GSM-CC calculations of ^{7}Be and ^{8}B is limited by the inert core of ^{4}He. The core is described by a WS potential (see Tab.2.3) for each considered partial wave $l = 0, 1$ and 2. The radius of the Coulomb potential is $r_c = 2.800$ fm.

Parameter	Value for protons	Value for neutrons
a	0.65 fm	0.65 fm
R_0	2.0 fm	2.0 fm
$V_{\text{o}}(l=0)$	61.5 MeV	70.6735 MeV
$V_{\text{so}}(l=0)$	0 MeV	0 MeV
$V_{\text{o}}(l=1)$	44.3967 MeV	70.6734 MeV
$V_{\text{so}}(l=1)$	7.80188 MeV	7.86276 MeV
$V_{\text{o}}(l=2)$	44.3967 MeV	0 MeV
$V_{\text{so}}(l=2)$	7.80188 MeV	0 MeV

Table 2.3 – Parameters of the WS potential for ^{4}He nucleus in the description of ^{7}Be and ^{8}B.

Valence nucleons can occupy the $0p_{3/2}$ and $0p_{1/2}$ discrete s.p. states (see Fig.2.3) and several non-resonant s.p. continuum states on discretized contours: $L^+_{s_{1/2}}$, $L^+_{p_{1/2}}$, $L^+_{p_{3/2}}$, $L^+_{d_{3/2}}$ and $L^+_{d_{5/2}}$. Each contour consists of three segments joining the points: $k_{\text{peak}} = 0.15 - i0.14$ fm^{-1}, $k_{\text{middle}} = 0.3$ fm^{-1} and $k_{\text{max}} = 2.0$ fm^{-1}, and each segment is discretized by 10 points. Hence, GSM and GSM-CC calculations are done in 152 shells: 31 $p_{3/2}$ and $p_{1/2}$ shells, and 30 $s_{1/2}$, $d_{3/2}$ and $d_{5/2}$ shells.

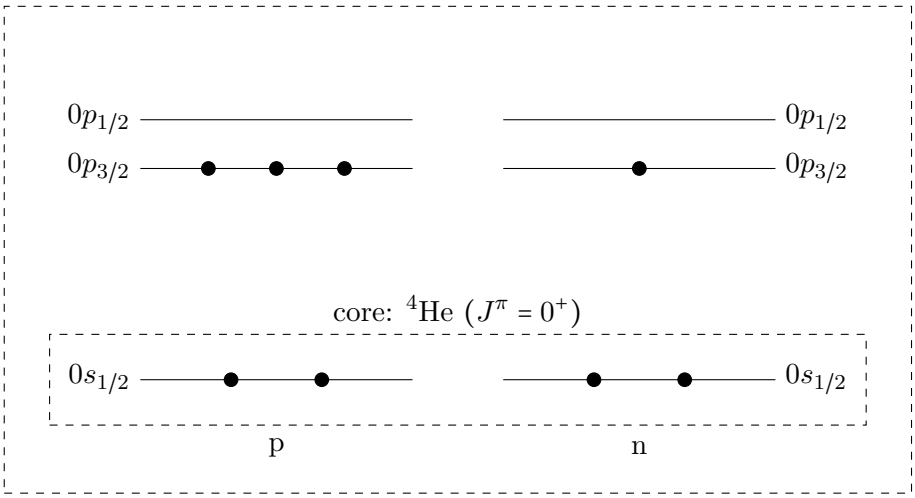

Figure 2.3 – The configuration space of ^{8}B.

The two-body interaction in ^{7}Be and ^{8}B is given by the FHT force [244, 245] described in Appendix A.6. The parameters of the FHT interaction are given in Tab.2.4 and in Appendix A.6 (see Tabs.A.1, A.2 and A.3).

In GSM, the ground state of ^{7}Be is bound by 9.378 MeV with respect to ^{4}He, which is close to the experimental value at $E_{\text{exp}} = 9.304$ MeV. Reaction channels are generated by a coupling of the ground state $J^\pi_{\text{targ}} = 3/2^-$ of ^{7}Be and the proton partial waves: $s_{1/2}$, $p_{1/2}$, $p_{3/2}$, $d_{3/2}$ and $d_{5/2}$. The composite states of ^{8}B $([^7\text{Be}(J^\pi_{\text{targ}}) \otimes p(l,j)]^{J^\pi_f})$ are 2^+_1 bound state, and 1^+_1, 3^+_1 resonances.

Parameter	Value [MeV]
$V_{\mathrm{C,odd,t}}$	4.00906
$V_{\mathrm{C,even,t}}$	-3.22579
$V_{\mathrm{C,odd,s}}$	2.22077
$V_{\mathrm{C,even,s}}$	-9.51008
$V_{\mathrm{SO,odd,t}}$	-1448.32
$V_{\mathrm{SO,even,t}}$	0
$V_{\mathrm{T,odd,t}}$	15.3946
$V_{\mathrm{T,even,t}}$	-15.4834

Table 2.4 – Parameters of the FHT interaction for ^{7}Be and ^{8}B calculations. The first indices "C", "SO" and "T" are for central, spin-orbit and tensor respectively, and the last indices "s" and "t" are for singlet and triplet.

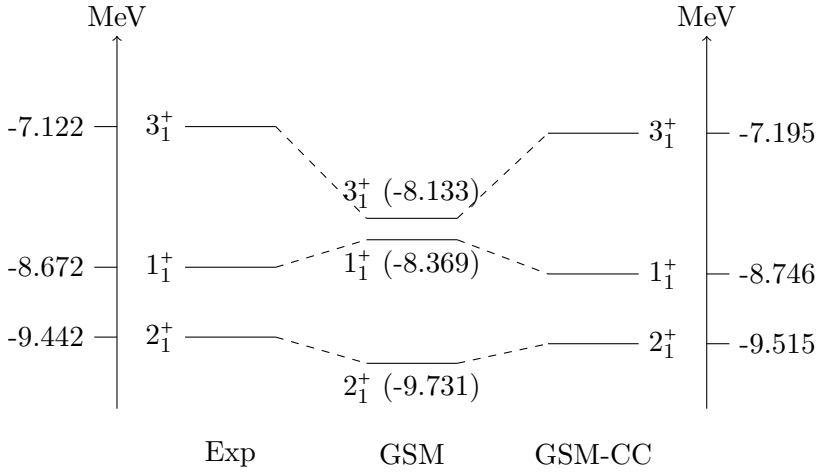

Figure 2.4 – Spectrum of ^{8}B with a core of ^{4}He. Energies are given relative to the ^{4}He core.

The spectra of ^{8}B calculated using GSM and GSM-CC are compared with the experimental data in Fig.2.4. In GSM-CC calculations, the channel-channel coupling potentials $V_{c,c'}$ have been slightly adjusted for each considered state of ^{8}B. The new potentials are: $\tilde{V}_{c,c'} = c(J^\pi)V_{c,c'}$, where $c(J^\pi)$ are the corrective factors. Values of these multiplicative corrective factors are: $c(2^+_1) = 1.0122$, $c(1^+_1) = 1.0668$, and $c(3^+_1) = 1.0225$. According to (2.7), the 1^+_1 resonance peak in ^{8}B is expected at $E_{\mathrm{CM}} = 0.632$ MeV. Similarly, the 3^+_1 resonance peak is expected at $E_{\mathrm{CM}} = 2.183$ MeV. Both resonances should be seen in M1 transitions. The 1^+_1 resonance could also be seen in E2 transitions. The calculated proton separation energy using Eq.(2.7) is $S_{\mathrm{p}}^{(\mathrm{th})} = 0.137$ MeV, in agreement with the experimental value $S_{\mathrm{p}} = 0.1375$ MeV.

The proton and neutron effective charges in this reaction correspond to the theoretical estimates and equal: $e^p_{\mathrm{eff}}(\mathrm{E1}) = 0.375$, $e^n_{\mathrm{eff}}(\mathrm{E1}) = -0.625$ and: $e^p_{\mathrm{eff}}(\mathrm{E2}) = 0.4531$, $e^n_{\mathrm{eff}}(\mathrm{E2}) = -0.0781$ for E1 and E2 transitions, respectively.

2.2.3 Description of the ^{7}Li$(n,\gamma)^8$Li reaction

The ^{7}Li$(n,\gamma)^8$Li reaction is the mirror reaction of ^{7}Be$(p,\gamma)^8$B. The ground state $J^\pi_{\mathrm{targ}} = 3/2^-_1$ of ^{7}Li is bound by 7.25 MeV with respect to the neutron emission threshold. The final nucleus ^{8}Li has two bound states $J^\pi = 2^+_1$ and 1^+_1 below the neutron emission threshold at the energy $S_{\mathrm{n}} = 2.03262$ MeV.

The model space in GSM and GSM-CC calculations of ^{7}Li and ^{8}Li is limited by the inert core ^{4}He. The core is described by a WS potential (see Tab.2.5) for each considered partial wave $l = 0, 1$ and 2. The

radius of the Coulomb potential is $r_c = 2.800$ fm.

Parameter	Value for protons	Value for neutrons
a	0.65 fm	0.65 fm
R_0	2.0 fm	2.0 fm
$V_{\rm o}(l=0)$	71.0752 MeV	43.6438 MeV
$V_{\rm so}(l=0)$	0 MeV	0 MeV
$V_{\rm o}(l=1)$	71.0752 MeV	43.6438 MeV
$V_{\rm so}(l=1)$	7.90622 MeV	7.84517 MeV
$V_{\rm o}(l=2)$	0 MeV	43.6438 MeV
$V_{\rm so}(l=2)$	0 MeV	0 MeV

Table 2.5 – Parameters of the WS potential for ^{4}He nucleus in the description of ^{7}Li and ^{8}Li.

Valence nucleons can occupy the $0p_{3/2}$ and $0p_{1/2}$ discrete s.p. states (see Fig.2.5) and several non-resonant s.p. continuum states on discretized contours: $L^+_{s_{1/2}}$, $L^+_{p_{1/2}}$, $L^+_{p_{3/2}}$, $L^+_{d_{3/2}}$ and $L^+_{d_{5/2}}$. Each contour consists of three segments joining the points: $k_{\rm peak} = 0.15 - i0.14$ fm^{-1}, $k_{\rm middle} = 0.3$ fm^{-1} and $k_{\rm max} = 2.0$ fm^{-1}, and each segment is discretized by 10 points. The GSM and GSM-CC calculations are done in 152 shells: in 31 $p_{3/2}$ and $p_{1/2}$ shells, and 30 $s_{1/2}$, $d_{3/2}$ and $d_{5/2}$ shells.

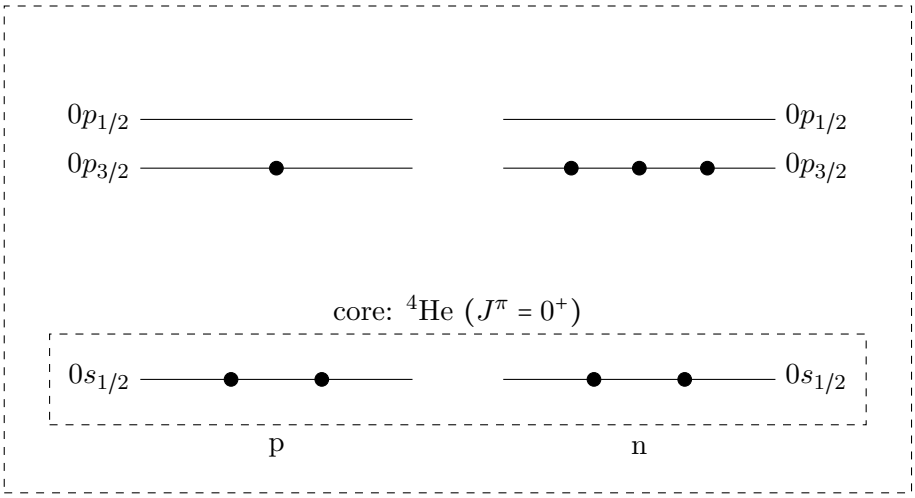

Figure 2.5 – The configuration space of ^{8}Li.

The two-body interaction in ^{7}Li and ^{8}Li is given by FHT force [244, 245]. The parameters of the FHT interaction are given in Tab.2.6 and in Appendix A.6 (see Tabs.A.1, A.2 and A.3).

In GSM, the ground state of ^{7}Li is bound by 11.228 MeV with respect to ^{4}He, *i.e.* close to the experimental value ($E_{\rm exp} = 10.948$ MeV). Reaction channels are generated by a coupling of the ground state $J^\pi_{\rm targ} = 3/2^-$ of ^{7}Li and the proton partial waves: $s_{1/2}$, $p_{1/2}$, $p_{3/2}$, $d_{3/2}$ and $d_{5/2}$. The composite states of ^{8}Li $[^7{\rm Li}(J^\pi_{\rm targ}) \otimes p(l,j)]^{J^\pi_f}$ are 2^+_1, 1^+_1 bound states, and 3^+_1 resonance.

The spectra of ^{8}Li calculated using GSM and GSM-CC are compared with the experimental data in Fig.2.6. The channel-channel coupling potentials in GSM-CC calculations have been slightly adjusted for each considered state of ^{8}Li, as described in Sec.2.2.2 for ^{8}B. Values of the multiplicative corrective factors are: $c(2^+_1) = 1.0380$, $c(1^+_1) = 1.0594$ and $c(3^+_1) = 1.0320$.

The 3^+_1 resonance peak in ^{8}Li is expected at $E_{\rm CM} = 0.223$ MeV. This resonance should be seen in M1 and E2 transitions. The calculated neutron separation energy according to (2.7) is $S_{\rm n}^{\rm (th)} = 2.032$ MeV, in agreement with the experimental value $S_{\rm n} = 2.03262$ MeV.

Parameter	Value [MeV]
$V_{\mathrm{C,odd,t}}$	4.03185
$V_{\mathrm{C,even,t}}$	-4.95286
$V_{\mathrm{C,odd,s}}$	2.23361
$V_{\mathrm{C,even,s}}$	-7.63465
$V_{\mathrm{SO,odd,t}}$	-1456.55
$V_{\mathrm{SO,even,t}}$	0
$V_{\mathrm{T,odd,t}}$	15.4822
$V_{\mathrm{T,even,t}}$	-15.5716

Table 2.6 – Parameters of the FHT interaction for ^{7}Li and ^{8}Li calculations. For more information, see the Tab.2.4.

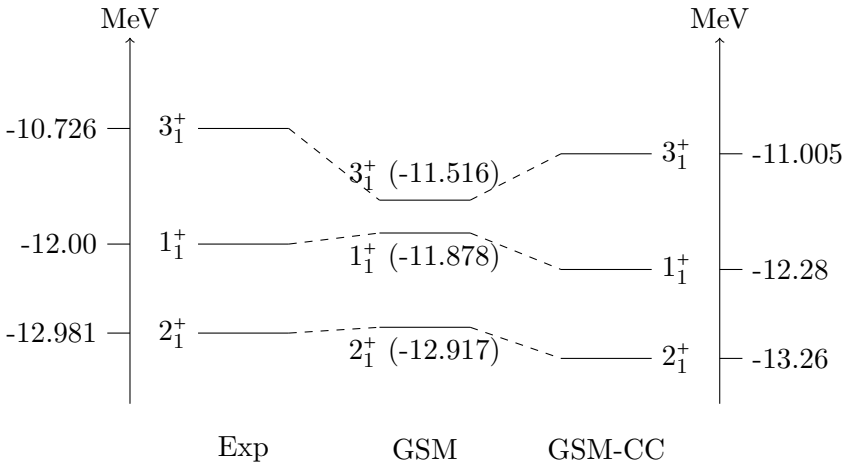

Figure 2.6 – Spectrum of ^{8}Li with a core of ^{4}He. Energies are given relative to the ^{4}He core.

The proton and neutron effective charges in this reaction correspond to theoretical estimates and equal: $e^{p}_{\mathrm{eff}}(\mathrm{E1}) = 0.625$, $e^{n}_{\mathrm{eff}}(\mathrm{E1}) = -0.375$ and: $e^{p}_{\mathrm{eff}}(\mathrm{E2}) = 0.7660$, $e^{n}_{\mathrm{eff}}(\mathrm{E2}) = -0.0534$ for E1 and E2 transitions respectively.

2.3 Proton/neutron radiative capture cross section

The differential cross section for proton capture $\mathrm{A}(p,\gamma)\mathrm{B}$ can be calculated from Fermi's golden rule, which relates the cross section to the matrix elements of a transition operator between an initial state $|i\rangle$ of energy E_i and a final state $|f\rangle$ of energy E_f. In the present study, the differential cross section is calculated following the derivation given in Ref. [246]:

$$\frac{d\sigma}{d\Omega_\gamma} = \frac{1}{8\pi}\left(\frac{k_\gamma}{k}\right)\left(\frac{e^2}{\hbar c}\right)\left(\frac{\mu_u c^2}{\hbar c}\right)\frac{1}{2s+1}\frac{1}{2J_{\text{targ}}+1} \times \sum_{\substack{M_i,M_f,\\ M_{\text{targ}},M_L,\\ P,m_s}} \left|\sum_L i^L\sqrt{2\pi(2L+1)}\left(\frac{k_\gamma^L}{k}\right)\sqrt{\frac{L+1}{L}}\frac{P}{(2L+1)!!}D^L_{M_L P}(\varphi_\gamma,\theta_\gamma,0)\,\langle\Psi_f(J_f,M_f)|\hat{\mathcal{M}}_{L,M_L}|\Phi_i(M_i)\rangle\right|^2 \tag{2.15}$$

$$= \frac{1}{2\pi}\left(\frac{k_\gamma}{k}\right)\left(\frac{e^2}{\hbar c}\right)\left(\frac{\mu_u c^2}{\hbar c}\right)\frac{1}{2s+1}\frac{1}{2J_{\text{targ}}+1}\sum_{\substack{M_i,M_f,\\ M_{\text{targ}},M_L,\\ P,m_s}} \left|\sum_L g^L_{M_L,P}(k,k_\gamma,\varphi_\gamma,\theta_\gamma)\,\langle\Psi_f(J_f,M_f)|\hat{\mathcal{M}}_{L,M_L}|\Phi_i(M_i)\rangle\right|^2 \tag{2.16}$$

where:

$$g^L_{M_L,P}(k,k_\gamma,\varphi_\gamma,\theta_\gamma) = i^L\sqrt{2\pi(2L+1)}\left(\frac{k_\gamma^L}{k}\right)\sqrt{\frac{L+1}{L}}\frac{P}{(2L+1)!!}D^L_{M_L P}(\varphi_\gamma,\theta_\gamma,0) \tag{2.17}$$

and:

- k_γ, in fm^{-1}, is the linear momentum of the emitted photon : $k_\gamma = (E_f - E_i)/(\hbar c)$.
- $e^2/(\hbar c)$ is the electromagnetic coupling constant.
- k, in fm^{-1}, is the linear momentum of the incoming proton in the CM frame of reference.
- $\mu_u c^2$, in MeV, is the reduced mass of the system $(A+1)$.
- s is the spin of the proton and J_{targ} the total spin of the target.
- $P = \pm 1$ is the polarization of the photon.
- L and M_L are the multipoles and multipole projections of the photon.
- $D^L_{M_L P}(\varphi_\gamma,\theta_\gamma,0)$ is the Wigner D-matrix, function of the angular variables θ_γ and φ_γ of the photon.
- $\hat{\mathcal{M}}_{L,M_L}$ is the electromagnetic transition operator.

The final state $|f\rangle$ corresponds to the CC state $|\Psi_f(J_f,M_f)\rangle$ of a total angular momentum J_f and projection M_f. The initial state $|i\rangle$ has a fixed value of the total angular momentum projection M_i, and it is denoted $|\Phi_i(M_i)\rangle$ in Eq.(2.16) with:

$$|\Phi_i(M_i)\rangle = \sum_{J_i,c_e} i^{l_{c_e}} e^{i\sigma_{l_{c_e}}}\sqrt{2l_{c_e}+1}\,|\Psi_i(J_i,M_i,c_e)\rangle\,\langle l_{c_e},0,s,m_s|(l_{c_e},s)j_{c_e},m_s\rangle\,\langle j_{c_e},m_s,J_{\text{targ}},M_{\text{targ}}|(j_{c_e},J_{\text{targ}})J_i,M_i\rangle \tag{2.18}$$

where $|\Psi_i(J_i,M_i,c_e)\rangle$ is the initial CC state with a total angular momentum J_i and an entrance channel[3] c_e. This state can be expressed in terms of channels as usual:

$$|\Psi_i(J_i,M_i,c_e)\rangle = \sum_c |\Psi_i(J_i,M_i,c_e)\rangle_c \tag{2.19}$$

[3]For each c_e value, the entrance channel corresponds to a different channel c.

Thus, the differential cross section writes:

$$\frac{d\sigma}{d\Omega_\gamma} = \frac{1}{2\pi}\left(\frac{k_\gamma}{k}\right)\left(\frac{e^2}{\hbar c}\right)\left(\frac{\mu_u c^2}{\hbar c}\right)\frac{1}{2s+1}\frac{1}{2J_{\text{targ}}+1} \times \sum_{\substack{M_i,M_f,\\ P,m_s,\\ M_{\text{targ}},M_L}} \left| \sum_L g^L_{M_L,P}(k,k_\gamma,\varphi_\gamma,\theta_\gamma) \sum_{J_i,c_e} \langle \Psi_f(J_f,M_f)|\hat{\mathcal{M}}_{L,M_L}|\Psi_i(J_i,M_i,c_e)\rangle \times \langle l_{c_e},0,s,m_s|(l_{c_e},s)j_{c_e},m_s\rangle \langle j_{c_e},m_s,J_{\text{targ}},M_{\text{targ}}|(j_{c_e},J_{\text{targ}})J_i,M_i\rangle \right|^2 \tag{2.20}$$

Now the summations can be arranged so that terms depending of the angular projection are put together:

$$\begin{aligned}\frac{d\sigma}{d\Omega_\gamma} = \frac{1}{2\pi}\left(\frac{k_\gamma}{k}\right)\left(\frac{e^2}{\hbar c}\right)\left(\frac{\mu_u c^2}{\hbar c}\right)\frac{1}{2s+1}\frac{1}{2J_{\text{targ}}+1}\sum_{J_i}\sum_L\sum_{c_e}\langle \Psi_f(J_f)\|\hat{\mathcal{M}}_L\|\Psi_i(J_i,c_e)\rangle^* \\ \times \sum_P [g^L_{M_L,P}(k,k_\gamma,\varphi_\gamma,\theta_\gamma)]^* \times \sum_{M_f,M_i,M_L}(-1)^{2(J_f-M_f)}\begin{pmatrix} J_f & L & J_i \\ -M_f & M_L & M_i\end{pmatrix} \\ \times \sum_{m_s}\langle l_{c_e},0,s,m_s|(l_{c_e},s)j_{c_e},m_s\rangle \times \sum_{M_{\text{targ}}}\langle j_{c_e},m_s,J_{\text{targ}},M_{\text{targ}}|(j_{c_e},J_{\text{targ}})J_i,M_i\rangle\end{aligned} \tag{2.21}$$

Note that the differential cross section is in units of fm^2.

The operator $\hat{\mathcal{M}}_{L,M_L}$ separates into an electric part $\hat{\mathcal{M}}^E_{L,M_L}$ and a magnetic part $\hat{\mathcal{M}}^M_{L,M_L}$. Formulae for the operators $\hat{\mathcal{M}}^E_{L,M_L}$ and $\hat{\mathcal{M}}^M_{L,M_L}$ are given in Appendix A.5 both in the long wavelength approximation and without this approximation.

2.4 Method

In the radiative capture cross section calculations, matrix elements of the electromagnetic operators in Eqs.(A.60), (A.62), (A.63) and (A.65) have to be evaluated. The main difficulty comes from their infinite-range and the antisymmetry of the coupled-channel states. Indeed, a direct calculation of these matrix elements in Berggren basis is not possible because they diverge even using the exterior complex scaling method. Nevertheless, if the antisymmetry in the channel state $|r,c\rangle$ is neglected:

$$|r,c\rangle = |r\rangle \otimes [|J_{\text{targ},c},M_{\text{targ},c}\rangle \otimes |l_c,s_c;j_c,m_{j_c}\rangle]^J_M = |r\rangle \otimes |c\rangle \tag{2.22}$$

then the overlap between a bound state or a narrow resonance, and a scattering state converges using the exterior complex-scaling method. This approximation is valid only at large distances. In this case, the antisymmetry between the target and the projectile does not play a significant role:

$$\mathcal{A}[|J_{\text{targ},c},M_{\text{targ},c}\rangle \otimes |l_c,s_c;j_c,m_{j_c}\rangle]^J_M = [|J_{\text{targ},c},M_{\text{targ},c}\rangle \otimes |l_c,s_c;j_c,m_{j_c}\rangle]^J_M \tag{2.23}$$

where $J_{\text{targ},c}$ is the angular momentum of the target in the channel c with a projection $M_{\text{targ},c}$, l_c is the orbital momentum of the projectile, s_c its spin and j_c its total angular momentum with a projection m_{j_c}. The action of a given operator $\hat{O}^L_{M_L}$ on the target and on the projectile can be defined by considering the target as distinguishable from the projectile nucleons:

$$\hat{O}^L_{M_L} = \sum_{i\in A}\hat{O}^L_{M_L}(r_i,\Omega_i) + \hat{O}^L_{M_L}(r_{\text{proj}},\Omega_{\text{proj}}) \tag{2.24}$$

where $\hat{O}^L_{M_L}(r,\Omega)$ is the one-body operator associated with the many-body operator $\hat{O}^L_{M_L}$. The first sum acts only on the target A, and r_{proj} and Ω_{proj} are the coordinates of a projectile. Once again, this approximation is valid only at large distances. The calculation of the matrix elements of electromagnetic operators goes as follows:

- The matrix elements are expressed as a non-antisymmetrized (nas) part plus a rest:

$$\langle\Psi_f||\hat{O}^L||\Psi_i\rangle = \langle\Psi_f||\hat{O}^L||\Psi_i\rangle_{\text{nas}} + \left(\langle\Psi_f||\hat{O}^L||\Psi_i\rangle - \langle\Psi_f||\hat{O}^L||\Psi_i\rangle_{\text{nas}}\right) \tag{2.25}$$

- The estimation of the rest is achieved by separating the operator $\hat{O}^L$ into a short-range part $\hat{O}^L_<$ and a long-range part $\hat{O}^L_>$. Then the symmetrized and antisymmetrized matrix elements write:

$$\langle\Psi_f||\hat{O}^L||\Psi_i\rangle = \langle\Psi_f||\hat{O}^L_<||\Psi_i\rangle + \langle\Psi_f||\hat{O}^L_>||\Psi_i\rangle \tag{2.26}$$
$$\langle\Psi_f||\hat{O}^L||\Psi_i\rangle_{\text{nas}} = \langle\Psi_f||\hat{O}^L_<||\Psi_i\rangle_{\text{nas}} + \langle\Psi_f||\hat{O}^L_>||\Psi_i\rangle_{\text{nas}} \tag{2.27}$$

  At large distances the antisymmetry is not crucial and thus the matrix element $\langle\Psi_f||\hat{O}^L_>||\Psi_i\rangle$ can be approximated by $\langle\Psi_f||\hat{O}^L_>||\Psi_i\rangle_{\text{nas}}$. The rest is basically a short-range part and can be expanded in the HO basis:

$$\langle\Psi_f||\hat{O}^L_<||\Psi_i\rangle - \langle\Psi_f||\hat{O}^L_<||\Psi_i\rangle_{\text{nas}} \approx \langle\Psi_f||\hat{O}^L_<||\Psi_i\rangle^{\text{HO}} - \langle\Psi_f||\hat{O}^L_<||\Psi_i\rangle^{\text{HO}}_{\text{nas}} \tag{2.28}$$

- Finally, the matrix elements are evaluated as:

$$\langle\Psi_f||\hat{O}^L||\Psi_i\rangle = \langle\Psi_f||\hat{O}^L||\Psi_i\rangle_{\text{nas}} + \langle\Psi_f||\hat{O}^L_<||\Psi_i\rangle^{\text{HO}} - \langle\Psi_f||\hat{O}^L_<||\Psi_i\rangle^{\text{HO}}_{\text{nas}} \tag{2.29}$$

2.5 Matrix elements

The initial and final states in Eqs.(2.16) and (2.18) have angular momenta J_i and J_f, respectively, and angular momentum projections M_i and M_f, respectively. Their CC representation is given in Eq.(1.66). In the present case, the channel state $|r,c\rangle$ is defined as:

$$|r,c\rangle = \mathcal{A}\left(|r\rangle \otimes [|J_{\text{targ},c}, M_{\text{targ},c}\rangle \otimes |l_c, s_c; j_c, m_{j_c}\rangle]^J_M\right) \tag{2.30}$$

The evaluation of matrix elements in Eq.(2.29) goes as follows:

- The matrix element $\langle\Psi_f||\hat{O}^L||\Psi_i\rangle_{\text{nas}}$ in Eq.(2.29) are not antisymetrized. The operator $\hat{O}^L$ (Eq.(2.24)) is written as: $\hat{O}^L_{\text{targ}} + \hat{O}^L_{\text{proj}}$, where $\hat{O}^L_{\text{targ}}$ acts only on the target state and $\hat{O}^L_{\text{proj}}$ on the projectile state. Thus, using Wigner-Eckart theorem, one obtains for the matrix elements of the electromagnetic operator acting on the target states:

$$\begin{aligned}
{}_{c_f}\langle\Psi_f||\hat{O}^L_{\text{targ}}||\Psi_i\rangle_{c_i} &= \int_0^\infty dr\, r^2 \frac{u_{c_f}(r)}{r} \int_0^\infty dr'\, r'^2 \frac{u_{c_i}(r')}{r'} \langle r|r'\rangle \\
&\times \langle l_{c_f}, s_{c_f}; j_{c_f}, m_{j_{c_f}} | l_{c_i}, s_{c_i}; j_{c_i}, m_{j_{c_i}}\rangle \langle J_{T_{c_f}}||\hat{O}^L_{\text{targ}}||J_{T_{c_i}}\rangle \\
&= (-1)^{J_{T_f}+j_f+J_i+L}\sqrt{(2J_f+1)(2J_i+1)} \begin{Bmatrix} J_{T_f} & J_{T_i} & L \\ J_i & J_f & j_i \end{Bmatrix} \langle J_{T_f}||\hat{O}^L||J_{T_i}\rangle \\
&\times \delta_{l_i l_f}\delta_{j_i j_f} \int_0^\infty dr\, u_{c_f}(r) u_{c_i}(r)
\end{aligned} \tag{2.31}$$

where $\langle r|r'\rangle = \delta_{r,r'}/r^2$. The initial and final channels are denoted c_i and c_f, respectively. Matrix elements of the electromagnetic operator acting on the projectile states are:

$$\begin{aligned}
{}_{c_f}\langle \Psi_f \| \hat{O}^L_{\text{proj}} \| \Psi_i \rangle_{c_i} &= \int_0^\infty dr\, r^2 \frac{u_{c_f}(r)}{r} \int_0^\infty dr'\, r'^2 \frac{u_{c_i}(r')}{r'} \langle r|r'\rangle \\
&\times \langle J_{T_{c_f}}, M_{T_{c_f}} | J_{T_{c_i}}, M_{T_{c_i}} \rangle \langle (l_{c_f}, s_{c_f}) j_{c_f} \| \hat{O}^L_{\text{proj}} \| (l_{c_i}, s_{c_i}) j_{c_i} \rangle \\
&= \delta_{T_i T_f} (-1)^{J_{T_i} + j_i + J_f + L} \sqrt{(2J_f+1)(2J_i+1)} \begin{Bmatrix} j_f & j_i & L \\ J_i & J_f & J_{T_i} \end{Bmatrix} \\
&\times \langle u_{c_f}, (l_{c_f}, s) j_{c_f} \| \hat{O}^L \| u_{c_i}, (l_{c_i}, s) j_{c_i} \rangle
\end{aligned} \tag{2.32}$$

No exterior complex scaling is necessary to calculate the overlap in Eq.(2.31) because $u_{c_i}(r)$ is the scattering wave function of a real energy and $u_{c_f}(r)$ is the bound state wave function.

- The antisymetrized matrix elements $\langle \Psi_f \| \hat{O}^L \| \Psi_i \rangle^{\text{HO}}$ are calculated by expressing the Berggren basis states in a HO basis. The reduced radial wave functions $u_c(r)$ can be written as:

$$\frac{u_c(r)}{r} = \langle r|u_c\rangle \tag{2.33}$$

where $|u_c\rangle$ is the channel dependent radial state. In this case, the HO expansion is:

$$\frac{u_c(r)}{r} = \langle r|u_c\rangle \to \frac{u_c^{\text{HO}}(r)}{r} = \sum_\alpha \langle r|u_\alpha\rangle \langle u_\alpha|u_c\rangle = \sum_\alpha u_\alpha(r) \langle u_\alpha|u_c\rangle = \langle r|u_c^{\text{HO}}\rangle \tag{2.34}$$

where $|u_\alpha\rangle$ is the radial HO state. The channel state $|r, c\rangle$ can be expressed with the help of the radial Berggren basis:

$$|r, c\rangle = \hat{\mathcal{A}} \left(|r\rangle \otimes |c\rangle \right) = \hat{\mathcal{A}} \left(\left(\sum_n \langle u_n|r\rangle |u_n\rangle \right) \otimes |c\rangle \right) = \sum_n \langle u_n|r\rangle |u_n, c\rangle \tag{2.35}$$

where the state $|u_n, c\rangle$ is:

$$|u_n, c\rangle = \left[\hat{a}^\dagger_{n, j_c, m_{j_c}} |J_{\text{targ},c}, M_{\text{targ},c}\rangle \right]^J_M \tag{2.36}$$

Hence, the CC representation (1.66) of initial and final states in Eqs.(2.16) and (2.18) can be written in HO basis as follows:

$$|\Psi\rangle^{\text{HO}} = \cancel{\sum_c} \sum_n \langle u_n|u_c^{\text{HO}}\rangle |u_n, c\rangle \tag{2.37}$$

Then the fully antisymetrized matrix elements of electromagnetic transition operators can be written as:

$${}^{\text{HO}}\langle \Psi_f \| \hat{O}^L \| \Psi_i \rangle^{\text{HO}} = \sum_{c_i, c_f} \sum_{n_i, n_f} \langle u_{c_i}^{\text{HO}}|u_{n_i}\rangle \langle u_{n_f}|u_{c_f}^{\text{HO}}\rangle \left[\langle J_{T_{c_f}}| \hat{a}_{n_f, j_{c_f}} \right]^J_M \hat{O}^L_{M_L} \left[\hat{a}^\dagger_{n_i, j_{c_i}} |J_{T_{c_i}}\rangle \right]^J_M \tag{2.38}$$

The HO expansion is hereby justified by the fact that the target states are localized.

- The last many-body matrix element in Eq.(2.29): ${}^{\rm HO}\langle\Psi_f||\hat{O}^L||\Psi_i\rangle^{\rm HO}_{\rm nas}$, is calculated using Eqs.(2.31) and (2.32) and replacing $u_c(r)$ by $u_c^{\rm HO}(r)$ (see Eq.(2.34)).

One-body matrix elements of the electromagnetic transition operators are listed in Appendix A.5. No exterior complex scaling is required to calculate these matrix elements, since the final state in the radiative capture process is always a bound state. The reduced angular momentum matrix elements associated with operators entering Eqs.(A.60), (A.62), (A.63) and (A.65) are also listed in Appendix A.5.

2.6 Results

In this section the GSM-CC results for the ^{17}F$(p,\gamma)^{18}$Ne, ^{7}Be$(p,\gamma)^{8}$B and ^{7}Li$(n,\gamma)^{8}$Li reactions are presented. In all calculations we consider only the ground state of the target nucleus. The astrophysical factor is calculated for the E1, M1 and E2 electromagnetic transitions and results are compared with those obtained in the SMEC, the microscopic cluster model of Ref. [218] and the NCSM/RGM.

2.6.1 ^{17}F$(p,\gamma)^{18}$Ne reaction

Figs.2.7, 2.8 and 2.9 show the E1, M1 and E2 astrophysical factors for ^{17}F$(p,\gamma)^{18}$Ne reaction.

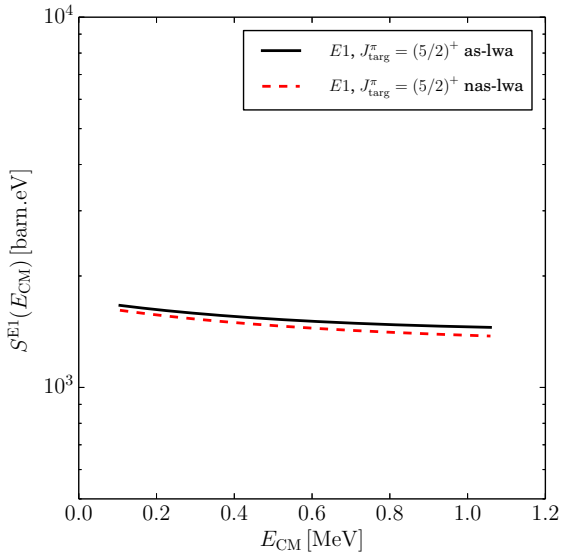

Figure 2.7 – Plot of the E1 astrophysical factor for the ^{17}F$(p,\gamma)^{18}$Ne reaction. The solid line corresponds to the fully antisymmetrized calculations, while the dashed line represents the non-antisymmetrized calculations, both in the long wavelength approximation. For more details, see the description in the text.

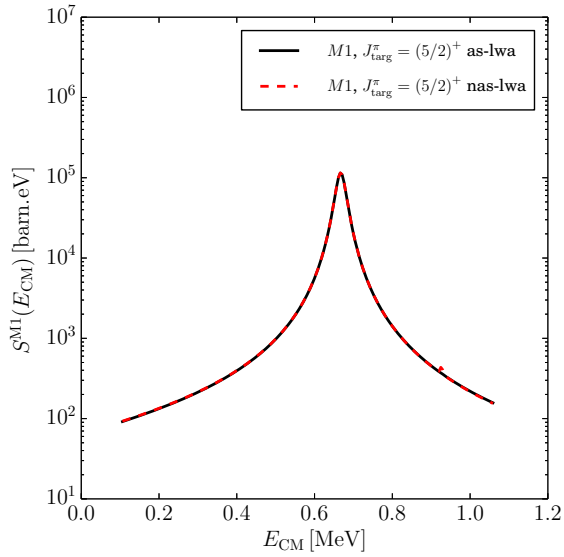

Figure 2.8 – The same as in Fig.2.7 but for the M1 transitions. The resonance peak corresponds to the 3^+_1 resonance of ^{18}Ne.

There is no resonant contribution in low-energy E1 transitions. The astrophysical factor in Fig.2.7 is consistent with results of Refs. [73] obtained in the SMEC (see Fig.2.11) and in the microscopic cluster model of Ref. [218] (see Fig.2.12). Quantitative differences can be explained by different model spaces in these calculations. For example, SMEC calculations have been performed with the ^{12}C core, *i.e.* the model space consists of three valence protons and two valence neutrons in ^{17}F, and four valence protons and two valence neutrons in ^{18}Ne. In SMEC, the $1/2^+$ excited state of the target has been also taken into account.

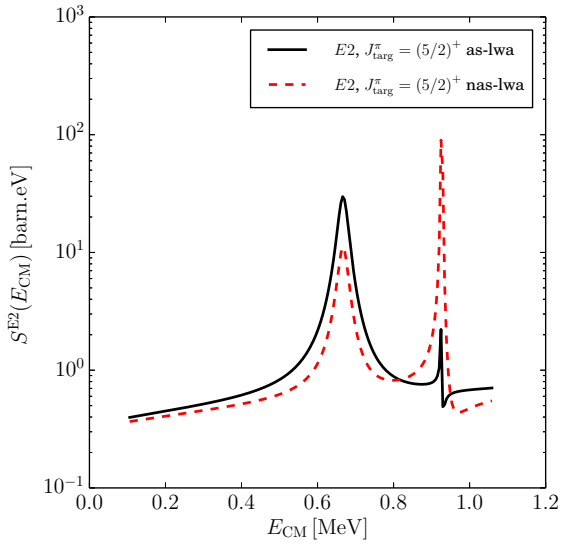

Figure 2.9 – The same as in Fig.2.7 but for the E2 transitions. The resonance peak corresponds to the 3^+_1 resonance of ^{18}Ne.

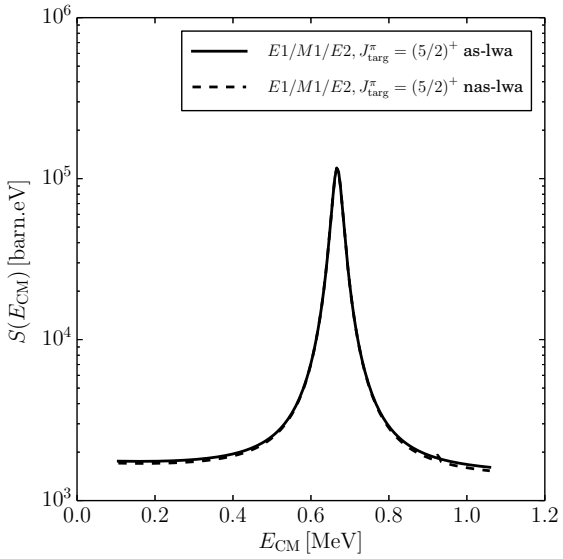

Figure 2.10 – Plot of the total astrophysical factor for the reaction ^{17}F$(p,\gamma)^{18}$Ne. The solid line corresponds to the fully antisymmetrized calculations, while the dashed line represents only the non-antisymmetrized calculations, both in the long wavelength approximation. For more details, see the text.

The composite states of ^{18}Ne included in SMEC calculations were the same as in the present GSM-CC calculations.

One can see that the E1 astrophysical factor in GSM-CC is slightly larger than in SMEC but is close to the result obtained in the microscopic cluster model. In the microscopic cluster model, the three first states of ^{17}F: $5/2^+$, $1/2^+$ and $3/2^+$, and the composite states of ^{18}Ne: 0^+_1, 2^+_1, 4^+_1, 2^+_2 and 3^+_1 are considered in the bound state approximation. The resemblance of SMEC and cluster model results to the outcome of GSM-CC calculations in which inelastic channels have been neglected, suggests that the contribution of these channels to the E1 astrophysical factor in ^{18}Ne is rather small. Moreover, as shown in Fig.2.7, the antisymmetrization of initial and final states in the calculation of matrix elements of the electromagnetic operators does not contribute significantly to the astrophysical factor, even at slightly higher-energies. This is because proton radiative capture of a proton occurs at the periphery of the target nucleus.

The astrophysical factor for M1 transitions is shown in Fig.2.8. The peak at $E_{\rm CM} = 0.642$ MeV corresponds to the 3^+_1 resonance of ^{18}Ne observed experimentally at $E_{\rm CM} = 0.638$ MeV. This result is consistent with the result of Refs. [73, 218]. In the present case, the astrophysical factor for M1 transitions is slightly higher than found in SMEC, but is close to the result in the microscopic cluster model. As shown in Fig.2.8, the antisymmetry of initial and final states in the calculation of matrix elements of the electromagnetic operators is inessential for the M1 astrophysical factor.

The E2 astrophysical factor which is plotted in Fig.2.9, has a small resonant contribution at around the energy of a 3^+_1 resonance. This result is consistent with those of Refs. [73, 218] shown in Figs.2.11 and 2.12. The resonant contribution seen at ~ 0.9 MeV, corresponds to the 3^+_2 resonance which is seen only in GSM-CC.

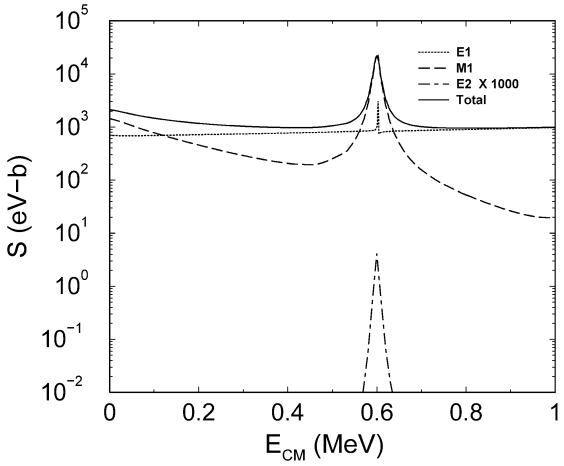

Figure 2.11 – The astrophysical factor and its E1, M1 and E2 components for the ^{17}F$(p,\gamma)^{18}$Ne reaction calculated in SMEC (from Ref. [73]).

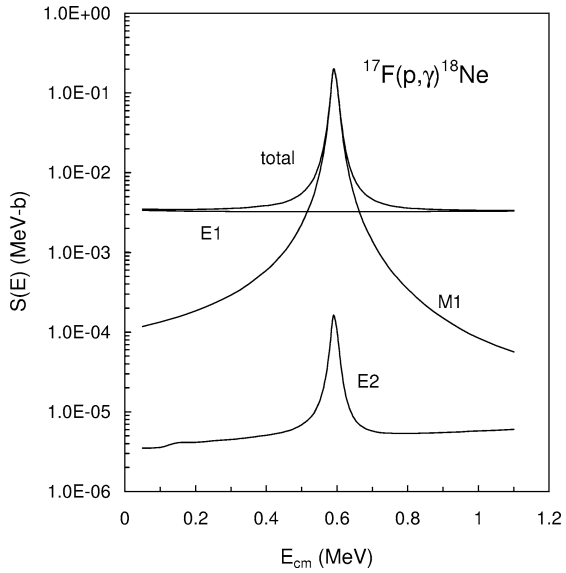

Figure 2.12 – The astrophysical factor and its E1, M1 and E2 components for the ^{17}F$(p,\gamma)^{18}$Ne reaction calculated in the microscopic cluster model (from Ref. [218]).

2.6.2 ^{7}Be$(p,\gamma)^{8}$B reaction

Figs.2.13, 2.14 and 2.15 show the E1, M1 and E2 astrophysical factors for ^{7}Be$(p,\gamma)^{8}$B reaction. The influence of the long wavelength approximation on the astrophysical factor has been considered in this reaction.

There is no resonant contribution in E1 transitions. The astrophysical factor in Fig.2.13 is consistent with the SMEC results of Ref. [67] shown in Fig.2.18. In SMEC the separation energy has been adjusted to the experimental value, and contrary to the present work, the $1/2^-$ excited state of the target has been taken into account. Results in Fig.2.13 are also consistent with those of Ref. [208] obtained in the NCSM/RGM approach and shown in Fig.2.19. In NCSM/RGM, excited states of the target: $3/2^-_1$, $1/2^-_1$, $7/2^-_1$, $5/2^-_1$ and $5/2^-_2$ have been considered in the bound state approximation. The quantitative agreement between GSM-CC without inelastic channels and NCSM/RGM results confirm that the contribution of inelastic channels to the E1 astrophysical factor in this reaction is small. As shown in Fig.2.13, the antisymmetry does not contribute significantly, even at high-energy. The same observation can be done for the long wavelength approximation.

The astrophysical factor for M1 transitions is shown in Fig.2.14. The 1^+_1 and 3^+_1 resonances of ^{8}B can be seen at $E_{\rm CM}$ = 0.79 MeV and $E_{\rm CM}$ = 2.34 MeV, respectively. These resonances are observed experimentally at $E_{\rm CM}$ = 0.632 MeV and $E_{\rm CM}$ = 2.182 MeV, respectively. The antisymmetrization of initial and final states in the calculation of matrix elements of the electromagnetic operators, decreases by a factor ~ 2 the heights of the cross section at the maximum of these resonances. The long wavelength approximation does not change the M1 astrophysical factor.

The E2 astrophysical factor (see Fig.2.15) has two peaks. The first one corresponds to the 1^+_1 resonance at $E_{\rm CM}$ = 0.632 MeV, and the second corresponds to the 1^+_2 resonance obtained in both GSM and GSM-CC calculations, but which was not observed experimentally at around these energies. For the E2 transition, the antisymmetry of initial and final states in the calculation of matrix elements of the electromagnetic operators decreases the height of the low-energy 1^+_1 resonance, but increases the height of the 1^+_2 resonance. Removing the long wavelength approximation in calculations slightly decreases the E2 astrophysical factor.

Finally, the sum of E1, M1 and E2 contributions to the astrophysical factor is compared in Fig.2.16

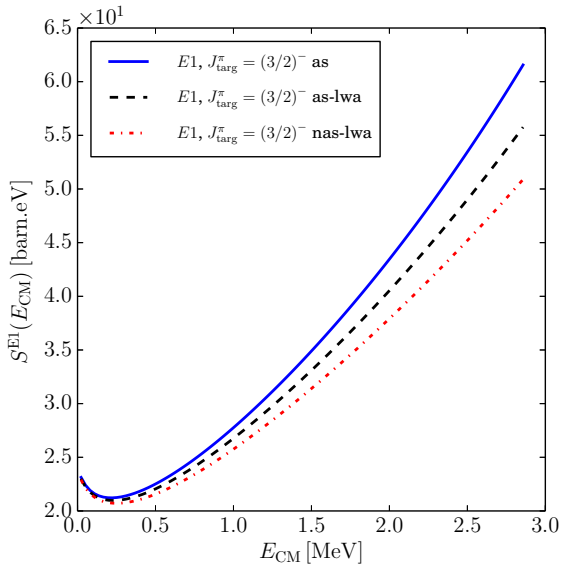

Figure 2.13 – Plot of the E1 astrophysical factor for the ^{7}Be$(p,\gamma)^8$B reaction. The solid line represents the exact, fully antisymmetrized GSM-CC calculation. Calculations in the long wavelength approximation are represented by the dashed and dotted lines in the fully antisymmetrized and non-antisymmetrized cases, respectively. For more details, see the description in the text.

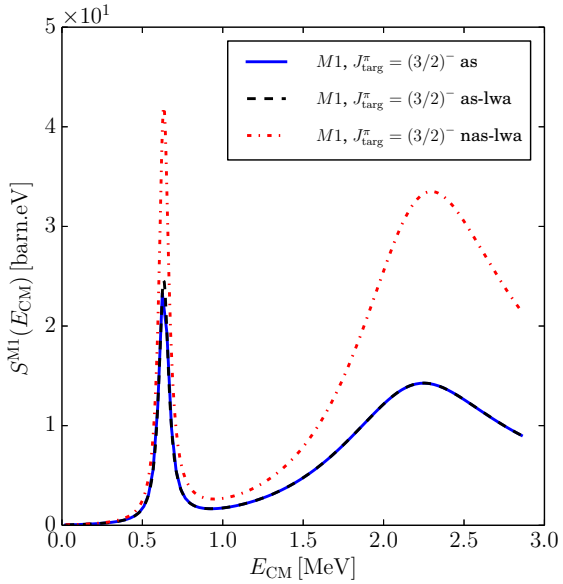

Figure 2.14 – The same as in Fig.2.13 but for the M1 transitions. The two peaks correspond to the 1^+_1 and 3^+_1 resonances of ^{8}B.

with the recent experimental data. A good overall agreement is obtained at low-energy, but the height of the 1^+_1 resonance is about half of the experimental one, and its width ($\Gamma_{\text{GSM-CC}} = 72.9$ keV) is twice the experimental value ($\Gamma_{\text{exp}} = 35.6$ keV). The 3^+_1 resonance in GSM-CC is also broader ($\Gamma_{\text{GSM-CC}} = 1.057$ MeV) than found experimentally ($\Gamma_{\text{exp}} = 0.350$ MeV). Results are slightly affected by the long wavelength approximation at energies above the 3^+_1 resonance.

It has been shown that the long wavelength approximation and the antisymmetry of initial and final states in the calculation of matrix elements of the electromagnetic operators affect the total astrophysical factor slightly. The last test consists of investigating the influence on the astrophysical factors S^{E1}, S^{M1} and S^{E2} of additional reaction channels built from the first excited state $J^\pi = 1/2^-$ of the target nucleus ^{7}Be. Experimentally this state is bound by 8.875 MeV with respect to ^{4}He, whereas in GSM it is bound by 6.962 MeV. The multiplicative corrective factors: $c(2^+_1) = 1.0133$, $c(1^+_1) = 1.0602$ and $c(3^+_1) = 1.0233$ for channel coupling potentials have been used to adjust the position of ^{8}B resonances. The E1, M1 and E2 contributions to the astrophysical factor are shown on Figs.2.20, 2.21 and 2.22, respectively.

The E1 and E2 contributions to the astrophysical factor are decreased slightly when taking into account the excited state $J^\pi = 1/2^-$ of the target nucleus ^{7}Be, while the M1 contribution is increased of a factor ~ 3 at the resonance peak.

The comparison with experimental data in Fig.2.23 shows a better agreement when the excited state of the target nucleus is included, in particular at the 3^+_1 resonance peak.

The extrapolation of the astrophysical factor at low energies with a polynomial fit of order 4:

$$S(E_{\text{CM}}) = 23.214 - 37.291E_{\text{CM}} + 212.372E^2_{\text{CM}} - 575.437E^3_{\text{CM}} + 663.972E^4_{\text{CM}} \tag{2.39}$$

is shown in Fig.2.17. The value at the threshold is $S^{(\text{GSM-CC})}(0) = 23.214$ barn.eV. Tab.2.7 gives values of $S(0)$ for different experiments. The GSM-CC value of the astrophysical factor at $E_{\text{CM}} = 0$ is

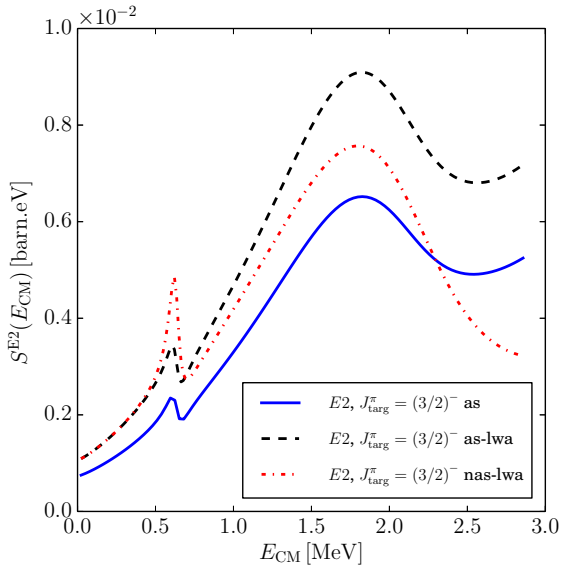

Figure 2.15 – The same as in Fig.2.13 but for the E2 transitions. The two peaks correspond to the 1^+_1 and 1^+_2 resonances of ^{8}B.

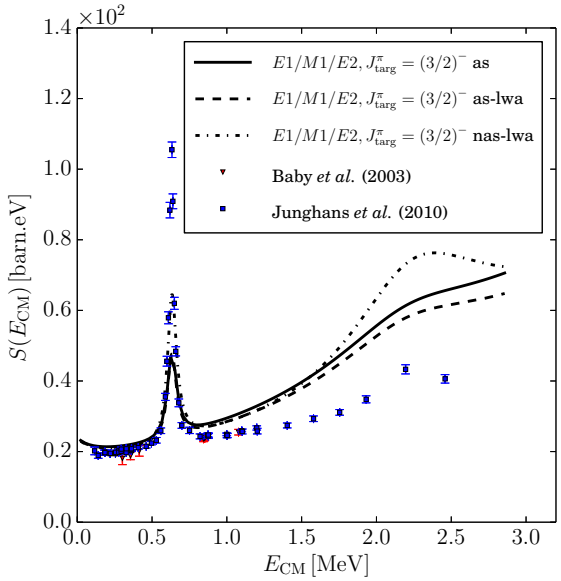

Figure 2.16 – Plot of the total astrophysical factor for the ^{7}Be$(p,\gamma)^8$B reaction. Data are taken from Refs. [226] and [230]. The solid line represents the exact, fully antisymmetrized GSM-CC calculation. Calculations in the long wavelength approximation are represented by the dashed and dotted lines in the antisymmetrized and non-antisymmetrized cases, respectively. For more details see the description in the text.

higher than the accepted experimental value: $S^{(\mathrm{Exp})}(0) = 20.9 \pm 0.6$ barn.eV [230], and values obtained in SMEC: $S^{(\mathrm{SMEC})}(0) = 19.594$ barn.eV and NCSM/RGM: $S^{(\mathrm{NCSM/RGM})}(0) = 19.4$ barn.eV. On the contrary, $S^{(\mathrm{GSM\text{-}CC})}(0)$ is lower than the astrophysical factor $S^{(\mathrm{cluster})}(0) \approx 25$ barn.eV of the microscopic cluster model.

Reference	$S(0)$ [barn.eV]
Hass *et al.* (1999) [247]	20.3 ± 1.2
Hammache *et al.* (2001) [223]	18.8 ± 1.7
Strieder *et al.* (2001) [248]	18.4 ± 1.6
Junghans *et al.* (2002) [224]	22.3 ± 0.7
Baby *et al.* (2003) [226]	21.2 ± 0.7
Junghans *et al.* (2010) [230]	21.5 ± 0.6

Table 2.7 – Extrapolated experimental values of the astrophysical factor at E_{CM}. These values should be compared with the GSM-CC result: $S^{(\mathrm{GSM\text{-}CC})}(0) = 23.214$ barn.eV.

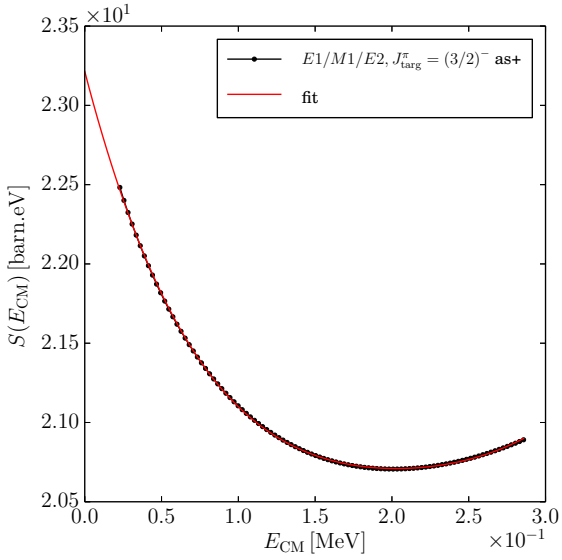

Figure 2.17 – Fit of the astrophysical factor including E1 and M1 transitions for the ^{7}Be$(p,\gamma)^8$B reaction at low energies. The extrapolated value of the astrophysical factor at $E_{\text{CM}} = 0$ is $S^{(\text{GSM-CC})}(0) = 23.214$ barn.eV. For more details, see the discussion in the text.

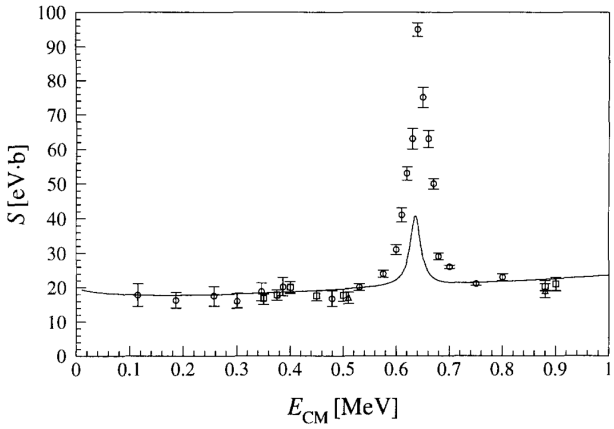

Figure 2.18 – Plot of the astrophysical factor for the ^{7}Be$(p,\gamma)^8$B reaction calculated in SMEC (from Ref. [67]).

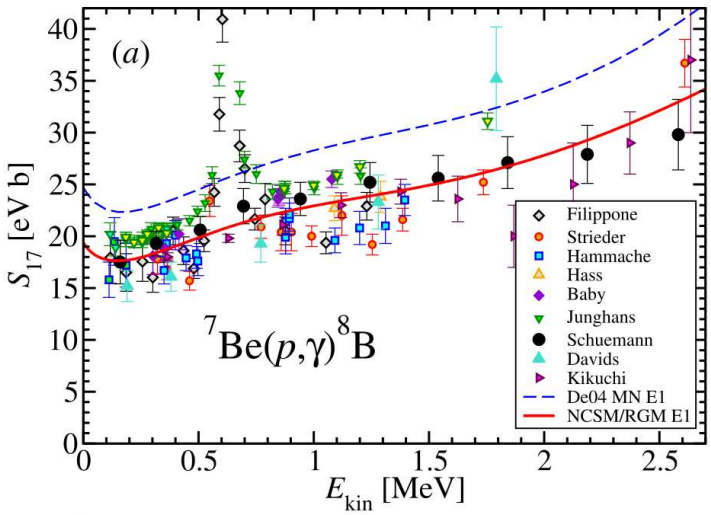

Figure 2.19 – Plot of the E1 astrophysical factor for the ^{7}Be$(p,\gamma)^8$B reaction calculated in NCSM/RGM (from Ref. [208]). Solid and dashed lines correspond to NCSM/RGM and microscopic cluster model results (from Ref. [236]), respectively.

2.6.3 ^{7}Li$(n,\gamma)^8$Li reaction

Figs.2.24, 2.25 and 2.26 show the E1, M1 and E2 cross sections for ^{7}Li$(n,\gamma)^8$Li reaction. The influence of the long wavelength approximation on the cross section has been considered in this reaction. The shape of the s-wave neutron capture cross section $\sigma \propto 1/\sqrt{E_{\text{CM}}}$ is well reproduced (see Fig.2.24). There is no resonant contribution in E1 electromagnetic transitions, and the antisymmetrization of initial and

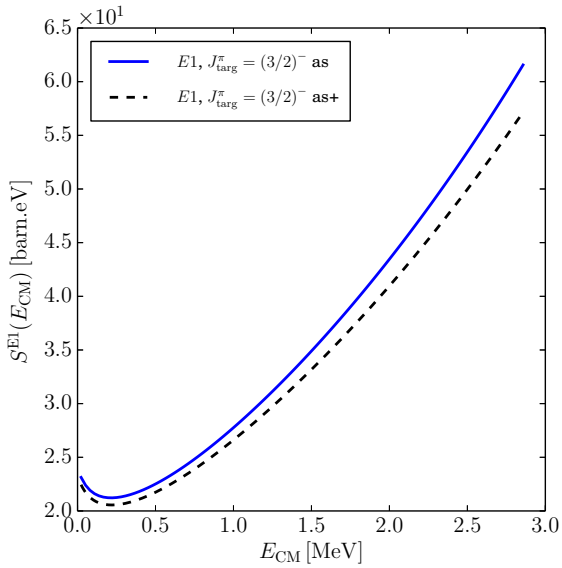

Figure 2.20 – Plot of the E1 astrophysical factor for the ^{7}Be$(p,\gamma)^8$B reaction. The solid and dashed lines represent the exact, fully antisymmetrized GSM-CC calculation without and with the excited state of the target $J^\pi = 1/2^-$, respectively. For more details, see the description in the text.

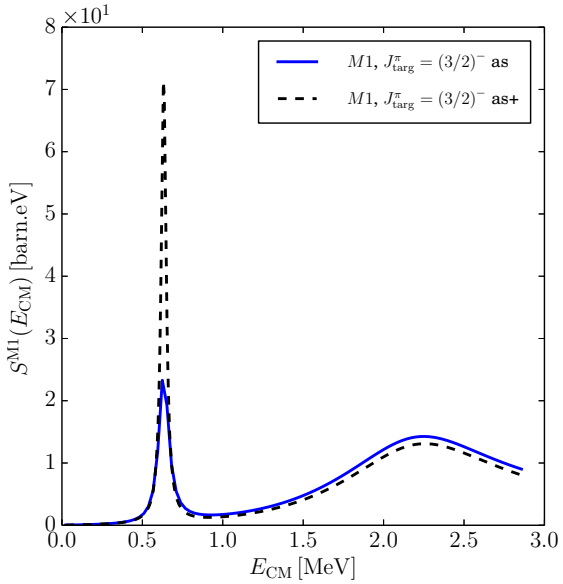

Figure 2.21 – The same as in Fig.2.20 but for the M1 transitions. The two peaks correspond to the 1^+_1 and 3^+_1 resonances of ^{8}B.

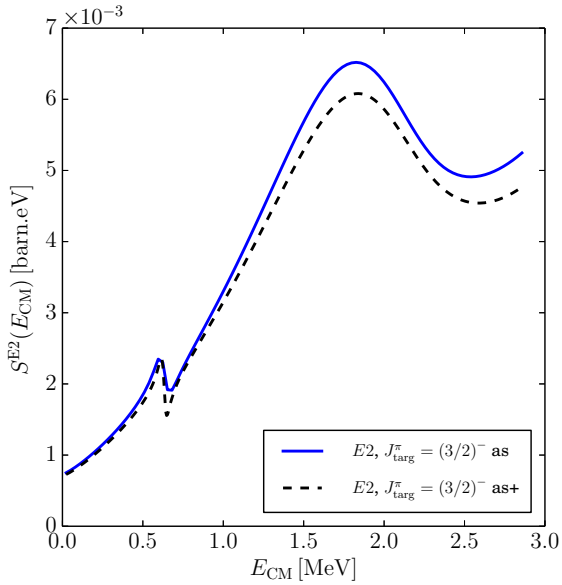

Figure 2.22 – The same as in Fig.2.20 but for the E2 transitions. The two peaks correspond to the 1^+_1 and 1^+_2 resonances of ^{8}B.

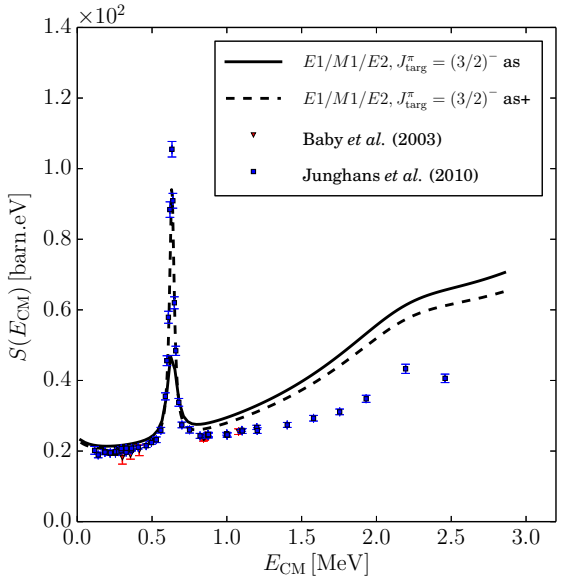

Figure 2.23 – Plot of the total astrophysical factor for the ^{7}Be$(p,\gamma)^8$B reaction. Data are taken from Refs. [226] and [230]. The solid and dashed lines represent the exact, fully antisymmetrized GSM-CC calculation without and with the excited state of the target, respectively. For more details see the description in the text.

final states in the calculation of matrix elements of the electromagnetic operators does not contribute significantly. Removing the long wavelength approximation in calculations slightly decreases the E1 cross section.

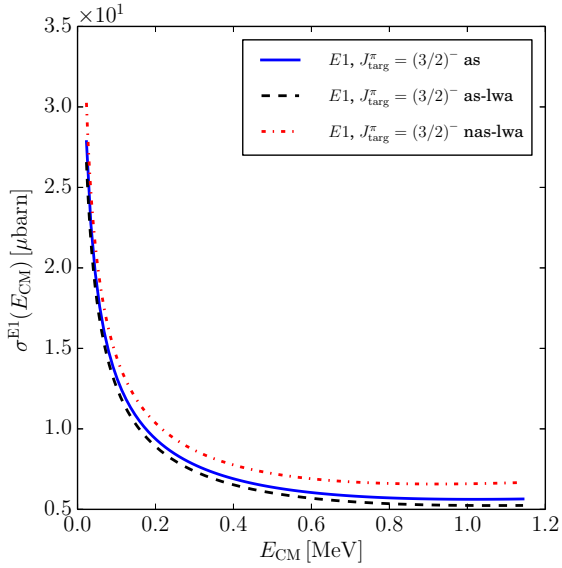

Figure 2.24 – Plot of the E1 cross section for the ^{7}Li$(n,\gamma)^8$Li reaction. The solid line represents the exact, fully antisymmetrized calculation. Calculations in the long wavelength approximation are represented by the dashed and dotted lines in the fully antisymmetrized and non-antisymmetrized cases, respectively. For more details, see the description in the text.

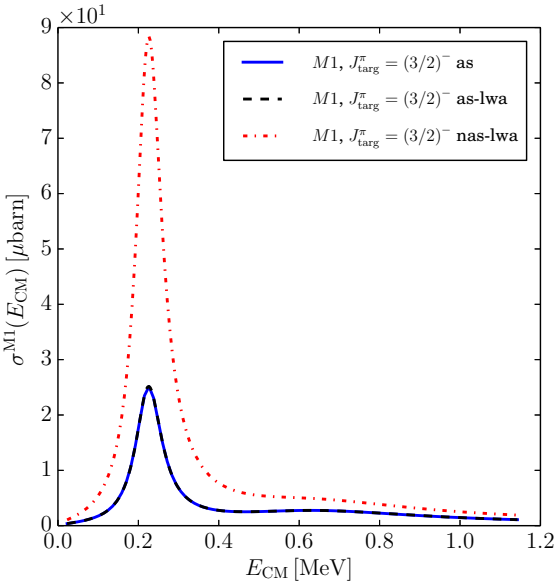

Figure 2.25 – The same as in Fig.2.24 but for the M1 transitions. The peak corresponds to the 3^+_1 resonance of ^{8}Li.

The radiative neutron capture cross section for M1 transitions is shown in Fig.2.25. The 3^+_1 resonance of ^{8}Li can be observed at the experimental value $E_{\rm CM}$ = 0.223 MeV. The same resonance energy is obtained in SMEC [67] as shown in Fig.2.28. In this case, the antisymmetry of initial and final states in the calculation of matrix elements of the electromagnetic operators decreases the height of a 3^+_1 resonance by a factor of ~ 4. The long wavelength approximation does not change the M1 cross section.

The E2 component of the neutron radiative capture cross section which is plotted in Fig.2.26, has two resonant contributions at the 3^+_1 and 1^+_2 resonance energies. The 1^+_2 resonance is obtained in both GSM and GSM-CC calculations. The antisymmetrization of initial and final states diminishes strongly the E2 contribution at the 3^+_1 resonance. The long wavelength approximation, in this case, enhances the E2 cross section.

Finally, the sum of E1, M1 and E2 contributions to the neutron radiative capture cross section is compared in Fig.2.27 with the experimental data [249]. A good overall agreement is obtained, but the GSM-CC cross sections are slightly below the data. The total cross section is only slightly affected by the long wavelength approximation.

It has been shown that the long wavelength approximation and the antisymmetry of initial and final states in the calculation of matrix elements of the electromagnetic operators affect the total cross section slightly. The last test consists of investigating the influence on the cross sections $\sigma^{\rm E1}$, $\sigma^{\rm M1}$ and $\sigma^{\rm E2}$ of additional reaction channels built from the first excited state $J^\pi = 1/2^-$ of the target nucleus ^{7}Li. Experimentally this state is bound by 10.471 MeV with respect to ^{4}He, whereas in GSM it is bound by 9.260 MeV. The multiplicative corrective factors: $c(2^+_1)$ = 1.03705, $c(1^+_1)$ = 1.04805 and $c(3^+_1)$ = 1.03205 for channel coupling

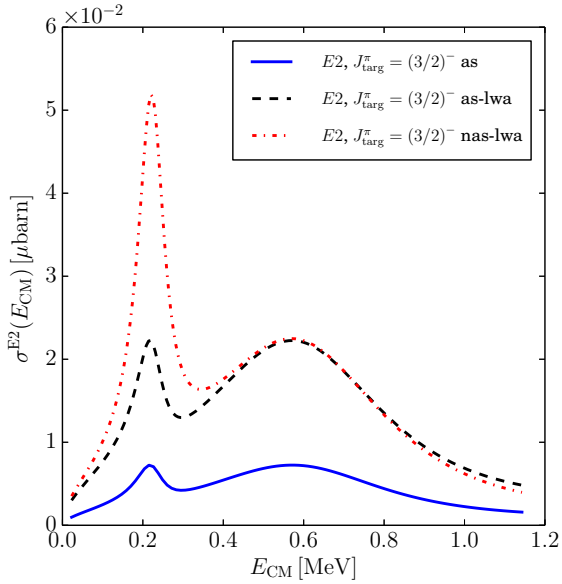

Figure 2.26 – The same as in Fig.2.24 but for the E2 transitions. The two peaks correspond to the 3^+_1 and 1^+_2 resonance of ^{8}Li.

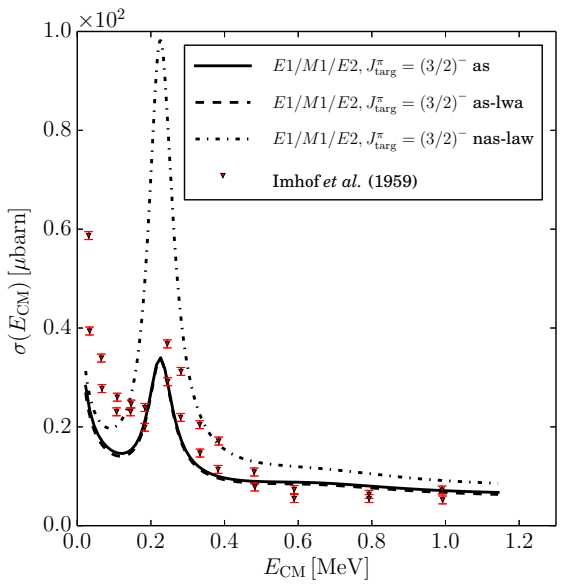

Figure 2.27 – Plot of the total cross section for the ^{7}Li$(n,\gamma)^8$Li reaction. Data are taken from Ref. [249]. The solid line represents the exact, fully antisymmetrized GSM-CC calculation. Calculations in the long wavelength approximation are represented by the dashed and dotted lines in the antisymmetrized and non-antisymmetrized cases, respectively. For more details see the description in the text.

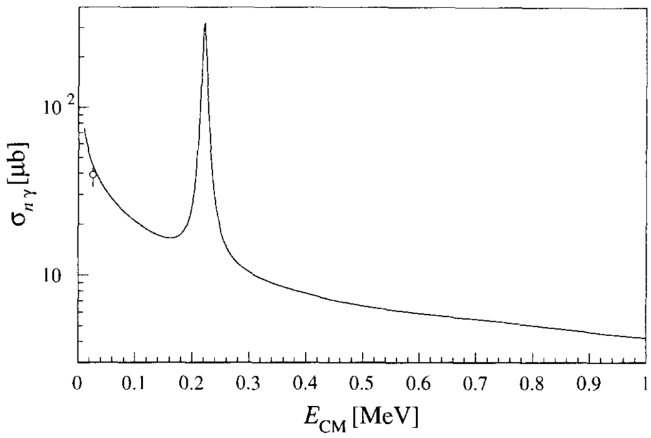

Figure 2.28 – Plot of the total cross section for the ^{7}Li$(n,\gamma)^8$Li reaction calculated in SMEC (from Ref. [67]).

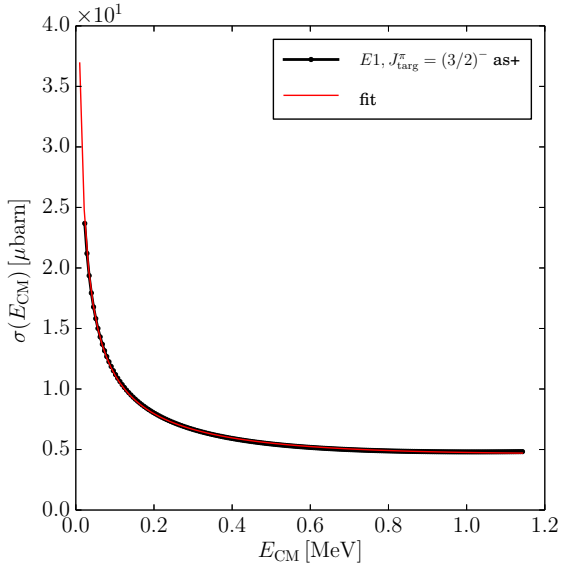

Figure 2.29 – Fit of the total radiative neutron capture cross section at low energies for the ^{7}Li$(n,\gamma)^8$Li reaction. For more details, see the description in the text.

potentials have been used to adjust the position of ^{8}Li resonances. The E1, M1 and E2 contributions to the cross section are shown on Figs.2.30, 2.31 and 2.32, respectively.

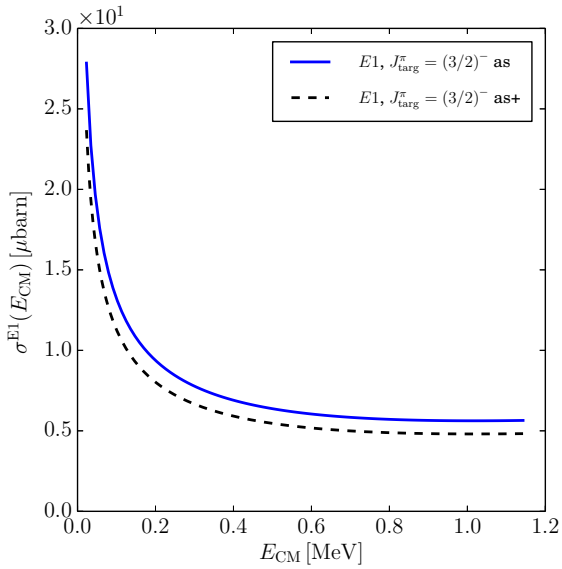

Figure 2.30 – Plot of the E1 cross section for the ^{7}Li$(n,\gamma)^8$Li reaction. The solid and dashed lines represent the exact, fully antisymmetrized GSM-CC calculation without and with the excited state of the target $J^\pi = 1/2^-$, respectively. For more details, see the description in the text.

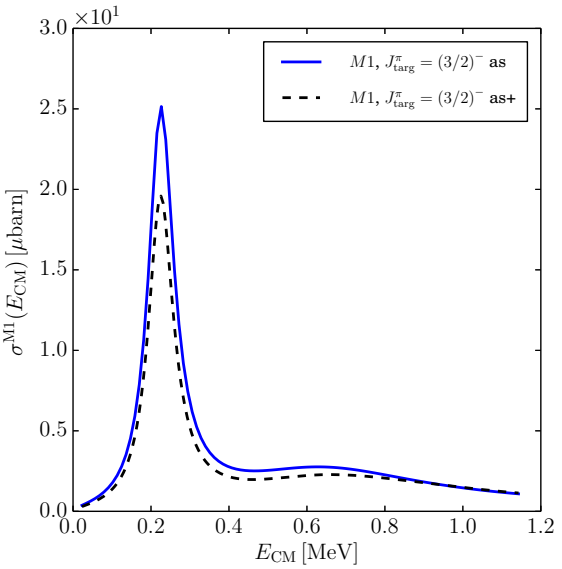

Figure 2.31 – The same as in Fig.2.30 but for the M1 transitions. The peak corresponds to the 3^+_1 resonance of ^{8}Li.

The E1 and M1 contributions to the cross section are decreased slightly when taking into account the excited state $J^\pi = 1/2^-$ of the target nucleus ^{7}Li. The E2 contribution is strongly decreased and the 1^+_2 peak has been removed.

The comparison with experimental data in Fig.2.33 shows a small decreasing of the total cross section.

The extrapolation of the calculated total radiative neutron capture cross section at low $E_{\rm CM}$ energies using the expansion:

$$\sigma(E_{\rm CM}) = \frac{3.858}{\sqrt{E_{\rm CM}}} - 1.931 + 2.832\sqrt{E_{\rm CM}} \tag{2.40}$$

is shown in Fig.2.29. The analogous extrapolation of SMEC results gives [67]:

$$\sigma^{\rm (SMEC)}\,(E_{\rm CM}) = \frac{8.1789}{\sqrt{E_{\rm CM}}} - 1.5234 - 8.2634\sqrt{E_{\rm CM}} \tag{2.41}$$

The energy dependence for $E_{\rm CM} \to 0$ of the radiative neutron capture cross sections in GSM-CC and SMEC differs by a factor ~ 2. This may be due to different interactions, model spaces and effective charges in both approaches. Contrary to the proton radiative capture reactions, neutron radiative capture process happens inside of the target nucleus and, hence, depends strongly on details of the microscopic wave functions involved, the effective nucleon-nucleon interaction, and polarization effects. In the microscopic cluster model of Ref. [241], the neutron radiative capture cross section at $E_{\rm CM} = 25$ keV has been calculated for various phenomenological interactions. These values vary in the interval: $44.5\ \mu\,\text{barn} < \sigma^{\rm (cluster)}(25\ \text{keV}) < 54.2\ \mu\,\text{barn}$. In GSM-CC, the formula (2.40) gives: $\sigma^{\rm (GSM\text{-}CC)}(25\ \text{keV}) = 21.57\ \mu\,\text{barn}$.

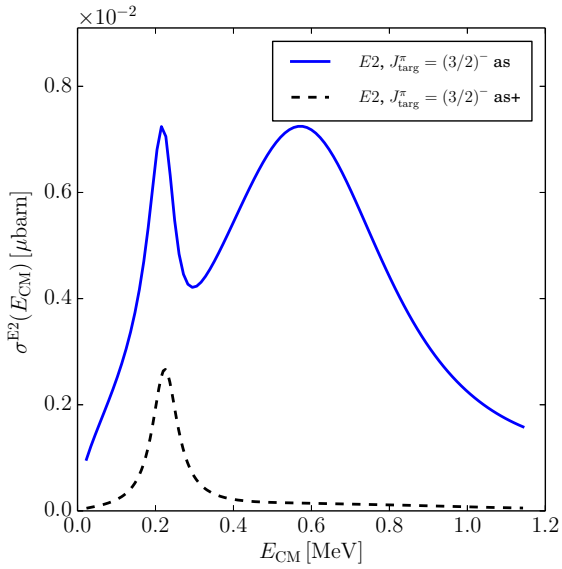

Figure 2.32 – The same as in Fig.2.30 but for the E2 transitions. The two peaks correspond to the 1^+_1 and 1^+_2 resonances of ^{8}Li.

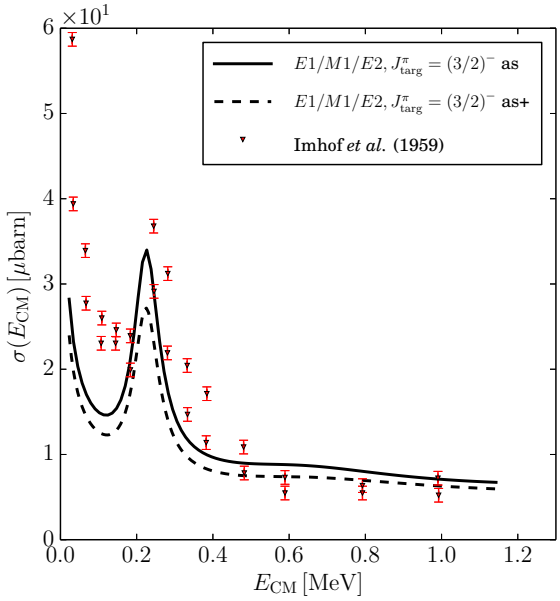

Figure 2.33 – Plot of the total cross section for the ^{7}Li$(n,\gamma)^8$Li reaction. Data are taken from Ref. [249]. The solid and dashed lines represent the exact, fully antisymmetrized GSM-CC calculation without and with the excited state of the target, respectively. For more details see the description in the text.

Chapter 3

Spectroscopy of dipolar anions in the Berggren ensemble

3.1 Introduction

In atomic and molecular physics, the internal structure of nuclei is of no importance since electrons are only sensitive to the Coulomb potential due to protons. At the atomic scale, the typical length is the Bohr radius: $a_0 \approx 5.29 \times 10^{-11}$ m which is the size of hydrogen atom, and the typical energy is the Rydberg: 1 Ry $\approx$ 13.605691 eV which is the electron binding energy in the ground state of hydrogen. Various interaction potentials are involved in the description of atoms and molecules, like the Coulomb potential $\propto -1/r$, the quadrupolar potential $\propto -1/r^4$ or the van der Waals potential $\propto -1/r^6$. The dipolar potential $\propto -1/r^2$, which describes the interaction between a neutral molecule with an electric dipole moment μ and an electron (see Fig.3.1), is of particular interest since it is a long-range potential.

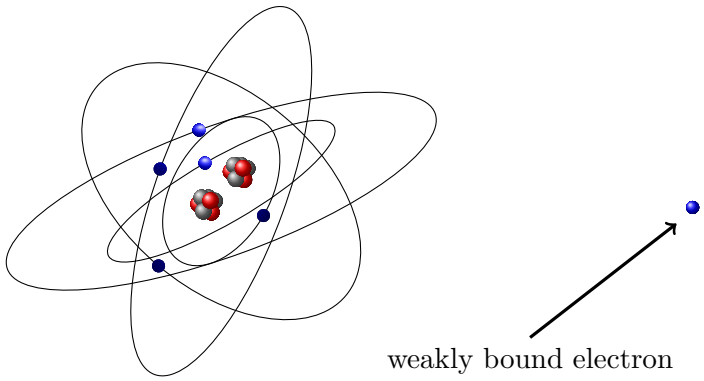

Figure 3.1 – Classical representation of a dipolar anion.

The first paper about dipolar anions appeared in 1947 when Fermi and Teller [250] studied the capture of negative mesons in matter. They discovered without giving a demonstration that when a negative meson is captured by a hydrogen nucleus, that the binding energy of the electron becomes zero if the distance between a meson and a proton is 0.639 a_0. Twenty years later, this value has been found theoretically in the case of a point-like dipole [251]. Investigations of a finite distance $2s$ between the dipole charges on the binding energy of an external electron, started soon after. This finite-size effect is equivalent to the influence of the dipole moment $\mu = 2sq$ ($q > 0$) on the spectrum of the external electron. It is thus possible to find the critical dipole moment μ_c for which the dipolar anion has a zero binding energy. This point was discussed first by Levy-Leblond [251]. Results for a point-like dipole have been generalized to the case of an extended dipole ($2s \neq 0$) with an infinite moment of inertia. In this limit, it has been shown that the critical dipole

moment should increase. The approximation of a fixed dipole (the limit of an infinite moment of inertia) has been removed by Garrett [49,51,52] who considered a rotating dipole. In particular, the dependence of the critical dipole moment on the dipole size $\mu_c = f(s)$ has been studied and rotational degrees of freedom of the molecule have been included. At the same time, the effect of a repulsive short-range potential on the binding energy of an external electron was investigated by Crawford [252]. The singularity which appears in the point dipole case if the distance r between an electron and a dipole goes to zero, can be avoided if a strongly repulsive short-range term is added to the potential. Including this correction generates an infinite number of bound states if $\mu > \mu_c$ and no bound states if $\mu < \mu_c$. Moreover, in the limit $\mu \to \mu_c, (\mu > \mu_c)$, all states converge to a single state with zero binding energy. Also, Garrett [253–255] showed the importance of the polarization terms and the quadrupolar interaction on the binding energy of an external electron and performed the first calculation of spectra of dipolar anions using a full pseudo-potential which takes into account finite size effects, repulsive core, polarization and quadrupolar interaction, and including rotational degrees of freedom. It was found that the rotational motion reduces the number of states of a given total angular momentum J^π to about four, in agreement with experimental findings. Secondly, the pseudo-potential gives reasonable predictions for the binding energy of an electron compared with experimental data. In addition, it has been shown that a greater moment of inertia leads to a smaller critical dipole moment. Recently, these calculations have been extended to linear electric quadrupole systems [256,257]. Up to now, the unbound part of the spectrum of multipolar anions has not been studied theoretically but the probable existence of resonant states of dipolar anions has been shown in Ref. [258].

Dipolar anions are weakly bound systems with, in the ground state, a typical binding energy of the valence electron of about -10^{-2} Ry and a root mean square (r.m.s.) radius of about $7 - 10\ a_0$. They can thus be considered as molecular halo systems [259–262]. The description of dipolar anions is a challenge for theory, in particular their unbound spectrum, due to both the weak binding of the valence electron and the long-range dipole potential.

In this chapter, the Hamiltonian of dipolar anions is described in Sec.3.2, together with the considered approximations (Sec.3.2.1) and the pseudo-potential method (Sec.3.2.2). Then in Sec.3.3 the CC formulation of the problem is presented, and its resolution is given both in DIM (Sec.3.3.3.1) and in the Berggren Ensemble Method (Sec.3.3.3.2). The formula to calculate the density of the valence electron in the body-fixed frame is derived in Sec.3.4. Then, bound spectra and r.m.s. radius of the LiI^-, $LiCl^-$, LiF^- and LiH^- dipolar anions are presented in Sec.3.5. A discussion of the critical dipole moment is done in Sec.3.5.3, and a comparison between dipolar anions considered as molecular halo systems and nuclear halo systems is done in Sec.3.5.5. Finally, the detailed discussion of the HCN^- dipolar anion is presented in Sec.3.6. The Hamiltonian is presented in Sec.3.6.1. The identification of resonances is discussed in Sec.3.6.2, and results are in Sec.3.6.4. In particular, the intrinsic density of the valence electron is calculated for bound states and resonances in Sec.3.6.4.2, and the properties of the unbound states of HCN^- are discussed in Sec.3.6.4.3 and 3.6.4.4.

3.2 Hamiltonian of dipolar anions

3.2.1 Hamiltonian

The dipolar anion is composed of a neutral polar molecule with a dipole moment greater than the critical dipole moment μ_{cr} and a valence electron. The Hamiltonian is:

$$\hat{H} = \hat{H}_e + \hat{H}_{mol} + \hat{V} \tag{3.1}$$

where $\hat{H}_e$ is the Hamiltonian of the valnce electron, $\hat{H}_{mol}$ is the Hamiltonian of the neutral polar molecule, and $\hat{V}$ the interaction between the electron and the molecule. In the present case, several simplifications can be done since:

- The spin-orbit interaction can be neglected [255], because the valence electron is expected to be far from the molecule due to the long-range dipolar interaction $\propto -1/r^2$.
- The molecule is viewed as a closed-shell system.
- The vibrational motions of the molecule and of the core electrons are much faster than both the rotational motion of the molecule and the orbital motion of the valence electron [263].

Then, the main ingredients in the Hamiltonian $\hat{H}$ are the rotation of the molecule considered as a rigid rotor, the orbital motion of the valence electron and the coupling potential. Fig.3.2 shows a classical representation of dipolar anions.

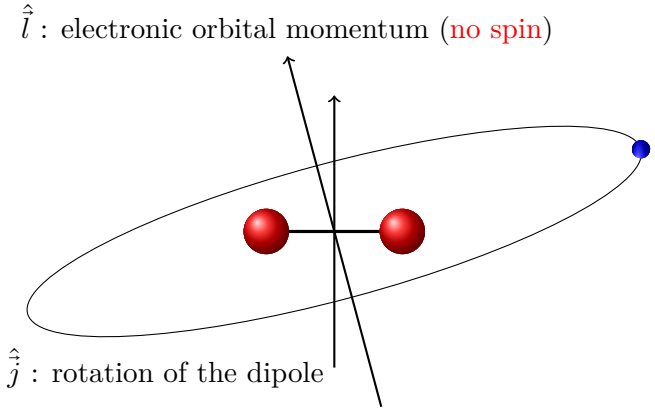

Figure 3.2 – Angular momentum couplings in dipolar anions.

Thus the Hamiltonian (3.1) becomes:

$$\hat{H} = \frac{\hat{\vec{p}}_e^2}{2m_e} + \frac{\hat{\vec{j}}^2}{2I} + \hat{V} \tag{3.2}$$

where I is the moment of inertia of the neutral molecule and $\hat{\vec{j}}$ its angular momentum, $\hat{\vec{p}}_e$ is the linear momentum of the valence electron and m_e its mass. In order to specify the angular momenta in (3.2), the momentum squared of the electron can be written as:

$$\hat{\vec{p}}_e^2 = \hat{p}_\parallel^2 + \hat{p}_\perp^2 \tag{3.3}$$

with:

$$\begin{aligned} \hat{p}_\parallel &= \frac{1}{2r}(\hat{\vec{r}}.\hat{\vec{p}} + \hat{\vec{p}}.\hat{\vec{r}}) \\ \hat{p}_\perp &= \frac{1}{r}\|\hat{\vec{r}} \wedge \hat{\vec{p}}\| \\ r &= \|\hat{\vec{r}}\|_{\text{op}} \end{aligned} \tag{3.4}$$

The definition of the norm of an operator $\|\hat{O}\|_{\text{op}}$ can be found in Ref. [264]. Then, the electron orbital momentum $\hat{\vec{l}}$ is defined as $\hat{\vec{l}} = \hat{\vec{r}} \wedge \hat{\vec{p}}$, and so the momentum squared of the valence electron writes:

$$\hat{\vec{p}}_e^2 = \hat{p}_\parallel^2 + \frac{\hat{\vec{l}}^2}{r^2} \tag{3.5}$$

Finally, the Hamiltonian (3.2) writes:

$$\hat{H} = \frac{\hat{\vec{p}}_{\parallel}^2}{2m_e} + \frac{\hat{\vec{l}}^2}{2m_e r^2} + \frac{\hat{\vec{j}}^2}{2I} + \hat{V} \tag{3.6}$$

and the total angular momentum writes:

$$\hat{\vec{J}} = \hat{\vec{l}} + \hat{\vec{j}} \tag{3.7}$$

3.2.2 Potential and the multipole expansion

In spherical coordinates, the interaction $\hat{V}$ is given by a one-body pseudo-potential $V(r,\theta)$ [254, 255]:

$$V(r,\theta) = V_\mu(r,\theta) + V_\alpha(r,\theta) + V_{Q_{zz}}(r,\theta) + V_{\mathrm{SR}}(r) \tag{3.8}$$

where θ is the angle between the dipolar charge separation $\vec{s}$ and the position of electron $\vec{r}$. Different terms in (3.8) are:

1. The dipole potential of the molecule:

$$V_\mu(r,\theta) = -\mu \frac{e}{4\pi\varepsilon_0} \sum_{\lambda=1,3,\dots} \left(\frac{r_<}{r_>}\right)^\lambda \frac{1}{s r_>} P_\lambda(\cos(\theta)) \tag{3.9}$$

2. The induced dipole potential:

$$V_\alpha(r,\theta) = -\frac{e^2}{4\pi\varepsilon_0} \frac{1}{2r^4} \left[\alpha_0 + \alpha_2 P_2(\cos(\theta))\right] f(r) \tag{3.10}$$

   where α_0 and α_2 are the spherical and quadrupole polarizabilities of the linear molecule.

3. The potential due to the permanent quadrupole moment of the molecule:

$$V_{Q_{zz}}(r,\theta) = -\frac{e}{4\pi\varepsilon_0} \frac{1}{r^3} Q_{zz} P_2(\cos(\theta)) f(r) \tag{3.11}$$

4. The short-range potential:

$$V_{\mathrm{SR}}(r) = V_0 \exp(-(r/r_c)^6), \tag{3.12}$$

   where r_c is a range radius and $V_{\mathrm{SR}}(r)$ accounts for the exchange effects and compensates for spurious effects induced by the cut-off function:

$$f(r) = 1 - e^{-\left(\frac{r}{r_0}\right)^6} \tag{3.13}$$

   introduced in Eqs.(3.10,3.11) to avoid a singularity at $r \to 0$. The parameter r_0 in Eq.(3.13) is an effective short-range cutoff for long-range interactions.

It is then possible to use the multipole expansion of $V(r,\theta)$ in order to separate the radial and angular parts:

$$V(r,\theta) = \sum_{\lambda=0}^{\infty} V_\lambda(r) P_\lambda(\cos(\theta)) \tag{3.14}$$

where the $P_\lambda(x)$ are the Legendre polynomials of order λ. They are related to the spherical harmonics by:

$$P_\lambda(\vec{u}_{\vec{r}}.\vec{u}_{\vec{s}}) = \frac{4\pi}{2\lambda+1}\sum_{m_\lambda} Y^\lambda_{m_\lambda}(\vec{u}_{\vec{s}})^* Y^\lambda_{m_\lambda}(\vec{u}_{\vec{r}}) \tag{3.15}$$

where $\vec{u}_{\vec{r}}$ and $\vec{u}_{\vec{s}}$ are the unit vectors in the electron direction $\vec{r}$ and in the molecule direction $\vec{s}$. Using the relation:

$$Y^\lambda_{m_\lambda}(\vec{u}_{\vec{s}})^* = (-1)^{m_\lambda} Y^\lambda_{-m_\lambda}(\vec{u}_{\vec{s}}) \tag{3.16}$$

the Legendre polynomials are:

$$P_\lambda(\vec{u}_{\vec{r}}.\vec{u}_{\vec{s}}) = \frac{4\pi}{2\lambda+1}\sum_{m_\lambda} (-1)^{m_\lambda} Y^\lambda_{-m_\lambda}(\vec{u}_{\vec{s}}) Y^\lambda_{m_\lambda}(\vec{u}_{\vec{r}}) \tag{3.17}$$

In order to express the operator $\hat{V}$ corresponding to the pseudo-potential $V(r,\theta)$ in the position basis, one has to introduce tensor operators $\hat{\mathbf{T}}^k(i)$ in the space $\mathcal{E}_i$ with elements $\hat{T}^k_{m_k}(i)$. It can be shown that it exists a particular class of tensor operators, denoted $\hat{\mathbf{Y}}^l$ and usually referred to as the tensor spherical harmonics or the vector spherical harmonics, which behave like spherical harmonics under the action of the angular momentum operators. One element of the tensor product of two tensor spherical harmonics is given by:

$$\begin{aligned}\hat{T}^J_{M_J}(1,2) &= [\hat{\mathbf{Y}}^{j_1}(1)\otimes\hat{\mathbf{Y}}^{j_2}(2)]^J_{M_J} \\ &= \sum_{m_{j_1},m_{j_2}} \langle j_1,m_{j_1},j_2,m_{j_2}|j_1,j_2;J,M_J\rangle\, \hat{Y}^{j_1}_{m_{j_1}}(1)\hat{Y}^{j_2}_{m_{j_2}}(2)\end{aligned} \tag{3.18}$$

To do the analogy between operators $\hat{Y}^l_{m_l}(i)$ and spherical harmonics $Y^l_{m_l}(\theta,\varphi)$, a rotational invariant product of tensor operators has to be built. It is done for $J = M_J = 0$ in Eq.(3.18):

$$[\hat{\mathbf{Y}}^{j_1}(1)\otimes\hat{\mathbf{Y}}^{j_2}(2)]^{J=0}_{M_J=0} = \sum_{m_{j_1},m_{j_2}} \langle j_1,m_{j_1},j_2,m_{j_2}|0,0;0,0\rangle\, \hat{Y}^{j_1}_{m_{j_1}}(1)\hat{Y}^{j_2}_{m_{j_2}}(2)\delta_{j_1,j_2} \tag{3.19}$$

where $M_J = m_{j_1} + m_{j_2} = 0$ so $m_{j_1} = m_{j_2} = m_\lambda$, and $j_1 = j_2 = \lambda$ because of $J = 0$. Then using the special value of the Clebsch-Gordan coefficient, one finds:

$$\begin{aligned}[\hat{\mathbf{Y}}^\lambda(1)\otimes\hat{\mathbf{Y}}^\lambda(2)]^{J=0}_{M_J=0} &= \sum_{m_\lambda}\frac{(-1)^{\lambda-m_\lambda}}{\sqrt{2\lambda+1}}\hat{Y}^\lambda_{-m_\lambda}(2)\hat{Y}^\lambda_{m_\lambda}(1) \\ &= \frac{(-1)^\lambda}{\sqrt{2\lambda+1}}\sum_{m_\lambda}(-1)^{m_\lambda}\hat{Y}^\lambda_{-m_\lambda}(2)\hat{Y}^\lambda_{m_\lambda}(1)\end{aligned} \tag{3.20}$$

In analogy with the Legendre polynomials, an operator $\hat{P}_\lambda$ can be defined as:

$$\begin{aligned}\hat{P}_\lambda &= \frac{4\pi}{2\lambda+1}\sum_{m_\lambda}(-1)^{m_\lambda}\hat{Y}^\lambda_{-m_\lambda}(2)\hat{Y}^\lambda_{m_\lambda}(1) \\ &= \frac{4\pi}{\sqrt{2\lambda+1}}(-1)^\lambda[\hat{\mathbf{Y}}^\lambda(1)\otimes\hat{\mathbf{Y}}^\lambda(2)]^{J=0}_{M_J=0}\end{aligned} \tag{3.21}$$

It is then possible to define the potential operator as:

$$\begin{aligned}\hat{V} &= \sum_{\lambda=0}^{\infty} V_\lambda(\hat{r})\hat{P}_\lambda \\ &= \sum_{\lambda=0}^{\infty} V_\lambda(\hat{r})\frac{4\pi}{\sqrt{2\lambda+1}}(-1)^\lambda[\hat{\mathbf{Y}}^\lambda(1)\otimes\hat{\mathbf{Y}}^\lambda(2)]^{J=0}_{M_J=0}\end{aligned} \tag{3.22}$$

3.3 Methods

3.3.1 Definition of channels

Dipolar anions are modelled by the Hamiltonian (3.6). They have a total angular momentum $\hat{\vec{J}}$ coming from the rotational motion of the dipole and of the valence electron (see Eq.(3.7)). An important point in the description of dipolar anions is that the orbital angular momentum $\hat{\vec{l}}$ of the valence electron and the rotational angular momentum $\hat{\vec{j}}$ of the dipolar molecule, are strongly coupled and the corresponding energy scales may be comparable. Consequently, the CC formalism presented in (1.2.2) is well adapted to deal with this problem. Indeed, each solution of the Schrödinger equation is given for a total angular momentum J, where all possible couplings of $\hat{\vec{l}}$ and $\hat{\vec{j}}$, satisfying the Eq.(3.7), contribute. The centrifugal and rotational terms in the Hamiltonian favor low l- and j-values, so that a truncation of high l- and j-values is possible. It is the reason why in CC calculations there is a truncation cutoff $l_{\max}$, and allowed j values are:

$$|J - l_{\max}| \leq j \leq J + l_{\max} \tag{3.23}$$

The channel states $|c\rangle$ which, with the exception of the relative motion, contain all the information about the electron-dipolar molecule system, can be split into an electronic part and a dipole part:

$$|c\rangle = |c_{\mathrm{e}}\rangle \otimes |c_{\mathrm{d}}\rangle \tag{3.24}$$

In the present case, the dipole channel state is a solution of the equation:

$$\frac{\hat{\vec{j}}^2}{2I}|c_{\mathrm{d}}\rangle = E_{\mathrm{d}}|c_{\mathrm{d}}\rangle \tag{3.25}$$

Obviously: $|c_{\mathrm{d}}\rangle = |j, m_j\rangle$. In the same way the electron channel is just: $|c_{\mathrm{e}}\rangle = |l, m_l\rangle$. States associated with the relative distance between the dipole and the valence electron form a radial basis of the space $\mathcal{E}_{\mathrm{rel}}$:

$$\int_0^\infty dr\, r^2 |r\rangle\langle r| = \hat{\mathbb{1}}_{\mathcal{E}_{\mathrm{rel}}} \tag{3.26}$$

Thus for a given total angular momentum J, a basis of the full space $\mathcal{E}$ is:

$$\left(\int_0^\infty dr\, r^2 |r\rangle\langle r|\right) \otimes \left(\sum_{c_{\mathrm{e}}} |c_{\mathrm{e}}\rangle\langle c_{\mathrm{e}}|\right) \otimes \left(\sum_{c_{\mathrm{d}}} |c_{\mathrm{d}}\rangle\langle c_{\mathrm{d}}|\right) = \hat{\mathbb{1}}_{\mathcal{E}} \tag{3.27}$$

or in other words:

$$\sum_{l,j}\sum_{m_l,m_j}\int_0^\infty dr\, r^2 (|r\rangle \otimes |l, m_l, j, m_j\rangle)(\langle r| \otimes \langle l, m_l, j, m_j|) = \hat{\mathbb{1}}_{\mathcal{E}} \tag{3.28}$$

The closure relation in the basis of uncoupled states can be used to simplify the Eq.(3.28):

$$\sum_{l,j}\sum_{M_J}\int_0^\infty dr\, r^2 (|r\rangle \otimes |l, j; J, M_J\rangle)(\langle r| \otimes \langle l, j; JM_J|) = \hat{\mathbb{1}}_{\mathcal{E}} \tag{3.29}$$

Hereafter, the calculations are done for a fixed value of the total angular momentum projection $M_J = J$. Finally, the eigenstates $|\Psi\rangle$ of the Hamiltonian Eq.(3.6) can be expanded as:

$$\begin{aligned} |\Psi\rangle &= \sum_{l,j}\int_0^\infty dr\, r^2 (|r\rangle \otimes |l, j; J, M_J\rangle)(\langle r| \otimes \langle l, j; JM_J|)\,|\Psi\rangle \\ &= \sum_{l,j}\int_0^\infty dr\, r^2 \frac{u_{l,j}^{J,M_J}(r)}{r}(|r\rangle \otimes |l, j; J, M_J\rangle) \end{aligned} \tag{3.30}$$

with the radial channel wave functions:

$$(\langle r| \otimes \langle l, j; JM_J|)\,|\Psi\rangle = \frac{u_{l,j}^{J,M_J}(r)}{r} \tag{3.31}$$

Usually, the channel index is denoted $c = (l, j) = (l_c, j_c)$ where l and j are now labelled by c, and thus:

$$|\Psi\rangle = \sum_c \int_0^\infty dr\, r^2 \frac{u_c(r)}{r} (|r\rangle \otimes |l_c, j_c; J, M_J\rangle) \tag{3.32}$$

This is the channel state expansion of the eigenstate of the Hamiltonian Eq.(3.6).

3.3.2 Coupled-channel equations

In order to derive the CC equations, we insert the expansion (3.32) into the Schrödinger equation:

$$\begin{aligned} & \hat{H}\,|\Psi\rangle = E\,|\Psi\rangle \\ \Leftrightarrow \quad & \sum_c \int_0^\infty dr\, r^2 \frac{u_c(r)}{r} \hat{H}(|r\rangle \otimes |l_c, j_c; J, M_J\rangle) = E \sum_c \int_0^\infty dr\, r^2 \frac{u_c(r)}{r} (|r\rangle \otimes |l_c, j_c; J, M_J\rangle) \end{aligned} \tag{3.33}$$

The CC equations are obtained from (3.33) by projecting on a particular channel $\langle r'| \otimes \langle l_{c'}, j_{c'}; J, M_J|$:

$$\begin{aligned} & \sum_c \int_0^\infty dr\, r^2 \frac{u_c(r)}{r} (\langle r'| \otimes \langle l_{c'}, j_{c'}; J, M_J|) \hat{H} (|r\rangle \otimes |l_c, j_c; J, M_J\rangle) \\ & = E \sum_c \int_0^\infty dr\, r^2 \frac{u_c(r)}{r} (\langle r'| \otimes \langle l_{c'}, j_{c'}; J, M_J|)(|r\rangle \otimes |l_c, j_c; J, M_J\rangle) \end{aligned} \tag{3.34}$$

$$\tag{3.35}$$

or in a more concise way:

$$\sum_c \int_0^\infty dr\, r^2 \frac{u_c(r)}{r} (H_{c',c}(r', r) - E N_{c',c}(r', r)) = 0 \tag{3.36}$$

with:

$$N_{c',c}(r', r) = (\langle r'| \otimes \langle l_{c'}, j_{c'}; J, M_J|)(|r\rangle \otimes |l_c, j_c; J, M_J\rangle) = \frac{\delta(r - r')}{r^2} \delta_{c,c'} \tag{3.37}$$

and:

$$H_{c',c}(r', r) = \left(-\frac{\hbar^2}{2m_e} \frac{1}{r} \frac{\partial^2 (r\cdot)}{\partial r^2} + \frac{\hbar^2 l_c(l_c+1)}{2m_e r^2} + \frac{\hbar^2 j_c(j_c+1)}{2I} \right) \frac{\delta(r - r')}{r^2} \delta_{c,c'} + (\langle r'| \otimes \langle l_{c'}, j_{c'}; J, M_J|) \hat{V} (|r\rangle \otimes |l_c, j_c; J, M_J\rangle) \tag{3.38}$$

The potential matrix element:

$$V_{c',c}(r', r) = (\langle r'| \otimes \langle l_{c'}, j_{c'}; J, M_J|) \hat{V} (|r\rangle \otimes |l_c, j_c; J, M_J\rangle) \equiv V_{c',c}(r) \tag{3.39}$$

can be evaluated using the multipolar expansion (3.22):

$$V_{c',c}(r) = \sum_{\lambda=0}^{\infty} V_\lambda(r)\, \langle l_{c'}, j_{c'}; J, M_J | \hat{P}_\lambda | l_c, j_c; J, M_J \rangle \frac{\delta(r - r')}{r^2} \tag{3.40}$$

with:

$$\langle l_{c'}, j_{c'}; J, M_J|\hat{P}_\lambda|l_c, j_c; J, M_J\rangle$$
$$= (-1)^{j_{c'}+j_c+j_c} \begin{Bmatrix} j_{c'} & l_{c'} & J \\ l & j & \lambda \end{Bmatrix} \begin{pmatrix} j_{c'} & \lambda & j \\ 0 & 0 & 0 \end{pmatrix} \begin{pmatrix} l_{c'} & \lambda & l \\ 0 & 0 & 0 \end{pmatrix} \sqrt{(2l_{c'}+1)(2l_c+1)(2j_{c'}+1)(2j_c+1)} \quad (3.41)$$

The Hamiltonian and overlap matrix elements (Eqs.(3.38) and (3.37)) can be inserted into the general CC equations (3.36) to obtain:

$$\left(\frac{\hbar^2}{2m_e}\frac{1}{r}\frac{\partial^2(r\cdot)}{\partial r^2} - \frac{\hbar^2 l_c(l_c+1)}{2m_e r^2} - \frac{\hbar^2 j_c(j_c+1)}{2I} + E\right)\frac{u_c(r)}{r} = \sum_{c'} V_{c,c'}(r)\frac{u_{c'}(r)}{r} \quad (3.42)$$

or in a dimensionless form:

$$\left(\frac{1}{r}\frac{\partial^2(r\cdot)}{\partial r^2} - \frac{l_c(l_c+1)}{r^2} - \frac{j_c(j_c+1)}{I} + k^2\right)\frac{u_c(r)}{r} = \sum_{c'} V_{c,c'}(r)\frac{u_{c'}(r)}{r} \quad (3.43)$$

In these equations, r is in units of the Bohr radius a_0, the moment of inertia I is in units of $m_e a_0^2$, k^2 is in units of a_0^{-2}, and the eigenenergy E and the radial potential $V_\lambda(r)$ are in units of $R_\infty hc$ with:

$$E = \frac{\hbar^2 k^2}{2\mu} \quad (3.44)$$

and:

$$R_\infty hc = \frac{\hbar^2}{2m_e a_0^2} \approx 13.605691 \text{ eV} \quad (3.45)$$

The dimensionless CC equations are obtained with the help of the following formula:

$$\frac{1}{R_\infty hc}\frac{e^2}{4\pi\varepsilon_0}\frac{1}{a_0} = \frac{\alpha\hbar c}{R_\infty hc a_0} = 2 \quad (3.46)$$

3.3.3 Resolution of the coupled-channel equations

3.3.3.1 Direct integration method

The direct integration method in the dipolar anion case is basically the same as in the nuclear case (see Sec.1.2.3.6). The difference between these two cases is that the radial wave functions $u_c(r)$ for dipolar anions have the correct behavior at $r \sim 0$, contrary to the radial wave functions $w_c(r)$ in a nuclear case. Moreover, due to the dipolar potential the asymptotic behavior of $u_c(r)$ for $r \to \infty$ is not known analytically. The principal motivation for using DIM to describe dipolar anions is that in many applications this method is more precise than the finite-basis diagonalization. In particular, the DIM works very well in the nuclear case for bound states and resonances. Thus, as in the nuclear case, the CC equations (3.43) are solved separately in the internal region: $0 \le r \le r_\mathrm{m}$, where the centrifugal potential is appreciable, and in the asymptotic region: $r_\mathrm{m} \le r \le R_\mathrm{max}$, where the centrifugal potential is small. In the internal region, radial wave functions $u_c(r)$ are expanded in the forward basis:

$$u_c(r) = \sum_b A_b^{(0)} u_{c,b}^{(0)}(r) \quad (3.47)$$

where $A_b^{(0)}$ is a constant to be determined by the matching conditions at $r = r_\mathrm{m}$. For a fixed channel b, the forward basis states have the following boundary conditions:

$$u_{c,b}^{(0)}(r) \underset{r\sim 0}{\sim} r^{l_b+1} \qquad (c=b)$$
$$\underset{r\sim 0}{\sim} o(r^{l_b+1}) \qquad (c\neq b) \tag{3.48}$$

The $c \neq b$ case can be specified by looking at the asymptotic form of Eq.(3.43) for the forward basis states $u_{c,b}^{(0)}(r)$ in the limit $r \sim 0$:

$$\frac{\partial^2 u_{c,b}^{(0)}(r)}{\partial r^2} = \frac{l_c(l_c+1)}{r^2} u_{c,b}^{(0)}(r) + \left(V_{c,c}(0) + \frac{j_c(j_c+1)}{I} - k^2 \right) u_{c,b}^{(0)}(r) + \sum_{c'\neq c} V_{c,c'}(0) u_{c',b}^{(0)}(r) + \mathcal{O}(u_{c,b}^{(0)}(r)) \tag{3.49}$$

Due to the boundary conditions (3.48), the second term on the right-hand side of Eq.(3.49) and all terms in the sum for which $c' \neq b$ are $\mathcal{O}(r^{l_b+1})$, and $u_{b,b}^{(0)} = r^{l_b+1}$. Thus, Eq.(3.49) becomes:

$$\frac{\partial^2 u_{c,b}^{(0)}(r)}{\partial r^2} = \frac{l_c(l_c+1)}{r^2} u_{c,b}^{(0)}(r) + V_{c,b}(0) r^{l_b+1} + \mathcal{O}(u_{c,b}^{(0)}(r)) \tag{3.50}$$

This equation can be directly integrated if the terms $o(r^{l_b+1})$ for $c \neq b$ are neglected. Then, the boundary conditions for $c \neq b$ write:

$$u_{c,b}^{(0)}(r) \underset{r\sim 0}{\sim} V_{c,b}(0) \frac{r^{l_b+3}}{2l_b+5} \ln\left(\frac{r}{r_\mathrm{m}}\right) \qquad (c\neq b, l_c = l_b+2)$$
$$\underset{r\sim 0}{\sim} V_{c,b}(0) \frac{r^{l_b+3}}{(l_b+2)(l_b+3) - l_c(l_c+1)} \qquad (c\neq b, l_c \neq l_b+2) \tag{3.51}$$

Remark:

In the internal region, there is a discontinuity of the dipolar potential at $r = s$, where s is the size of the dipole. The integration of the CC equations has thus to be done from $r = 0$ to $r = s$ and from $r = s$ to $r = r_\mathrm{m}$ with the appropriate matching conditions at $r = s$ and $r = r_\mathrm{m}$.

In the asymptotic region, the radial wave functions $u_c(r)$ are expanded in the backward basis:

$$u_c(r) = \sum_b A_b^{(+)} u_{c,b}^{(+)}(r) \tag{3.52}$$

where $A_b^{(+)}$ is a constant to be determined with the matching conditions at $r = r_\mathrm{m}$. For a fixed channel b, the backward basis states have the following boundary conditions:

$$u_{c,b}^{(+)}(r) \underset{r\to\infty}{\neq} 0 \qquad (c=b)$$
$$\underset{r\to\infty}{=} 0 \qquad (c\neq b) \tag{3.53}$$

The explicit form of the outgoing boundary conditions Eq.(3.53) are given hereinafter. The radial wave functions $u_c(r)$ are obtained with the matching conditions at $r = r_\mathrm{m}$, which specifies the constants $A_b^{(0)}$ and $A_b^{(+)}$:

$$\sum_b \left(A_b^{(0)} u_{c,b}^{(0)}(r_\mathrm{m}) - A_b^{(+)} u_{c,b}^{(+)}(r_\mathrm{m}) \right) = 0 \tag{3.54}$$

$$\sum_b \left(A_b^{(0)} \left. \frac{\partial u_{c,b}^{(0)}(r)}{\partial r} \right|_{r=r_\mathrm{m}} - A_b^{(+)} \left. \frac{\partial u_{c,b}^{(+)}(r)}{\partial r} \right|_{r=r_\mathrm{m}} \right) = 0 \tag{3.55}$$

In order to deal with the unknown asymptotic of the dipolar potential, an approximation scheme has been developed. At large distances, $V_{c,c'}(r)$ can be written as:

$$V_{c,c'}(r) = \frac{\chi_{c,c'}}{r^2} + V^{(3)}(r) \tag{3.56}$$

where $\chi_{c,c'}$ is a constant and $V^{(3)}(r)$ decreases as $-r^{-3}$ for $r \to \infty$. In this approximation, it is assumed that $V^{(3)}(r) = 0$ in the asymptotic region. As the numerical integration up to $r \approx 100\ a_0$ is stable, the error made by neglecting $V^{(3)}(r)$ is around $10^{-6}\ a_0^{-3}$, *i.e.* the asymptotic region has been practically reached.

To apply the standard outgoing boundary conditions, an effective angular momentum $l_b^{(\mathrm{eff})}$ is defined which takes into account the dipolar potential. In the limit of an infinite moment of inertia $I \to \infty$, the Schrödinger equation is:

$$\frac{d^2 u_c(r)}{dr^2} = \frac{l_c(l_c+1)}{r^2} u_c(r) + \sum_{c'} \frac{\chi_{c,c'}}{r^2} u_{c'}(r) - k^2 u_c(r) \tag{3.57}$$

The outgoing solution of (3.57) in the backward basis can be written in terms of the spherical Hankel functions:

$$u_{c,b}^{(+)}(r) = g_{c,b} H^+_{l_b^{(\mathrm{eff})}}(\eta_b, kr) \tag{3.58}$$

where η_b is the Sommerfeld parameter of the channel b, and $l_b^{(\mathrm{eff})}$ is the effective angular momentum solution of the equation:

$$l_c(l_c+1) g_{c,b} + \sum_{c'} \chi_{c,c'} g_{c',b} = l_b^{(\mathrm{eff})}(l_b^{(\mathrm{eff})}+1) g_{c,b} \tag{3.59}$$

for constants $g_{c,b}$. Indeed, it follows from Eqs.(3.57) and (3.59) that:

$$\frac{d^2 u_c^{(+)}(r)}{dr^2} = \left(\frac{l_b^{(\mathrm{eff})}(l_b^{(\mathrm{eff})}+1)}{r^2} - k^2 \right) u_{c,b}^{(+)}(r) \tag{3.60}$$

so the physical interpretation of $l_b^{(\mathrm{eff})}$ in terms of an effective angular momentum is justified.

If I is finite, the general solutions of the Schrödinger equation with the dipolar potential are no longer analytical at large distances. Nevertheless, it is possible to construct an adiabatic approximation for $u_c(r)$ in the asymptotic region. The Schrödinger equation is then written in the asymptotic region as Eq.(3.57):

$$\frac{d^2 u_c(r)}{dr^2} = \frac{l_c(l_c+1)}{r^2} u_c(r) + \sum_{c'} \frac{\chi_{c,c'}}{r^2} u_{c'}(r) - k_c^2 u_c(r) \tag{3.61}$$

where k is replaced by the channel momentum k_c defined as:

$$k_c^2 = k^2 - \frac{j_c(j_c+1)}{I} \tag{3.62}$$

This approximation can be applied if $|E| \gg j_c(j_c+1)/I$ for all channels of importance. The relative error on a basis function $u_{(c,b)}^{(+)}(r)$ associated with this approximation:

$$\sum_{c'} \left| \frac{\chi_{c,c'}}{r^2} \frac{g_{c',b}}{g_{c,b}} \left(\frac{H^+_{\eta_b, l_b^{(\mathrm{eff})}}(k_{c'} r)}{H^+_{\eta_b, l_b^{(\mathrm{eff})}}(k_c r)} - 1 \right) \right| \tag{3.63}$$

is of the order of $|k_c - k_{c'}|/r^2$. In practical calculations, $I \sim 10^5$ and $j_{max} \sim 7$. This gives: $j_{\max}(j_{\max}+1)/I \sim 10^{-4}$. Consequently, if $|E| > 10^{-3}$ Ry, the error $|k_c - k_{c'}|/r^2 < 10^{-6}\ a_0^{-3}$ for $r \sim 100\ a_0$ is close to that which is associated with the neglect of $V^{(3)}(r)$. The proposed ansatz accounts for the coupling term in many cases. However, this approximation breaks down for weakly-bound and unbound states with $|E| < 10^{-4}$ Ry, thus a more adequate theoretical method based on a resonant state expansion needs to be introduced.

3.3.3.2 Berggren expansion method

The long-range dipolar potential is expected to have delocalized states. Consequently, the use of the one-body Berggren basis to expand the channel states Eq.(3.29) and the Hamiltonian matrix elements Eq.(3.38) is relevant. The optimal Berggren basis is given by the diagonal part in the channel state basis of the Hamiltonian matrix without the rotor terms, denoted $\hat{H}_{\text{diag}}$. The rotor Hamiltonian is removed from the definition of $\hat{H}_{\text{diag}}$ in order to have a threshold energy at 0, otherwise the rotor motion adds a non-zero contribution for $j \neq 0$. The Berggren states are thus the solution of the equation:

$$\hat{H}_{\text{diag}} |\phi_i\rangle = e\,|\phi_i\rangle \tag{3.64}$$

where i is the index of the Berggren state, and e_i its eigenenergy. Each Berggren state is labelled by the channel index $c = (l, j)$ and the linear momentum k, writes $|\phi_{k,c}\rangle$. Eq.(3.64) in the channel state basis thus writes:

$$\left(\frac{\hbar^2}{2m_e}\frac{d^2}{dr^2} - \frac{\hbar^2 l(l+1)}{2m_e r^2} + \frac{\hbar^2 k^2}{2m_e}\right)\phi_{k,c}(r) = V_{c,c}(r)\phi_{k,c}(r) \tag{3.65}$$

with:

$$|\phi_{k,c}\rangle = |\phi^{\text{rel}}_{k,c}\rangle \otimes |l, j; J, M_J\rangle \tag{3.66}$$

and:

$$(\langle r| \otimes \langle l, j; J, M_J|)\,|\phi_{k,c}\rangle = \langle r|\phi^{\text{rel}}_{k,c}\rangle = \frac{\phi^{\text{rel}}_{k,c}(r)}{r} \tag{3.67}$$

The Schrödinger equation can thus be expanded in Berggren basis:

$$\sum_{i,i'} |\phi_{i'}\rangle\,\langle\phi_{i'}|\hat{H}|\phi_i\rangle\,\langle\phi_i|\Psi\rangle = E\sum_i |\phi_i\rangle\,\langle\phi_i|\Psi\rangle \tag{3.68}$$

and projected on a particular state $\langle\phi_{i''}|$:

$$\begin{aligned}
&\sum_{i,i'} \langle\phi_{i''}|\phi_{i'}\rangle\,\langle\phi_{i'}|\hat{H}|\phi_i\rangle\,\langle\phi_i|\Psi\rangle = E\sum_i \langle\phi_{i''}|\phi_i\rangle\,\langle\phi_i|\Psi\rangle \\
\Leftrightarrow\quad &\sum_i \langle\phi_{i''}|\hat{H}|\phi_i\rangle\,\langle\phi_i|\Psi\rangle = E\,\langle\phi_{i''}|\Psi\rangle \\
\Leftrightarrow\quad &\sum_i H_{i'',i}\Psi_i = E\Psi_{i''}
\end{aligned} \tag{3.69}$$

with $H_{i'',i} = \langle\phi_{i''}|\hat{H}|\phi_i\rangle$ and $\Psi_i = \langle\phi_i|\Psi\rangle$. The diagonal terms can be easily calculated:

$$H_{i,i} = \langle\phi_i|\left(\hat{H}_{\text{diag}} + \frac{\hat{\vec{j}}^2}{2I}\right)|\phi_i\rangle = e + \frac{\hbar^2 j(j+1)}{2I} \tag{3.70}$$

Finally, the diagonalization of the matrix:

$$\begin{pmatrix} H_{0,0}-e & \cdots & H_{0,i} & \cdots \\ \vdots & \ddots & & \\ H_{i,0} & & H_{i,i}-e & \\ \vdots & & & \ddots \end{pmatrix} \begin{pmatrix} \Psi_0 \\ \vdots \\ \Psi_i \\ \vdots \end{pmatrix} = 0 \tag{3.71}$$

gives eigenenergies and eigenstates of the dipolar anions described by $\hat{H}$. This method is referred to as the Berggren expansion method.

3.4 Electronic density in the body-fixed frame

In the description of dipolar anions, the couplings between the angular momentum $\hat{\vec{j}}$ of the neutral dipolar molecule, and the orbital angular momentum $\hat{\vec{l}}$ of the external electron, which leads to the total angular momentum $\hat{\vec{J}}$, is of particular importance. Indeed, without these couplings there are no bound states or resonances. Thus, the electronic density in the body-fixed frame (intrinsic frame), must reflect the richness of these angular momenta couplings. This intrinsic density can be obtained with a passive rotation $\hat{R}(\Omega)$ acting on the coordinate axis, in order to superimpose the new (Oz) axis denoted (Oz') and the rotor direction. The starting coordinate frame is denoted $(\mathcal{S})$, and the body-fixed frame $(\mathcal{S}')$. The passive rotation thus changes the projection operators $\hat{l}_z$, $\hat{j}_z$ and $\hat{J}_z$ to $\hat{l}_{z'}$, $\hat{j}_{z'}$ and $\hat{J}_{z'}$, respectively. The angular momenta projections in both coordinate frames are summarized in Tab.3.1.

Angular momentum	Projection in $(\mathcal{S})$	Projection in $(\mathcal{S}')$
l	m_l	K_l
j	m_j	K_j
J	M_J	K_J

Table 3.1 – Conventions used in the angular momenta projections in $(\mathcal{S})$ and $(\mathcal{S}')$.

with:

$$(\mathcal{S}) : m_l + m_j = M_J \quad \rightarrow \quad (\mathcal{S}') : K_l + K_j = K_J \tag{3.72}$$

In the present case, $K_j = 0$ because the (Oz') axis and the rotor direction coincide and the conservation of the total projections (3.72) leads to $K_l = K_J$. Common eigenvectors of the operators of square angular momenta and of the z and z' component of angular momenta operators in both coordinate frames are given in Tab.3.2.

Operators in $(\mathcal{S})$	Eigenvectors in $(\mathcal{S})$	Operators in $(\mathcal{S}')$	Eigenvectors in $(\mathcal{S}')$
$\hat{\vec{l}}^2, \hat{l}_z$	$\lvert l, m_l\rangle$	$\hat{\vec{l}}^2, \hat{l}_{z'}$	$\lvert l, K_l\rangle$
$\hat{\vec{j}}^2, \hat{j}_z$	$\lvert j, m_j\rangle$	$\hat{\vec{j}}^2, \hat{j}_{z'}$	$\lvert j, K_j\rangle$
$\hat{\vec{J}}^2, \hat{J}_z$	$\lvert l, j; J, M_J\rangle$	$\hat{\vec{J}}^2, \hat{J}_{z'}$	$\lvert l, j; J, K_J\rangle$

Table 3.2 – Eigenvectors of the square angular momenta operators and of the z and z' component of angular momenta operators in $(\mathcal{S})$ and $(\mathcal{S}')$.

In the CC framework, the eigenstates of dipolar anions are of the form:

$$|\Psi\rangle = \sum_{l,j} |u_{l,j}\rangle \otimes |l, j; J, M_J\rangle \tag{3.73}$$

The angular part can be rotated in the body-fixed frame, *i.e.* with Ω such as $K_j = 0$ and $K_l = K_J$:

$$\begin{aligned}\hat{R}(\Omega)\,|l,j;J,M_J\rangle &= |l,j;J,M_J\rangle_\Omega \\ &= \sum_{K_J} D^J_{K_J,M_J}(\Omega)\,|J,K_J\rangle \\ &= \sum_{K_J} D^J_{K_J,M_J}(\Omega) \sum_{K_l,K_j} |l,K_l,j,K_j\rangle\,\langle l,K_l,j,K_j|J,K_J\rangle \\ &= \sqrt{\frac{2j+1}{8\pi^2}} \sum_{K_J} \langle l,K_J,j,0|J,K_J\rangle\, D^J_{K_J,M_J}(\Omega)\,|l,K_J,j,0\rangle \end{aligned} \tag{3.74}$$

The Ω index indicates that the state is rotated in a particular orientation $\Omega = (\alpha,\beta,\gamma)$ defined by the Euler angles. The normalization factor comes from the restriction to the angular momentum states with a projection m_j in $(\mathcal{S})$ and a projection K_j in $(\mathcal{S}')$. Finally, the rotated eigenstate $\hat{R}(\Omega)\,|\Psi\rangle$ is:

$$\begin{aligned}|\Psi\rangle_\Omega &= \sum_{l,j} |u_{l,j}\rangle \otimes |l,j;J,M_J\rangle_\Omega \\ &= \sum_{l,j} |u_{l,j}\rangle \otimes \left(\sqrt{\frac{2j+1}{8\pi^2}} \sum_{K_J} \langle l,K_J,j,0|J,K_J\rangle\, D^J_{K_J,M_J}(\Omega)\,|l,K_J,j,0\rangle \right) \\ &= \sum_{K_J} |\Psi_{K_J}\rangle_\Omega \end{aligned} \tag{3.75}$$

The generalization of these derivations to three angular momenta is done in Refs. [265, 266] based on Refs. [243, 267].

The radial density operator is defined by:

$$\hat{\rho} = |\vec{r}\rangle\,\langle\vec{r}| = |r,\theta,\varphi\rangle\,\langle r,\theta,\varphi| \tag{3.76}$$

where r, θ and φ are the spherical coordinates of the external electron in the body fixed frame. Thus, for a fixed orientation Ω in the body fixed frame and a given K_J component $|\Psi_{K_J}\rangle_\Omega$ in Eq.(3.75), the intrinsic density is:

$$\begin{aligned}\rho_{J,K_J}(r,\theta) &= \int d\Omega\,{}_\Omega\langle\Psi_{K_J}|\hat{\rho}|\Psi_{K_J}\rangle_\Omega \\ &= \sum_{l,l'}\sum_{j} \frac{2j+1}{2J+1} \frac{u^*_{l,j}(r)}{r} \frac{u_{l',j'}(r)}{r} \langle l,K_J,j,0|J,K_J\rangle\,\langle l',K_J,j',0|J,K_J\rangle\, {Y^l_{K_J}}^*(\theta,0) Y^{l'}_{K_J}(\theta,0) \end{aligned} \tag{3.77}$$

The total density in the body fixed frame is thus given by:

$$\rho_J(r,\theta) = \sum_{K_J} \rho_{J,K_J}(r,\theta) \tag{3.78}$$

3.5 Bound states of LiI⁻, LiCl⁻, LiF⁻ and LiH⁻

This section contains the study of the bound states spectra of LiI⁻, LiCl⁻, LiF⁻ and LiH⁻ using the BEM and the DIM. Results presented in the section have been published in Ref. [53].

3.5.1 Parameters of the calculations

Tests of DIM and BEM have been performed for the $LiCl^-$ dipolar anion.

Results of the DIM depend on:

- The parameters of the pseudo-potential (3.8).

  They are fixed to reproduce the experimental value of the ground state energy of the $LiCl^-$ anion: $E_{exp} = -4.483 \cdot 10^{-2}$ Ry [268]. The most important term in the pseudo-potential is the dipole potential V_μ which depends only on the dipole moment μ and the size s of the neutral molecule. Remaining parameters of the pseudo-potential are taken from Ref. [255], namely: $\alpha_0 = 15.3\ a_0^3$, $\alpha_2 = 1.1\ a_0^3$, $r_0 = 2.2\ a_0$, $r_c = 2.828\ a_0$, $Q_{zz} = 3.28\ ea_0^2$, and $V_0 = 2.0$ Ry. The moment of inertia parameters are: $I = 150,000\ m_e a_0^2$ for $LiCl^-$, $240,000\ m_e a_0^2$ for LiI^-, $82,000\ m_e a_0^2$ for LiF^-, and $26,000\ m_e a_0^2$ for LiH^-. The dipole moment of each molecule considered in this work is known experimentally and has been taken from the NIST database.

- The cutoff value of the electron orbital angular momentum l_{max} .

  For $l_{max} = 9$, the ground state energy of the $LiCl^-$ anion is reproduced by taking the charge separation $s_{DIM}^{(9)} = 0.336\ a_0$. To remove the dependence of the results on l_{max}, the ground state energy of $LiCl^-$ is extrapolated for $l_{max} \to \infty$ and the size of the charge separation s is adjusted to reproduce the experimental binding energy. In this case, $s_{DIM}^{(\infty)} = 0.337\ a_0$.

- The matching radius r_m.

  In the resolution of CC equations, the value of $r_m = a_0$ is determined by investigating the stability of the DIM results with respect to the change of r_m.

In order to compare results obtained in DIM and in BEM, the pseudo-potential parameters remain the same in both methods. Also, the cutoff value of the electron orbital momentum $l_{max} = 9$ is the same.

The BEM results depend on:

- The discretization of the complex contour in the Berggren basis.

  Three segments defining the complex contour (see Fig.1.2) are given by the connection of the following points: $k_1 = (0,0)$, $k_2 = (0.15, -i0.04)$, $k_3 = (1,0)$, and $k_4 = k_{max}$ in units of a_0^{-1}. Each scattering contour has been discretized with 220 points. Since the applications carried out in this section concerns bound states, the real-energy scattering contour could be used as well.

- The maximal value k_{max} of the real momentum in a definition of the complex contour.

  This value has been chosen such that (i) BEM results are practically independent of l_{max}, (ii) a good numerical precision could be attained, and (iii) the s-value is approximately the same as in DIM. The cutoff parameter is thus equal to $k_{max} = 1.53\ a_0^{-1}$ for each partial wave.

- The size of the dipole s.

  This value has been extrapolated in order to obtain l_{max}-independent results: $s_{BEM}^{(9)} = s_{BEM}^{(\infty)} = 0.336\ a_0$.

3.5.2 Numerical tests and benchmarking

A first comparison between DIM and BEM results is done by looking at the channel wave functions for $r \approx s$. The dipolar potential (3.9) is not differentiable at $r = s$ and, therefore, it cannot be treated in BEM exactly because the channel wave functions expanded in Berggren basis are analytic by construction. On the other hand, in DIM it is sufficient to add a second matching radius at $r = s$ to obtain the exact result.

In practice, this procedure adds a node beyond $r = s$ in DIM channel wave functions, which is absent in BEM. This is illustrated in Fig.3.3 for a $(j_c = 0, l_c = 0)$ channel wave function corresponding to the first excited $J^\pi = 0_2^+$ state of $LiCl^-$. Beyond $r = s$, the channel wave functions calculated with both methods are very close and, as it will be shown later, this near-origin pathology has a very small impact on the eigenenergies of dipolar anions.

As discussed in 3.3.3.1, DIM is inadequate for states with very small energies, while BEM has been shown to be very precise in this case. On the other hand, for states with binding energies typically greater than 10^{-2} Ry, BEM yields channel wave functions that exhibit spurious low-amplitude oscillations. Fig.3.4 illustrates such wiggles in the tail of the channel wave function $u_{j_c=0,l_c=0}$ of the $J^\pi = 0_1^+$ ground state of $LiCl^-$. For such well-bound states, the standard size of the Berggren basis in terms of the number of contour discretization points and k_{max}, is not sufficient. The DIM is thus preferable for such cases, as the asymptotic behavior of well-bound states is treated almost exactly.

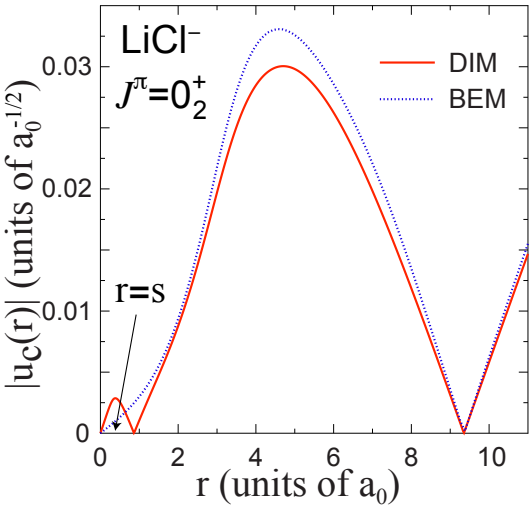

Figure 3.3 – (Color online) The modulus of the channel wave function $u_{j_c=0,l_c=0}$ near $r = 0$ for the $J^\pi = 0_2^+$ first excited state of $LiCl^-$ calculated in DIM (solid line) and BEM (dotted line) with $l_{max} = 9$. At large distances, spurious wiggles appear in BEM results (see the inset) due to the basis truncation.

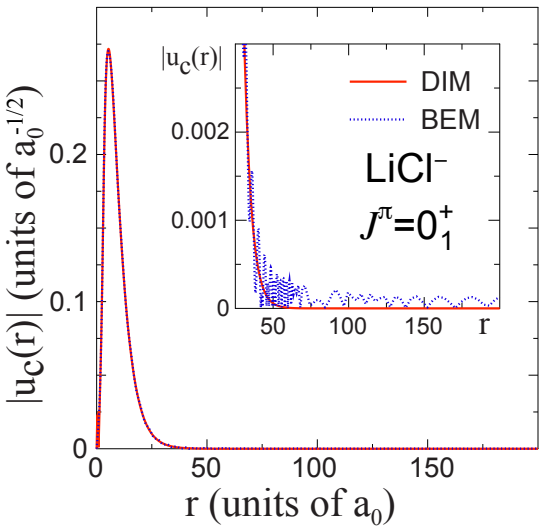

Figure 3.4 – (Color online) The modulus of the channel wave function $u_{j_c=0,l_c=0}$ for the $J^\pi = 0_1^+$ ground state of $LiCl^-$ calculated in DIM (solid line) and BEM (dotted line) with $l_{max} = 9$. The charge separation s of LiCl has been adjusted in both approaches to reproduce the experimental ground state energy in the limit $l_{max} \to \infty$.

The direct integration becomes numerically unstable when the channel orbital angular momentum becomes large, around $l_c = 10$, even for the states with relatively large binding energies. In this case, the matrix formed from the matching conditions Eq.(1.143), which is the generalization of the Jost function to an arbitrary number of channels, is ill-conditioned[1] and its eigenvector of zero eigenvalue becomes imprecise. This results in a discontinuity at r_m and spurious occupation of channels with large orbital angular momentum $l_c > 10$. This is illustrated in Fig.3.5 for the $J^\pi = 0_1^+$ ground state of $LiCl^-$.
As a result, the energy and spatial extension of the electron cloud distribution of the CC eigenstate become incorrect.

The convergence of the $LiCl^-$ ground state energy with respect to l_{max} is shown in Fig.3.6. There is an exponential convergence of calculated DIM energies with l_{max} for $6 \le l_{max} \le 10$ and a clear deviation for $l_{max} \ge 11$, which is related to the discontinuity of channel wave functions for $l_{max} > 10$. The energy

[1]The inverse is difficult to calculate, or in other words a small error on the matrix elements generates a big error on the wave functions.

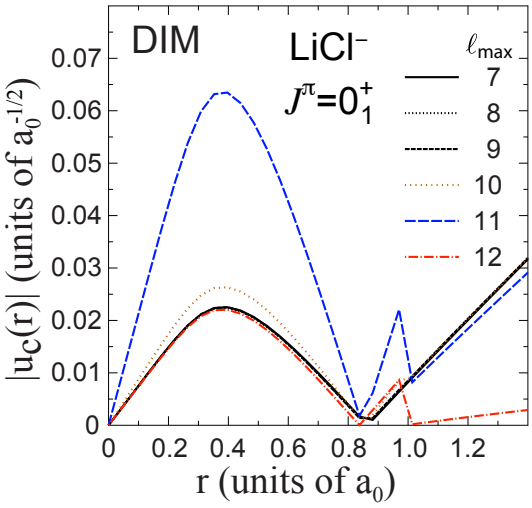

Figure 3.5 – (Color online) The modulus of the channel wave function $u_{j_c=0,l_c=0}$ for the $J^\pi = 0_1^+$ ground state of $LiCl^-$ calculated in DIM with several values of l_{max}. For $l_{max} \geq 10$, one may notice the development of a discontinuity at the matching point $r_m = a_0$. In such cases, the channel wave function becomes ill-conditioned, introducing serious errors in CC eigenenergy and eigenfunction.

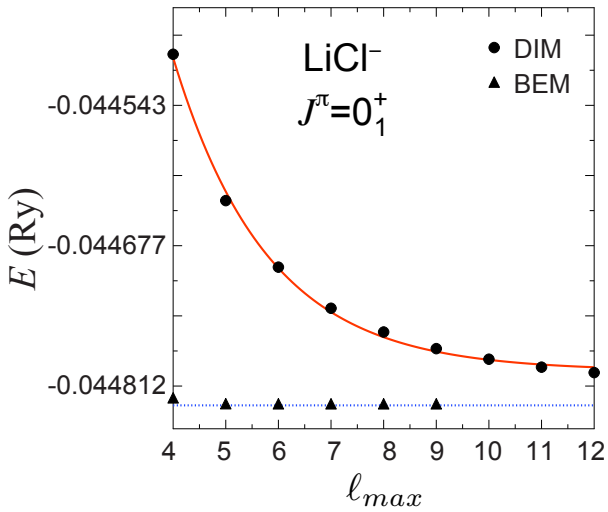

Figure 3.6 – (Color online) The dependence of the $LiCl^-$ ground state energy on l_{max} in DIM (dots) and BEM (triangles). The DIM results converge exponentially (red line). This allows us to determine the asymptotic value of energy at $l_{max} \to \infty$.

calculated in BEM is perfectly stable with l_{max}.

The rapid converge of BEM with l_{max} is due to k_{max}-truncation of the single-particle basis that suppresses contributions from large-l_c configurations. This is illustrated in Fig.3.7, which displays the average modulus of the off-diagonal matrix element of the channel-channel coupling in BEM:

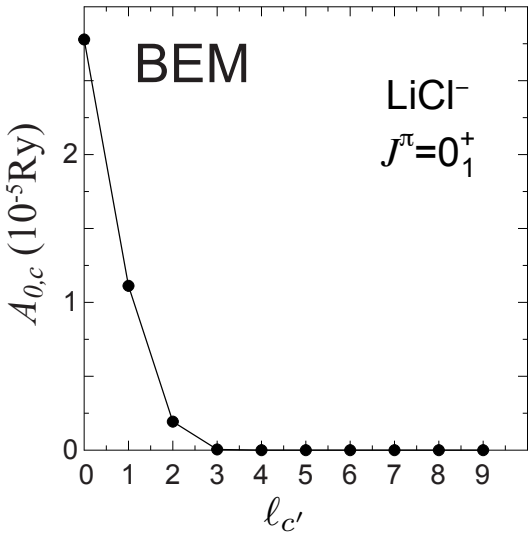

Figure 3.7 – Average off-diagonal matrix element $A_{0,c}$ Eq.(3.79) of the channel-channel coupling in BEM between the channel $(j_c = 0, l_c = 0)$ and c' for the $J^\pi = 0_1^+$ ground state of $LiCl^-$.

$$A_{c,c'} = \frac{1}{N^2} \sum_{n,n'}^{N} \langle \phi_{n',c'} | V | \phi_{n,c} \rangle \tag{3.79}$$

between the first channel $c = (j_c = 0, l_c = 0)$ and the higher-$l_{c'}$ channels c'. Only the channels with $l_c \leq 5$ and $|l_c - l_{c'}| \leq 3$ contribute significantly to the channel coupling matrix element. Using the same truncation, the DIM yields numerically stable results. In this case, the energies of well-bound states ($|E| > 10^{-2}$ Ry) agree in both methods.

The numerical instability of DIM at large $l_{\max}$ leads to a collapse of calculated radii. Fig.3.8 shows the dependence of the ground state r.m.s. radius of $LiCl^-$ on $l_{\max}$. This result, together with discussion of Fig.3.7, suggests that the BEM can provide practical guidance on the minimal number of channels in the CC approach.

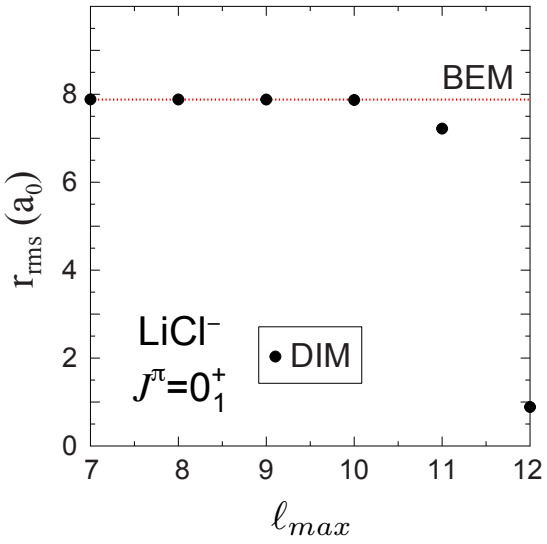

Figure 3.8 – (Color online) The dependence of the $LiCl^-$ ground state r.m.s. radius on $l_{\max}$ DIM (dots) and BEM (dotted line). The DIM results are stable up to $l_{\max} = 10$.

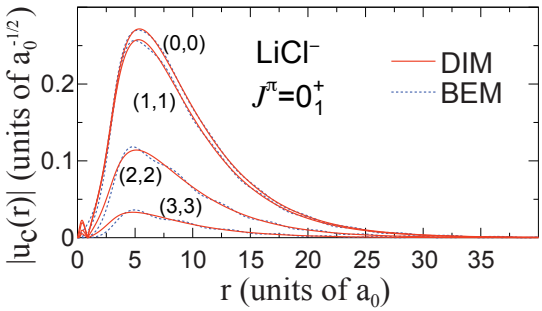

Figure 3.9 – (Color online) Most important channel wave functions $u_c(r)$ for the $J^\pi = 0_1^+$ ground state of $LiCl^-$, as calculated in DIM (solid line) and BEM (dashed line) with $l_{\max} = 9$.

In practical applications, spurious oscillations in BEM channel wave functions for well-bound states can be taken care of by extrapolating wave functions from the intermediate region of r, where they are reliably calculated, into the asymptotic region. This can be done by applying the analytical expression:

$$\tilde{u}_c(r) \equiv \lim_{r \gg 0} u_c(r) = e^{ik_c r} \sum_{j=1}^{M} \frac{\alpha_j^{(c)}}{r^j}, \tag{3.80}$$

where k_c is the channel momentum and $\alpha_j^{(c)}$ are parameters to be determined by the fit. The precision of this procedure can be assessed by computing the norm of the eigenstate. Using this procedure, one obtains perfectly stable r.m.s. radii in BEM for different values of $l_{\max}$, as can be seen in Fig.3.8.

Figs.3.9 and 3.11 compare the four most important channel wave functions (l_c, j_c) of DIM and BEM corresponding to the three lowest $J_i^\pi = 0_i^+$ eigenstates of $LiCl^-$.

For the ground state, both approaches predict the same energy $E = -4.483 \cdot 10^{-2}$ Ry and the channel functions are practically identical. For the first excited state, the agreement is still reasonable. Here, the energy in DIM is $E = -7.374 \cdot 10^{-4}$ Ry while BEM gives slightly more binding: $E = -8.241 \cdot 10^{-4}$ Ry. Consequently, the BEM wave functions decrease faster than those computed with DIM. For a second excited

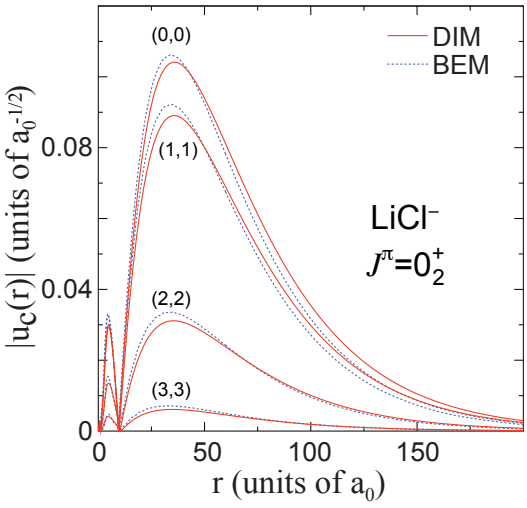

Figure 3.10 – (Color online) Similar to Fig.3.9 but for the first excited $J^\pi = 0_2^+$ state of $LiCl^-$.

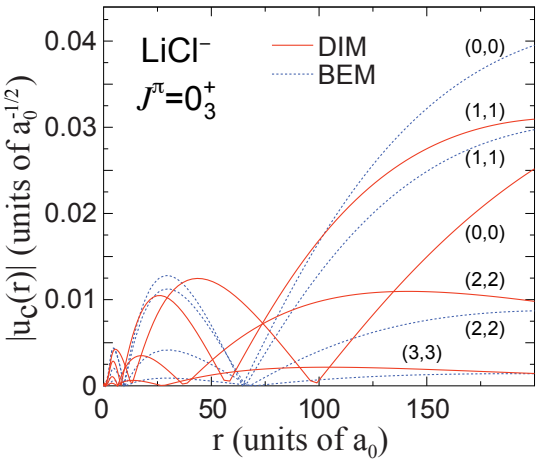

Figure 3.11 – (Color online) Similar to Fig.3.9 but for the second excited $J^\pi = 0_3^+$ state of $LiCl^-$.

0_3^+ state, both methods differ markedly. This state has a sub-threshold nature, with $E_{\rm DIM} = -7.051 \cdot 10^{-6}$ Ry and $E_{\rm BEM} = -9.907 \cdot 10^{-6}$ Ry. For this extremely diffuse state, the direct integration method fails completely. This is manifested by the very different nodal structure of channel wave functions in DIM seen in Fig.3.11.

Remark:

Figs.3.7 and 3.9 show that for bound states of dipolar anions, the dominant channel wave functions are always associated with low electron orbital angular momentum ($l_c = 0, 1$). For high-spin bound states of anions, the angular momentum is generated mainly by the rotational motion of the dipolar core. and dipole angular momentum j_c. In this case, the energy scales associated with the rotational motion of the molecule and the motion of the weakly bound valence electron may be comparable. Consequently, bound states of dipolar anions are characterized by a strong coupling between the electron orbital angular momentum and the dipole angular momentum.

3.5.3 Critical dipole moment

A stringent test of the computational framework is provided by the analytic result $\mu_{\rm cr} = 0.639\, ea_0$ for the fixed dipole ($I \to \infty$) [251]. For a dipole moment in the interval $0.6 \le \mu \le 3.0$, BEM calculations have been performed and only the eigenenergies which satisfy $E < E_{\rm lim} = -10^{-8}$ have been retained to extract the critcal dipole moment. This criteria leads to an interval $\Delta\mu \simeq 0.377$ of the dipole moment. In this energy interval, $\mu_{\rm cr}$ can be obtained using the expression:

$$E(\mu) = (\mu + b)^{\frac{a}{\mu}} e^c \tag{3.81}$$

to extrapolate the calculated energy down to $E = 0$. An excellent energy fit in the subthreshold region does not guarantee an excellent estimate of the critical dipole moment. The values of $\mu_{\rm cr}$ extracted by this extrapolation procedure can be considered reliable only if $\Delta\mu$, which depends on the chosen precision $E_{\rm lim}$, is close to the critical dipole moment. In the studied cases, this criterion is approximately satisfied only for the ground state and the first excited 0^+ state. The critical dipole moments for these states in anions with the dipole length $s = 4a_0$ are shown in Tab.3.3 for various moments of inertia.

$I\,[\,m_e a_0^2]$	$\mu_{\rm cr}^{(0)}\,[\,ea_0]$		$\mu_{\rm cr}^{(1)}\,[\,ea_0]$	
	BEM	Ref. [49]	BEM	Ref. [49]
10^4	0.937	0.843	1.024	1.515
10^6	0.674	0.750	0.633	1.145
10^8	0.639	0.715	0.622	0.974
10^{10}	0.639	—	0.622	—
10^{15}	0.639	—	0.62	—

Table 3.3 – Critical dipole moments for dipolar anions in the two lowest 0^+ states calculated in this work (BEM) and in Ref. [49] for the charge separation $s = 4a_0$ and different moments of inertia I. The analytic result at $I \to \infty$ [250, 251] is $\mu_{\rm cr} = 0.639\ ea_0$.

The agreement with the analytic limit is excellent for the ground state configuration, and is fairly good for the first excited 0^+ state. This is very encouraging, considering the slow convergence with I and various sources of numerical errors in the $E \to 0$ regime [52].

3.5.4 Results for spectra and radii

Energies and r.m.s. radii of the lowest bound 0^+ and 1^- states of LiI^-, $LiCl^-$, LiF^-, and LiH^- dipolar anions predicted in this study are listed in Tab.3.4. For each total angular momentum J^π there are at most three bound eigenstates in each system. The r.m.s. radius $r_{\rm rms}$ of an electron cloud shows a spectacular increase when the binding energy of the state decreases. For the subthreshold states, such as 0_3^+ and 1_3^-, the radius is of the order of hundreds to thousands a_0.

Energy spectra and radii of dipolar anions do not change significantly in the limit $l_{\rm max} \to \infty$. Usually, the extrapolated results for both E and $r_{\rm rms}$ agree very well with those in Tab.3.4 ($l_{\rm max} = 9$). For instance, the extrapolated values for the 1_2^+ state in LiH^- are $E = -7.931 \cdot 10^{-5}$ Ry and $r_{\rm rms} = 1.147 \cdot 10^2\ a_0$.

The DIM and BEM results are generally consistent for both energy and radii though significant quantitative differences persist for excited, weakly-bound states of anions where the DIM is not expected to work. In the case of LiF^-, the BEM predicts the existence of the third 0_3^+ state at an energy $-6.1 \cdot 10^{-8}$ Ry, which is absent in DIM.

It is instructive to compare our DIM results with those obtained in Ref. [255] using a similar approach. Table 3.5 lists energies of the lowest 0^+ bound states of LiI^-, $LiCl^-$, LiF^-, and LiH^- dipolar anions obtained in both studies, and Table 3.6 shows the adopted values of dipole moments.

The two calculations agree reasonably well for the lowest-lying states, but some difference stems from slightly different dipole moments used in Ref. [255] and here. Indeed, while the charge separation in both studies was adjusted to reproduce the experimental ground state energy of $LiCl^-$, the fitted values of s in both calculations are different: $s = 0.3335\ a_0$ in Ref. [255] and $s_{\rm DIM} = 0.336\ a_0$ here.

The largest deviations, seen for weakly-bound states, can be traced back to the cutoff value of the electron orbital angular momentum when solving CC equations. In Ref. [255], the adopted value of $l_{\rm max}$ was small, typically $l_{\rm max} = 4$ [269], whereas it is fairly large, $l_{\rm max} = 9$, in our work. As seen in Fig.3.6, energies of weakly-bound states obtained in DIM converge slowly with $l_{\rm max}$.

The BEM results have been benchmarked by using the traditional technique of direct integration of CC equations. While a fairly good agreement between the two methods has been found for well-bound states, the direct integration technique breaks down for weakly-bound states with energies $|E| < 10^{-4}$ Ry, which is comparable with the rotational energy of the anion. For those subthreshold configurations, the Berggren expansion is a tool of choice.

The inherent problem of the DIM is the lack of stability of results when the number of channels increases. Indeed, the method breaks down when the channel orbital angular momentum is $l_c > 9$. This problem does not appear in BEM, since the rapid convergence with $l_{\rm max}$ is guaranteed by an effective softening of

Anion	State	E [Ry]		r_{rms} [a_0]	
		DIM	BEM	DIM	BEM
LiI^-	0^+_1	-5.079(-2)	-5.023(-2)	7.569(0)	7.620(0)
	0^+_2	-9.374(-4)	-1.037(-3)	5.112(1)	4.759(1)
	0^+_3	-1.502(-5)	-1.797(-5)	3.719(2)	3.308(2)
	1^-_1	-5.079(-2)	-4.995(-2)	7.569(0)	7.641(0)
	1^-_2	-9.291(-4)	-1.023(-3)	5.112(1)	4.886(1)
	1^-_3	-1.261(-7)	-1.099(-5)	3.423(3)	3.464(2)
$LiCl^-$	0^+_1	-4.483(-2)	-4.483(-2)	7.885(0)	7.894(0)
	0^+_2	-7.374(-4)	-8.241(-4)	5.632(1)	5.017(1)
	0^+_3	-7.051(-6)	-9.907(-6)	5.124(2)	4.106(2)
	1^-_1	-4.482(-2)	-4.458(-2)	7.885(0)	7.915(0)
	1^-_2	-7.241(-4)	-8.067(-4)	5.633(1)	5.337(1)
	1^-_3	-3.062(-7)	-8.159(-7)	2.066(3)	8.831(2)
LiF^-	0^+_1	-2.795(-2)	-2.983(-2)	9.117(0)	8.991(0)
	0^+_2	-3.022(-4)	-3.525(-4)	8.098(1)	7.501(1)
	0^+_3	—	-6.101(-8)	—	3.363(3)
	1^-_1	-2.793(-2)	-2.968(-2)	9.117(0)	9.010(0)
	1^-_2	-2.782(-4)	-3.277(-4)	8.124(1)	7.520(1)
LiH^-	0^+_1	-2.149(-2)	-2.370(-2)	1.011(1)	9.698(0)
	0^+_2	-1.491(-4)	-1.922(-4)	1.058(2)	9.297(1)
	1^-_1	-2.142(-2)	-2.353(-2)	1.011(1)	9.717(0)
	1^-_2	-7.942(-5)	-1.231(-4)	1.146(2)	9.591(1)

Table 3.4 – Energies and r.m.s. radii for 0^+ and 1^- bound states of selected dipolar anions obtained in DIM ($l_{\mathrm{max}} = 9$) and BEM. The parameters of the calculation are given in 3.5.1. The numbers in parentheses denote powers of 10.

Anion	State	E [Ry]	
		This work	Ref. [255]
LiI^-	0^+_1	-5.079(-2)	-4.998(-2)
	0^+_2	-9.374(-4)	-1.022(-3)
	0^+_3	-1.502(-5)	-1.999(-5)
$LiCl^-$	0^+_1	-4.483(-2)	-4.483(-2)
	0^+_2	-7.374(-4)	-7.497(-4)
	0^+_3	-7.051(-6)	-9.775(-6)
LiF^-	0^+_1	-2.795(-2)	-2.793(-2)
	0^+_2	-3.022(-4)	-3.366(-4)
	0^+_3	—	-8.746(-7)
LiH^-	0^+_1	-2.149(-2)	-2.352(-2)
	0^+_2	-1.491(-4)	-1.926(-4)

Table 3.5 – Energies for 0^+ bound states of selected dipolar anions obtained in DIM in this work ($l_{\mathrm{max}} = 9$) and in Ref. [255]. The numbers in parentheses denote powers of 10.

the interaction through the momentum cutoff k_{max}, which suppresses contributions from high-l_c partial waves.

Anion	$\mu\,[\,ea_0]$	
	This work	Ref. [255]
LiI^-	2.911384272	2.911384272
$LiCl^-$	2.805158089	2.793355179
LiF^-	2.472316049	2.478610934
LiH^-	2.313370205	2.321238811

Table 3.6 – Dipole moments of selected dipolar anions adopted in this work and in Ref. [255].

3.5.5 Dipolar anions as extreme halo systems

In two-body halo systems with a relative angular momentum l, the mean squared radius $< r^2 >$ behaves as [270]:

$$\begin{aligned} &< r^2 > \sim \frac{1}{\Delta E} && \text{for } l = 0 \\ &< r^2 > \sim \frac{1}{\sqrt{\Delta E}} && \text{for } l = 1 \\ &< r^2 > && \text{remains finite for } l > 1 \end{aligned} \tag{3.82}$$

where ΔE is the binding energy of the system.

In Fig.3.12, results for LiI^-, $LiCl^-$, LiF^- and LiH^- lie on a straight line corresponding to a mean square radius which diverges as $1/\Delta E^\alpha$ with $\alpha = 0.9172$. In the present case, binding energies of dipolar anions are obtained from CC calculations which involve channels with orbital angular momenta l_c from 0 to $l_{\max}$. The dominant contributions to eigenenergies are for $l_c = 0$ but higher l_c contribute as well. Thus the value of α is slightly smaller than 1.

The comparison with nuclear and molecular halos in Figs.3.13 shows that the dipolar anions reach very large $< r^2 > /\Delta E$ ratios and can be considered as the extreme halo systems.

3.6 Bound and resonant states of HCN^-

3.6.1 Hamiltonian modification and calculation parameters

Modification of the Hamiltonian

Due to the presence of $r_>$ and $r_<$, the dipolar potential is discontinuous at $r = s = 2.04\ a_0$. Contrary to the $LiCl^-$ case, in the description of the HCN^- anions this discontinuity is removed. To remove it, the $r_>/r_<$ term in Eq.(3.9) is replaced by:

$$h_{a,d}(r) = \left(\frac{r}{s} f_d(r) + \frac{s}{r}(1 - f_d(r))\right) \mathrm{erf}(ar) \tag{3.83}$$

with $a = d = 1\ a_0$, and $r_>$ by:

$$r_>(d) = s f_d(r) + r(1 - f_d(r)) \tag{3.84}$$

Functions $f_d(r)$ and $\mathrm{erf}(ar)$ in Eqs.(3.83) and (3.84) are the Fermi function:

$$f_d(r) = \frac{1}{1 + e^{\frac{r-s}{d}}} \tag{3.85}$$

and error function:

$$\mathrm{erf}(r) = \frac{2}{\pi} \int_0^r dx\, e^{-x^2} \tag{3.86}$$

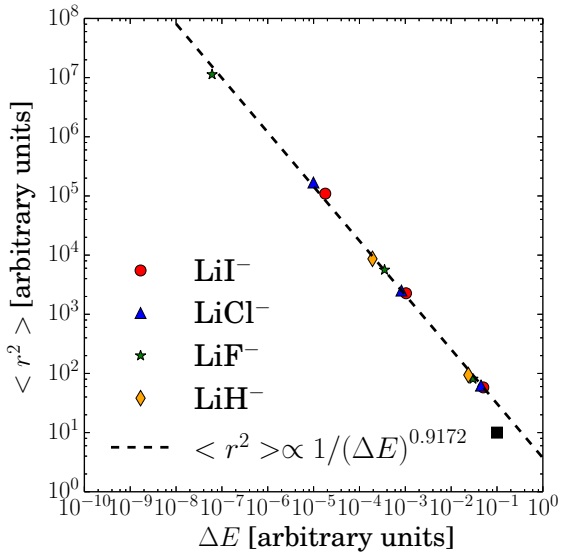

Figure 3.12 – Plot of the dimensionless mean square radius *vs.* dimensionless binding energy of LiI^-, $LiCl^-$, LiF^- and LiH^-. The black square indicates a typical atomic system with a r.m.s. radius of 10 a_0^2 and a binding energy of 10^{-1} Ry. The first group of points at binding energies of about $10^{-2} - 10^{-1}$ Ry corresponds to the ground states of considered dipolar anions calculated in BEM. The second group at binding energies of about $10^{-4} - 10^{-3}$ Ry contains the first excited states, and the last three points corresponds to the second excited states of dipolar anions presented in Tab.3.4.

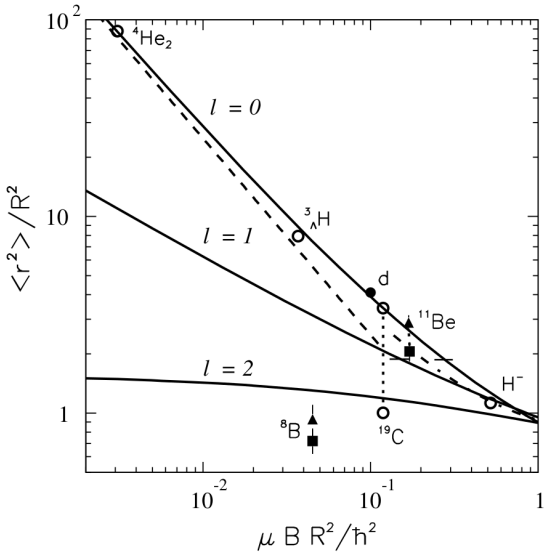

Figure 3.13 – Plot of the dimensionless mean square radius *vs.* dimensionless binding energy for various nuclear and molecular weakly bound systems (from Ref. [259]).

respectively.

——— *Parameters of the BEM calculation* ———

In BEM, results depend on:

- The pseudo-potential parameters.

  For the dipolar moment μ of the molecule, the experimental value has been chosen, namely: $\mu = 1.174\ ea_0$. The r_c parameter is adjusted: $r_c = 3.071622666\ a_0$, to reproduce the experimental value of the ground state ($J^\pi = 0^+$) energy [269]: $E^{\text{exp}}(0_1^+) = -1.1465789 \times 10^{-4}$ Ry. Remaining parameters of the pseudo-potential for the HCN^- anion are taken from Ref. [263]. These are: $\alpha_0 = 15.27\ a_0^3$, $\alpha_2 = 1.08\ a_0^3$, $Q_{zz} = 3.28\ ea_0^2$, $I = 7.42 \times 10^4\ m_e a_0^2$, $r_0 = 4.4\ a_0$, $V_0 = 4.0$ Ry and $s = 2.04\ a_0$. One may notice that the dipole core s in HCN^- anion is significantly larger than in $LiCl^-$ ($0.336\ a_0$) described in Sec.3.5.

- The cutoff parameter for the orbital angular momentum of an electron: $l_{\max} = 9$.

- The complex-contour and its discretization.

  For all (l_c, j_c), the complex contour $L^+_{l_c,j_c}$ is taken close to the real axis ($k_{\text{peak}} = 0.15 - i1.0 \times 10^{-7}\ a_0^{-1}$, $k_{\text{middle}} = 1.0\ a_0^{-1}$ and $k_{\max} = k_{\max}$), with $k_{\max} = 6\ a_0^{-1}$ for each total angular momentum J^π. Its precise form has been adjusted by looking at the convergence of bound state energies when changing the imaginary part of k_{peak}. Each segment of the contour $L^+_{l_c,j_c}$ is discretised with the same number of points ($n_{\text{seg}} = 55$), to achieve a good convergence and stability of bound state energies.

The $J^\pi = 1^-$ ground state energy is also known experimentally: $E^{\rm exp}(1^-_1) = -8.8198377 \times 10^{-5}$ Ry, but no special adjustment of the model parameters has been done to fit the experimental value. When the total angular momentum J^π changes, all model parameters except for the rotation point in the complex-scaling method remain unchanged.

3.6.2 Identification of the resonances

The diagonalization of a complex-symmetric Hamiltonian matrix in BEM yields a set of eigenenergies which are the poles of resolvent of the Hamiltonian (the physical states) and a large number of complex energy scattering states. The physical states are embedded in a discretised continuum of scattering states and their identification is not trivial.

Physical states should verify the following conditions:

- They are stable with respect to changes of the contour. This feature of resonant states has been found earlier in Refs. [29, 77].
- Their dominant channel wave functions exhaust large fraction of the real part of the norm.

The norm of an eigenstate $|\Psi\rangle$ of the Hamiltonian is given by:

$$\sqrt{\langle\Psi|\Psi\rangle} = \sqrt{\sum_{c,c'} \langle u_c|u_{c'}\rangle} = \sqrt{\sum_c n_c^2} = 1 \tag{3.87}$$

with $n_c = \sqrt{\langle u_c|u_c\rangle}$ the norm of the channel wave function. In general, the norms of individual channel wave functions for resonances are complex numbers and their real parts are not necessarily positive definite. It may happen that if a large number of weak channels $\{c_i\}$ with small negative norms $n_{c_i} < 0$ contribute to the resonance wave function, then the dominant channel c can have a norm $n_c > 1$. This means that the channel wave functions are auxiliary objects with no obvious probabilistic interpretation, contrary to the eigenstate of a Hamiltonian.

To check the stability of BEM eigenstates, the imaginary part of $k_{\rm peak}$ changes from 0 to $-1.0 \times 10^{-4}\ a_0^{-1}$ in all contours. Resulting contour variations change both real $\Delta\Re(E)$ and imaginary $\Delta\Im(E)$ parts of the eigenenergies but in all cases $\Delta\Re(E) \ll \Re(E)$. The precision of the method of identification is then evaluated by looking at the ratio $\Delta\Im(E)/\Im(E)$, which is in the range $[0.001, 0.3]$ for all resonances. An illustration is given for the spectrum of $J^\pi = 2^+$ resonances in Tab.3.7. All eigenenergies which are stable with respect to the contour changes are presented in Tab.3.4.

As shown in Tab.3.7, the relative variations of the real part of the resonance energies are always smaller than 1%, while the relative variations associated with the imaginary part can reach ~15%. Moreover, values of $\Delta\Im(E)/\Im(E)$ for different resonances can differ by three orders of magnitude. In general, a better stability of the BEM eigenstates and thus a smaller values of $\Delta\Im(E)/\Im(E)$, is found for resonances with several important channel wave functions contributing significantly to the total norm of the resonance wave function. A typical accumulation of eigenenergies when changing the form of the contour is shown in Fig.3.14.

The non-resonant continuum states (in black) do not show a comparable stability to the resonances (in red). It is interesting to notice that several resonances are found far away from of the region of a dense distribution of non-resonant continuum eigenstates.

The conclusion about the stability of Hamiltonian eigenstates remains qualitatively similar if the real part of $k_{\rm peak}$ varies from $0.14\ a_0^{-1}$ to $0.16\ a_0^{-1}$ to generate the contours variations. In this case, the relative variations of the real part of the eigenstate energies dominate as can be seen in Fig.3.15 for two near-threshold resonances. A zoom on one of the resonances shown in Fig.3.15 is shown in Fig.3.16.
The convergence of the eigenenergy with the changes of the contour is illustrated in Fig.3.16 by dots of a varying size. The physical value is denoted by a star. Corresponding variations of the non-resonant continuum state energies are bigger by at least one order of magnitude and in the scale of this figure only

State	$\Re(E)$ [Ry]	$\Delta\Re(E)/\Re(E)$ [%]	$\Im(E)$ [Ry]	$\Delta\Im(E)/\Im(E)$ [%]
2	2.508(-5)	2.467(-1)	-9.677(-6)	2.081(-1)
3	2.695(-4)	1.291(-4)	-3.455(-10)	1.321(+1)
4	2.766(-4)	1.369(-5)	-3.578(-9)	1.559(+1)
5	3.546(-4)	5.610(-4)	-7.198(-7)	1.602
6	3.668(-4)	3.696(-4)	-1.209(-6)	1.779
7	3.963(-4)	3.518(-3)	-2.337(-6)	4.553(-1)
8	3.979(-4)	2.066(-2)	-5.053(-5)	6.188(-2)
9	4.250(-4)	6.022(-3)	-1.038(-4)	3.022(-2)
10	6.484(-4)	9.703(-5)	-6.721(-7)	1.423
11	6.598(-4)	6.864(-4)	-8.317(-7)	2.518
12	6.813(-4)	6.770(-3)	-1.195(-5)	7.414(-1)
13	6.879(-4)	9.864(-4)	-1.596(-6)	1.554
14	7.402(-4)	5.053(-3)	-6.684(-5)	3.848(-2)
15	9.803(-4)	7.895(-4)	-7.863(-7)	1.450(+1)
16	1.051(-3)	4.805(-5)	-6.224(-7)	1.389
17	1.062(-3)	1.873(-4)	-8.536(-7)	2.659
18	1.071(-3)	1.819(-3)	-5.600(-6)	1.102
19	1.090(-3)	4.002(-4)	-4.892(-7)	7.672
20	1.113(-3)	8.048(-4)	-1.661(-6)	9.612
21	1.141(-3)	2.279(-3)	-2.712(-5)	1.306(-1)

Table 3.7 – Relative variation of the real and imaginary parts of the energy of $J^\pi = 2^+$ resonances.

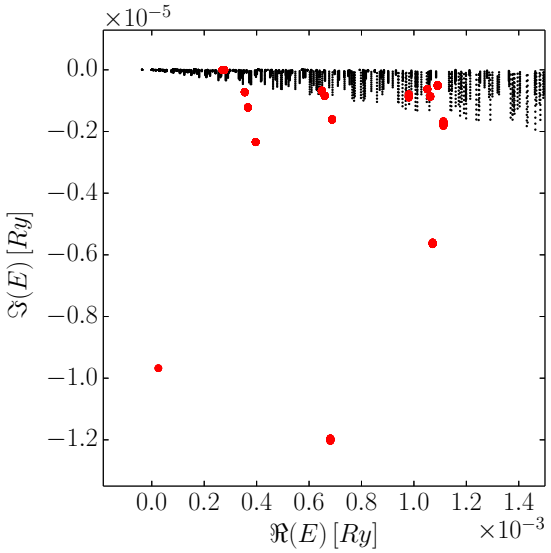

Figure 3.14 – Illustration of the stability of the real and imaginary parts of the eigenenergy of a $J^\pi = 2^+$ resonant state with the contour changes. The black dots denote the non-resonant continuum state eigenenergies, and the red dots denote the resonant state eigenenergies. For more details, see the discussion in the text.

few sparsely distributed black dots can be seen. A similar accumulation of eigenenergies can be seen in Fig.3.17 for an isolated resonance on the left hand side of Fig.3.14.

The stability of resonance eigenenergies with the $l_{\max}$ parameter is yet another test of the resonance identification. As an illustration, the convergence of $J^\pi = 2^+$ resonance energies with respect to $l_{\max}$ is

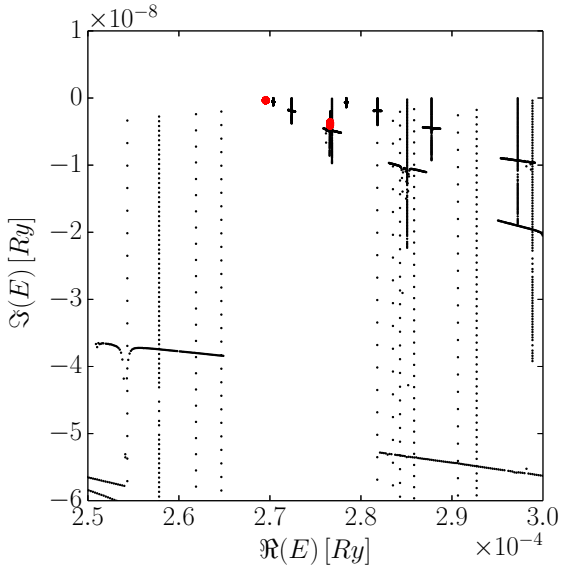

Figure 3.15 – The same as in Fig.3.14 with a zoom on two near-threshold resonances.

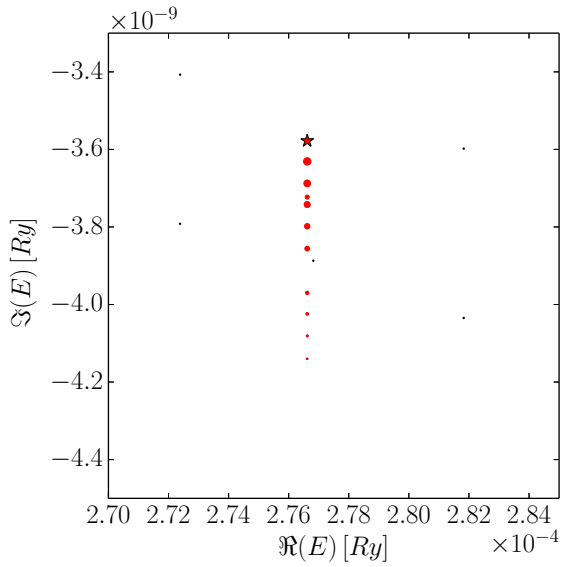

Figure 3.16 – The same as in Fig.3.14 with a zoom on a single resonance shown in Fig.3.15. The contour changes are illustrated by the increasing the size of dots, and the physical value is denoted with a star.

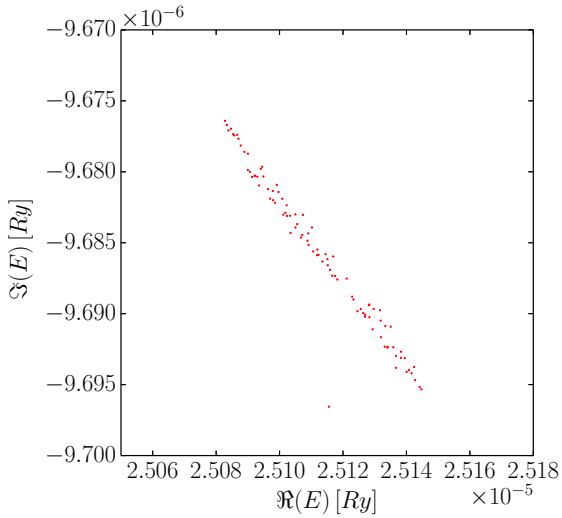

Figure 3.17 – The same as Fig.3.14 for an isolated resonance in the complex-energy plane.

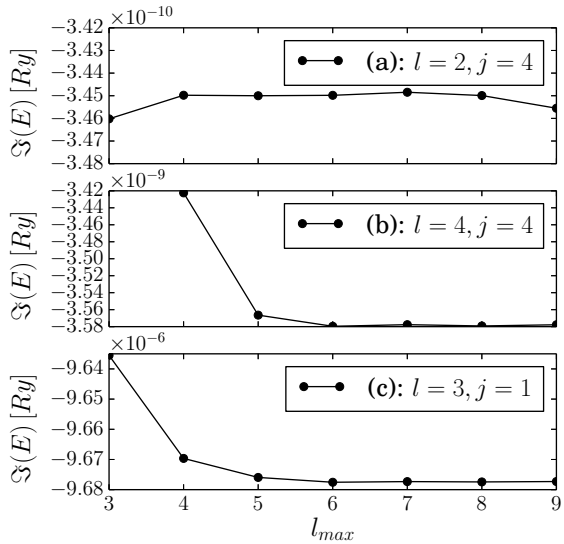

Figure 3.18 – The convergence of an imaginary part of the eigenenergy of $J^\pi = 2^+$ resonances is plotted as a function of $l_{\max}$. Quantum numbers (l_c, j_c) of the dominant channel are given in the inserts.

shown in Fig.3.18 for a fixed shape of $L^+_{l_c,j_c}$ contours. Resonances in Fig.3.18 are those shown before in Figs.3.15 and 3.17. In general, the imaginary part of the resonance energy is significantly more sensitive than the real part to the addition of channels with higher values of l_c and j_c. In Fig.3.18, the imaginary part $\Im(E)$ for resonances with the dominant channels $(l_c = 4, j_c = 4)$ (case (b)) and $(l_c = 3, j_c = 1)$ (case (c)) are converged already for $l_{\max} \geq 6$.

The convergence of the narrow resonance with the dominant channel $(l_c = 2, j_c = 4)$ (case (a)) is less

evident. Moreover, the imaginary part of the eigenenergy in this case is of the order of 10^{-10} Ry, at the limits of a numerical precision of the BEM calculations.

3.6.3 Extraction of the width from the flux conservation

The BEM calculation provides complex eigenenergies of the resonant states by expanding the state in the configuration space. The method is precise and largely independent from variations of both the contours ($L^{+}_{l_c,j_c}$) in the complex k-plane and the model space ($l_{\max}$).

Another way of calculating the resonance width, which will be tested in this section, is based on the flux conservation of particles in space [118, 271]. In this approach, the r-dependent resonance width $\Gamma(r)$ is expressed as (see Appendix A.7):

$$\Gamma(r) = i\frac{\hbar^2}{2\mu}\frac{\sum_c u'^{*}_c(r)u_c(r) - u'_c(r)u^{*}_c(r)}{\sum_{c'}\int_0^r dr' \left|u_{c'}(r')\right|^2} \tag{3.88}$$

This formula is equivalent to the Schrödinger equation but involves a numerically challenging calculation of the second derivative of channel wave functions. The numerical precision can be tested by expressing the Schrödinger equation (3.43) in the CC formalism. Indeed, if the Eq.(3.88) is satisfied then the second derivative of channel wave functions must be equal to:

$$\begin{aligned}\frac{d^2u^J_c(r)}{dr^2} = &\left(\frac{\ell_c(\ell_c+1)}{r^2} + \frac{j_c(j_c+1)}{I} - E_J\right)u^J_c(r) \\ &+ \sum_{c'} V^J_{cc'}(r)u^J_{c'}(r)\end{aligned} \tag{3.89}$$

The right-hand side of this equation is denoted 'potential' in Fig.3.19 and can be compared to the second derivative of channel wave functions obtained in the BEM. This comparison for 1^-_5 state is plotted in Fig.3.19.

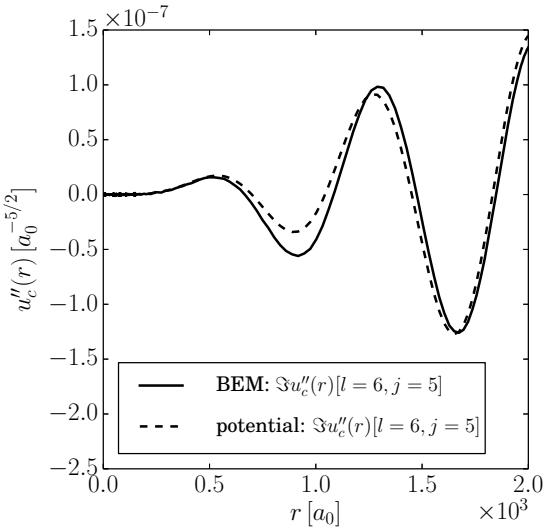

Figure 3.19 – The comparison of the imaginary part of $u''_c(r)$ obtained in BEM (the solid line) and directly by solving the Schrödinger equation (the dashed line). The calculation is done for the 1^-_5 state.

It can be seen that the imaginary part of the second derivative of the channel wave function in these two approaches is different. This discrepancy signifies the lack of precision of $\Gamma(r)$ because the nominator in Eq.(3.88) also writes:

$$u'^*_c(r)u_c(r) - u'_c(r)u^*_c(r) = 2i\Im(u'^*_c(r)u_c(r)) \tag{3.90}$$

and, therefore, it depends mainly on the imaginary part of the channel wave functions. The $\Gamma(r)$ width can also be calculated using the formula:

$$\Gamma_{\text{test}}(r) = \sum_c i\frac{\hbar^2}{2\mu}\frac{u''^*_c(r)u_c(r) - u''_c(r)u^*_c(r)}{\sum_{c'}|u_{c'}(r')|^2} \tag{3.91}$$

which is equivalent to Eq.(3.88). The width $\Gamma_{\text{test}}(r)$ depends also on the second derivative of the channel wave functions but there is no integration in the denominator. As an illustration, the $\Gamma(r)$ and $\Gamma_{\text{test}}(r)$ are plotted in Figs.3.20 and 3.21 for the 0^+_1 bound state in the interval $0 \le r \le 200\ a_0$ and the 1^-_5 resonance in the interval $200 \le r \le 2000\ a_0$, respectively.

The zero width for the 0^+_1 bound state is obtained with both Eqs.(3.88) and (3.91), because the imaginary parts of the channel wave functions are negligible and thus they do not contribute in the calculations.

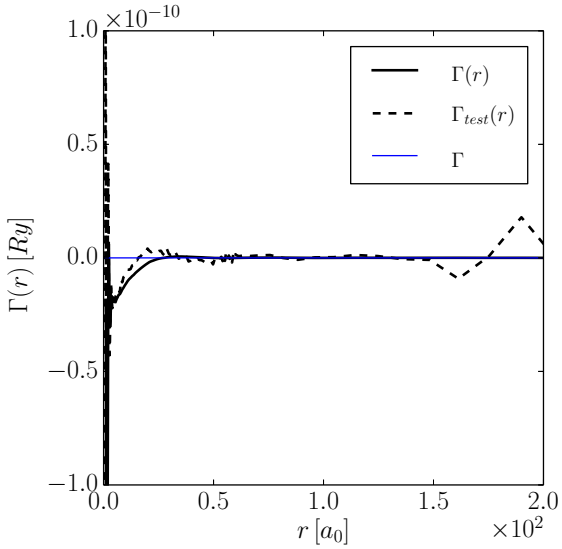

Figure 3.20 – Comparison between the widths ob- tained in BEM and with Eqs. (3.88) and (3.91) for the 0^+_1 bound state.

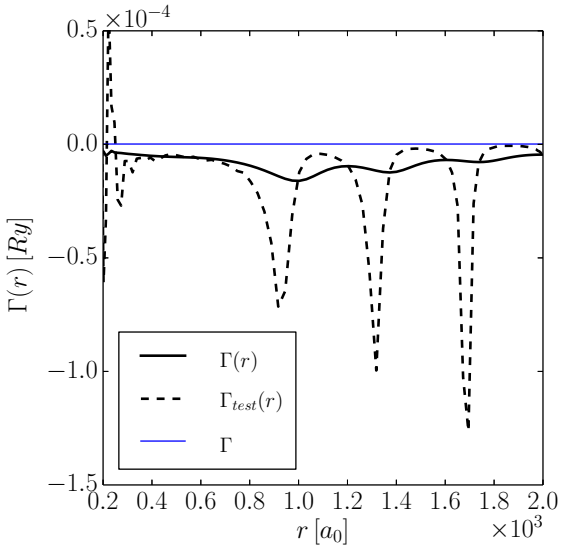

Figure 3.21 – The same as in Fig.3.20 but for the 1^-_5 resonance.

On the contrary, for the 1^-_5 resonance one observes that $\Gamma_{\text{test}}(r)$ is rapidly changing due to numerical imprecisions in the imaginary part of the channel wave functions. Moreover, $\Gamma(r)$ is not constant as one would expected in the precise calculation.

Strong fluctuations in the region $0 \le r \le 200\ a_0$ (see Fig.3.21) are due to the fact that the channel wave functions in the 1^-_5 state are very small (see Fig.3.22) and, hence, the denominator in Eq.(3.88) is also very small. The width $\Gamma(r)$ is thus obtained as the ratio of a positive or negative number and a very small positive number.

The results of calculations of the width using the Eq.(3.88) are summarized in Tab.3.8 for $J^\pi = 0^+$ states. Similar results have been found for other angular momenta $J > 0$. For all states shown in the Tab.3.8, the width $\Gamma(R_{max})$ strongly underestimates the width Γ obtained in the BEM.

Several tests have been done to improve and check the calculation of the second derivative of channel wave functions which is essential for the reliable extraction of the resonance using the flux conservation condition. These include (i) changing the value of the rotation point R for the complex scaling method, (ii) increasing the discretization of the integral in Eq.(3.88), (iii) using the same basis generated by the diagonal part of the potential in the whole interval $0 < r < R_{\text{max}}$. None of these test changed the results. This seems

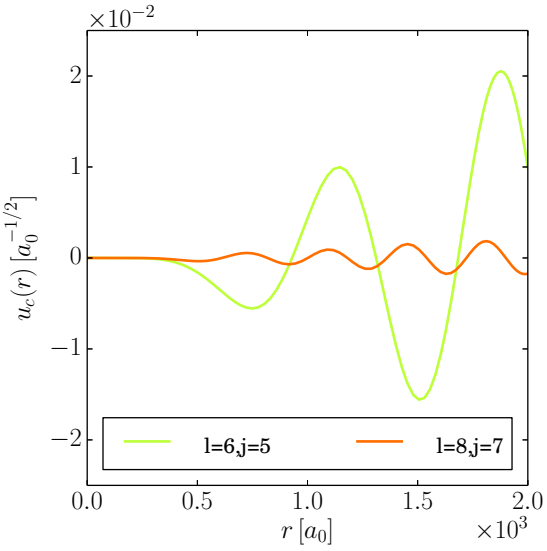

Figure 3.22 – The dominant channel wave functions for the 1_5^- state.

$J^\pi = 0^+$	Γ [Ry]	$\Gamma(R_{max})$ [Ry]
1	0	8.619(-9)
2	7.584(-6)	5.118(-7)
3	1.938(-4)	-1.036(-6)
4	2.484(-5)	-1.531(-5)
5	8.124(-4)	-2.327(-5)
6	3.248(-5)	-1.654(-6)
7	4.378(-4)	-1.861(-5)
8	3.916(-5)	3.826(-6)
9	4.270(-5)	5.102(-6)
10	6.902(-4)	-6.905(-6)
11	1.128(-5)	-1.038(-7)
12	2.202(-5)	2.922(-6)
13	2.838(-4)	2.062(-5)
14	6.524(-5)	1.764(-5)
15	6.936(-4)	7.578(-5)
16	8.902(-5)	1.170(-5)

Table 3.8 – Comparison between the widths obtained in the BEM and using the Eq. (3.88) for $J^\pi = 0^+$. R_{max} which is the maximal r value in the calculations equals 2000 a_0.

to indicate that the problems encountered in the calculation of the second derivative of the channel wave functions have the algorithmic origin. Indeed, the channel wave functions are given by the diagonalization with a relative precision of about $10^{-2} - 10^{-3}$, but at each successive derivative the relative precision drops by about two orders of magnitude. Thus, the first derivative is not always well calculated, and then the numerator in Eq.(3.88) is not correct. This explains why in the case of a bound state, where channel wave functions are real, the formula (3.88) works well. Also the calculation of the norm of the residual vector $\hat{H}\,|\Psi\rangle - E\hat{\mathbb{1}}\,|\Psi\rangle$ gives a result of about 10^{-12}, which indicates that the diagonalization is very precise.

Typically, a state expanded in the configuration space is more precise than its expansion in the coordinate space if a finite number of basis states is used. Indeed, the state resembles a Gaussian centered on a given linear momentum in the configuration space, while it oscillates several times in the coordinate space,

especially when it is a resonance. Consequently, more basis states are needed in the coordinate space than in the configuration space to describe the state up to a given precision. Moreover, no derivative occurs in the configuration representation of the Hamiltonian. This implies that a complex energy of the state calculated in the configuration space can be precise while the energy of the same state expressed in the coordinate space might not be. This precludes the calculation of the resonance width using Eq.(3.88), whereas the imaginary part of the energy calculated by the diagonalization of a Hamiltonian in the configuration space can be extremely precise.

3.6.4 Results

Results of BEM calculations for HCN^- anions are presented in this section. In Sec.3.6.4.1 the first calculated unbound spectrum of a dipolar anion is presented. Then in Sec.3.6.4.2 the intrinsic density of the valence electron is shown in the adiabatic limit. The study of possible rotational bands in the spectrum of HCN^- is done in Sec.3.6.4.3. Finally, properties of resonances are investigated in Sec.3.6.4.4.

3.6.4.1 Spectra

Spectra of HCN^- for $J^\pi = 0^+, 1^-, 2^+, 3^-$ and 4^+ bound states and resonances shown in Tab.3.9, are calculated in BEM with the previously defined parameters. The calculated energy of the 1^- band head: $E(1_1^-) = -8.965 \times 10^{-5}$ Ry is close to the experimental value: $E^{\text{exp}}(1_1^-) = -8.8198377 \times 10^{-5}$ Ry, without any adjustment. Moreover, as in Refs. [263, 269], there is no bound state for $J^\pi = 3^-$.

State	$E(0^+)$ [Ry]	$E(1^-)$ [Ry]	$E(2^+)$ [Ry]	$E(3^-)$ [Ry]	$E(4^+)$ [Ry]
1	-1.148(-4)	-8.965(-5)	-3.692(-5)	3.891(-8) -i 1.059(-8)	2.699(-5) -i 5.547(-9)
2	7.617(-5) -i 3.792(-6)	2.696(-5) -i 9.984(-10)	2.508(-5) -i 9.677(-6)	2.627(-4) -i 1.883(-6)	1.843(-4) -i 2.018(-6)
3	9.349(-4) -i 9.690(-5)	8.118(-5) -i 7.043(-7)	2.695(-4) -i 3.455(-10)	3.034(-4) -i 9.253(-6)	2.249(-4) -i 2.466(-5)
4	1.087(-3) -i 1.242(-5)	1.617(-4) -i 4.772(-10)	2.766(-4) -i 3.578(-9)	4.992(-4) -i 1.281(-6)	3.647(-4) -i 1.404(-6)
5	1.110(-3) -i 4.062(-4)	4.883(-4) -i 7.042(-7)	3.546(-4) -i 7.198(-7)	5.324(-4) -i 1.014(-6)	3.986(-4) -i 1.433(-6)
6	1.141(-3) -i 1.624(-5)	5.001(-4) -i 1.024(-6)	3.668(-4) -i 1.209(-6)	5.692(-4) -i 1.250(-4)	4.227(-4) -i 1.263(-4)
7	1.159(-3) -i 2.189(-4)	5.281(-4) -i 1.651(-6)	3.963(-4) -i 2.337(-6)	8.201(-4) -i 1.170(-5)	6.577(-4) -i 9.778(-7)
8	1.190(-3) -i 1.958(-5)	5.344(-4) -i 3.126(-5)	3.979(-4) -i 5.053(-5)	8.796(-4) -i 2.958(-7)	6.909(-4) -i 3.445(-7)
9	1.270(-3) -i 2.135(-5)	5.708(-4) -i 9.106(-5)	4.250(-4) -i 1.037(-4)	9.394(-4) -i 9.906(-5)	6.920(-4) -i 1.074(-5)
10	1.306(-3) -i 3.451(-4)	6.714(-4) -i 3.306(-4)	6.484(-4) -i 6.720(-6)	1.074(-3) -i 3.548(-4)	7.403(-4) -i 1.012(-4)
11	1.430(-3) -i 5.639(-6)	8.366(-4) -i 6.535(-7)	6.598(-4) -i 8.317(-7)	1.160(-3) -i 1.241(-5)	8.663(-4) -i 3.385(-4)
12	1.845(-3) -i 1.101(-5)	8.480(-4) -i 8.028(-7)	6.812(-4) -i 1.195(-5)	1.304(-3) -i 7.871(-7)	9.754(-4) -i 1.150(-5)
13	3.350(-3) -i 1.419(-4)	8.635(-4) -i 8.455(-6)	6.879(-4) -i 1.596(-6)	1.337(-3) -i 1.087(-7)	1.061(-3) -i 7.835(-7)
14	3.685(-3) -i 3.262(-5)	8.761(-4) -i 9.818(-7)	7.402(-4) -i 6.684(-5)	1.410(-3) -i 7.119(-5)	1.094(-3) -i 1.165(-7)
15	4.233(-3) -i 3.468(-4)	9.337(-4) -i 5.085(-5)	9.803(-4) -i 7.863(-7)	1.559(-3) -i 3.537(-4)	1.160(-3) -i 7.502(-5)
16	4.597(-3) -i 4.451(-5)	1.054(-3) -i 3.134(-4)	1.051(-3) -i 6.224(-7)	1.610(-3) -i 1.412(-5)	1.297(-3) -i 3.369(-4)
17		1.167(-3) -i 7.059(-7)	1.062(-3) -i 8.536(-7)	1.653(-3) -i 7.826(-4)	1.372(-3) -i 1.241(-5)
18		1.297(-3) -i 3.003(-4)	1.071(-3) -i 5.600(-6)	2.169(-3) -i 1.597(-5)	1.675(-3) -i 4.878(-5)
19		1.299(-3) -i 1.411(-6)	1.090(-3) -i 4.892(-7)	2.241(-3) -i 7.848(-4)	1.837(-3) -i 3.415(-4)
20		1.623(-3) -i 5.824(-7)	1.112(-3) -i 1.661(-6)		1.877(-3) -i 1.442(-5)
21		1.784(-3) -i 2.828(-4)	1.141(-3) -i 2.712(-5)		1.937(-3) -i 7.626(-4)
22					2.490(-3) -i 1.638(-5)
23					2.578(-3) -i 7.727(-4)

Table 3.9 – Energies of bound and resonance states $0^+, 1^-, 2^+, 3^-$ and 4^+ of the HCN^- dipolar anion obtained using the BEM. States are sorted by increasing real part of the energy. Numbers in the parentheses denote the powers of 10.

3.6.4.2 The intrinsic density in the adiabatic limit

In Tab.3.10, the band head energies of HCN^- anion are presented for $J^\pi = 0^+, 1^-, 2^+, 3^-, 4^+$ and 5^- in the adiabatic limit $I \to \infty$. As expected, the band head energies for different angular momenta are

degenerate. Figs.3.24 and 3.26 show the intrinsic densities for $J^\pi = 0_1^+$ and 4_1^+ states in the limit $I \to \infty$. These two intrinsic densities are identical even though the associated wave functions in the laboratory system are different (see Figs.3.23 and 3.25). The asymmetry of the intrinsic density comes from the charge asymmetry of the dipole. In all figures of the intrinsic density, the positive charge of the dipole is in the upper part of each figure.

State	E [Ry]
0^+	-1.2308(-4)
1^-	-1.2310(-4)
2^+	-1.2311(-4)
3^-	-1.2323(-4)
4^+	-1.2323(-4)
5^-	-1.2323(-4)

Table 3.10 – Ground state energies for $0^+, 1^-, 2^+, 3^-$, 4^+ and 5^- states of the HCN^- dipolar anion obtained in BEM in the limit $I \to \infty$. The numbers in parentheses denote powers of 10.

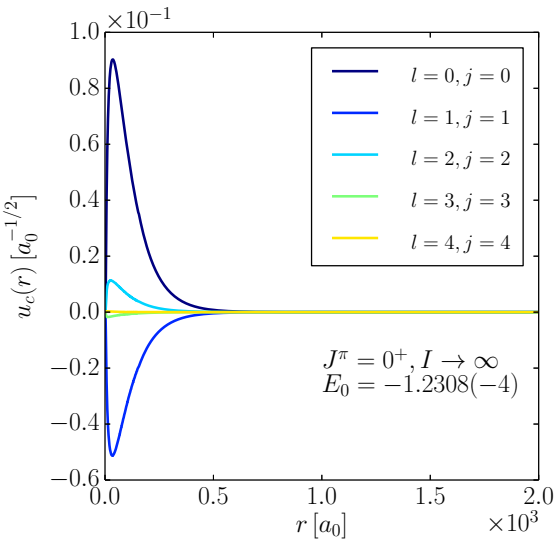

Figure 3.23 – Channel wave functions of the $J^\pi = 0_1^+$ ground state for $I \to \infty$.

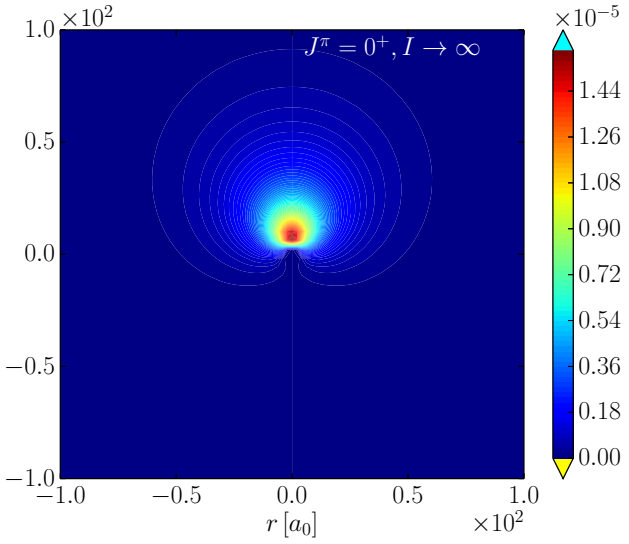

Figure 3.24 – The density of an external electron in the body-fixed frame ($K_J = 0$) for the $J^\pi = 0_1^+$ ground state in the limit $I \to \infty$.

3.6.4.3 Rotational bands

Excitation energies of the few lowest-energy bound and resonance states with different angular momenta are plotted in Fig.3.27 as a function of $J(J+1)$. Bound states $J^\pi = 0^+$, 1^-, 2^+ form a $K_J = 0$ rotational band and have the same intrinsic densities as shown in Figs.3.28, 3.29 and 3.30. The dominant channel wave function in bound states of HCN^- is always associated with the low electron orbital angular momentum ($l_c = 0, 1$). Similar features have been found in Sec.3.5.2 for bound states of $LiCl^-$.

Another $K_J = 0$ rotational band starts with resonances 0_2^+, 1_2^-. Except for $J^\pi = 0^+$ ($K_J = 0$) resonances, most of other resonances are strongly mixed with several equally important K_J-components in the wave function. Consequently, the identification of rotational bands in the continuum is not possible.

One may notice the appearance of energy gaps between the groups of resonances of the same J (see Fig.3.27). These different groups form series in J and suggest a simple classification in terms of the

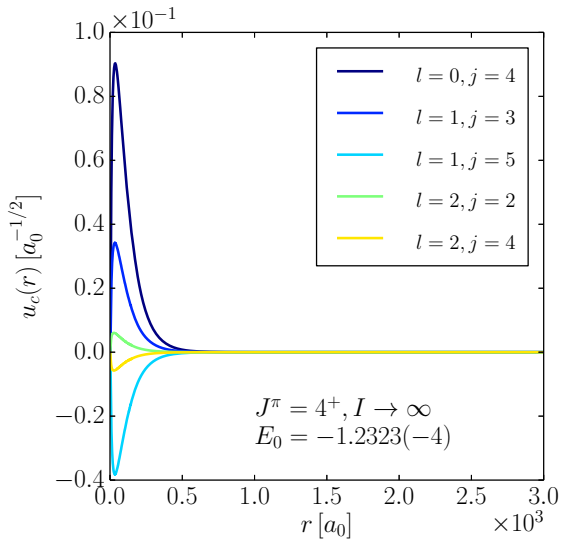

Figure 3.25 – Channel wave functions of the $J^\pi = 4_1^+$ state for $I \to \infty$.

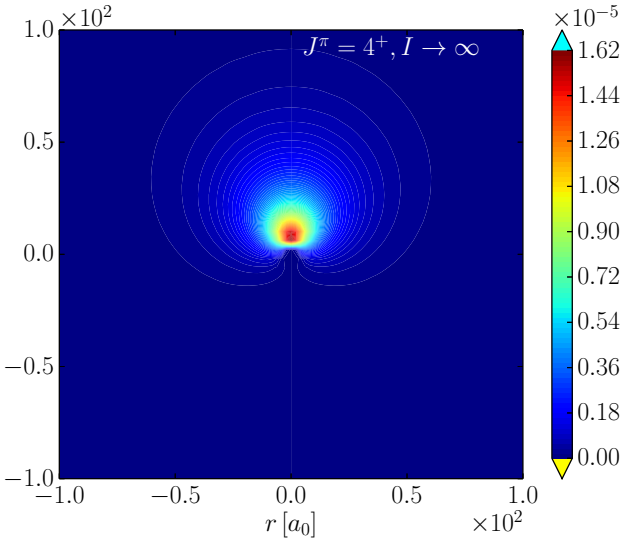

Figure 3.26 – The density of an external electron in the body-fixed frame ($K_J = 0$) for the $J^\pi = 4_1^+$ state in the limit $I \to \infty$. For all other projections ($K_J = 1, 2, 3$), a maximal density is 10^{-15}.

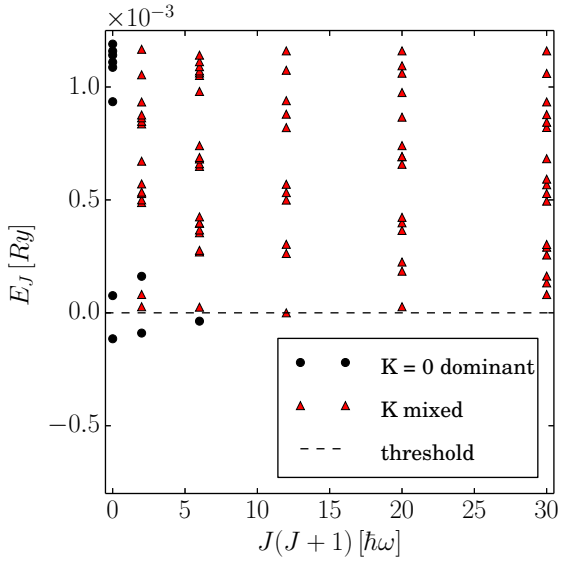

Figure 3.27 – Eigenenergies of the HCN^- dipolar anion for $J^\pi = 0^+$, 1^-, 2^+, 3^-, 4^+ and 5^- are plotted as a function of $J(J+1)$.

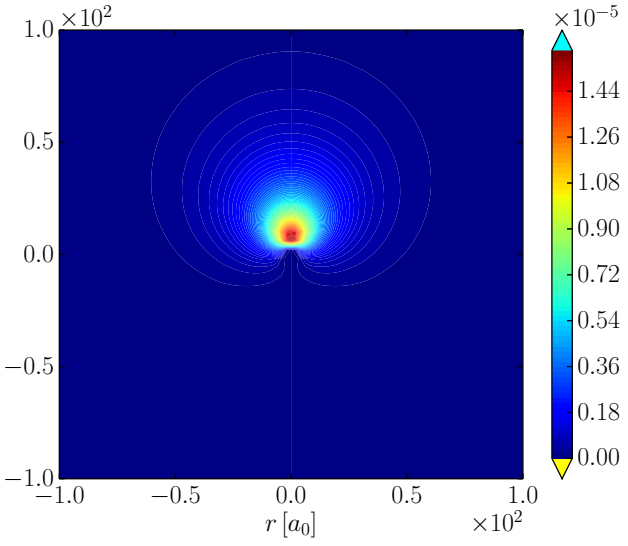

Figure 3.28 – The density of the external electron in the body-fixed frame, for the bound state $J^\pi = 0_1^+$, $K_J = 0$.

dominant channel wave function of each resonance (see the Tab.3.11). In this classification, some series seem to be incomplete e.g. low-l_c series 0, 1, 2, 3, 4. These missing resonances in each series could not be clearly identified in our calculation. Different low-energy series are plotted in Fig.3.31.

The decreasing values of resonance energy E_J with $J(J+1)$ in each series is due to the evolution of the dominant channel. Indeed, for a given series starting at $J = 0$ with a dominant channel (l_c, j_c), next terms of the series with $J = 1, 2, \cdots$ have dominant channels: $(l_c, j_c - 1)$, $(l_c, j_c - 2)$, etc. Thus, their respective energies correspond to dominant channels with decreasing j_c-value with a fixed l_c-value, or in other words to the dipolar molecule rotating slower.

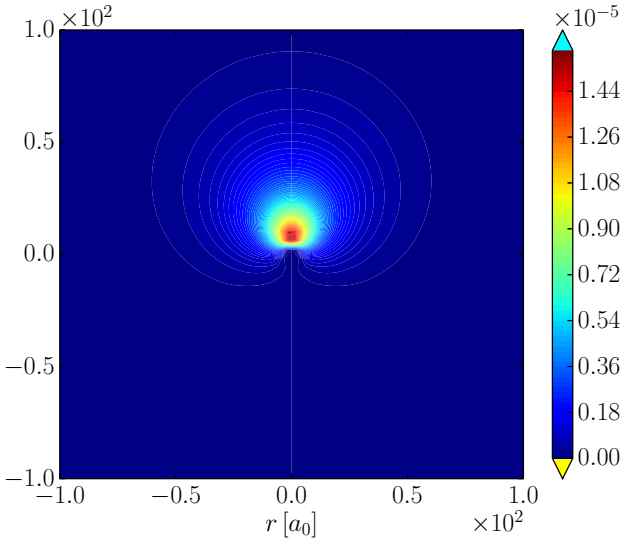

Figure 3.29 – The density of the external electron in the body-fixed frame, for the bound state $J^\pi = 1_1^-$, $K_J = 0$.

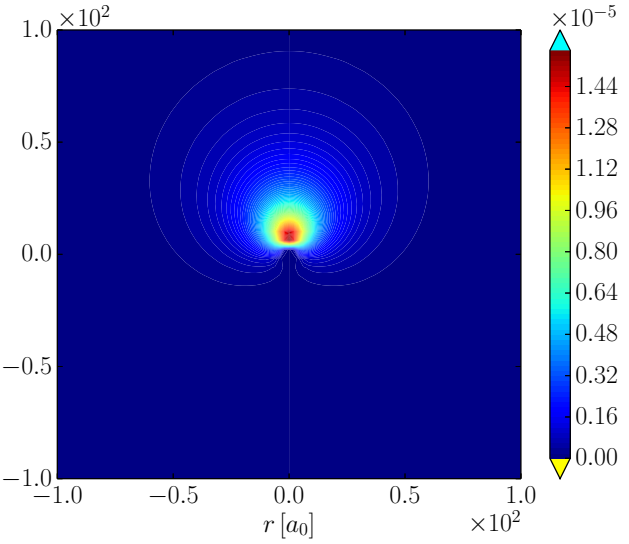

Figure 3.30 – The density of the external electron in the body-fixed frame, for the bound state $J^\pi = 2_1^+$, $K_J = 0$.

Series	Dominant channel (l_c, j_c) [number of states]					
	0^+	1^-	2^+	3^-	4^+	5^-
0	(2,2)[1]	(2,1)[1]				
1		(2,3)[1]				
2			(2,4)[1]			
3		(3,2)[1]	(3,1)[1]	(3,0)[1]		
4					(3,1)[1]	
5						(3,2)[1]
6			(4,4)[1]			
7	(6,6)[9]	(6,5)[6]	(6,4)[5]	(6,3)[2]	(6,2)[2]	(6,1)[2]
8		(6,7)[6]	(6,6)[5]	(6,5)[3]	(6,4)[3]	(6,3)[3]
9			(6,8)[5]	(6,7)[3]	(6,6)[4]	(6,5)[4]
10				(6,9)[4]	(6,8)[4]	(6,7)[4]
11					(6,10)[2]	(6,9)[3]
12						(6,11)[2]
13	(7,7)[1]					
14	(8,8)[3]	(8,7)[2]	(8,6)[2]	(8,5)[1]	(8,4)[1]	(8,3)[1]
15		(8,9)[1]		(8,7)[1]	(8,6)[1]	(8,5)[1]
16				(8,9)[2]	(8,8)[1]	(8,7)[1]
17				(8,11)[2]	(8,10)[2]	(8,9)[2]
18					(8,12)[2]	(8,11)[2]
19						(8,13)[2]
20	(9,9)[1]	(9,8)[1]				
21		(9,10)[1]				

Table 3.11 – The dominant channel of each group of J^π states in each series. The number of states found in each group is given in the square brackets.

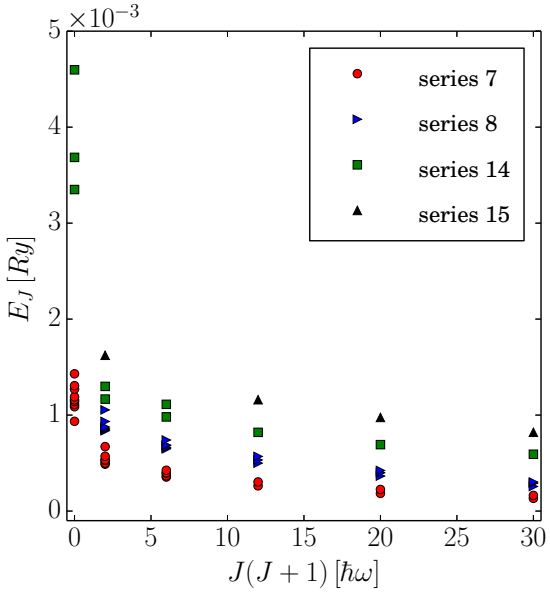

Figure 3.31 – Resonances of the HCN^- dipolar anion for $J^\pi = 0^+$, 1^-, 2^+, 3^-, 4^+ and 5^- are plotted as a function of $J(J+1)$. Colors are related with the series identified in Table 3.11.

3.6.4.4 Spectra in the complex-energy plane and intrinsic density analysis

The states shown in Tab.3.4 are plotted in Figs.3.32 and 3.33. In Fig.3.32, the states are classified according to the total angular momentum J, whereas in Fig.3.33 they are arranged by their localization in the complex-energy plane. Five groups of states in the complex-energy plane can be seen in Fig.3.33: the groups 0 and 1, which are well separated from other groups, and the groups 2, 3 and 4, which have a small overlap between them. The groups 2, 3 and 4 contain isolated resonances close to the dissociation threshold of the dipolar anion. The groups 0 and 1, at higher energies, contain the overlapping resonances of different angular momenta. These different groups in the complex-energy plane correspond to the localization in the decay width and *not* in the excitation energy.

Some observations concerning the resonances in these groups can be summarized:

- The first analysis consists of looking at the resonances with the same total angular momentum in a given group. In the group 3, such a set of resonances is formed by $J^\pi = 3_3^-$, 3_7^-, 3_{11}^-, 3_{16}^- and 3_{18}^- states having a single dominant channel. Their eigenenergy, the dominant channel wave function and its real part of the norm are shown in Tab.3.12.

State	E [Ry]	(l_c, j_c)	Norm
3_3^-	3.034(-4) - i 9.253(-6)	(6,3)	1.322
3_7^-	8.201(-4) - i 1.170(-5)	(8,5)/(6,3)	1.236/0.059
3_{11}^-	1.160(-3) - i 1.241(-5)	(8,7)/(6,5)	1.249/0.047
3_{16}^-	1.610(-3) - i 1.412(-5)	(8,9)/(6,7)	1.242/0.041
3_{18}^-	2.169(-3) - i 1.597(-5)	(8,11)/(6,9)	1.244/0.037

Table 3.12 – The eigenenergies, the dominant channel wave functions and their norm for a series of states $J^\pi = 3_3^-$, 3_7^-, 3_{11}^-, 3_{16}^- and 3_{18}^- in the group 3 of resonances in the complex-energy plane.

  Except for the 3_3^- state, the orbital angular momentum l_c of the dominant channel remains constant ($l_c = 8$) while the rotor angular momentum j_c varies. Also, except for the 3_3^- state, the second most important channel is almost negligible as compared to the dominant channel, and it has a

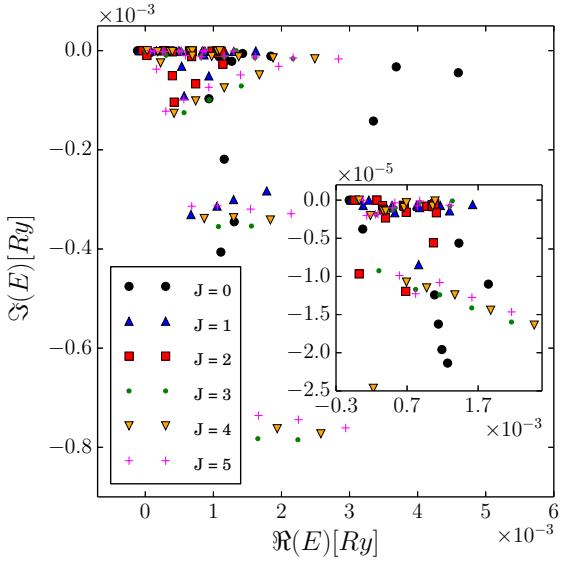

Figure 3.32 – Spectra of the HCN^- dipolar anion for different $J^\pi = 0^+, 1^-, 2^+, 3^-, 4^+$ and 5^- in the complex-energy plane.

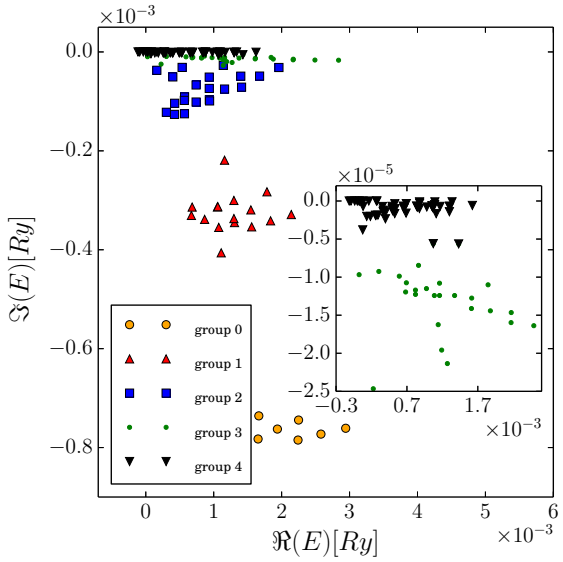

Figure 3.33 – The same as in Fig.3.32, different groups of states are shown with different colors.

constant orbital momentum ($l_c = 6$), while the angular momentum j_c varies. There is no dominant K_J projection in all these cases and, except for the first state, their intrinsic densities show a similar pattern for each K_J projection as shown in Figs.3.34, 3.35, 3.36 and 3.37.

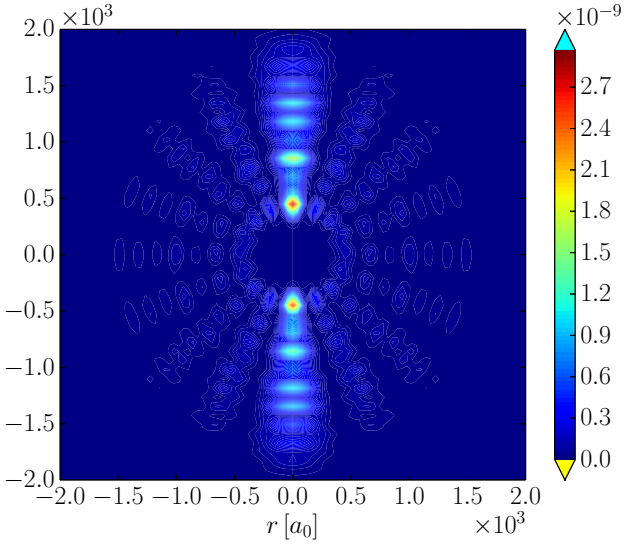

Figure 3.34 – The density of the external electron in the body-fixed frame for the $K_J = 0$ component of the resonance $E(3_3^-)$.

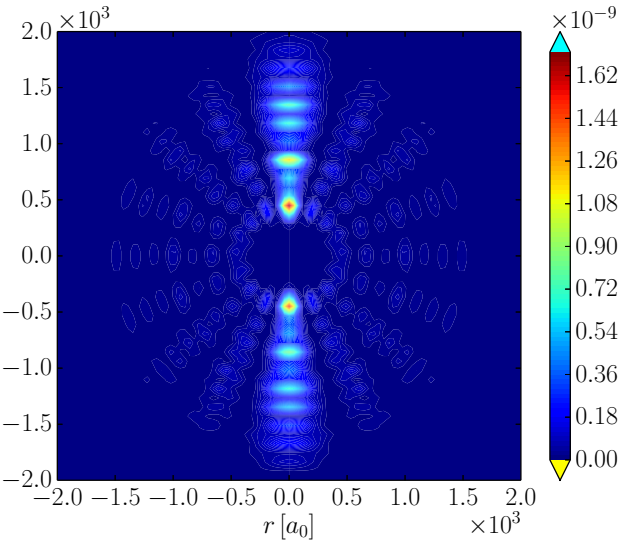

Figure 3.35 – The density of the external electron in the body-fixed frame for the $K_J = 0$ component of the resonance $E(3_7^-)$.

- The second analysis concentrates on a series of resonances with the same total angular momentum J in different groups in the complex-energy plane. Such a set of resonances with $J^\pi = 3^-$ is formed by $J^\pi = 3_3^-$ (group 3), 3_6^- (group 2), 3_{15}^- (group 1) and 3_{17}^- (group 0) states. Except for the first state ($J^\pi = 3_3^-$), they all have two dominant channel wave functions with weights equal to about 60% and 40%, as it is shown in Tab.3.13.

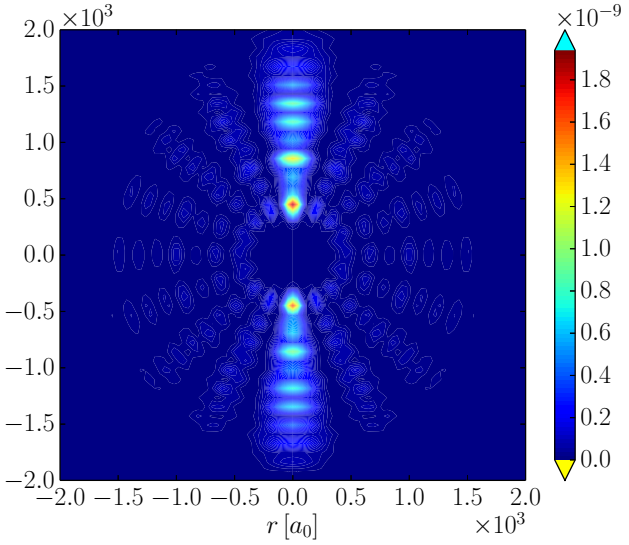

Figure 3.36 – The density of the external electron in the body-fixed frame for the $K_J = 0$ component of the resonance $E(3^-_{16})$.

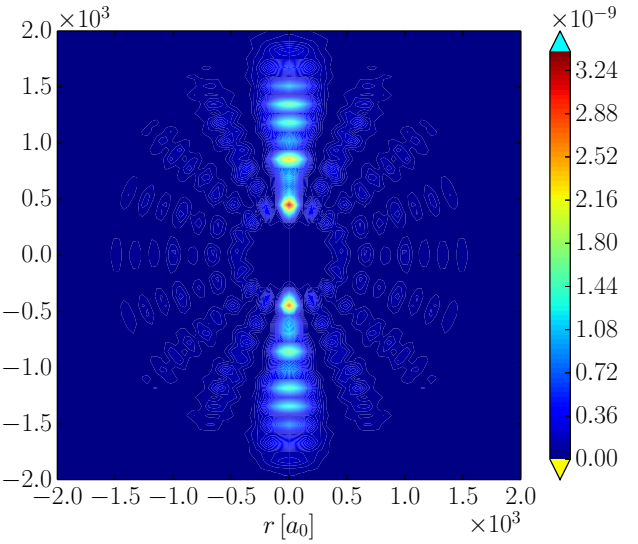

Figure 3.37 – The density of the external electron in the body-fixed frame for the $K_J = 0$ component of the resonance $E(3^-_{18})$.

State	E [Ry]	(l_c, j_c)	Norm
3^-_3	3.034(-4) - i 9.253(-6)	(6,3)	1.322
3^-_6	5.692(-4) -i 1.250(-4)	(6,5)/(7,6)	0.604/0.396
3^-_{15}	1.559(-3) -i 3.537(-4)	(6,9)/(7,10)	0.681/0.372
3^-_{17}	1.653(-3) -i 7.826(-4)	(8,9)/(9,10)	0.618/0.423

Table 3.13 – The eigenenergies, the dominant channel wave functions and their norm for the series of states $J^\pi = 3^-_3$, 3^-_6, 3^-_{15} and 3^-_{17} which belong to different groups of resonances in the complex-energy plane.

The dominant channels with a weight of about 60% for 3^-_6 and 3^-_{15} states, are related to the dominant channel of the 3^-_3 state because they have the same orbital momentum value ($l_c = 6$) and only the rotor angular momentum changes ($j_c = 3, 5, 9$). This fact is corroborated by the similarity of their intrinsic densities. The intrinsic densities for these three states are essentially different from the density for the 3^-_{17} state which is dominated by the channels with $l_c = 8, 9$ as shown in Figs.3.38, 3.39, 3.40 and 3.41. Again, there is no dominant K_J projection in all four cases.

- The third analysis consists of investigating a set of resonances with different total angular momenta in the same group in the complex-energy plane. This set of states in the group 2 is: $J^\pi = 0^+_3$, 1^-_{15}, 2^+_{14}, 3^-_9, 4^+_{10} and 5^-_{15}. They have one or two dominant channel wave functions, and the main dominant channel is almost the same for all states, as it is shown in Tab.3.14.

  Except for the 0^+_3 state, there is no dominant K_J component in all other states and the intrinsic densities have a similar pattern for all K_J projections as shown in Figs.3.42, 3.43, 3.44, 3.45, 3.46 and 3.47.

From this analysis, it appears that:

- Resonances in the same group and with a fixed J-value have dominant channels with the same orbital angular momentum l_c but different j_c. This observation suggests that these states are related to rotational bands of the dipolar core.

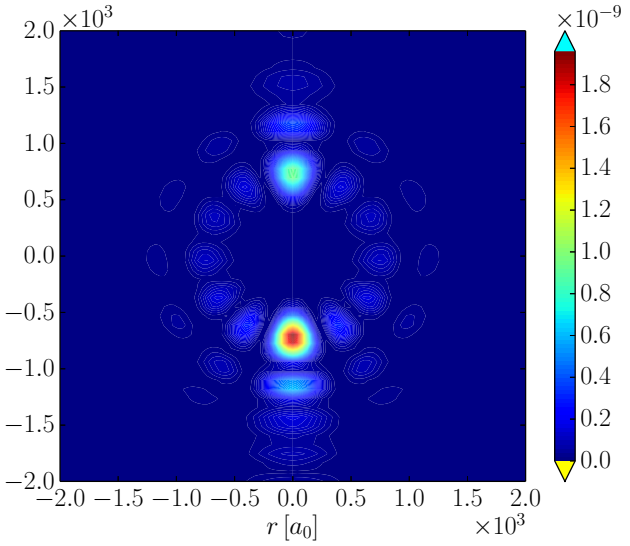

Figure 3.38 – The density of the external electron in the body-fixed frame for the $K_J = 0$ component of the resonance $E(3_3^-)$ (group 3).

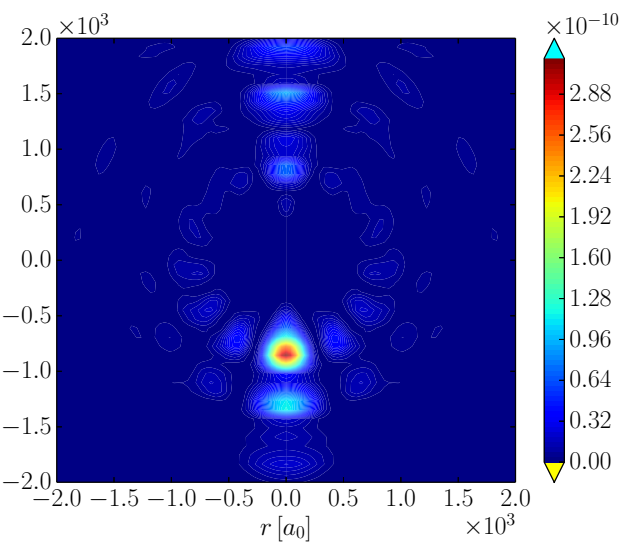

Figure 3.39 – The density of the external electron in the body-fixed frame for the $K_J = 0$ component of the resonance $E(3_6^-)$ (group 2).

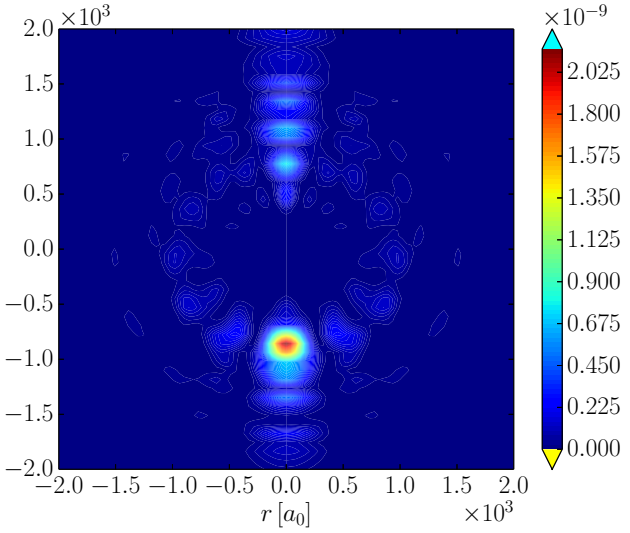

Figure 3.40 – The density of the external electron in the body-fixed frame for the $K_J = 0$ component of the resonance $E(3_{15}^-)$ (group 1).

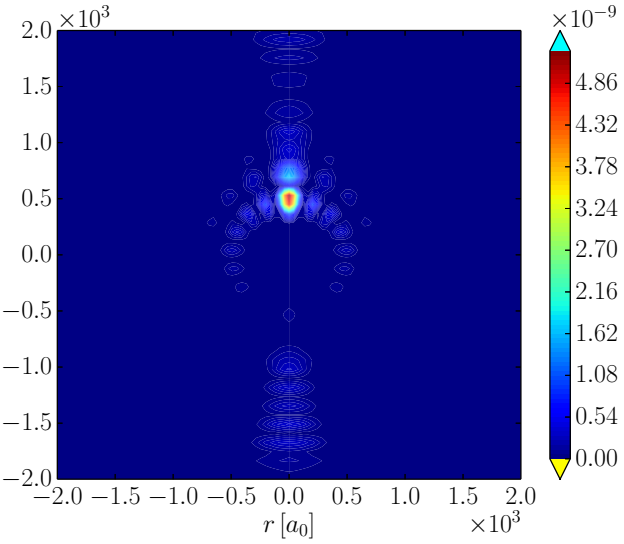

Figure 3.41 – The density of the external electron in the body-fixed frame for the $K_J = 0$ component of the resonance $E(3_{17}^-)$ (group 0).

- Resonances in different groups and with a fixed J-value do not present a regularity in their dominant channels.
- Resonances in the same group and with different J-values have almost the same dominant channels.

The classification of resonances by their dominant channels can be used further to generalize the previous analysis. This is done in Tab.3.15, where indices of groups are denoted in the brakets. Different colors are associated with different groups in Fig.3.33.

The groups 0 and 3 are mainly associated with dominant channels with $l_c = 8$, while it is $l_c = 6$ for the groups 1, 2 and 4. Because of the overlap between several groups, some states may not follow this simple observation.

State	E [Ry]	(l_c, j_c)	Norm
0^+_3	9.349(-4) - i 9.690(-5)	(6,6)	1.079
1^-_{15}	9.337(-4) - i 5.085(-5)	(6,7)	1.041
2^+_{14}	7.402(-4) - i 6.684(-5)	(6,6)/(7,7)	0.799/0.196
3^-_9	9.394(-4) - i 9.906(-5)	(6,7)/(7,8)	0.719/0.282
4^+_{10}	7.403(-4) - i 1.012(-4)	(6,6)/(7,7)	0.676/0.325
5^-_{15}	9.340(-4) - i 7.377(-5)	(6,7)/(7,8)	0.856/0.148

Table 3.14 – The eigenenergies, the dominant channel wave functions and their norm for the series of states $J^\pi = 0^+_3$, 1^-_{15}, 2^+_{14}, 3^-_9, 4^+_{10} and 5^-_{15} which are in the same group of resonances in the complex-energy plane.

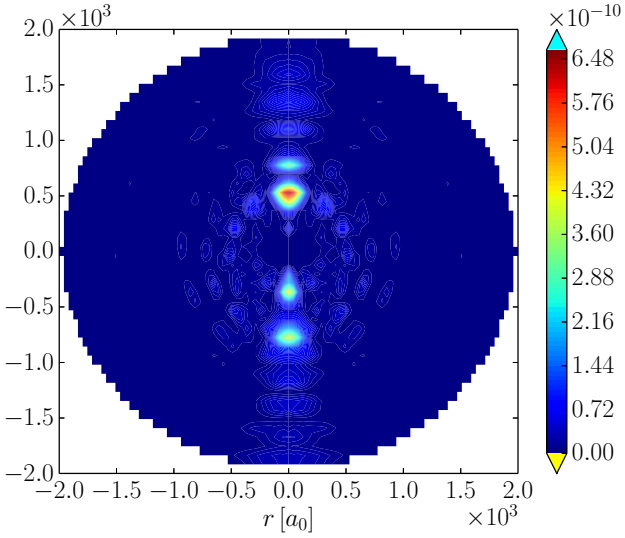

Figure 3.42 – The density of the external electron in the body-fixed frame for the $K_J = 0$ component of the resonance $E(0^+_3)$.

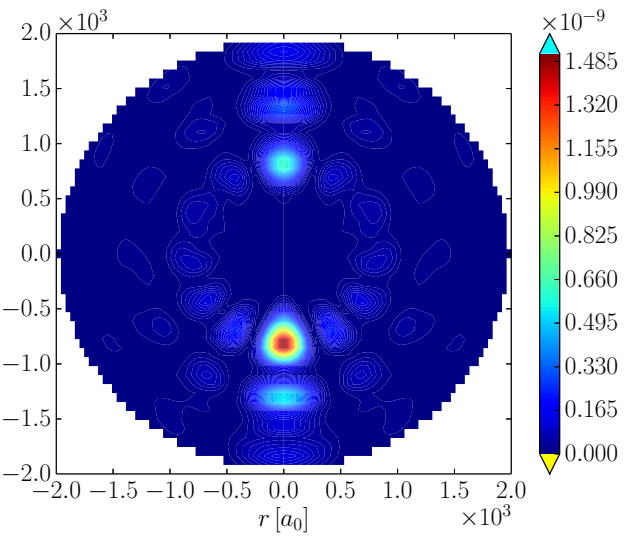

Figure 3.43 – The density of the external electron in the body-fixed frame for the $K_J = 0$ component of the resonance $E(1^-_{15})$.

States with a given J-value in the same group are all localized in columns in Tab.3.15. The dominant channels of these states are given by: (l_c, j_c), $(l_c, j_c + 2)$, $(l_c, j_c + 4)$, ... Consequently, these states differ only by the rotational motion of the dipole core, and thus correspond to the coupling of the orbital motion of the valence electron with the rotational motion of the molecule. Such groups of states with a complete rotational band in j_c are for example the $J^\pi = 5^-_3$, 5^-_6, 5^-_9, 5^-_{15}, 5^-_{19} and 5^-_{23} states in the group 2, which have dominant channels with $l_c = 6$ and $j_c = 1$, 3, 5, 7, 9 and 11 respectively. In this case, the band head of the rotational band of the dipole core has $j_c = 1$.

Finally, the classification of states by their dominant channels is sumarized in Tab.3.16. In rows on finds the series of states shown in Fig.3.31, whereas in columns there are groups of states with a fixed total angular momentum (see Fig.3.33).

The study of states with different total angular momenta J in the same group but can also be generalized. The example of group 1 in Fig.3.33 is examined in Tab.3.17. The dominant channels are denoted (l_c, j_c), the second most important channels are denoted (l_c, j_c)*, etc. Because there are no states with $J^\pi = 2^+$ in this group, the expected channels are denoted "(l_c, j_c)?".

All states of group 1 presented in Tab.3.17 have the dominant channel with $l_c = 6$, the second most important channel with $l_c = 7$ (or also $l_c = 8$ for $J^\pi = 1^-$ states) and the third most important with $l_c = 9$.

The study of the second most important channel also gives an information about the position of groups in the complex-energy plane. In groups 1, 2 and 4, the resonances have the dominant channels with $l_c = 6$,

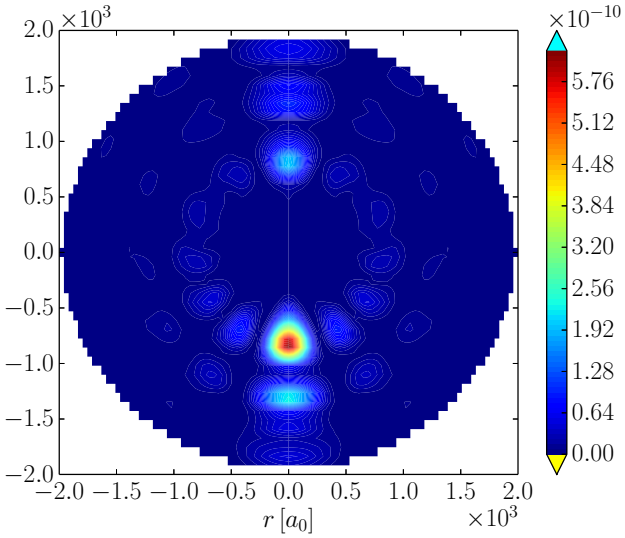

Figure 3.44 – The density of the external electron in the body-fixed frame for the $K_J = 0$ component of the resonance $E(2^+_{14})$.

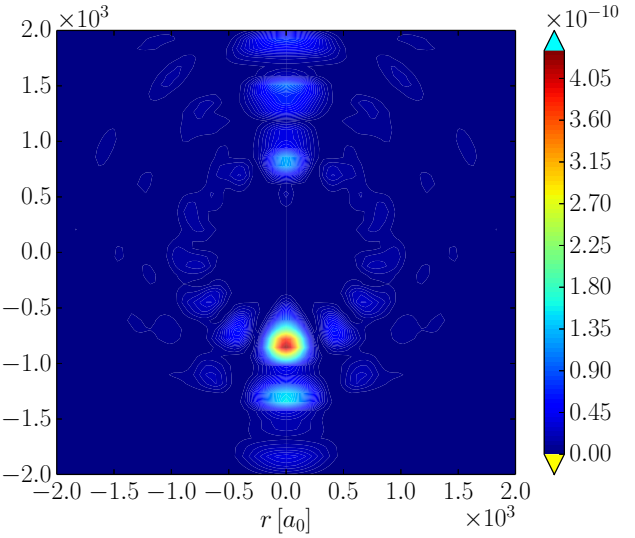

Figure 3.45 – The density of the external electron in the body-fixed frame for the $K_J = 0$ component of the resonance $E(3^-_9)$.

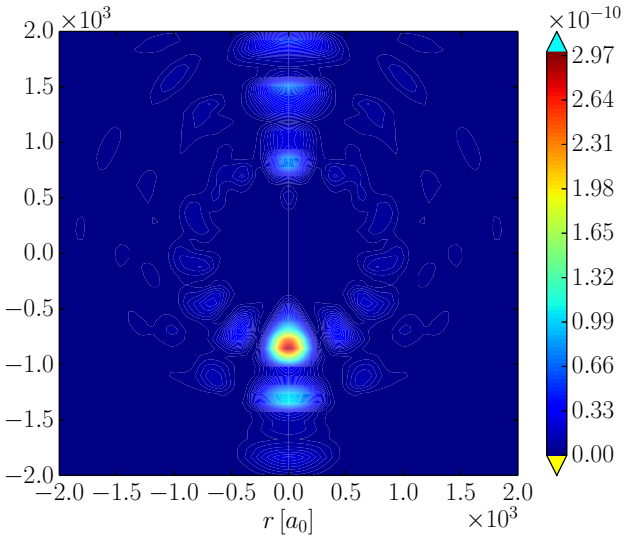

Figure 3.46 – The density of the external electron in the body-fixed frame for the $K_J = 0$ component of the resonance $E(4^+_{10})$.

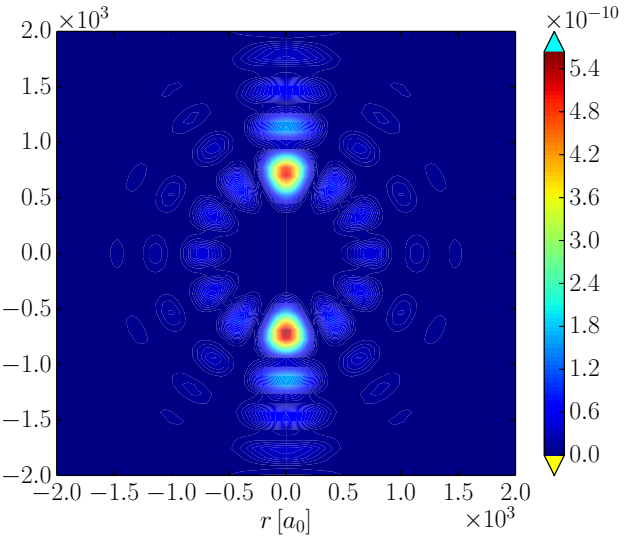

Figure 3.47 – The density of the external electron in the body-fixed frame for the $K_J = 0$ component of the resonance $E(5^-_{15})$.

and second most important channels with $l_c = 7$, while it is $l_c = 8$ for the dominant channels in groups 0 and 3, and $l_c = 9$ or 6 for the second most important channels.

The relative importance of these channels can be quantified by the norm of the channel wave functions in (Eq.(3.87)). The sum of the norms of channel wave functions must be equal one and, in general, there are two or three important contributions. In Tab.3.18, the mean value of the norm of the dominant and the second most important channel wave functions are presented for each group.

In conclusion, all resonances in each group have a dominant channel wave function with a fixed value of the electron orbital angular momentum l_c. On the other hand, several groups can have the same dominant electron orbital angular momentum. In each group, several subgroups corresponding to a rotational band of the dipole core (columns with a fixed orbital angular momentum in Tab.3.15) can be defined. The precise

Series	Dominant channel (l_c, j_c) and group index					
	0^+	1^-	2^+	3^-	4^+	5^-
	(0,0)[4]					
		(0,1)[4]				
			(0,2)[4]			
0	(2,2)[4]	(2,1)[4]	(2,0)			
1		(2,3)[4]	(2,2)	(2,1)		
2			(2,4)[4]	(2,3)	(2,2)	
3	(3,3)	(3,2)[4]	(3,1)[3,4]	(3,0)[4]		
4		(3,4)	(3,3)	(3,2)	(3,1)[4]	
5			(3,5)	(3,4)	(3,3)	(3,2)[4]
6		(4,5)	(4,4)[4]	(4,3)	(4,2)	(4,1)
7	(6,6)[1,2,3,4]	(6,5)[1,2,4]	(6,4)[2,4]	(6,3)[3,4]	(6,2)[3,4]	(6,1)[2,4]
8		(6,7)[1,2,3,4]	(6,6)[2,3,4]	(6,5)[2,4]	(6,4)[2,4]	(6,3)[2,4]
9			(6,8)[2,3,4]	(6,7)[1,2,4]	(6,6)[1,2,4]	(6,5)[1,2,4]
10				(6,9)[1,2,4]	(6,8)[1,2,4]	(6,7)[1,2,4]
11					(6,10)[1,2]	(6,9)[1,2,4]
12						(6,11)[1,2]
13	(7,7)[3]	(7,6)	(7,5)	(7,4)	(7,3)	(7,2)
14	(8,8)	(8,7)[4]	(8,6)[4]	(8,5)[3]	(8,4)[3]	(8,3)[3]
15		(8,9)[4]	(8,8)	(8,7)[3]	(8,6)[3]	(8,5)[3]
16			(8,10)	(8,9)[0,3]	(8,8)[3]	(8,7)[3]
17				(8,11)[0,3]	(8,10)[0,3]	(8,9)[0,3]
18					(8,12)[0,3]	(8,11)[0,3]
19						(8,13)[0,3]
20	(9,9)	(9,8)[1]	(9,7)	(9,6)	(9,5)	(9,4)
21		(9,10)[1]	(9,9)	(9,8)	(9,7)	(9,6)

Table 3.15 – The dominant channel of each group of J^π states in each series (see Tab.3.11). The indices of the groups of resonances in the complex-energy plane are given in the square brackets.

Series	Dominant channel (l_c, j_c)					
	$J = 0$	$J = 1$	$\cdots$	$J = l_c$	$J = l_c + 1$	$J = l_c + 2$
A	$(l_c, j_c = l_c)$	$(l_c, j_c = l_c - 1)$	$\ldots$	$(l_c, j_c = 0)$	–	–
B	–	$(l_c, j_c = l_c + 1)$	$\ldots$	$(l_c, j_c = 2)$	$(l_c, j_c = 1)$	–
C	–	–	$\ldots$	$(l_c, j_c = 4)$	$(l_c, j_c = 3)$	$(l_c, j_c = 2)$
D	⋮	⋮	⋮	⋮	⋮	⋮
E	–	–	–	$(l_c, j_c = l_c + J)$	$(l_c, j_c = l_c + J - 1)$	$(l_c, j_c = l_c + J - 2)$
F	–	–	–	–	$(l_c, j_c = l_c + J + 1)$	$(l_c, j_c = l_c + J)$
G	–	–	–	–	–	$(l_c, j_c = l_c + J + 2)$
H	–	–	–	–	–	–

Table 3.16 – Classification of states by their dominant channels. Rows correspond to series of states (bands) in Fig.3.31, and columns to groups of states with a fixed total angular momentum shown in Fig.3.33.

relation between the structure of dominant channels and the position of each group in the complex-energy plane has not been elucidated.

Series	Dominant channel (l_c, j_c)					
	0^+	1^-	2^+	3^-	4^+	5^-
7	(6,6)	(6,5)	(6,4)?			
8		(6,7)	(6,6)?			
9			(6,8)?	(6,7)	(6,6)	(6,5)
10				(6,9)	(6,8)	(6,7)
11					(6,10)	(6,9)
12						(6,11)
13	(7,7)*	(7,6)*	(7,5)?			
		(7,8)*	(7,7)?			
			(7,9)?	(7,8)*	(7,7)*	(7,6)*
				(7,10)*	(7,9)*	(7,8)*
					(7,11)*	(7,10)*
						(7,12)*
14		(8,7)*	(8,6)?			
15		(8,9)*	(8,8)?			
16			(8,10)?			
17						
18						
19						
20	(9,9)**	(9,8)	(9,7)?			
21		(9,10)	(9,9)?			(9,6)**
			(9,11)?	(9,10)**	(9,9)**	(9,8)***
				(9,12)**	(9,11)**	(9,10)**
					(9,13)**	(9,12)**
						(9,14)**

Table 3.17 – Dominant channels of resonances in the group 1. Stars denote the second, third, etc. dominant channels. No states with $J^\pi = 2^+$ could be identified in this group. Thus, possible channels in this case are denoted "?". See Tab.3.11 for indices of series.

Group	l_c of the dominant channels			
	6	7	8	9
0	–	–	60%	40%
3	1%	–	99%	–
1	70%	30%	–	–
2	90%	10%	–	–
4	100%	–	–	–

Table 3.18 – Contributions of the two most important channel wave functions to the norm of resonances in different groups of states (see Fig.3.33). Only states with dominant channel $l_c = 6$ for groups 1, 2 and 4, and $l_c = 8$ for groups 0 and 3 are included.

Conclusion

In the present work, unbound states of dipolar anions and proton/neutron radiative capture reactions on weakly bound nuclei have been studied in the framework of the GSM. The first objective was approached using a one-body GSM, the so-called Berggren ensemble method, to investigate spectra of dipolar anions. The second objective was to develop the GSM-CC approach for the description of one-nucleon radiative capture reactions and apply for few reactions of the astrophysical interest.

The theoretical description of the spectroscopy of dipolar anions is a challenging problem due to the long-range dipole potential, for which the asymptotic solutions are not known analytically. The application of GSM (BEM) for the description of bound and unbound spectra of dipolar anions gives promising results. For bound states of dipolar anions, the convergence of calculated binding energies and mean square radii has been significantly improved using the BEM. Contrary to the standard DIM, the asymptotic solutions of a dipolar potential, and couplings between channels at long distances are treated exactly in BEM. Hence, BEM is ideally suited for the description of very weakly bound states of dipolar anions. Moreover, in practical applications the full spectrum of a dipolar anion can be obtained in the BEM for the same computational effort as for one state in the DIM. High numerical precision of BEM allows to calculate energies of excited bound states sufficiently precisely to investigate the properties (radii) of dipolar anions in extreme conditions of binding energy. It was shown that dipolar anions form a fascinating family of extreme two-body halo systems.

The description of unbound spectra of HCN^- in BEM allowed to disclose a rich spectrum of resonances of this anion. These resonances form groups in the complex-energy plane with a similar electron decay width. Within the group, dominant channels in the resonance wave functions are all associated with the same orbital angular momentum l_c of the external electron. In each group, one can identify different subgroups of resonances which are characterized by the same total angular momentum J of the anion but different rotational angular momenta j_c of the neutral dipolar molecule. The study of the intrinsic density of the external electron provides a tool to compare states and determine their parentage. In this way, the $K_J = 0$ rotational band could be identified in weakly bound states of HCN^-. Above the dissociation threshold, one can also find regular series of resonances which are decreasing in energy with increasing J. The dominant channel in these resonances corresponds to a fixed orbital angular momentum of the electron l_c and decreasing angular momentum j_c of the dipolar core. In general, the resonances are strongly mixed in K_J and, consequently, rotational bands could not be identified unambiguously. The dissociation threshold appears as a frontier between two distinct regimes of coupling between the dipolar molecule and the external electron. Below the threshold, all states correspond to an electron in low orbital angular momentum state coupled to the rotating dipole to yield the rotational band in the total angular momentum of the anion. Above the threshold, anion rotational bands are replaced by down-sloping series of states with a fixed electron orbital angular momentum and a decreasing angular momentum of a dipole. On the other hand, the resonances of the same value of the electron orbital angular momentum form groups in the complex-energy plane of a similar decay width.

The GSM-CC formulation of the neutron and proton radiative capture reactions have been developed in this work. In GSM-CC, reactions are described in a microscopic framework with an exact treatment of the antisymmetry. The continuum of the target nucleus is described exactly, while the continuum of a combined system of target and projectile includes only the resonant continuum. Comparing the GSM-CC

results for resonant states with those of the GSM, one can see if configuration mixing in both descriptions are equivalent and, thus, if additional channels are required in GSM-CC calculation. With this condition, the GSM-CC becomes a unified approach for nuclear structure and reactions where the approximation concerning chosen channels can be verified and improve systematically.

The GSM-CC approach has been applied to the description of the $^{17}\mathrm{F}(p,\gamma)^{18}\mathrm{Ne}$, $^{7}\mathrm{B}(p,\gamma)^{8}\mathrm{B}$ and $^{7}\mathrm{Li}(n,\gamma)^{8}\mathrm{Li}$ reactions. Calculations of the proton/neutron radiative capture cross sections have been performed using schematic interactions, which are not sufficient to reproduce the experimental spectra. The description of proton and neutron radiative capture reactions requires a high precision value for the proton/neutron separation energies and, thus, the GSM-CC spectra of the composite systems ^{18}Ne, ^{8}B and ^{8}Li and the corresponding one-proton or one-neutron separation energies have been adjusted by a slight modification of CC potentials. Consequently, the effect of missing resonant and non-resonant channels has been hidden in the value of the effective CC coupling potentials. In the considered examples of $^{7}\mathrm{Be}(p,\gamma)^{8}\mathrm{B}$ and $^{7}\mathrm{Li}(n,\gamma)^{8}\mathrm{Li}$ reactions, the adjusted CC potentials differ from the original ones by less than 5%.

A good overall agreement with experimental data has been obtained for the proton and neutron radiative cross sections. In these first applications of the GSM-CC approach only the ground state of the target has been included in calculations. It has been shown that the antisymmetrization of the matrix elements of the electromagnetic operators does not play a significant role in most cases, in particular at low energies. The validity of the long wavelength approximation at low energies has been checked in $^{7}\mathrm{Be}(p,\gamma)^{8}\mathrm{B}$ and $^{7}\mathrm{Li}(n,\gamma)^{8}\mathrm{Li}$ reactions.

Future developments in atomic physics concern the application of BEM to the description of linear electric quadrupolar anions, which have a potential proportional to $-1/r^3$, and whose bound states properties are described in Refs. [256,257]. These anions are expected to be easier to treat since the pseudo-potential in this case is not long-range. Also, due to the two possible configurations $q(-2q)q$ and $(-q)2q(-q)$, interesting collective effects are expected.

The BEM can be also easily extended to describe elastic and inelastic scattering of an electron on a neutral dipolar or quadrupolar molecule. In the multi-electron molecular systems, the GSM can be applied for the description of the spectroscopy of weakly bound and unbound molecules. Future progress in theoretical studies of these exotic anions and multi-electron molecules could be investigated by experimental spectroscopic studies and the corresponding electron scattering reactions.

Future developments of the GSM-CC approach concern the inclusion of non-resonant channels build from the scattering states of the target nucleus. In principle, this final step in the construction of the GSM-CC should improve the description of reactions involving weakly bound targets as for example in the $^{6}\mathrm{He}(p,p')$ reaction. With this extension, nuclear structure and low energy reactions can be described with the same Hamiltonian in a unified formalism.

Description of transfer reactions in GSM-CC as, for example, (d,p) and (d,n) reactions, will be the next step. In this problem, the projectile and the target nuclei will be described in the GSM, with an exact treatment of the antisymmetry between the target and the projectile. For now, GSM calculations are done using schematic two-body interactions to show the applicability of this approach. As a possible future development, one could apply the *ab initio* NCGSM in the CC formulation for the description of (p,p'), (n,n'), (p,γ) and (n,γ) reactions in light nuclei with chiral interactions. Further possibility would be to use interactions derived from the EFT, adapted to the GSM/GSM-CC approaches which use an inert core.

In nuclear physics, the reconciliation of the description of nuclear structure and reactions, first attempted by Feshbach [21–23], Mahaux and Weidenmüller [24], motivated the development of generic tools for the description of MBOQSs. Nowadays, new phenomena observed in exotic nuclei close to the drip lines, such as neutron-skin and proton/neutron halo nuclei, the spontaneous two-proton radioactivity and the clustering effect can be described in a unified framework. Approaches dedicated to the description of nuclear MBOQS can improve theoretical prediction of cross sections at astrophysical energies, where the influence of the scattering environment cannot be neglected. Methods developed in nuclear physics for OQS can also be applied in atomic physics, as it has been done for dipolar anions in the present work. In particular, the

BEM allows the description of very weakly bound and unbound molecular systems where other approaches are inapplicable. This work takes place in the growing interest for OQSs in various fields of physics, and paves the way for the use of the Berggren basis in atomic and molecular physics.

Appendix A

Annexes

A.1 Jost functions

——— *Introduction* ———

For the potential $V(r)$ consisting of central and Coulomb parts, the reduced radial wave functions $u_l(k,r)$ are solutions of:

$$\frac{\partial^2 u_l(k,r)}{\partial r^2} = \left(\frac{l(l+1)}{r^2} + \frac{2m}{\hbar^2} V(r) - k^2 \right) u_l(k,r) \tag{A.1}$$

with l the orbital momentum of the particle and m its mass, and:

$$E = \frac{\hbar^2 k^2}{2m} \tag{A.2}$$

The reduced radial solutions $u_l(k,r)$, are regular at the origin:

$$u_l(k,r) \underset{r\sim 0}{\sim} C_0(k) r^{l+1} \tag{A.3}$$

with $C_0(k)$ a constant with respect to r which also depends on l. Consequently, due to the Cauchy-Lipschitz theorem (or Picard-Lindelöf theorem), the boundary condition Eq.(A.3) uniquely defines the solution $u_l(k,r)$. Moreover, at large distances when the nuclear part of the potential is negligible, the Berggren basis states are solutions of the equation:

$$\frac{\partial^2 u_l(k,r)}{\partial r^2} = \left(\frac{l(l+1)}{r^2} + \frac{2\eta k}{r} - k^2 \right) u_l(k,r) \tag{A.4}$$

with η the Sommerfeld parameter (1.46). The linearly independent solutions of Eq.(A.4) are regular and irregular Coulomb functions $F_{l,\eta}(kr)$ and $G_{l,\eta}(kr)$ respectively. To speak about incoming and outgoing solutions, it is more convenient to use the linearly independent incoming and outgoing Coulomb functions:

$$H^{\pm}_{l,\eta}(kr) = G_{l,\eta}(kr) \pm i F_{l,\eta}(kr) \tag{A.5}$$

Then the Berggren basis states $u_l(k,r)$ write:

$$u_l(k,r) \underset{r\to\infty}{\sim} C_+(k) H^+_{l,\eta}(kr) + C_-(k) H^-_{l,\eta}(kr) \tag{A.6}$$

where $C_-(k) = 0$ and $C_+(k) \neq 0$ are two constants with respect to r, which depend on l. For bound states and resonances $C_-(k) = 0$ and $C_+(k) \neq 0$, and for scattering states $C_-(k) \neq 0$ and $C_+(k) \neq 0$. Consequently, it is always possible to write:

$$u_l(k,r) = C_+(k)u_l^+(k,r) + C_-(k)u_l^-(k,r) \tag{A.7}$$

with $u_l^+(k,r)$ and $u_l^-(k,r)$ two linearly independent solutions of Eq.(A.1).

——— *Definition of the Jost functions* ———

The Jost function are defined by [107]:

$$\mathcal{J}^\pm(k) = W(u_l^\pm(k,r), u_l(k,r)) = u_l^\pm(k,r)\frac{du_l(k,r)}{dr} - u_l(k,r)\frac{du_l^\pm(k,r)}{dr} \tag{A.8}$$

with $W(f,g)$ the Wronskian. The outgoing Jost function $\mathcal{J}^+(k)$ is usually just called the Jost function.

——— *Properties* ———

Jost functions do not depend on r because $u_l(k,r)$ and $u_l^+(k,r)$ are linearly independent. The reduced radial wave functions can be expressed by Jost functions as:

$$u_l(k,r) = \frac{\mathcal{J}^-(k)u_l^+(k,r) - \mathcal{J}^+(k)u_l^-(k,r)}{2ik} \tag{A.9}$$

Indeed, at large distances, the incoming and outgoing wave functions $u_l^+(k,r)$ and $u_l^-(k,r)$ behave as $H_{l,\eta}^+(kr)$ and $H_{l,\eta}^-(kr)$ respectivly. Then it follows:

$$W(u_l^+(k,r), u_l^-(k,r)) = W(H_{l,\eta}^+(kr), H_{l,\eta}^-(kr)) \tag{A.10}$$

The right side of Eq.(A.10) can be evaluated using:

$$H_{l,\eta}^\pm(kr) \underset{r\to\infty}{\sim} i^{\mp l}e^{\pm i\sigma_l}e^{\pm i(kr-\eta\ln(2kr))} \tag{A.11}$$

with $\sigma_l = \arg(\Gamma(l+1+i\eta))$, and:

$$\begin{aligned}\frac{\partial H_{l,\eta}^\pm(kr)}{\partial r} &\underset{r\to\infty}{\sim} i^{\mp l}e^{\pm i\sigma_l}(\pm i)\left(k-\frac{\eta}{r}\right)e^{\pm i(kr-\eta\ln(2kr))} \\ &\underset{r\to\infty}{\sim} \pm i\left(k-\frac{\eta}{r}\right)\frac{\partial H_{l,\eta}^\pm(kr)}{\partial r}\end{aligned} \tag{A.12}$$

Thus $H_{l,\eta}^+(kr)H_{l,\eta}^-(kr) = 1$ and the Wronskian (A.10) equals:

$$\begin{aligned}W(H_{l,\eta}^+(kr), H_{l,\eta}^-(kr)) &= H_{l,\eta}^+(kr)\frac{\partial H_{l,\eta}^-(kr)}{\partial r} - H_{l,\eta}^-(kr)\frac{\partial H_{l,\eta}^+(kr)}{\partial r} \\ &= H_{l,\eta}^+(kr)H_{l,\eta}^-(kr)(-i)\left(k-\frac{\eta}{r}\right) - H_{l,\eta}^-(kr)H_{l,\eta}^+(kr)(+i)\left(k-\frac{\eta}{r}\right) \\ &= -2ik\end{aligned} \tag{A.13}$$

Then, Eq.(A.9) is obtained in the following way:

$$\begin{aligned}2iku_l(k,r) &= -u_l(k,r)W(H_{l,\eta}^+(kr), H_{l,\eta}^-(kr)) \\ &= -u_l(k,r)W(u_l^+(k,r), u_l^-(k,r)) \\ &= \left(u_l^-(k,r)\frac{\partial u_l(k,r)}{\partial r}u_l^+(k,r) - u_l(k,r)\frac{\partial u_l^-(k,r)}{\partial r}u_l^+(k,r)\right) \\ &\quad - \left(u_l^+(k,r)\frac{\partial u_l(k,r)}{\partial r}u_l^-(k,r) - u_l(k,r)\frac{\partial u_l^+(k,r)}{\partial r}u_l^-(k,r)\right) \\ &= \mathcal{J}^-(k)u_l^+(k,r) - \mathcal{J}^+(k)u_l^-(k,r)\end{aligned} \tag{A.14}$$

The derivative of the Jost function $\mathcal{J}^+(k)$ can be obtained by considering two wave functions $v(k,r)$ and $w(k',r)$ at different energies $k \neq k'$. They are not linearly independent, thus their Wronskian depends on r:

$$\begin{aligned}\frac{\partial W(v(k,r),w(k',r))}{\partial r} &= \frac{\partial}{\partial r}\left(v(k,r)\frac{\partial w(k',r)}{\partial r} - w(k',r)\frac{\partial v(k,r)}{\partial r}\right)\\ &= \frac{\partial v(k,r)}{\partial r}\frac{\partial w(k',r)}{\partial r} + v(k,r)\frac{\partial^2 w(k',r)}{\partial r^2}\\ &\quad - \frac{\partial w(k',r)}{\partial r}\frac{\partial v(k,r)}{\partial r} - w(k',r)\frac{\partial^2 v(k,r)}{\partial r^2}\end{aligned} \tag{A.15}$$

The wave functions $v(k,r)$ and $w(k',r)$ are solutions of the equations:

$$\begin{aligned}\frac{\partial^2 v(k,r)}{\partial r^2} &= \left(\frac{l(l+1)}{r^2} + \frac{2m}{\hbar^2}V(r) - k^2\right)v(k,r)\\ \frac{\partial^2 w(k',r)}{\partial r^2} &= \left(\frac{l(l+1)}{r^2} + \frac{2m}{\hbar^2}V(r) - k'^2\right)w(k',r)\end{aligned} \tag{A.16}$$

Inserting (A.16) in Eq.(A.15) one obtains:

$$\begin{aligned}\frac{\partial W(v(k,r),w(k',r))}{\partial r} &= v(k,r)\frac{\partial^2 w(k',r)}{\partial r^2} - w(k',r)\frac{\partial^2 v(k,r)}{\partial r^2}\\ &= (k^2 - k'^2)v(k,r)w(k',r)\end{aligned} \tag{A.17}$$

The integration along a segment $[a,b] \in \mathbb{R}$ leads to:

$$\begin{aligned}&\int_a^b dr\,\frac{\partial W(v(k,r),w(k',r))}{\partial r} = \int_a^b dr\,(k^2 - k'^2)v(k,r)w(k',r)\\ \Leftrightarrow\quad &W(v(k,r),w(k',r))\,|_{r=b} - W(v(k,r),w(k',r))\,|_{r=a}\\ &= (k^2 - k'^2)\int_a^b dr\,v(k,r)w(k',r)\end{aligned} \tag{A.18}$$

The derivative of Eq.(A.18) with respect to k' gives:

$$\begin{aligned}&\frac{\partial}{\partial k'}W(v(k,r),w(k',r))\Big|_{r=b} - W(v(k,r),w(k',r))\Big|_{r=a}\\ &\quad= \frac{\partial}{\partial k'}\left((k^2 - k'^2)\int_a^b dr\,v(k,r)w(k',r)\right)\\ \Leftrightarrow\quad &W\left(v(k,r),\frac{\partial w(k,r)}{\partial k'}\right)\Big|_{r=b} - W\left(v(k,r),\frac{\partial w(k,r)}{\partial k'}\right)\Big|_{r=a}\\ &\quad= -2k'\int_a^b dr\,v(k,r)w(k',r) + (k^2 - k'^2)\int_a^b dr\,v(k,r)\frac{\partial w(k,r)}{\partial k}\end{aligned} \tag{A.19}$$

In particular, for $k' = k$:

$$W\left(v(k,r),\frac{\partial w(k,r)}{\partial k}\right)\Big|_{r=b} - W\left(v(k,r),\frac{\partial w(k,r)}{\partial k}\right)\Big|_{r=a} = -2k\int_a^b dr\,v(k,r)w(k,r) \tag{A.20}$$

Finally, for a bound state ($k^2 < 0$) the derivative of the Jost function $\mathcal{J}^+(k)$ is expressed as:

$$\begin{aligned}\frac{\partial \mathcal{J}^+(k)}{\partial k} &= \frac{\partial}{\partial k} W(u_l^+(k,r), u_l(k,r)) \\ &= \frac{\partial u_l^+(k,r)}{\partial k}\frac{\partial u_l(k,r)}{\partial r} + u_l^+(k,r)\frac{\partial^2 u_l(k,r)}{\partial k \partial r} - \frac{\partial u_l(k,r)}{\partial k}\frac{\partial u_l^+(k,r)}{\partial r} - u_l(k,r)\frac{\partial^2 u_l^+(k,r)}{\partial k \partial r} \\ &= W\left(u_l^+(k,r), \frac{\partial u_l(k,r)}{\partial k}\right) + W\left(\frac{\partial u_l^+(k,r)}{\partial k}, u_l(k,r)\right) \end{aligned} \tag{A.21}$$

Here the Wronskians do not depend on r. In order to connect the terms in Eq.(A.21) with those in Eq.(A.20), we use the relation:

$$W\left(\frac{\partial u_l^+(k,r)}{\partial k}, u_l(k,r)\right) = -W\left(u_l(k,r), \frac{\partial u_l^+(k,r)}{\partial k}\right) \tag{A.22}$$

and the fact that $C_0(k) = 1$ for bound states. Moreover:

$$\begin{aligned} & u_l(k,r) \underset{r\to 0}{\sim} C_0(k) r^{l+1} \\ \Rightarrow \quad & \frac{\partial u_l(k,r)}{\partial k}\Big|_{r=0} = \frac{\partial}{\partial r}\left(\frac{\partial u_l(k,r)}{\partial k}\right)\Big|_{r=0} = 0 \\ \Rightarrow \quad & W\left(u_l^+(k,r), \frac{\partial u_l(k,r)}{\partial r}\right)\Big|_{r=0} = 0 \end{aligned} \tag{A.23}$$

and

$$\begin{aligned} & u_l^+(k,r) \underset{r\to\infty}{\sim} H_{l,\eta}^+(kr) \underset{r\to\infty}{\to} 0 \\ \Rightarrow \quad & W\left(u_l(k,r), \frac{\partial u_l^+(k,r)}{\partial k}\right)\Big|_{r\to\infty} = 0 \end{aligned} \tag{A.24}$$

Thus, Eq.(A.21) takes the form:

$$\begin{aligned}\frac{\partial \mathcal{J}^+(k)}{\partial k} &= W\left(u_l^+(k,r), \frac{\partial u_l(k,r)}{\partial k}\right)\Big|_{r=r'} - W\left(u_l(k,r), \frac{\partial u_l^+(k,r)}{\partial k}\right)\Big|_{r=r'} \\ &\quad - W\left(u_l^+(k,r), \frac{\partial u_l(k,r)}{\partial r}\right)\Big|_{r=0} + W\left(u_l(k,r), \frac{\partial u_l^+(k,r)}{\partial k}\right)\Big|_{r\to\infty} \\ &= \left(W\left(u_l^+(k,r), \frac{\partial u_l(k,r)}{\partial k}\right)\Big|_{r=r'} - W\left(u_l^+(k,r), \frac{\partial u_l(k,r)}{\partial r}\right)\Big|_{r=0}\right) \\ &\quad + \left(W\left(u_l(k,r), \frac{\partial u_l^+(k,r)}{\partial k}\right)\Big|_{r\to\infty} - W\left(u_l(k,r), \frac{\partial u_l^+(k,r)}{\partial k}\right)\Big|_{r=r'}\right) \end{aligned} \tag{A.25}$$

Using the formula (A.20), one can obtain a final expression for the derivative of the (outgoing) Jost function:

$$\begin{aligned}\frac{\partial \mathcal{J}^+(k)}{\partial k} &= -2k\int_0^{r'} dr'\, u_l^+(k,r')u_l(k,r') - 2k\int_{r'}^{\infty} dr'\, u_l(k,r')u_l^+(k,r') \\ &\underset{r'\to\infty}{\to} -2k\int_0^{\infty} dr'\, u_l^+(k,r')u_l(k,r') \end{aligned} \tag{A.26}$$

where the second integral goes to zero when $r' \to \infty$ because of the asymptotic behavior of $u_l^+(k,r)$ for $k^2 < 0$. Eq.(A.26) can be evaluated at a pole $k = k_0$ corresponding to a bound state ($\mathcal{J}^+(k_0) = 0$) for which the reduced radial wave function $u_l(k,r)$ is differentiable. Then, the Eq.(A.9) becomes:

$$u_l(k_0,r) = \frac{\mathcal{J}^-(k_0)u_l^+(k_0,r)}{2ik_0} \tag{A.27}$$

Inserting (A.27) into Eq.(A.26), taken at $k = k_0$, leads to:

$$\left.\frac{\partial \mathcal{J}^+(k)}{\partial k}\right|_{k=k_0} = i\mathcal{J}^-(k_0)\int_0^\infty dr'\,\left.\left(u_l^+(k,r')\right)^2\right|_{k=k_0} \tag{A.28}$$

This equation holds also for resonances, but in that case the integral has to be regularized.

——— *Link with the scattering matrix* ———

In the scattering theory, the reduced radial wave functions $u_l(k,r)$ (see Eq.(A.7)) are usually written as:

$$u_l(k,r) = A(u_l^-(k,r) - Su_l^+(k,r)) \tag{A.29}$$

with A a constant, and S a partial scattering matrix element, both depending on l. Then, by comparing Eq.(A.29) with Eqs.(A.7) and (A.9), one finds:

$$A = C_-(k) = -\frac{\mathcal{J}^+(k)}{2ik} \tag{A.30}$$

and:

$$S = -\frac{C_+}{C_-} = \frac{\mathcal{J}^-(k)}{\mathcal{J}^+(k)} \tag{A.31}$$

A.2 Berggren basis

The Berggren basis can be obtained straightforwardly from the Newton basis using properties of the Jost function [77, 272].

The Newton basis is:

$$\sum_{n\in(b)} |u(k_n)\rangle\langle u(k_n)| + \int_0^\infty dk\,|u(k)\rangle\langle u(k)| = \hat{\mathbb{1}} \tag{A.32}$$

The sum runs over bound states and the integral is over the real-energy continuum. The bound states are normalized as usual, while the continuum states are normalized to the Dirac distribution:

$$\langle u(k)|u(k')\rangle = \delta(k-k') \tag{A.33}$$

The real-energy contour can be deformed into a complex-energy contour L^+ as shown in Fig.1.2. Using the Cauchy residue theorem, one obtains:

$$\int_{L^+} dk\,|u(k)\rangle\langle\tilde{u}(k)| = 2\pi i\sum_m \text{Res}\left(|u(k)\rangle\langle\tilde{u}(k)|\right)|_{k=k_m} + \int_0^\infty dk\,|u(k)\rangle\langle u(k)| \tag{A.34}$$

where $\langle\tilde{u}(k)|$ is the time-reversal of $|u(k)\rangle$, and k_m is the linear momentum of a pole of the $|u(k)\rangle\langle\tilde{u}(k)|$ operator[1]. The problem is to evaluate the residual term. Using the normalization condition for scattering states Eq.(1.50) in Eq.(A.7), one finds:

[1] It is a pole if the norm of the operator diverges.

$$C^+(k) = \sqrt{(C^+(k))^2} = \sqrt{(-C^+(k)C^-(k))\left(-\frac{C^+(k)}{C^-(k)}\right)} = \sqrt{-\frac{1}{2\pi}\frac{\mathcal{J}^-(k)}{\mathcal{J}^+(k)}} \tag{A.35}$$

and thus (idem for $C^-(k)$), the radial wave functions can be written in a symmetric form:

$$u(k,r) = \sqrt{-\frac{1}{2\pi}\frac{\mathcal{J}^-(k)}{\mathcal{J}^+(k)}}u^+(k,r) + \sqrt{-\frac{1}{2\pi}\frac{\mathcal{J}^+(k)}{\mathcal{J}^-(k)}}u^-(k,r) \tag{A.36}$$

Near the pole k_m, $\mathcal{J}^+(k) \to 0$ and thus:

$$|u(k)\rangle\langle\tilde{u}(k)| \underset{k\to k_m}{\sim} -\frac{1}{2\pi}\frac{\mathcal{J}^-(k)}{\mathcal{J}^+(k)}|u^+(k_m)\rangle\langle\tilde{u}^+(k_m)| \tag{A.37}$$

Also for $k \to k_m$, the Jost function $\mathcal{J}^+(k)$ can be written as a Taylor series:

$$\mathcal{J}^+(k) \underset{k\to k_m}{\sim} (k-k_m)\left.\frac{\partial\mathcal{J}^+(k)}{\partial k}\right|_{k=k_m} \tag{A.38}$$

where the derivative is given in Eq.(A.28). The residue can thus be evaluated by inserting Eqs.(A.38) and (A.28) into Eq.(A.37):

$$|u(k)\rangle\langle\tilde{u}(k)| \underset{k\to k_m}{\sim} -\frac{1}{2\pi i}\frac{1}{k-k_m}\frac{|u^+(k_m)\rangle\langle\tilde{u}^+(k_m)|}{\int_0^\infty dr'\,(u^+(k_m,r'))^2} \tag{A.39}$$

Normalized resonant states are defined as:

$$|u(k_m)\rangle\langle\tilde{u}(k_m)| = \frac{|u^+(k_m)\rangle\langle\tilde{u}^+(k_m)|}{\int_0^\infty dr'\,(u^+(k_m,r'))^2} \tag{A.40}$$

and thus:

$$\begin{aligned}|u(k)\rangle\langle\tilde{u}(k)| &\underset{k\to k_m}{\sim} -\frac{1}{2\pi i}\frac{1}{k-k_m}|u(k_m)\rangle\langle\tilde{u}(k_m)| \\ &\underset{k\to k_m}{\sim} \frac{1}{k-k_m}\,\mathrm{Res}\left(|u(k)\rangle\langle\tilde{u}(k)|\right)|_{k=k_m}\end{aligned} \tag{A.41}$$

and the residue equals:

$$\mathrm{Res}\left(|u(k)\rangle\langle\tilde{u}(k)|\right)|_{k=k_m} = -\frac{1}{2\pi i}|u(k_m)\rangle\langle\tilde{u}(k_m)| \tag{A.42}$$

Inserting (A.42) in Eq.(A.34), one can express the continuous part of the Newton basis as:

$$\begin{aligned}\int_0^\infty dk\,|u(k)\rangle\langle u(k)| &= \int_{L^+} dk\,|u(k)\rangle\langle\tilde{u}(k)| - 2\pi i\sum_m \mathrm{Res}\left(|u(k)\rangle\langle\tilde{u}(k)|\right)|_{k=k_m} \\ &= \int_{L^+} dk\,|u(k)\rangle\langle\tilde{u}(k)| + \sum_m |u(k_m)\rangle\langle\tilde{u}(k_m)|\end{aligned} \tag{A.43}$$

and derive the Berggren basis:

$$\sum_{n\epsilon(b)} |u(k_n)\rangle \langle u(k_n)| + \int_{L^+} dk\ |u(k)\rangle \langle \tilde{u}(k)| + \sum_m |u(k_m)\rangle \langle \tilde{u}(k_m)| = \hat{\mathbb{1}}$$
$$\sum_{n\epsilon(b,r)} |u(k_n)\rangle \langle u(k_n)| + \int_{L^+} dk\ |u(k)\rangle \langle \tilde{u}(k)| = \hat{\mathbb{1}} \tag{A.44}$$

Index n in (A.44) runs over both bound states (b) and resonances (r).

A.3 Moore-Penrose pseudo inverse

In the orthogonalization of channel wave functions (see Sec.1.2.3.3), the existence of the matrix $O^{-\frac{1}{2}}$ associated to $\hat{O}^{-\frac{1}{2}}$ is not always guaranteed, because of the possible presence of zero eigenvalues. Indeed, the inverse of a matrix M is obtained with the following method:

$$M = PDP^{-1} \quad \Rightarrow \quad M^{-1} = P^{-1}D^{-1}P \tag{A.45}$$

where D is a diagonal matrix, and thus:

$$D = \begin{pmatrix} \lambda_0 & 0 & 0 \\ 0 & \lambda_1 & 0 \\ 0 & 0 & \lambda_2 \end{pmatrix} \quad \Rightarrow \quad D^{-1} = \begin{pmatrix} \lambda_0^{-1} & 0 & 0 \\ 0 & \lambda_1^{-1} & 0 \\ 0 & 0 & \lambda_2^{-1} \end{pmatrix} \tag{A.46}$$

The problem appears if one of the eigenvalues is equal to zero. In this case, the Moore-Penrose pseudoinverse is used:

$$D = \begin{pmatrix} \lambda_0 & 0 & 0 \\ 0 & 0 & 0 \\ 0 & 0 & \lambda_2 \end{pmatrix} \quad \Rightarrow \quad D^{-1} = \begin{pmatrix} \lambda_0^{-1} & 0 & 0 \\ 0 & 0 & 0 \\ 0 & 0 & \lambda_2^{-1} \end{pmatrix} \tag{A.47}$$

The zero eigenvalues are just ignored, which in the present case is equivalent to removing a channel state from the basis. The Moore-Penrose pseudoinverse is thus used to remove remaining non-orthogonal channel states due to the presence of physically equivalent channels. It is a pathological situation which appears mainly when there is just one active particle in the target. Indeed, for example if a channel state $|c_0\rangle$ is associated with a projectile state $|a\rangle$ and a target state $|b\rangle$, and another channel state $|c_1\rangle$ is associated with a projectile state $|b\rangle$ and a target state $|a\rangle$, then even if there are two mathematically different channels they are physically equivalent.

A.4 CNO cycles and pp chains

Proton and neutron radiative capture reactions presented in Sec.2 are involved in several astrophysical chains, which are presented hereafter. These reactions are written in red.

1. The proton-proton (pp) chains are:

$$\text{pp-I:} \qquad {}^3\text{He}({}^3\text{He}, 2p){}^4\text{He} \tag{A.48}$$

$$\text{pp-II:} \qquad {}^3\text{He}({}^4\text{He}, \gamma){}^7\text{Be}(e^-, \nu_e){}^7\text{Li}(p, {}^4\text{He}){}^4\text{He} \tag{A.49}$$

$$\text{pp-III:} \qquad {}^3\text{He}({}^4\text{He}, \gamma){}^7\text{Be}(p, \gamma){}^8\text{B}(\beta^+){}^8\text{Be}(2{}^4\text{He}) \tag{A.50}$$

2. The stationary hydrogen burning chain:

$$p(p,e+\nu)\mathrm{d}(p,\gamma)^3\mathrm{He}(^3\mathrm{He},2p)^4\mathrm{He}(^3\mathrm{He},\gamma)^7\mathrm{Be}(p,\gamma)^8\mathrm{B}(\beta^+)2^4\mathrm{He} \tag{A.51}$$

3. The cold and hot CNO cycles:

$$\text{CNO-I} \quad {}^{12}\mathrm{C}(p,\gamma)^{13}\mathrm{N}(\beta^+)^{13}\mathrm{C}(p,\gamma)^{14}\mathrm{N}(p,\gamma)^{15}\mathrm{O}(\beta^+)^{15}\mathrm{N}(p,\alpha)^{12}\mathrm{C} \tag{A.52}$$

$$\text{HCNO-I} \quad {}^{12}\mathrm{C}(p,\gamma)^{13}\mathrm{N}(p,\gamma)^{14}\mathrm{O}(\beta^+)^{14}\mathrm{N}(p,\gamma)^{15}\mathrm{O}(\beta^+)^{15}\mathrm{N}(p,\alpha)^{12}\mathrm{C} \tag{A.53}$$

$$\text{CNO-II} \quad {}^{15}\mathrm{N}(p,\gamma)^{16}\mathrm{O}(p,\gamma)^{17}\mathrm{F}(\beta^+)^{17}\mathrm{O}(p,\alpha)^{14}\mathrm{N}(p,\gamma)^{15}\mathrm{O}(\beta^+)^{15}\mathrm{N} \tag{A.54}$$

$$\text{HCNO-II} \quad {}^{15}\mathrm{N}(p,\gamma)^{16}\mathrm{O}(p,\gamma)^{17}\mathrm{F}(p,\gamma)^{18}\mathrm{Ne}(\beta^+)^{18}\mathrm{F}(p,\alpha)^{15}\mathrm{O}(\beta^+)^{15}\mathrm{N} \tag{A.55}$$

$$\text{CNO-III} \quad {}^{17}\mathrm{O}(p,\gamma)^{18}\mathrm{F}(\beta^+)^{18}\mathrm{O}(p,\alpha)^{15}\mathrm{N}(p,\gamma)^{16}\mathrm{O}(p,\gamma)^{17}\mathrm{F}(\beta^+)^{17}\mathrm{O} \tag{A.56}$$

$$\text{HCNO-III} \quad {}^{18}\mathrm{F}(p,\gamma)^{19}\mathrm{Ne}(\beta^+)^{19}\mathrm{F}(p,\alpha)^{16}\mathrm{O}(p,\gamma)^{17}\mathrm{F}(p,\gamma)^{18}\mathrm{Ne}(\beta^+)^{18}\mathrm{F} \tag{A.57}$$

$$\text{CNO-IV} \quad {}^{19}\mathrm{F}(p,\alpha)^{16}\mathrm{O}(p,\gamma)^{17}\mathrm{F}(\beta^+)^{17}\mathrm{O}(p,\gamma)^{18}\mathrm{F}(\beta^+)^{18}\mathrm{O}(p,\gamma)^{19}\mathrm{F} \tag{A.58}$$

4. One possible chain in the Big Bang nucleosynthesis:

$$^1\mathrm{H}(n,\gamma)^2\mathrm{H}(n,\gamma)^3\mathrm{H}(d,n)^4\mathrm{He}(t,\gamma)^7\mathrm{Li}(n,\gamma)^8\mathrm{Li} \tag{A.59}$$

A.5 Radiative capture

The operator $\hat{\mathcal{M}}_{L,M_L}$ separates into an electric part $\hat{\mathcal{M}}^E_{L,M_L}$ and a magnetic part $\hat{\mathcal{M}}^M_{L,M_L}$:

$$\begin{aligned}\hat{\mathcal{M}}^E_{L,M_L} = &\sum_i e_i \frac{(2L+1)!!}{(L+1)k_\gamma^L}\left[S_L'(k_\gamma \hat{r}_i) + \frac{k_\gamma \hat{r}_i}{2} S_L(k_\gamma \hat{r}_i)\right]\hat{Y}^L_{M_L}(\Omega_i) \\ &+ \sum_i e_i \frac{(2L+1)!!}{(L+1)k_\gamma^L}\frac{\hbar c}{2m_p c^2} g_i^s \left[\frac{S_L(k_\gamma \hat{r}_i)}{\hat{r}_i}\right]\left(\hat{\vec{l}}_i \cdot \hat{\vec{s}}_i\right)\hat{Y}^L_{M_L}(\Omega_i)\end{aligned} \tag{A.60}$$

$$\hat{\mathcal{M}}^{M}_{L,M_L} = \frac{\hbar c}{2m_p c^2}\sum_i \frac{(2L+1)!!}{(L+1)k_\gamma^L}\left[g_i^l\vec{\nabla}_i\left(\frac{S_L(k_\gamma\hat{r}_i)}{k_\gamma\hat{r}_i}\hat{Y}^L_{M_L}(\Omega_i)\right)\cdot\hat{\vec{l}}_i + g_i^s\vec{\nabla}_i\left(S'_L(k_\gamma\hat{r}_i)Y^L_{M_L}(\Omega_i)\right)\cdot\hat{\vec{s}}_i\right]$$
$$+\frac{\hbar c}{2m_p c^2}\sum_i\frac{(2L+1)!!}{(L+1)k_\gamma^L}g_i^s\left(k_\gamma S_L(k_\gamma\hat{r}_i)\right)\left(\hat{\vec{s}}_i\cdot\vec{u}_{r_i}\right)\hat{Y}^L_{M_L}(\Omega_i) \tag{A.61}$$

$$= -\frac{\hbar c}{2m_p c^2}\sum_i\frac{(2L+1)!!}{(L+1)k_\gamma^L}g_i^l\sqrt{\frac{L+1}{2L+1}}\left(S'_L(k_\gamma\hat{r}_i) - \left(\frac{L+1}{\hat{r}_i}\right)\frac{S_L(k_\gamma\hat{r}_i)}{k_\gamma\hat{r}_i}\right)[\hat{\mathbf{Y}}^{L+1}(\Omega_i)\otimes\hat{\vec{l}}_i]^L_{M_L}$$
$$+\frac{\hbar c}{2m_p c^2}\sum_i\frac{(2L+1)!!}{(L+1)k_\gamma^L}g_i^l\sqrt{\frac{L}{2L+1}}\left(S'_L(k_\gamma\hat{r}_i) + \left(\frac{L}{\hat{r}_i}\right)\frac{S_L(k_\gamma\hat{r}_i)}{k_\gamma\hat{r}_i}\right)[\hat{\mathbf{Y}}^{L-1}(\Omega_i)\otimes\hat{\vec{l}}_i]^L_{M_L}$$
$$-\frac{\hbar c}{2m_p c^2}\sum_i\frac{(2L+1)!!}{(L+1)k_\gamma^L}g_i^s\sqrt{\frac{L+1}{2L+1}}\left[\left(\frac{L(L+1)}{(k_\gamma\hat{r}_i)^2}-1\right)S_L(k_\gamma\hat{r}_i) - \left(\frac{L}{\hat{r}_i}\right)S'_L(k_\gamma\hat{r}_i)\right][\hat{\mathbf{Y}}^{L+1}(\Omega_i)\otimes\hat{\vec{s}}_i]^L_{M_L}$$
$$+\frac{\hbar c}{2m_p c^2}\sum_i\frac{(2L+1)!!}{(L+1)k_\gamma^L}g_i^s\sqrt{\frac{L}{2L+1}}\left[\left(\frac{L(L+1)}{(k_\gamma\hat{r}_i)^2}-1\right)S_L(k_\gamma\hat{r}_i) + \left(\frac{L+1}{\hat{r}_i}\right)S'_L(k_\gamma\hat{r}_i)\right][\hat{\mathbf{Y}}^{L-1}(\Omega_i)\otimes\hat{\vec{s}}_i]^L_{M_L}$$
$$+\frac{\hbar c}{2m_p c^2}\sum_i\frac{(2L+1)!!}{(L+1)k_\gamma^L}g_i^s\left(k_\gamma S_L(k_\gamma\hat{r}_i)\right)\left(\hat{\vec{s}}_i\cdot\vec{u}_{r_i}\right)\hat{Y}^L_{M_L}(\Omega_i) \tag{A.62}$$

where

- i runs over all considered nucleons, with $\hat{\vec{l}}_i$ and $\hat{\vec{s}}_i$ the orbital and spin angular momenta, respectively
- $\hat{Y}^L_{M_L}(\Omega)$ is a spherical harmonics of order L and projection M_L
- S_L is the Ricatti-Bessel function of order L
- $\hat{r}_i$, Ω_i are the radial and angular coordinates of the nucleon i, respectively, and $\vec{u}_{r_i} = \hat{\vec{r}}_i/\hat{r}_i$
- e_i is the dimensionless charge of the nucleon i, 1 for proton, 0 for neutron
- g_i^s is the dimensionless magnetic spin moment of the nucleon i and equals 5.5857 for proton, -3.8263 for neutron
- $m_p c^2$, in MeV, is the mass of the proton
- g_i^l is the dimensionless magnetic orbital momentum times $L+1$ of the nucleon i, and is 2 for proton, 0 for neutron

Using the long wavelength approximation, Eqs.(A.60), and (A.62) become:

$$\hat{\mathcal{M}}^{E}_{L,M_L} = \sum_i e_i\hat{r}_i^L\hat{Y}^L_{M_L}(\Omega_i) \tag{A.63}$$

$$\hat{\mathcal{M}}^{M}_{L,M_L} = \frac{\hbar c}{2m_p c^2}\sum_i\left[\frac{g_i^l}{L+1}\vec{\nabla}_i\left(\hat{r}_i^L\hat{Y}^L_{M_L}(\Omega_i)\right)\cdot\hat{\vec{l}}_i + g_i^s\vec{\nabla}_i\left(r_i^L Y^L_{M_L}(\Omega_i)\right)\cdot\hat{\vec{s}}_i\right] \tag{A.64}$$
$$= \frac{\hbar c}{2m_p c^2}\sum_i\sqrt{L(2L+1)}\hat{r}_i^{L-1}\frac{g_i^l}{L+1}[\hat{\mathbf{Y}}^{L-1}(\Omega_i)\otimes\hat{\vec{l}}_i]^{L_{M_L}}$$
$$+\frac{\hbar c}{2m_p c^2}\sum_i\sqrt{L(2L+1)}\hat{r}_i^{L-1}g_i^s[\hat{\mathbf{Y}}^{L-1}(\Omega_i)\otimes\hat{\vec{s}}_i]^{L_{M_L}} \tag{A.65}$$

Eqs.(A.60), (A.62), (A.63) and (A.65) have been written so that only one one-body operator appears in each sum running over i.

The one-body matrix elements of the electromagnetic transition operators can be in the present case:

$$S'_L(k_\gamma \hat{r}) + \frac{k_\gamma \hat{r}}{2} S_L(k_\gamma \hat{r}) \tag{A.66}$$

$$\frac{S_L(k_\gamma \hat{r})}{\hat{r}} \tag{A.67}$$

$$S'_L(k_\gamma \hat{r}) - \left(\frac{L+1}{\hat{r}}\right) \frac{S_L(k_\gamma \hat{r})}{k_\gamma \hat{r}} \tag{A.68}$$

$$S'_L(k_\gamma \hat{r}) + \left(\frac{L}{\hat{r}}\right) \frac{S_L(k_\gamma \hat{r})}{k_\gamma \hat{r}} \tag{A.69}$$

$$\left(\frac{L(L+1)}{(k_\gamma \hat{r})^2} - 1\right) S_L(k_\gamma \hat{r}) - \left(\frac{L}{\hat{r}}\right) S'_L(k_\gamma \hat{r}) \tag{A.70}$$

$$\left(\frac{L(L+1)}{(k_\gamma \hat{r})^2} - 1\right) S_L(k_\gamma \hat{r}) + \left(\frac{L+1}{\hat{r}}\right) S'_L(k_\gamma \hat{r}) \tag{A.71}$$

$$k_\gamma S_L(k_\gamma \hat{r}) \tag{A.72}$$

$$\hat{r}^L \tag{A.73}$$

$$\hat{r}^{L-1} \tag{A.74}$$

The reduced angular matrix elements associated to operators entering Eqs.(A.60), (A.62), (A.63) and (A.65) read:

$$\langle (l_f, s) j_f \| \hat{\mathbf{Y}}^L \| (l_i, s) j_i \rangle = \frac{1 + (-1)^{l_i + L + l_f}}{2} (-1)^{j_f + \frac{1}{2}} \sqrt{\frac{1}{4\pi}} \sqrt{2j_f + 1} \sqrt{2j_i + 1} \sqrt{2L + 1} \begin{pmatrix} j_f & L & j_i \\ \frac{1}{2} & 0 & -\frac{1}{2} \end{pmatrix} \tag{A.75}$$

$$\langle (l_f, s) j_f \| \left(\hat{\vec{l}} \cdot \hat{\vec{s}}\right) \hat{\mathbf{Y}}^L \| (l_i, s) j_i \rangle = \frac{j_f(j_f+1) - l_f(l_f+1) - \frac{3}{4}}{2} \langle (l_f, s) j_f \| \hat{\mathbf{Y}}^L \| (l_i, s) j_i \rangle \tag{A.76}$$

$$\begin{aligned} \langle (l_f, s) j_f \| [\hat{\mathbf{Y}}^{L_\pm} \otimes \hat{\vec{l}}]^L \| (l_i, s) j_i \rangle &= (-1)^{\frac{1}{2} + j_i + l_i} \sqrt{2j_f + 1} \sqrt{2j_i + 1} \sqrt{2L + 1} \\ &\times (-1)^{l_f} \sqrt{2l_f + 1} \sqrt{2l_i + 1} \sqrt{2L_\pm + 1} \sqrt{\frac{1}{4\pi}} \begin{pmatrix} l_f & L_\pm & l_i \\ 0 & 0 & 0 \end{pmatrix} \\ &\times \sqrt{l_i(l_i+1)(2l_i+1)} \begin{Bmatrix} l_f & \frac{1}{2} & j_f \\ j_i & L & l_i \end{Bmatrix} \begin{Bmatrix} L_\pm & 1 & L \\ l_i & l_f & l_i \end{Bmatrix} \end{aligned} \tag{A.77}$$

$$\begin{aligned} \langle (l_f, s) j_f \| [\hat{\mathbf{Y}}^{L_\pm} \otimes \hat{\vec{s}}]^L \| (l_i, s) j_i \rangle &= \sqrt{2j_f + 1} \sqrt{2j_i + 1} \sqrt{2L + 1} \sqrt{\frac{3}{2}} \begin{Bmatrix} l_f & \frac{1}{2} & j_f \\ l_i & \frac{1}{2} & j_i \\ L_\pm & 1 & L \end{Bmatrix} (-1)^{l_f} \\ &\times \sqrt{2l_f + 1} \sqrt{2l_i + 1} \sqrt{2L_\pm + 1} \sqrt{\frac{1}{4\pi}} \begin{pmatrix} l_f & L_\pm & l_i \\ 0 & 0 & 0 \end{pmatrix} \end{aligned} \tag{A.78}$$

$$\langle (l_f,s)j_f \| \left(\hat{\vec{s}}\cdot\vec{u}_r\right)\hat{\mathbf{Y}}^L \| (l_i,s)j_i\rangle = (-1)^{\frac{1}{2}+l_f+1+j_f}\ \sqrt{2j_f+1}\ \sqrt{\frac{3}{2}}\ \sqrt{\frac{4\pi}{3}} \begin{Bmatrix} l_f & \frac{1}{2} & j_f \\ \frac{1}{2} & l_f+1 & 1 \end{Bmatrix}$$
$$\times (-1)^{l_f}\ \sqrt{2l_f+1}\ \sqrt{2(l_f+1)+1}\ \sqrt{3}\ \sqrt{\frac{1}{4\pi}} \begin{pmatrix} l_f & 1 & l_f+1 \\ 0 & 0 & 0 \end{pmatrix}$$
$$\times \langle (l_f+1,s)j_f \| \hat{\mathbf{Y}}^L \| (l_i,s)j_i\rangle \ \text{ if } j_f = l_f+\frac{1}{2} \tag{A.79}$$

$$= (-1)^{\frac{1}{2}+l_f-1+j_f}\ \sqrt{2j_f+1}\ \sqrt{\frac{3}{2}}\ \sqrt{\frac{4\pi}{3}} \begin{Bmatrix} l_f & \frac{1}{2} & j_f \\ \frac{1}{2} & l_f-1 & 1 \end{Bmatrix}$$
$$\times (-1)^{l_f}\ \sqrt{2l_f+1}\ \sqrt{2(l_f-1)+1}\ \sqrt{3}\ \sqrt{\frac{1}{4\pi}} \begin{pmatrix} l_f & 1 & l_f-1 \\ 0 & 0 & 0 \end{pmatrix}$$
$$\times \langle (l_f-1,s)j_f \| \hat{\mathbf{Y}}^L \| (l_i,s)j_i\rangle \ \text{ if } j_f = l_f-\frac{1}{2} \tag{A.80}$$

where $L_\pm = L \pm 1$.

A.6 The Furutani-Horiuchi-Tamagaki (FHT) interaction

The FHT interaction between two particles i and j writes:

$$V_{ij} = V_{ij}^{\mathrm{c}} + V_{ij}^{\mathrm{so}} + V_{ij}^{\mathrm{T}} + V_{ij}^{\mathrm{Co}} \tag{A.81}$$

The central potential V_{ij}^{c} writes:

$$V_{ij}^{\mathrm{c}} = \sum_{n=1}^{3} V_{0,n}^{\mathrm{c}} e^{-\beta_n^{\mathrm{c}} r^2} (W_n^{\mathrm{c}} + B_n^{\mathrm{c}} P^\sigma - H_n^{\mathrm{c}} P^\tau - M_n^{\mathrm{c}} P^\sigma P^\tau) \tag{A.82}$$

where r is the distance between the two particles, β_n^{c} is the range of gaussians, P^σ and P^τ are the spin exchange and isospin exchange operators, respectively, and W_n^{c}, B_n^{c}, H_n^{c} and M_n^{c} are the exchange parameters. The spin-orbit potential V_{ij}^{so} writes:

$$V_{ij}^{\mathrm{so}} = \vec{L}.\vec{S} \sum_{n=1}^{2} V_{0,n}^{\mathrm{so}} e^{-\beta_n^{\mathrm{so}} r^2} (W_n^{\mathrm{so}} - H_n^{\mathrm{so}} P^\tau) \tag{A.83}$$

where $\vec{L}$ is the relative orbital angular momentum between the two particles and $\vec{S} = \vec{s}_i + \vec{s}_j$ with $\vec{s}_{i/j}$ the spin of the particle i/j. The tensor potential V_{ij}^{T} writes:

$$V_{ij}^{\mathrm{T}} = O_{\mathrm{T}} \sum_{n=1}^{3} V_{0,n}^{\mathrm{T}} e^{-\beta_n^{\mathrm{T}} r^2} (W_n^{\mathrm{T}} - H_n^{\mathrm{T}} P^\tau) \tag{A.84}$$

where the tensorial operator O_{T} is:

$$O_{\mathrm{T}} = \left(\frac{3(\vec{\sigma}_i.\vec{r})(\vec{\sigma}_j.\vec{r})}{r^2} - \vec{\sigma}_i.\vec{\sigma}_j \right) r^2 \tag{A.85}$$

and where $\vec{\sigma}_{i/j}$ are the Pauli matrices. The Coulomb potential is standard.

It is convenient to rewrite the FHT interaction using projection operators on singlet and triplet states of spin and isospin (π_{s}^σ, π_{t}^σ, π_{s}^τ and π_{t}^τ):

$$\pi_{\rm s}^{\sigma} = \frac{1}{4} - \vec{s}_i.\vec{s}_j$$
$$\pi_{\rm t}^{\sigma} = \frac{3}{4} + \vec{s}_i.\vec{s}_j$$
$$P^{\sigma} = \frac{1}{2} + 2\vec{s}_i.\vec{s}_j = \pi_{\rm t}^{\sigma} - \pi_{\rm s}^{\sigma} \tag{A.86}$$

Eqs.(A.86) have the same form for projection operators $\pi_{\rm s}^{\tau}$ and $\pi_{\rm t}^{\tau}$ on singlet and triplet states of isospin. Then, potentials Eqs.(A.82), (A.83) and (A.84) can be written as:

$$V^{\rm c}(r) = V_{\rm tt}^{\rm c} f_{\rm tt}^{\rm c}(r)\pi_{\rm t}^{\sigma}\pi_{\rm t}^{\tau} + V_{\rm ts}^{\rm c} f_{\rm ts}^{\rm c}(r)\pi_{\rm t}^{\sigma}\pi_{\rm s}^{\tau} + V_{\rm st}^{\rm c} f_{\rm st}^{\rm c}(r)\pi_{\rm s}^{\sigma}\pi_{\rm t}^{\tau} + V_{\rm ss}^{\rm c} f_{\rm ss}^{\rm c}(r)\pi_{\rm s}^{\sigma}\pi_{\rm s}^{\tau} \tag{A.87}$$

$$V^{\rm so}(r) = \vec{L}.\vec{S}(V_{\rm tt}^{\rm so} f_{\rm tt}^{\rm so}(r)\pi_{\rm t}^{\sigma}\pi_{\rm t}^{\tau} + V_{\rm ts}^{\rm so} f_{\rm ts}^{\rm so}(r)\pi_{\rm t}^{\sigma}\pi_{\rm t}^{\tau}) \tag{A.88}$$

$$V^{\rm T}(r) = O_{\rm T}(V_{\rm tt}^{\rm T} f_{\rm tt}^{\rm T}(r)\pi_{\rm t}^{\sigma}\pi_{\rm t}^{\tau} + V_{\rm ts}^{\rm T} f_{\rm ts}^{\rm T}(r)\pi_{\rm t}^{\sigma}\pi_{\rm t}^{\tau}) \tag{A.89}$$

The functions $f_{\sigma\tau}(r)$ depend on the $V_{0,n}$, W_n, B_n, H_n and M_n constants and of the gaussians. In practical applications, one adjusts directly the coupling constants $V_{aa'}^{\rm c/so/T}$ in Eqs.(A.87-A.89), where a and a' are indices of either singlet (s) or triplet (t) states. Parameters of the FHT interaction are given in Tabs.A.1, A.2 and A.3.

n	$V_{0,n}^{\rm c}$ [MeV]	$\beta_n^{\rm c}$ [fm^{-2}]	$W_n^{\rm c}$	$B_n^{\rm c}$	$H_n^{\rm c}$	$M_n^{\rm c}$
1	-6.0	0.160	-0.2363	1.1530	0.5972	-0.5139
2	-546.0	1.127	0.4242	0.4055	0.1404	0.030
3	1655.0	3.400	0.4474	0.3985	0.1015	0.0526

Table A.1 – Parameters of the central potential in the FHT interaction.

n	$V_{0,n}^{\rm so}$ [MeV]	$\beta_n^{\rm so}$ [fm^{-2}]	$W_n^{\rm so}$	$H_n^{\rm so}$
1	1918.0	5.0	0.50	-0.5
2	-1519.0	3.0	0.50	-0.5

Table A.2 – Parameters of the spin-orbite potential in the FHT interaction.

n	$V_{0,n}^{\rm T}$ [MeV]	$\beta_n^{\rm T}$ [fm^{-2}]	$W_n^{\rm T}$	$H_n^{\rm T}$
1	-16.96	0.53	0.3277	0.6723
2	-369.50	1.92	0.4102	0.5898
3	1688	8.95	0.50	0.5

Table A.3 – Parameters of the tensor potential in the FHT interaction.

A.7 Width of a resonance channel state

The width of a resonance channel state in the CC formulation of a Schrödinger equation can be calculated from the conservation of the flux of particles in space [118,271]. Multiplying the Schrödinger equation from the right by $u_c^*(r)$:

$$u_c^*(r)\left(\frac{\partial^2}{\partial r^2} - \frac{l(l+1)}{r^2} - \frac{j(j+1)}{I} + \frac{2m_e}{\hbar^2}E\right)u_c(r) = \frac{2m_e}{\hbar^2}u_c^*(r)\sum_{c'}V_{c,c'}(r)u_{c'}(r) \tag{A.90}$$

and substracting the complex conjugate of this equation, one finds:

$$u''_c(r)u_c^*(r) - u''^*_c(r)u_c(r) = -i\Gamma\frac{2m_e}{\hbar^2}u_c(r)u_c^*(r) + \sum_{c'}V_{c,c'}(r)(u_{c'}(r)u_c^*(r) - u_{c'}^*(r)u_c(r)) \tag{A.91}$$

where $E = \Re(E) + i\Gamma/2$. Then Eq.(A.91) is integrated over r' in the interval $[0, r]$:

$$\begin{aligned}\int_0^r dr'\,&(u''_c(r')u_c^*(r') - u''^*_c(r')u_c(r')) \\ &= -i\Gamma\frac{2m_e}{\hbar^2}\int_0^r dr'\,|u_c(r')|^2 + \sum_{c'}\int_0^r dr'\,V_{c,c'}(r')(u_{c'}(r')u_c^*(r') - u_{c'}^*(r')u_c(r'))\end{aligned} \tag{A.92}$$

But clearly:

$$\int_0^r dr'\,(u''_c(r')u_c^*(r') - u''^*_c(r')u_c(r')) = u'_c(r)u_c^*(r) - u'^*_c(r)u_c(r) \tag{A.93}$$

and:

$$\sum_{c,c'}\int_0^r dr'\,V_{c,c'}(r')(u_{c'}(r')u_c^*(r') - u_{c'}^*(r')u_c(r')) = 0 \tag{A.94}$$

Thus by summing over the channels c, the final expression of the width is:

$$\Gamma(r) = i\frac{\hbar^2}{2m_e}\frac{\sum_c u'_c(r)u_c^*(r) - u'^*_c(r)u_c(r)}{\sum_{c'}\int_0^r dr'\,|u_c(r')|^2} \tag{A.95}$$

Bibliography

[1] J. Dobaczewski, N. Michel, W. Nazarewicz, M. Płoszajczak, and J. Rotureau. Shell structure of exotic nuclei. *Prog. Part. Nucl. Phys.* ***59****, 432 (2007).*

[2] M. Hjorth-Jensen W. Nazarewicz C. Forssén, G. Hagen and J. Rotureau. Living on the edge of stability, the limits of the nuclear landscape. *Phys. Scr. T* ***152****, 014022 (2013).*

[3] I. Tanihata. Nuclear structure studies using high-energy radioactive nuclear beams. Radii and nucleon momentum distributions of exotic nuclei. *Nucl. Phys. A* ***478****, 795c (1988).*

[4] M. V. Zhukov, B. V. Danilin, D. V. Fedorov, J. M. Bang, I. J. Thompson, and J. S. Vaagen. Bound state properties of Borromean halo nuclei: ^{6}He and ^{11}Li. *Phys. Rep.* ***231****, 151 (1993).*

[5] M. Theis, G. Thalhammer, K. Winkler, M. Hellwig, G. Ruff, R. Grimm, and J. Hecker Denschlag. Tuning the scattering length with an optically induced Feshbach resonance. *Phys. Rev. Lett.* ***93****, 123001 (2004).*

[6] J. Main and G. Wunner. Rydberg atoms in external fields as an example of open quantum systems with classical chaos. *J. Phys. B: At. Mol. Opt. Phys.* ***27****, 2835 (1994).*

[7] В. И. Ефимов. Слабосвязанные состояния трех резонансно взаимодействующих частиц. Ядерная Физика ***12****, 1080 (1970).*

[8] E. Braaten and H. W. Hammer. Universality in few-body systems with large scattering length. *Phys. Rep.* ***428****, 259 (2006).*

[9] T. Kraemer, M. Mark, P. Waldburger, J. G. Danzl, C. Chin, B. Engeser, A. D. Lange, K. Pilch, A. Jaakkola, H. C. Nägerl, and R. Grimm. Evidence for Efimov quantum states in an ultracold gas of caesium atoms. *Nature* ***440****, 315 (2006).*

[10] R. H. Dicke. Coherence in spontaneous radiation processes. *Phys. Rev.* ***93****, 99 (1954).*

[11] N. Auerbach and V. Zelevinsky. Super-radiant dynamics, doorways and resonances in nuclei and other open mesoscopic systems. *Rep. Prog. Phys.* ***74****, 106301 (2011).*

[12] T. Kato. *Perturbation theory for linear operators.* Springer, 1995.

[13] M. R. Zirnbauer, J. J. M. Verbaarschot, and H. A. Weidenmüller. Destruction of order in nuclear spectra by a residual GOE interaction. *Nucl. Phys. A* ***411****, 161 (1983).*

[14] C. Dembowski, B. Dietz, H. D. Gräf, H. L. Harney, A. Heine, W. D. Heiss, and A. Richter. Observation of a chiral state in a microwave cavity. *Phys. Rev. Lett.* ***90****, 034101 (2003).*

[15] J. Okołowicz, M. Płoszajczak, and W. Nazarewicz. On the origin of nuclear clustering. *Prog. Theor. Phys. Supp.* ***196****, 230 (2012).*

[16] J. Okołowicz, W. Nazarewicz, and M. Płoszajczak. Toward understanding the microscopic origin of nuclear clustering. *Fortschr. Phys.* ***61****, 66 (2013).*

[17] N. Moiseyev. *Non-Hermitian quantum mechanics.* Cambridge University Press, 2011.

[18] M. Goeppert-Mayer. On closed shells in nuclei. *Phys. Rev.* ***74****, 235 (1948).*

[19] M. Goeppert-Mayer. On closed shells in nuclei. II. *Phys. Rev.* ***75****, 1969 (1949).*

[20] J. H. D. Jensen O. Haxel and H. E. Suess. On the "magic numbers" in nuclear structure. *Phys. Rev.* ***75****, 1766 (1949).*

[21] H. Feshbach. Unified theory of nuclear reactions. *Ann. Phys.* ***5****, 357 (1958).*

[22] H. Feshbach. A unified theory of nuclear reactions II. *Ann. Phys.* ***19****, 287 (1962).*

[23] H. Feshbach. The unified theory of nuclear reactions III. Overlapping resonances. *Ann. Phys.* ***43****, 410 (1967).*

[24] C. Mahaux and H. A. Weidenmüller. *Shell-model approach to nuclear reactions.* North-Holland Pub. Co., 1969.

[25] H. W. Barz, I. Rotter, and J. Höhn. Coupled channels calculations in the continuum shell model with complicated configurations. *Nucl. Phys. A* ***275****, 111 (1977).*

[26] I. Rotter, H. W. Barz, and J. Höhn. Threshold effects in nuclear reactions and the line shape of resonances. *Nucl. Phys. A* ***297****, 237 (1978).*

[27] K. Bennaceur, N. Michel, F. Nowacki, J. Okołowicz, and M. Płoszajczak. Shell model description of $^{16}\mathrm{O}(p,\gamma)^{17}\mathrm{F}$ and $^{16}\mathrm{O}(p,p)^{16}\mathrm{O}$ reactions. *Phys. Lett. B* ***488****, 75 (2000).*

[28] J. Okołowicz, M. Płoszajczak, and I. Rotter. Dynamics of quantum systems embedded in a continuum. *Phys. Rep.* ***374****, 271 (2003).*

[29] N. Michel, W. Nazarewicz, M. Płoszajczak, and K. Bennaceur. Gamow shell model description of neutron-rich nuclei. *Phys. Rev. Lett.* ***89****, 042502 (2002).*

[30] R. Id Betan, R. J. Liotta, N. Sandulescu, and T. Vertse. Two-particle resonant states in a many-body mean field. *Phys. Rev. Lett.* ***89****, 042501 (2002).*

[31] N. Michel, W. Nazarewicz, M. Płoszajczak, and T. Vertse. Shell model in the complex energy plane. *J. Phys. G: Nucl. Part. Phys.* ***36****, 013101 (2009).*

[32] T. Berggren. On the use of resonant states in eigenfunction expansions of scattering and reaction amplitudes. *Nucl. Phys. A* ***109****, 265 (1968).*

[33] T. Berggren. Completeness relations, Mittag-Leffler expansions and the perturbation theory of resonant states. *Nucl. Phys. A* ***389****, 261 (1982).*

[34] P. Navrátil and B. R. Barrett. No-core shell model calculations with starting-energy-independent multivalued effective interactions. *Phys. Rev. C.* ***54****, 2986 (1996).*

[35] S. Quaglioni and P. Navrátil. *Ab initio* many-body calculations of nucleon-nucleus scattering. *Phys. Rev. C.* ***79****, 044606 (2009).*

[36] P. Navrátil, S. Quaglioni, I. Stetcu, and B. R. Barrett. Recent developments in no-core shell model calculations. *J. Phys. G: Nucl. Part. Phys.* ***36****, 083101 (2009).*

[37] H. Kümmel, K. H. Lührmann, and J. G. Zabolitzky. Many-fermion theory in exp S-(or coupled cluster) form. *Phys. Rep.* ***36****, 1 (1978).*

[38] D. J. Dean and M. Hjorth-Jensen. Coupled-cluster approach to nuclear physics. *Phys. Rev. C* ***69****, 054320 (2004).*

[39] R. J. Bartlett and M. Musial. Coupled-cluster theory in quantum chemistry. *Rev. Mod. Phys.* ***79****, 291 (2007).*

[40] G. Papadimitriou, J. Rotureau, N. Michel, M. Płoszajczak, and B. R. Barrett. Ab-initio no-core Gamow shell model calculations with realistic interactions. *Phys. Rev. C* ***88****, 044318 (2013).*

[41] J. A. Wheeler. On the mathematical description of light nuclei by the method of resonating group structure. *Phys. Rev.* ***52****, 1107 (1937).*

[42] K. Wildermuth and Y. C. Tang. *A unified theory of the nucleus.* Academic Press, 1977.

[43] S. Quaglioni and P. Navrátil. *Ab initio* many-body calculations of $n-{}^3$H, $n-{}^4$He, $p-{}^{3,4}$He, and $n-{}^{10}$Be scattering. *Phys. Rev. Lett.* ***101****, 092501 (2008).*

[44] G. Hagen, T. Papenbrock, M. Hjorth-Jensen, and D. J. Dean. Coupled-cluster computations of atomic nuclei. *Rep. Prog. Phys.* ***77****, 096302 (2014).*

[45] Y. Jaganathen, N. Michel, and M. Płoszajczak. Gamow shell model description of proton scattering on ^{18}Ne. *Phys. Rev. C* ***89****, 034624 (2014).*

[46] I. M. Gel'fand, G. E. Shilov, N. Ya. Vilenkin, and M. I. Graev. *Generalized functions.* Academic Press , New-York, 1964.

[47] K. Maurin. *Generalized Eigenfunction expansions and unitary representations of topological groups.* Polish Scientific Publishers, Warsaw, 1968.

[48] A. Böhm. *The rigged Hilbert space and quantum mechanics.* Lect. Notes in Phys. 78, Springer, New York, 1978.

[49] W. R. Garrett. Critical binding of electron-dipole rotor systems; electronically excited states. *J. Chem. Phys.* ***73****, 5721 (1980).*

[50] W. R. Garrett. Critical binding of an electron by a non-stationary, point-dipole rotor. *Phys. Rev. A* ***22****, 1769 (1980).*

[51] W. R. Garrett. Critical binding of an electron to a non-stationary electric dipole. *Chem. Phys. Lett.* ***5****, 393 (1970).*

[52] W. R. Garrett. Critical binding of an electron to a rotationally excited dipolar system. *Phys. Rev. A* ***3****, 961 (1971).*

[53] K. Fossez, N. Michel, W. Nazarewicz, and M. Płoszajczak. Bound states of dipolar molecules studied with the Berggren expansion method. *Phys. Rev. A* ***87****, 042515 (2013).*

[54] K. Fossez, N. Michel, W. Nazarewicz, M. Płoszajczak, and Y. Jaganathen. Bound and resonance states of the dipolar anion of hydrogen cyanide: competition between threshold effects and rotation in an open quantum system. *To be published.*

[55] J. H. Bartlett Jr. Structure of atomic nuclei. *Phys. Rev.* ***41****, 370 (1932).*

[56] J. H. Bartlett Jr. Structure of atomic nuclei. II. *Phys. Rev.* ***42****, 145 (1932).*

[57] W. M. Elsasser. Sur le principe de Pauli dans les noyaux. *J. Phys. Radium* ***4***, *549 (1933).*

[58] W. M. Elsasser. Sur le principe de Pauli dans les noyaux. II. *J. Phys. Radium* ***5***, *389 (1934).*

[59] W. M. Elsasser. Sur le principe de Pauli dans les noyaux. III. *J. Phys. Radium* ***5***, *635 (1934).*

[60] B. A. Brown. The nuclear shell model towards the drip lines. *Prog. Part. Nucl. Phys.* ***47***, *517 (2001).*

[61] F. Nowacki A. Poves E. Caurier, G. Martinez-Pinedo and A. P. Zuker. The shell model as a unified view of nuclear structure. *Rev. Mod. Phys.* ***77***, *427 (2005).*

[62] U. Fano. Effects of configuration interaction on intensities and phase shifts. *Phys. Rev.* ***124***, *1866 (1961).*

[63] R. J. Philpott. Continuum shell model with full correction for target recoil. *Nucl. Phys. A* ***289***, *109 (1977).*

[64] D. Halderson and R. J. Philpott. Recoil corrected continuum shell model calculations for four-nucleon systems. *Nucl. Phys. A* ***321***, *295 (1979).*

[65] I. Rotter. A continuum shell model for the open quantum mechanical nuclear system. *Rep. Prog. Phys.* ***54***, *635 (1991).*

[66] K. Bennaceur, F. Nowacki, J. Okołowicz, and M. Płoszajczak. A study of nuclei of astrophysical interest in the continuum shell model. *J. Phys. G* ***24***, *1631 (1998).*

[67] K. Bennaceur, F. Nowacki, J. Okołowicz, and M. Płoszajczak. Study of the ^{7}Be$(p,\gamma)^{8}$B and ^{7}Li$(n,\gamma)^{8}$Li capture reactions using the shell model embedded in the continuum. *Nucl. Phys. A* ***651***, *289 (1999).*

[68] K. Bennaceur, F. Nowacki, J. Okołowicz, and M. Płoszajczak. Analysis of the ^{16}O$(p,\gamma)^{17}$F capture reaction using the shell model embedded in the continuum. *Nucl. Phys. A* ***671***, *203 (2000).*

[69] R. Shyam, K. Bennaceur, J. Okołowicz, and M. Płoszajczak. Structure effects on the Coulomb dissociation of ^{8}B at relativistic energies. *Nucl. Phys. A* ***669***, *65 (2000).*

[70] N. Michel, J. Okołowicz, F. Nowacki, and M. Płoszajczak. First-forbidden mirror beta-decays in $A = 17$ mass region. *Nucl. Phys. A* ***703***, *202 (2002).*

[71] J. Rotureau, J. Okołowicz, and M. Płoszajczak. Microscopic theory of the two-proton radioactivity. *Phys. Rev. Lett.* ***95***, *042503 (2005).*

[72] J. Rotureau, J. Okołowicz, and M. Płoszajczak. Theory of the two-proton radioactivity in the continuum shell model. *Nucl. Phys. A* ***767***, *13 (2006).*

[73] R. Chatterjee, J. Okołowicz, and M. Płoszajczak. Description of the ^{17}F$(p,\gamma)^{18}$Ne radiative capture reaction in the continuum shell model. *Nucl. Phys. A* ***764***, *528 (2006).*

[74] B. Blank and M. Płoszajczak. Two-proton radioactivity. *Rep. Prog. Phys.* ***71***, *046301 (2008).*

[75] J. Okołowicz and M. Płoszajczak. Exceptional points in the scattering continuum. *Phys. Rev. C* ***80***, *034619 (2009).*

[76] J. Okołowicz, N. Michel, W. Nazarewicz, and M. Płoszajczak. Asymptotic normalization coefficients and continuum coupling in mirror nuclei. *Phys. Rev. C* ***85***, *064320 (2012).*

[77] N. Michel, W. Nazarewicz, M. Płoszajczak, and J. Okołowicz. Gamow shell-model description of weakly bound nuclei and unbound nuclear states. *Phys. Rev. C* ***67****, 054311 (2003).*

[78] R. Id Betan, R. J. Liotta, N. Sandulescu, and T. Vertse. Shell model in the complex energy plane and two-particle resonances. *Phys. Rev. C* ***67****, 014322 (2003).*

[79] N. Michel, W. Nazarewicz, and M. Płoszajczak. Proton-neutron coupling in the Gamow shell model: the lithium chain. *Phys. Rev. C* ***70****, 064313 (2004).*

[80] N. Michel, W. Nazarewicz, M. Płoszajczak, and J. Rotureau. Gamow shell-model description of weakly bound and unbound nuclear states. *Revista Mexicana De Fisica* ***5 Suplemento 2****, 74 (2004).*

[81] J. Dobaczewski, N. Michel, W. Nazarewicz, M. Płoszajczak, and M. V. Stoitsov. Structure of exotic nuclei. *A new era of nuclear structure physics , 162 (2004).*

[82] R. Id Betan, R. J. Liotta, N. Sandulescu, and T. Vertse. A shell model representation with antibound states. *Phys. Lett. B* ***584****, 48 (2004).*

[83] G. Hagen, J. S. Vaagen, and M. Hjorth-Jensen. The contour deformation method in momentum space, applied to subatomic physics. *J. Phys. A: Math. Gen.* ***37****, 8991 (2004).*

[84] G. Hagen, M. Hjorth-Jensen, and J. S. Vaagen. Effective interaction techniques for the Gamow shell model. *Phys. Rev. C* ***71****, 044314 (200).*

[85] T. Berggren and P. Lind. Resonant state expansion of the resolvent. *Phys. Rev. C* ***47****, 768 (1993).*

[86] T. Berggren. Expectation value of an operator in a resonant state. *Phys. Lett. B* ***373****, 1 (1996).*

[87] B. Gyarmati and T. Vertse. On the normalization of Gamow functions. *Nucl. Phys. A* ***160****, 523 (1971).*

[88] G. Ludwig. *Foundations of Quantum Mechanics.* Vol. I, Springer, New York, 1983.

[89] G. Ludwig. *Foundations of Quantum Mechanics.* Vol. II, Springer, New York, 1983.

[90] G. Ludwig. *An axiomatic basis for quantum mechanics. Derivation of Hilbert space structure.* Vol. I, Springer, New York, 1985.

[91] G. Ludwig. *An Axiomatic Basis of Quantum Mechanics. Quantum mechanics and macrosystems.* Vol. II, Springer, New York, 1987.

[92] J.-P. Antoine. *Quantum mechanics beyond Hilbert space.* Springer Berlin Heidelberg, 1998.

[93] J.-P. Antoine, A. Böhm, and S. Wickramasekara. *Compendium of quantum physics: Rigged Hilbert spaces for the Dirac formalism of quantum mechanics.* Springer Verlag, Berlin Heidelberg, 2009.

[94] A. M. Lane. Studies in intermediate coupling: III. The lithium isotopes. *Proc. Phys. Soc. A* ***68****, 189 (1955).*

[95] D. Kurath. Intermediate coupling in the 1p-shell. *Phys. Rev.* ***101****, 216 (1956).*

[96] B. A. Loiseau and Y. Nogami. Three-nucleon force. *Nucl. Phys. B* ***2****, 470 (1967).*

[97] R. B. Wiringa, S. C. Pieper, J. Carlson, and V. R. Pandharipande. Quantum Monte Carlo calculations of $A = 8$ nuclei. *Phys. Rev. C* ***62****, 014001 (2000).*

[98] S. C. Pieper, K. Varga, and R. B. Wiringa. Quantum Monte Carlo calculations of $A = 9, 10$ nuclei. *Phys. Rev. C* ***66****, 044310 (2002).*

[99] E. Epelbaum, A. Nogga, W. Glöckle, H. Kamada, Ulf-G. Meißner, and H. Witala. Three-nucleon forces from chiral effective field theory. *Phys. Rev. C* ***66****, 064001 (2002).*

[100] P. Navrátil and W. E. Ormand. *Ab initio* shell model with a genuine three-nucleon force for the *p*-shell nuclei. *Phys. Rev. C* ***68****, 034305 (2003).*

[101] A. P. Zuker. Three-body monopole corrections to realistic interactions. *Phys. Rev. Lett.* ***90****, 042502 (2003).*

[102] T. Otsuka, T. Suzuki, J. D. Holt, A. Schwenk, and Y. Akaishi. Three-body forces and the limit of oxygen isotopes. *Phys. Rev. Lett.* ***105****, 032501 (2010).*

[103] G. Hagen, M. Hjorth-Jensen, G. R. Jansen, R. Machleidt, and T. Papenbrock. Continuum effects and three-nucleon forces in neutron-rich oxygen isotopes. *Phys. Rev. Lett.* ***108****, 242501 (2012).*

[104] H. W. Barz, I. Rotter, and J. Höhn. Shell-model aspects in coupled channel calculations using Feshbach projection technique. *Phys. Lett. B* ***37****, 4 (1971).*

[105] D. Halderson and R. J. Philpott. Radiative capture to ^{4}He. *Nucl. Phys. A* ***359****, 365 (1981).*

[106] A. Volya and V. Zelevinsky. Continuum shell model. *Phys. Rev. C* ***74****, 064314 (2006).*

[107] R. G. Newton. *Scattering theory of waves and particles*. Springer-Verlag, New York Heidelberg Berlin, second edition, 1982.

[108] A. Volya and V. Zelevinsky. Discrete and continuum spectra in the unified shell model approach. *Phys. Rev. Lett.* ***94****, 052501 (2005).*

[109] J. Rotureau. Modèle en couches avec plusieurs particules dans le continuum : description de la radioactivité deux protons. *Thèse de doctorat, Caen (2005).*

[110] S. Baroni, P. Navrátil, and S. Quaglioni. *Ab initio* description of the exotic unbound ^{7}He nucleus. *Phys. Rev. Lett.* ***110****, 022505 (2013).*

[111] S. Baroni, P. Navrátil, and S. Quaglioni. Unified *ab initio* approach to bound and unbound states: No-core shell model with continuum and its application to ^{7}He. *Phys. Rev. C* ***87****, 034326 (2013).*

[112] N. Michel, W. Nazarewicz, M. Płoszajczak, and J. Rotureau. Antibound states and halo formation in the Gamow shell model. *Phys. Rev. C* ***74****, 054305 (2006).*

[113] N. Michel, W. Nazarewicz, and M. Płoszajczak. Isospin mixing and the continuum coupling in weakly bound nuclei. *Phys. Rev. C* ***82****, 044315 (2010).*

[114] R. Id Betan, R. J. Liotta, N. Sandulescu, T. Vertse, and R. Wyss. Complex shell model representation including antibound states. *Phys. Rev. C* ***72****, 054322 (2005).*

[115] G. Gamow. Zur Quantentheorie des Atomkernes. *Z. Physik* ***51****, 204 (1928).*

[116] A. F. J. Siegert. On the derivation of the dispersion formula for nuclear reactions. *Phys. Rev.* ***56****, 750 (1939).*

[117] G. Breit and E. Wigner. Capture of slow neutrons. *Phys. Rev.* ***49****, 519 (1936).*

[118] J. Humblet and L. Rosenfeld. Theory of nuclear reactions I. Resonant states and collision matrix. *Nucl. Phys.* ***26****, 529 (1961).*

[119] K. Sasada. Spectrum analysis of the conductance of open quantum dots. *PhD thesis, University of Tokyo (2007).*

[120] A. Böhm, M. Gadella, and S. Maxson. Extending the stationary quantum mechanics of being to a nonstationary quantum theory of becoming and decaying. *Computers Math. Applic.* ***34****, 427 (1997).*

[121] R. E. Peierls. Interpretation and properties of propagators. *Proc. Glasgow Conf. Nucl. Meson Phys., 296 (1954) , 296 (1954).*

[122] P. A. M. Dirac. *The principles of quantum mechanics.* Clarendon press, Oxford, 4th ed. edition, 1958.

[123] J. von Neumann. *Foundations of quantum mechanics.* Princeton university press, Princeton, 1955.

[124] J. von Neumann. On rings of operators. Reduction theory. *Ann. Math. Phys.* ***50****, 401 (1949).*

[125] M. Gadella and F. Gómez. A unified mathematical formalism for the Dirac formulation of quantum mechanics. *Found. Phys.* ***32****, 815 (2002).*

[126] L. C. Mejlbo. On the solution of the commutation relation $PQ - QP = -iI$. *Math. Scand.* ***13****, 129 (1963).*

[127] P. Kristensen, L. Mejlbo, and E. Thue Poulsen. Tempered distributions in infinitely many dimensions II, displacement operators. *Math. Scand.* ***14****, 129 (1964).*

[128] P. Kristensen, L. Mejlbo, and E. Thue Poulsen. Tempered distributions in infinitely many dimensions I. Canonical field operators. *Commun. math. Phys.* ***1****, 175 (1965).*

[129] L. Schwartz. *Théorie des distributions.* Hermann, Paris, 1966.

[130] A. Böhm. Rigged Hilbert spaces. *Int. Cent. Theor. Phys. (ICTP)* ***64/9****, 1 (1964).*

[131] J. E. Roberts. The Dirac bra and ket formalism. *J. Math. Phys.* ***7****, 1097 (1966).*

[132] J. E. Roberts. Rigged Hilbert spaces in quantum mechanics. *Commun. math. Phys.* ***3****, 98 (1966).*

[133] J. P. Antoine. Dirac formalism and symmetry problems in quantum mechanics. I. General Dirac formalism. *J. Math. Phys.* ***10****, 53 (1969).*

[134] J. P. Antoine. Dirac formalism and symmetry problems in quantum mechanics. II. Symmetry problems. *J. Math. Phys.* ***10****, 2276 (1969).*

[135] O. Melsheimer. Rigged Hilbert space formalism as an extended mathematical formalism for quantum systems. I. General theory. *J. Math. Phys.* ***15****, 902 (1974).*

[136] O. Melsheimer. Rigged Hilbert space formalism as an extended mathematical formalism for quantum systems. II. Transformation theory in nonrelativistic quantum mechanics. *J. Math. Phys.* ***15****, 917 (1974).*

[137] R. de la Madrid. On the inconsistency of the Bohm-Gadella theory with quantum mechanics. *J. Phys. A: Math. Gen.* ***39****, 9255 (2006).*

[138] R. de la Madrid. The rigged Hilbert space approach to the Gamow states. *J. Math. Phys.* ***53****, 102113 (2012).*

[139] R. de la Madrid. Time as a dynamical variable in quantum decay. *Nucl. Phys. A* ***913****, 217 (2013).*

[140] N. N. Bogolubov, A. A. Logunov, and I. T. Todorov. *Introduction to axiomatic quantum field theory.* W. A. Benjamin, Reading, Massachusetts, 1975.

[141] A. D. Dubin and M. A. Hennings. *Quantum mechanics, algebras and distributions.* CRC Press Inc., 1990.

[142] A. Böhm. *Quantum mechanics: Foundations and applications.* Springer, New York, 3rd ed. edition, 1993.

[143] L. E. Ballentine. *Quantum mechanics. A modern development.* world Scientific Publishing Co. Pte. Ltd., 1998.

[144] A. Z. Capri. *Nonrelativistic quantum mechanics.* World Scientific Pub. Co. Inc., 3rd ed. edition, 2003.

[145] R. de la Madrid. The resonance amplitude associated with the Gamow states. *Nucl. Phys. A* ***812****, 13 (2008).*

[146] A. Böhm. Resonance poles and Gamow vectors in the rigged Hilbert space formulation of quantum mechanics. *J. Math. Phys.* ***22****, 2813 (1981).*

[147] A. Böhm and M. Gadella. Dirac kets, Gamow vectors and Gel'fand triplets. *Lect. Notes in Phys.* ***348****, 1 (1989).*

[148] O. Civitarese and M. Gadella. Physical and mathematical aspects of Gamow states. *Phys. Rep.* ***396****, 41 (2004).*

[149] J. P. Antoine. Chapter I: Quantum theory beyond Hilbert space. *Lect. Notes Phys.* ***504****, 1 (1998).*

[150] Я. Б. Зельдович [Ya. B. Zel'dovich]. К теории нестабильных состояний [on the theory of unstable states]. ЖЭТФ ***39****, 776 (1961) [JETP* ***12****, 542 (1961)].*

[151] N. Michel. Direct demonstration of the completeness of the eigenstates of the Schrödinger equation with local and non-local potentials bearing a Coulomb tail. *J. Math. Phys.* ***49****, 022109 (2008).*

[152] J. R. Taylor. *Scattering theory: The quantum theory on nonrelativistic collisions.* John Wiley and Sons, Inc., New York, 1972.

[153] V. I. Kukulin. *Theory of resonances: Principles and applications.* Springer Verlag, 1989.

[154] W. D. Heiss and R. G. Nazmitdinov. Spectral singularities and zero energy bound states. *Eur. Phys. J. D.* ***63****, 369 (2011).*

[155] N. Moiseyev. Quantum theory of resonances: calculating energies, widths and cross-sections by complex scaling. *Phys. Rep.* ***302****, 212 (1998).*

[156] N. Hokkyo. A remark on the norm of the unstable state. A role of adjoint wave functions in non–self-adjoint quantum systems. *Prog. Theor. Phys.* ***33****, 1116 (1965).*

[157] W. J. Romo. Inner product for resonant states and shell-model applications. *Nucl. Phys. A* ***116****, 617 (1968).*

[158] G. Garcia-Calderon and R. Peierls. Resonant states and their uses. *Nucl. Phys. A* ***265****, 443 (1976).*

[159] B. Gyarmati. Decaying states. A tribute to Tore Berggren's memory on the occasion of the 40th anniversary of his seminal paper. *Int. Workshop on Many-body open quantum systems: From atomic nuclei to quantum dots , (2007).*

[160] W. P. Reinhardt. Complex coordinates in the theory of atomic and molecular structure and dynamics. *Ann. Rev. Phys. Chem.* ***33****, 223 (1982).*

[161] J. Aguilar and J. M. Combes. A class of analytic perturbations for one-body Schrödinger Hamiltonians. *Commun. Math. Phys.* ***22****, 269 (1971).*

[162] E. Balslev and J. M. Combes. Spectral properties of many-body Schrödinger operators with dilatation-analytic interaction. *Commun. Math. Phys.* ***22****, 280 (1971).*

[163] B. Simon. Quadratic form techniques and the Balslev-Combes theorem. *Commun. Math. Phys.* ***27****, 1 (1972).*

[164] D. Babbitt and E. Balslev. A characterization of dilatation-analytic potentials and vectors. *J. Func. Anal.* ***18****, 1 (1975).*

[165] B. Simon. The definition of molecular resonance curves by the method of exterior complex scaling. *Phys. Lett. A* ***71****, 211 (1979).*

[166] T. Berggren. On the interpretation of complex cross sections for production of resonant final states. *Phys. Lett. B* ***73****, 389 (1978).*

[167] A. Böhm. Time asymmetry and quantum theory of resonances and decay. *Int. J. Theor. Phys.* ***42****, 2317 (2003).*

[168] A. Bürgers and J. M. Rost. Complex expectation values and Lewis structures for resonant states. *J. Phys. B: At. Mol. Opt. Phys.* ***29****, 3825 (1996).*

[169] R. D. Lawson. *Theory of the nuclear shell model.* Clarendon Press, 1980.

[170] H. J. Lipkin. Center-of-mass motion in the nuclear shell model. *Phys. Rev.* ***110****, 1395 (1958).*

[171] R. R. Whitehead, A. Watt, B. J. Cole, and I. Morrison. Computational methods for shell-model calculations. *Adv. Nucl. Phys.* ***9****, 123 (1977).*

[172] Y. Suzuki and K. Ikeda. Cluster-orbital shell model and its application to the He isotopes. *Phys. Rev. C* ***38****, 410 (1988).*

[173] C. Lanczos. An iteration method for the solution of the eigenvalue problem of linear differential and integral operators. *Journal of Research of the National Bureau of Standards* ***45****, 255 (1950).*

[174] E. R. Davidson. The iterative calculation of a few of the lowest eigenvalues and corresponding eigenvectors of large real-symmetric matrices. *J. Comput. Phys.* ***17****, 87 (1975).*

[175] N. Michel, W. Nazarewicz, and M. Płoszajczak. Threshold effects in multi-channel coupling and spectroscopic factors in exotic nuclei. *Phys. Rev. C* ***75****, 031301(R) (2007).*

[176] N. Michel, W. Nazarewicz, and M. Płoszajczak. Continuum coupling and single-nucleon overlap integrals. *Nucl. Phys. A* ***794****, 29 (2007).*

[177] G. Papadimitriou, A. T. Kruppa, N. Michel, W. Nazarewicz, M. Płoszajczak, and J. Rotureau. Charge radii and neutron correlation in helium halo nuclei. *Phys. Rev. C* ***84****, 051304(R) (2011).*

[178] K. Suzuki and S. Y. Lee. Convergent theory for effective interaction in nuclei. *Prog. Theor. Phys.* ***64****, 2091 (1980).*

[179] G. Hagen, M. Hjorth-Jensen, and J. S. Vaagen. State-dependent interactions for the Gamow shell model. *J. Phys. G: Nucl. Part. Phys.* ***31****, S1337 (2005).*

[180] G. Hagen, M. Hjorth-Jensen, and N. Michel. Gamow shell model and realistic nucleon-nucleon interactions. *Phys. Rev. C* ***73****, 064307 (2006).*

[181] H. Masui, K. Katō, N. Michel, and M. Płoszajczak. Precise comparison of the gaussian expansion method and the gamow shell model. *Phys. Rev. C* ***89****, 044317 (2014).*

[182] J. Rotureau, N. Michel, W. Nazarewicz, M. Płoszajczak, and J. Dukelsky. Density matrix renormalisation group approach for many-body open quantum systems. *Phys. Rev. Lett.* ***97****, 110603 (2006).*

[183] J. Rotureau, N. Michel, W. Nazarewicz, M. Płoszajczak, and J. Dukelsky. Density matrix renormalization group approach to two-fluid open many-fermion systems. *Phys. Rev. C* ***79****, 014304 (2009).*

[184] H. Friedrich. *Theoretical atomic physics.* Springer-Verlag, third ed., 2006.

[185] P. Fröbrich and R. Lipperheide. *Theory of nuclear reactions.* Clarendon press, Oxford, 1996.

[186] S. Saito. Chap. II: Theory of resonating group method and generator coordinate method, and orthogonality condition model. *Suppl. Prog. Theor. Phys.* ***62****, 11 (1977).*

[187] Y. C. Tang, M. Le Mere, and D. R. Thompson. Resonating-group method for nuclear many-body problems. *Phys. Rep.* ***47****, 167 (1978).*

[188] T. Fliessbach and H. Walliser. The structure of the resonating group equation. *Nucl. Phys. A* ***377****, 84 (1982).*

[189] J. M. Hutson. Coupled channel methods for solving the bound-state Schrödinger equation. *Comp. Phys. Commun.* ***84****, 1 (1994).*

[190] I. J. Thompson. Coupled reaction channels calculations in nuclear physics. *Comput. Phys. Rep.* ***7****, 167 (1988).*

[191] Y. Jaganathen, N. Michel, and M. Płoszajczak. Weakly bound systems, continuum effects, and reactions. *J. Phys.: Conf. Series* ***403****, 012022 (2012).*

[192] N. Michel. A simple and efficient numerical scheme to integrate non-local potentials. *Eur. Phys. J. A* ***42****, 523 (2009).*

[193] J. Stoer and R. Bulirsch. *Introduction to numerical analysis.* Springer-Verlag, New York Berlin Heidelberg, 1991.

[194] K. Hagino and H. Sagawa. Continuum QRPA in the coordinate space representation. *Nucl. Phys. A* ***695****, 82 (2001).*

[195] E. Khan, N. Sandulescu, M. Grasso, and Nguyen Van Giai. Continuum quasiparticle random phase approximation and the time-dependent Hartree-Fock-Bogoliubov approach. *Phys. Rev. C* ***66****, 024309 (2002).*

[196] K. Hagino, Nguyen Van Giai, and H. Sagawa. Continuum QRPA response for deformed neutron-rich nuclei. *Nucl. Phys. A* ***731****, 264 (2004).*

[197] G. G. Dussel, R. Id Betan, R. J. Liotta, and T. Vertse. One- and two-quasiparticle states in the complex energy plane. *Nucl. Phys. A* ***789****, 182 (2007).*

[198] V. D. Efros, W. Leidemann, and G. Orlandini. Response functions from integral transforms with a Lorentz kernel. *Phys. Lett. B* ***338****, 130 (1994).*

[199] V. D. Efros, W. Leidemann, G. Orlandini, and N. Barnea. The Lorents integral transform (LIT) method and its applications to perturbation-induced reactions. *J. Phys. G: Nucl. Part. Phys* ***34****, R459 (2007).*

[200] K. M. Nollett, S. C. Pieper, and R. B. Wiringa. Quantum Monte Carlo calculations of neutron-α scattering. *Phys. Rev. Lett.* ***99****, 022502 (2007).*

[201] G. Hagen, T. Papenbrock, D. J. Dean, and M. Hjorth-Jensen. Medium-mass nuclei from chiral nucleon-nucleon interactions. *Phys. Rev. Lett.* ***101****, 092502 (2008).*

[202] R. Machleidt and D. R. Entem. Chiral effective field theory and nuclear forces. *Phys. Rep.* ***503****, 1 (2011).*

[203] G. Hagen, D. J. Dean, M. Hjorth-Jensen, and T. Papenbrock. Complex coupled-cluster approach to an *ab initio* description of open quantum systems. *Phys. Lett. B* ***656****, 169 (2007).*

[204] G. Hagen, T. Papenbrock, and M. Hjorth-Jensen. *Ab initio* computation of the ^{17}F proton halo state and resonances in $A = 17$ nuclei. *Phys. Rev. Lett.* ***104****, 182501 (2010).*

[205] G. Hagen and N. Michel. Elastic proton scattering of medium mass nuclei from coupled-cluster theory. *Phys. Rev. C* ***86****, 021602(R) (2012).*

[206] G. Hagen, M. Hjorth-Jensen, G. R. Jansen, R. Machleidt, and T. Papenbrock. Evolution of shell structure in neutron-rich calcium isotope. *Phys. Rev. Lett.* ***109****, 032502 (2012).*

[207] P. Navrátil, R. Roth, and S. Quaglioni. *Ab initio* many-body calculations of nucleon scattering on ^{4}He, ^{7}Li, ^{7}Be, ^{12}C, and ^{16}O. *Phys. Rev. C* ***82****, 034609 (2010).*

[208] R. Roth P. Navrátil and S. Quaglioni. *Ab initio* many-body calculation of the ^{7}Be$(p,\gamma)^{8}$B radiative capture. *Phys. Lett. B* ***704****, 379 (2011).*

[209] P. Navrátil and S. Quaglioni. *Ab initio* many-body calculations of deuteron- ^{4}He scattering and ^{6}He states. *Phys. Rev. C.* ***83****, 044609 (2011).*

[210] P. Navrátil and S. Quaglioni. *Ab initio* many-body calculations of the ^{3}H$(d,n)^{4}$He and ^{3}He$(d,p)^{4}$He fusion reactions. *Phys. Rev. Lett* ***108****, 042503 (2012).*

[211] S. Quaglioni, P. Navrátil, R. Roth, and W. Horiuchi. From nucleons to nuclei to fusion reactions. *J. Phys.: Conf. Ser.* ***402****, 012037 (2012).*

[212] A. Aprahamian, K. Langanke, and M. Wiescher. Nuclear structure aspects in nuclear astrophysics. *Prog. Part. Nucl. Phys.* ***54****, 535 (2005).*

[213] H. Grawe, K. Langanke, and G. Martínez-Pinedo. Nuclear structure and astrophysics. *Rep. Prog. Phys.* ***70****, 1525 (2007).*

[214] C. A. Bertulani and A. Gade. Nuclear astrophysics with radioactive beams. *Phys. Rep.* ***485****, 195 (2010).*

[215] E. G. Adelberger, A. Garcia, R. G. H. Robertson, K. A. Snover, A. B. Balantekin, K. Heeger, M. J. Ramsey-Musolf, D. Bemmerer, A. Junghans, C. A. Bertulani, J. W. Chen, H. Costantini, P. Prati, M. Couder, E. Uberseder, M. Wiescher, R. Cyburt, B. Davids, S. J. Freedman, M. Gai, D. Gazit, L. Gialanella, G. Imbriani, U. Greife, M. Hass, W. C. Haxton, T. Itahashi, K. Kubodera, K. Langanke, D. Leitner, M. Leitner, P. Vetter, L. Winslow, L. E. Marcucci, T. Motobayashi, A. Mukhamedzhanov, R. E. Tribble, K. M. Nollet, F. M. Nunes, T. S. Park, P. D. Parker, R. Schiavilla, E. C. Simpson, C. Spitaleri, F. Strieder, H. P. Trautvetter, K. Suemmere, and S. Typel. Solar fusion cross sections. II. The *pp* chain and CNO cycles. *Rev. Mod. Phys.* ***83****, 195 (2011).*

[216] S. Parete-Koon, W. R. Hix, M. S. Smith, S. Starrfield, D. W. Bardayan, M. W. Guidry, and A. Mezzacappa. A new $^{17}\mathrm{F}(p,\gamma)^{18}\mathrm{Ne}$ reaction rate and its implications for nova nucleosynthesis. *The Astrophysical Journal* ***598****, 1239 (2003).*

[217] R. K. Wallace and S. E. Woosley. Explosive hydrogen burning. *The Astrophysical Journal Suppl. Ser.* ***45****, 389 (1981).*

[218] M. Dufour and P. Descouvemont. The $^{17}\mathrm{F}(p,\gamma)^{18}\mathrm{Ne}$ reaction at stellar energies. *Nucl. Phys. A 730, 316 (2004).*

[219] S. N. Ahmed, A. E. Anthony, E. W. Beier, A. Bellerive, S. D. Biller, J. Boger, M. G. Boulay, M. G. Bowler, T. J. Bowles, S. J. Brice, T. V. Bullard, Y. D. Chan, M. Chen, X. Chen, B. T. Cleveland, G. A. Cox, X. Dai, F. Dalnoki-Veress, P. J. Doe, R. S. Dosanjh, G. Doucas, M. R. Dragowsky, C. A. Duba, F. A. Duncan, M. Dunford, J. A. Dunmore, E. D. Earle, S. R. Elliott, H. C. Evans, G. T. Ewan, J. Farine, H. Fergani, F. Fleurot, J. A. Formaggio, M. M. Fowler, K. Frame, B. G. Fulsom, N. Gagnon, K. Graham, D. R. Grant, R. L. Hahn, J. C. Hall, A. L. Hallin, E. D. Hallman, A. S. Hamer, W. B. Handler, C. K. Hargrove, P. J. Harvey, R. Hazama, K. M. Heeger, W. J. Heintzelman, J. Heise, R. L. Helmer, R. J. Hemingway, A. Hime, M. A. Howe, P. Jagam, N. A. Jelley, J. R. Klein, M. S. Kos, A. V. Krumins, T. Kutter, C. C. M. Kyba, H. Labranche, R. Lange, J. Law, I. T. Lawson, K. T. Lesko, J. R. Leslie, I. Levine, S. Luoma, R. MacLellan, S. Majerus, H. B. Mak, J. Maneira, A. D. Marino, N. McCauley, A. B. McDonald, S. McGee, G. McGregor, C. Mifflin, K. K. S. Miknaitis, G. G. Miller, B. A. Moffat, C. W. Nally, B. G. Nickel, A. J. Noble, E. B. Norman, N. S. Oblath, C. E. Okada, R. W. Ollerhead, J. L. Orrell, S. M. Oser, C. Ouellet, S. J. M. Peeters, A. W. P. Poon, B. C. Robertson, R. G. H. Robertson, E. Rollin, S. S. E. Rosendahl, V. L. Rusu, M. H. Schwendener, O. Simard, J. J. Simpson, C. J. Sims, D. Sinclair, P. Skensved, M. W. E. Smith, N. Starinsky, R. G. Stokstad, L. C. Stonehill, R. Tafirout, Y. Takeuchi, G. Tešić, M. Thomson, M. Thorman, R. Van Berg, R. G. Van de Water, C. J. Virtue, B. L. Wall, D. Waller, C. E. Waltham, H. Tseung, D. L. Wark, N. West, J. B. Wilhelmy, J. F. Wilkerson, J. R. Wilson, J. M. Wouters, M. Yeh, and K. Zuber. Measurement of the total active $^{8}\mathrm{B}$ solar neutrino flux at the Sudbury neutrino observatory with enhanced neutral current sensitivity. *Phys. Rev. Lett.* ***92****, 181301 (2004).*

[220] B. W. Filippone, A. J. Elwyn, C. N. Davids, and D. D. Koetke. Measurement of the $^{7}\mathrm{Be}(p,\gamma)^{8}\mathrm{B}$ reaction cross section at low energies. *Phys. Rev. Lett.* ***50****, 412 (1983).*

[221] B. W. Filippone, A. J. Elwyn, C. N. Davids, and D. D. Koetke. Proton capture cross section of $^{7}\mathrm{Be}$ and the flux of high energy solar neutrinos. *Phys. Rev. C* ***28****, 2222 (1983).*

[222] F. Hammache, G. Bogaert, P. Aguer, C. Angulo, S. Barhoumi, L. Brillard, J. F. Chemin, G. Claverie, A. Coc, M. Hussonnois, M. Jacotin, J. Kiener, A. Lefebvre, J. N. Scheurer, J. P. Thibaud, and E. Virassamynaïken. New measurement and analysis of the $^{7}\mathrm{Be}(p,\gamma)^{8}\mathrm{B}$ cross section. *Phys. Rev. Lett.* ***80****, 928 (1998).*

[223] F. Hammache, G. Bogaert, P. Aguer, C. Angulo, S. Barhoumi, L. Brillard, J. F. Chemin, G. Claverie, A. Coc, M. Hussonnois, M. Jacotin, J. Kiener, A. Lefebvre, C. Le Naour, S. Ouichaoui, J. N. Scheurer,

V. Tatischeff, J. P. Thibaud, and E. Virassamynaïken. Low-energy measurement of the ^{7}Be$(p,\gamma)^8$B cross section. *Phys. Rev. Lett.* ***86****, 3985 (2001).*

[224] A. R. Junghans, E. C. Mohrmann, K. A. Snover, T. D. Steiger, E. G. Adelberger, J. M. Casandjian, H. E. Swanson, L. Buchmann, S. H. Park, and A. Zyuzin. ^{7}Be$(p,\gamma)^8$B astrophysical S factor from precision cross section measurement. *Phys. Rev. Lett.* ***88****, 041101 (2002).*

[225] A. R. Junghans, E. C. Mohrmann, K. A. Snover, T. D. Steiger, E. G. Adelberger, J. M. Casandjian, H. E. Swanson, L. Buchmann, S. H. Park, A. Zyuzin, and A. M. Laird. Precise measurement of the ^{7}Be$(p,\gamma)^8$B S factor. *Phys. Rev. C* ***68****, 065803 (2003).*

[226] L. T. Baby, C. Bordeanu, G. Goldring, M. Hass, L. Weissman, V. N. Fedoseyev, U. Köster, Y. Nir-El, G. Haquin, H. W. Gäggeler, R. Weinreich, and ISOLDE Collaboration. New measurement of the proton capture rate on ^{7}Be and the $S_{17}(0)$ factor. *Phys. Rev. C* ***67****, 065805 (2003).*

[227] L. T. Baby, C. Bordeanu, G. Goldring, M. Hass, L. Weissman, V. N. Fedoseyev, U. Köster, Y. Nir-El, G. Haquin, H. W. Gäggeler, R. Weinreich, and ISOLDE Collaboration. Precision measurement of the ^{7}Be$(p,\gamma)^8$B cross section with an implanted ^{7}Be target. *Phys. Rev. Lett.* ***90****, 022501 (2003).*

[228] L. T. Baby, C. Bordeanu, G. Goldring, M. Hass, L. Weissman, V. N. Fedoseyev, U. Köster, Y. Nir-El, G. Haquin, H. W. Gäggeler, R. Weinreich, and ISOLDE Collaboration. Erratum: New measurement of the proton capture rate on ^{7}Be and the $S_{17}(0)$ factor. *Phys. Rev. C* ***69****, 019902(E) (2004).*

[229] L. T. Baby, C. Bordeanu, G. Goldring, M. Hass, L. Weissman, V. N. Fedoseyev, U. Köster, Y. Nir-El, G. Haquin, H. W. Gäggeler, R. Weinreich, and ISOLDE Collaboration. Erratum: Precision measurement of the ^{7}Be$(p,\gamma)^8$B cross section with an implanted ^{7}Be target. *Phys. Rev. Lett.* ***92****, 029901 (2004).*

[230] A. R. Junghans, K. A. Snover, E. C. Mohrmann, E. G. Adelberger, and L. Buchmann. Updated S factors for the ^{7}Be$(p,\gamma)^8$B reaction. *Phys. Rev. C* ***81****, 012801(R) (2010).*

[231] G. Baur, C. A. Bertulani, and H. Rebel. Coulomb dissociation as a source of information on radiative capture processes of astrophysical interest. *Nucl. Phys. A* ***458****, 188 (1986).*

[232] F. Schümann, F. Hammache, S. Typel, F. Uhlig, K. Sümmerer, I. Böttcher, D. Cortina, A. Förster, M. Gai, H. Geissel, U. Greife, N. Iwasa, P. Koczoń, B. Kohlmeyer, R. Kulessa, H. Kumagai, N. Kurz, M. Menzel, T. Motobayashi, H. Oeschler, A. Ozawa, M. Płoskoń, W. Prokopowicz, E. Schwab, P. Senger, F. Strieder, C. Sturm, Zhi-Yu Sun, G. Surówka, A. Wagner, and W. Waluś. Measurement of the Coulomb dissociation of ^{8}B at 254 mev/nucleon and the ^{8}B solar neutrino flux. *Phys. Rev. Lett.* ***83****, 232501 (1999).*

[233] B. Davids, W. W. Anthony, T. Aumann, S. M. Austin, T. Baumann, D. Bazin, R. R. C. Clement, C. N. Davids, H. Esbensen, P. A. Lofy, T. Nakamura, B. M. Sherrill, and J. Yurkon. $S_{17}(0)$ Determined from the Coulomb breakup of 83 mev/nucleon ^{8}B. *Phys. Rev. Lett.* ***86****, 2750 (2001).*

[234] F. Schümann, F. Hammache, S. Typel, F. Uhlig, K. Sümmerer, I. Böttcher, D. Cortina, A. Förster, M. Gai, H. Geissel, U. Greife, N. Iwasa, P. Koczoń, B. Kohlmeyer, R. Kulessa, H. Kumagai, N. Kurz, M. Menzel, T. Motobayashi, H. Oeschler, A. Ozawa, M. Płoskoń, W. Prokopowicz, E. Schwab, P. Senger, F. Strieder, C. Sturm, Zhi-Yu Sun, G. Surówka, A. Wagner, and W. Waluś. Coulomb dissociation of ^{8}B and the low-energy cross section of the ^{7}Be$(p,\gamma)^8$B solar fusion reaction. *Phys. Rev. Lett.* ***90****, 232501 (2003).*

[235] F. Schümann, S. Typel, F. Hammache, K. Sümmerer, F. Uhlig, I. Böttcher, D. Cortina, A. Förster, M. Gai, H. Geissel, U. Greife, E. Grosse, N. Iwasa, P. Koczoń, B. Kohlmeyer, R. Kulessa, H. Kumagai, N. Kurz, M. Menzel, T. Motobayashi, H. Oeschler, A. Ozawa, M. Płoskoń, W. Prokopowicz, E. Schwab, P. Senger, F. Strieder, C. Sturm, Zhi-Yu Sun, G. Surówka, A. Wagner, and W. Waluś. Low-energy cross section of the ^{7}Be$(p,\gamma)^8$B solar fusion reaction from the Coulomb dissociation of ^{8}B. *Phys. Rev. C* ***73****, 015806 (2006).*

[236] P. Descouvemont. Reanalysis of the ^{7}Be$(p,\gamma)^8$B S factor in a microscopic model. *Phys. Rev. C* ***70****, 065802 (2004).*

[237] M. Wiescher, R. Steininger, and F. Käppeler. ^{7}Li$(n,\gamma)^8$Li - Trigger reaction to a primordial r-process? *The Astrophysical Journal* ***344****, 464 (1989).*

[238] M. Heil, F. Käppeler, M. Wiescher, and A. Mengoni. The (n,γ) cross section of ^{7}Li. *The Astrophysical Journal* ***507****, 997 (1998).*

[239] Y. Nagai, M. Igashira, T. Takaoka, T. Kikuchi, T. Shima, A. Tomyo, A. Mengoni, and T. Otsuka. ^{7}Li$(n,\gamma)^8$Li reaction and the S_{17} factor at $E_{\mathrm{c.m.}} > 500$ kev. *Phys. Rev. C* ***71****, 055803 (2005).*

[240] R. Izsák, Á. Horváth, Á. Kiss, Z. Seres, A. Galonsky, C. A. Bertulani, Z. Fülöp, T. Baumann, D. Bazin, K. Ieki, C. Bordeanu, N. Carlin, M. Csanád, F. Deák, P. DeYoung, N. Frank, T. Fukuchi, A. Gade, D. Galaviz, C. R. Hoffman, W. A. Peters, H. Schelin, M. Thoennessen, and G. I. Veres. Determining the ^{7}Li(n,γ) cross section via Coulomb dissociation of ^{8}Li. *arXiv:1312.3498v1 [nucl-ex] , (2013).*

[241] P. Descouvemont and D. Baye. Microscopic study of the ^{7}Li$(n,\gamma)^8$Li and ^{7}Be$(p,\gamma)^8$B reactions in a multiconfiguration three-cluster model. *Nucl. Phys. A* ***567****, 341 (1994).*

[242] W. F. Hornyak. *Nuclear structure.* Academic Press Inc, 1975.

[243] A. Bohr and B. R. Mottelson. *Nuclear structure, Vol. 2: Nuclear deformations.* World Scientific Pub. Co., Singapore, 1998.

[244] H. Furutani, H. Horiuchi, and R. Tamagaki. Structure of the second 0^+ state of ^{4}He. *Prog. Theor. Phys.* ***60****, 307 (1978).*

[245] H. Furutani, H. Horiuchi, and R. Tamagaki. Cluster-model study of the $T = 1$ states in $A = 4$ system. *Prog. Theor. Phys.* ***62****, 981 (1979).*

[246] S. B. Dubovichenko and A. V. Dzhazairov-Kakhramanov. Electromagnetic effects in light nuclei and the cluster potential model. *Fiz. Elem. Chastits. At. Yadra* ***28****, 1529 (1997).*

[247] M. Hass, C. Broude, V. Fedoseev, G. Goldring, G. Huber, J. Lettry, V. Mishin, H. J. Ravn, V. Sebastian, L. Weissman, and ISOLDE Collaboration. A new measurement of the ^{7}Be$(p,\gamma)^8$B cross-section with an implanted ^{7}Be target. *Phys. Lett. B* ***462****, 237 (1999).*

[248] F. Strieder, L. Gialanella, G. Gyürky, F. Schümann, R. Bonetti, C. Broggini, L. Campajola, P. Corvisiero, H. Costantini, A. D'Onofrio, A. Formicola, Z. Fülöp, G. Gervino, U. Greife, A. Guglielmetti, C. Gustavino, G. Imbriani, M. Junker, P. G. P. Moroni, A. Ordine, P. Prati, V. Roca, D. Rogalla, C. Rolfs, M. Romano, E. Somorjai, O. Straniero, F. Terrasi, H. P. Trautvetter, and S. Zavatarelli. Absolute cross section of ^{7}Be$(p,\gamma)^8$B. *Nucl. Phys. A* ***696****, 219 (2001).*

[249] W. L. Imhof, R. G. Johnson, F. J. Vaughn, and M. Walt. Cross sections for the Li$^7(n,\gamma)$Li^8 reaction. *Phys. Rev.* ***114****, 1037 (1959).*

[250] E. Fermi and E. Teller. The capture of negative mesotrons in matter. *Phys. Rev.* ***72****, 399 (1947).*

[251] J. M. Levy-Leblond. Electron capture by polar molecules. *Phys. Rev.* ***153****, 1 (1967).*

[252] O. H. Crawford. Bound states of a charged particle in a dipole field. *Proc. Phys. Soc., London* ***91****, 279 (1967).*

[253] W. R. Garrett. Permanent and induced dipole requirements in ab initio calculations of electron affinities of polar molecules. *J. Chem. Phys.* ***71****, 651 (1979).*

[254] W. R. Garrett. Thermally stable negative ions of polar molecules. *J. Chem. Phys.* ***69****, 2621 (1978).*

[255] W. R. Garrett. Excited states of polar negative ions. *J. Chem. Phys.* ***77****, 3666 (1982).*

[256] W. R. Garrett. Critical electron binding to linear electric quadrupole systems. *J. Chem. Phys.* ***128****, 194309 (2008).*

[257] W. R. Garrett. Quadrupole-bound anions: Efficacy of positive versus negative quadrupole moments. *J. Chem. Phys.* ***136****, 054116 (2012).*

[258] W. R. Garrett. Rotational resonances in molecular scattering of ultra-low-energy electrons. *Phys. Rev. A* ***11****, 509 (1975).*

[259] D. V. Fedorov K. Riisager and A. S. Jensen. Quantum halos. *Europhys. Lett.,* ***49****, 547 (2000).*

[260] A. S. Jensen, K. Riisager, D. V. Fedorov, and E. Garrido. Structure and reactions of quantum halos. *Rev. Mod. Phys.* ***76****, 215 (2004).*

[261] K. Riisager. Halos and related structures. *Phys. Scr. T* ***152****, 014001 (2013).*

[262] R. E. Grisenti, W. Schöllkopf, J. P. Toennies, G. C. Hegerfeldt, T. Köhler, and M. Stoll. Determination of the bond length and binding energy of the helium dimer by diffraction from a transmission grating. *Phys. Rev. Lett.* ***85****, 2284 (2000).*

[263] W. R. Garrett. Non-Born-Oppenheimer approximation for very weakly bound states of molecular anions. *J. Chem. Phys.* ***133****, 224103 (2010).*

[264] C. D. Aliprantis and K. C. Border. *Infinite dimensional analysis. A hitchhiker's guide.* Springer, Third Ed., 2006.

[265] H. Esbensen and C. N. Davids. Coupled-channels treatment of deformed proton emitters. *Phys. Rev. C* ***63****, 014315 (2000).*

[266] C. N. Davids and H. Esbensen. Decay rate of triaxially deformed proton emitters. *Phys. Rev. C* ***69****, 034314 (2004).*

[267] A. Bohr and B. R. Mottelson. *Nuclear structure, Vol. 1: Single-particle motion.* World Scientific Pub. Co., Singapore, 1998.

[268] J. L. Carlsten, I. R. Peterson, and W. C. Lineberger. Binding of an electron by the field of a molecular dipole $LiCl^-$. *Chem. Phys. Lett.* ***37****, 5 (1976).*

[269] S. Ard, W. R. Garrett, R. N. Compton, L. Adamowicz, and S. G. Stepanian. Rotational states of dipole-bound anions of hydrogen cyanide. *Chem. Phys. Lett.* ***473****, 223 (2009).*

[270] K. Riisager, A. S. Jensen, and P. Møller. Two-body halos. *Nucl. Phys. A* ***548****, 393 (1992).*

[271] A. T. Kruppa and W. Nazarewicz. Gamow and R-matrix approach to proton emitting nuclei. *Phys. Rev. C* ***69****, 054311 (2004).*

[272] N. Michel. Description des noyaux faiblement liés par le modèle en couches avec couplage au continuum. *Thèse de doctorat, Caen (2003).*

Titre : Réactions de capture radiative et spectroscopie d'anions multipolaires dans le cadre du Gamow Shell Model

Les systèmes quantiques ouverts, dont les propriétés sont profondément affectées par l'environnement, sont étudiés dans divers domaines de la physique : physique nucléaire, physique atomique et moléculaire, optique quantique, etc. Ces systèmes à N-corps, en dépit de leur particularités, possèdent des propriétés génériques qui sont communes à tous les systèmes liés et non-liés près du seuil. Le couplage au continuum est essentiel pour décrire les réactions nucléaires à basse énergie d'intérêt astrophysique, la formation des états à halo dans les noyaux, les agrégats moléculaires et les anions dipolaires, ou encore les corrélations à deux neutrons ou de particule alpha proche du seuil (*clustering*). Récemment, l'extension du modèle en couche nucléaire aux systèmes quantiques ouverts, le *Gamow Shell Model* (GSM), basé sur l'utilisation de la base de Berggren, a été appliquée avec succès à la description du spectre résonant de différents noyaux atomiques. La formulation du GSM dans la représentation des canaux-couplés (GSM-CC) permet de décrire diverses réactions nucléaires à basse énergies.

Dans le présent manuscrit, le GSM-CC est formulé pour la description des réactions de capture radiative d'un proton ou d'un neutron d'intérêt astrophysique et appliqué aux réactions : $^{17}\mathrm{F}(p,\gamma)^{18}\mathrm{Ne}$, $^{7}\mathrm{Be}(p,\gamma)^{8}\mathrm{B}$ et $^{7}\mathrm{Li}(n,\gamma)^{8}\mathrm{Li}$. De plus, pour la première fois, le GSM a été appliqué en physique atomique à la description des spectres d'anions dipolaires. Une étude systématique du cyanure d'hydrogène (HCN^-) a permis l'identification de bandes d'états collectives à la fois dans le régime de fort couplage, pour les états à halo faiblement liés, et dans le régime de faible couplage au dessus du seuil de dissociation. Dans le régime de fort couplage, une bande rotationnelle $K_J = 0$ de l'anion a été trouvée. Au dessus du seuil, le nombre quantique K_J n'est pas conservé. Les résonances dans ce régime forment des bandes rotationnelles selon le moment angulaire du dipôle, tandis que les énergies et temps de vie dépendent essentiellement du moment angulaire orbital de l'électron externe.

Mots clefs : Physique nucléaire, atomes, résonances, moments dipolaires, sections efficaces, structure nucléaire, réactions directes.

Title: Radiative capture reactions and spectroscopy of multipolar anions in the framework of Gamow Shell Model.

Small open quantum systems, whose properties are profoundly affected by the environment of continuum states, are intensely studied in various fields of Physics: nuclear physics, atomic and molecular physics, quantum optics, etc. These different many-body systems, in spite of their specific features, have generic properties which are common to all weakly bound or unbound systems close to the threshold. Coupling to the continuum is essential to describe the low-energy nuclear reactions of astrophysical interest, the formation of halo states in nuclei, atomic clusters and dipolar anions, or the near-threshold two neutron and alpha particle correlations (clustering). Recently, the open quantum system extension of the nuclear shell model, the Gamow shell model (GSM), based on the Berggren ensemble, has been applied successfully for the description of resonant states spectra in atomic nuclei. The coupled-channel formulation of the GSM (GSM-CC) allows to describe various low-energy nuclear reactions.

In this work, the GSM-CC is formulated and applied for the description of proton/neutron radiative capture reactions of astrophysical interest, such as: $^{17}\mathrm{F}(p,\gamma)^{18}\mathrm{Ne}$, $^{7}\mathrm{Be}(p,\gamma)^{8}\mathrm{B}$ and $^{7}\mathrm{Li}(n,\gamma)^{8}\mathrm{Li}$. Moreover, for the first time, the GSM has been applied in atomic physics for the description of spectra of dipolar anions. Systematic investigation of the hydrogen cyanide dipolar anion (HCN^-) allowed to identify the collective bands of states both in the strong coupling regime, for weakly bound halo states, and in the weak coupling regime above the dissociation threshold. In the strong coupling regime, $K_J = 0$ anion a rotational band has been found. Above the threshold, K_J quantum number is not conserved. Resonances in this regime form rotational bands according to the angular momentum of the rotating molecule, whereas the bandhead energies and the lifetimes depend predominantly on the external electron wave function.

Keywords: Nuclear physics, atoms, resonances, dipole moments, cross sections, nuclear structure, direct reactions.